Doctoral Dissertation
Doctoral Program in Civil and Environmental Engineering (35th Cycle)

Structural Assessment of 50-year-old Prestressed Concrete Bridge Girders

By

Pierclaudio Savino

******

Supervisor(s):
Prof. F. Tondolo, Supervisor
Prof. D. Sabia, Co-Supervisor

Doctoral Examination Committee:
Prof. B. Belletti, Referee, University of Parma
Prof. A. Recupero, Referee, University of Messina
Prof. N. Spinella, University of Messina
Prof. A.P. Fantilli, Politecnico di Torino
Prof. G.C. Marano, Politecnico di Torino

Politecnico di Torino
2023

Declaration

I hereby declare that, the contents and organization of this dissertation constitute my own original work and does not compromise in any way the rights of third parties, including those relating to the security of personal data.

Pierclaudio Savino

2023

* This dissertation is presented in partial fulfillment of the requirements for **Ph.D. degree** in the Graduate School of Politecnico di Torino (ScuDo).

I would like to dedicate this thesis to my guardian angels, who held my hand when I first entered this world and continue to light my way from the heavens.

Acknowledgment

It was in November 2020 when I was granted a PhD student position at the Department of Structural, Geotechnical and Building Engineering at Politecnico di Torino, with the primary goal of planning and executing an experimental campaign aimed at assessing the structural performance of full-scale bridge elements. This was the beginning of an intense, challenging, and unforgettable journey towards my doctoral thesis. Therefore, there are several people who have made all this possible and who need to be acknowledged.

First of all, I would like to thank my supervisor, Prof. Francesco Tondolo, and my co-supervisor, Prof. Donato Sabia, who believed in my ability to undertake this ambitious research project and gave me the opportunity to start this unforgettable experience. I am grateful for giving me the possibility to choose my own direction in several research interests and to develop my independence. At the same time, I am grateful for their guidance, which facilitated not only my technical development but also my personal growth. I must also express my gratitude to Eng. Antonino Quattrone and Prof. Alessandro Fantilli for generously sharing their expertise and providing invaluable insights during our discussions. I would express my gratitude to all the members of the Management Committee for their vision in establishing the BRIDGE|50 research project and making possible this significant experimental campaign for the benefit of the scientific community and management authorities.

In any complex experiment, the dedication and hard work of a committed team are essential prerequisites for success. Therefore, I wish to extend my heartfelt thanks to all the technicians of the MastrLAB laboratory. Their tireless efforts and constant presence, even in adverse conditions, have been instrumental in achieving our common objectives. Together, we have worked side by side, braving the ice of winter and the fire of summer, but through an enjoyable working environment we have achieved our destination.

Lastly, I am deeply grateful to my family and friends for their support and inspiration throughout this journey. I have a special debt of gratitude to my wife for her extraordinary patience and motivation, which have sustained me during the most challenging phases of my research.

In conclusion, I am deeply indebted to each of these individuals and entities for their indispensable role in shaping my academic and personal growth during this transformative journey. Your support and guidance have been the secret of my success, and I am grateful for the impact you have had on my life.

Abstract

The management of existing civil infrastructure, particularly bridges, is a complex and critical challenge in the field of civil engineering. Bridge deterioration has become a pressing issue due to factors such as increased traffic loads, environmental impacts, use of de-icing salts, limited maintenance programs, and poor-quality structural materials. As a result, bridges can exhibit both structural deficiencies and functional obsolescence, highlighting the importance of their thorough assessment in modern civil engineering. Structural assessment is a multi-stage process that involves refining analytical models, planning diagnostic campaigns, and gaining a comprehensive understanding. However, this process is often constrained by resource limitations, low accessibility, and the need for accurate parameter estimation. Consequently, a systematic and rational approach is essential to address the technical and economic challenges associated with structural assessment. While several countries have developed safety assessment guidelines based on different formats, there is a notable gap in terms of a suitable framework to establish reliable and feasible techniques to achieve a predetermined and acceptable level of knowledge. In order to limit this gap, the present research defined a robust and practical framework for the structural assessment of existing prestressed concrete (PC) bridges. To accomplish this objective, a comprehensive experimental program was undertaken as part of the BRIDGE|50 research project, focusing on full-scale testing of PC bridge girders removed after 50 years of service. The aim of this program was to provide extensive data on the

performance of aging girders, facilitating informed decision-making processes for bridge management agencies.

This thesis deals with several key areas of investigation in the context of the structural assessment of existing PC bridges. Firstly, a thorough durability assessment was conducted, employing visual inspection and non-destructive testing (NDT) techniques. These techniques, including half-cell potential mapping, concrete resistivity measurement, carbonation depth evaluation, and corrosion current density measurements, effectively assessed the extent and rate of deterioration and provided valuable insight into the structural condition of bridges. The mechanical characterization of the materials was carried out using destructive methods. For concrete's mechanical properties, an integrated approach with both destructive and NDT techniques has been also used, allowing for the investigation of larger areas and reducing material uncertainties in a cost-effective manner. For prestress loss estimates, several methods have been used involving destructive tests, NDT, and analytical models. A valuable procedure has been proposed to estimate the prestress loss for girders still in service, based on the so-called saw-cut method. In addition, a comprehensive analysis of the structural behavior was carried out through full-scale load tests on the PC girders. These tests included different levels of damage and loading configurations, allowing a detailed examination of the structural behavior under different scenarios. By inducing different loading conditions to stimulate different resistance mechanisms, the resulting load-deflection curves, midspan strains, and failure modes were thoroughly analyzed. The outcomes of these analyses provided a comprehensive insight into the performance of existing PC bridges under realistic conditions. Finally, a comparative analysis of different safety formats was carried out within a multi-level framework, ranging from deterministic to probabilistic approaches. By integrating these safety formats into the assessment process, more informed decisions could be made based on the research findings.

In conclusion, this research highlights the urgent need for a robust and practical framework for the structural assessment of existing PC bridges. The experimental program undertaken as part of this study provides valuable insight into the performance and condition of aging bridge girders. By incorporating NDT, characterization of mechanical properties, and comprehensive analysis of structural behavior, the research presents a holistic approach to bridge assessment, thereby aiding in the development of effective maintenance and management strategies for existing PC bridges.

Contents

1. Introduction..1
  1.1 Background...1
  1.2 Literature review..5
  1.3 Scientific approach and scope of the thesis 14
    References..17
2. Corso Grosseto viaduct..21
  2.1 History 21
  2.2 Geometry 24
  2.3 Material..25
  2.4 Girder reinforcing...26
  2.5 Demolition operation...27
  2.6 BRIDGE|50 research project 30
    References..33
3. Full-scale tests on PC girders 35
  3.1 Introduction 35
  3.2 Non-destructive assessment of deterioration................................36
    3.2.1 Visual inspection...37
    3.2.2 Corrosion measurements...40
  3.3 Full-scale load tests 50
    3.3.1 Loading tests plan 51
    3.3.2 Loading frame..53

3.3.3 Measurement system......55
3.3.4 Three-point bending test results......58
3.3.4 Four-point bending test results......65
3.3.5 Four-point bending test of PC box girder......73
3.4 Material tests......78
3.4.1 Rebound hammer test......79
3.4.2 Uniaxial concrete compressive tests......88
3.4.3 Tensile splitting strength test......93
3.4.4 Reinforcing steel tensile tests......95
References......99
4. Assessment of prestress loss in 50-year-old PC bridge girders......104
4.1 Introduction......104
4.2 Experimental program for prestress loss assessment......111
4.2.1 Residual prestress from cracking load test......112
4.2.2 Residual prestress from decompression load test......117
4.2.3 Residual prestress from saw-cut method......119
4.2.4 Residual prestress from strand-cutting method......124
4.2.5 Comparison of experimental results on prestress loss......127
4.3 Analytical prediction of prestress loss......129
4.3.1 Prestress loss according to Eurocode's model......130
4.3.2 Prestress loss according to AASHTO's refined model......134
4.3.3 Proposed model based on Eurocode's formulation......139
4.3.4 Analytical models comparison......141
4.3.5 Probabilistic analysis of prestress loss prediction......144
References......151
5. Structural assessment......156
5.1 Introduction......156
5.2 Structural analysis......158

5.2.1 Load distribution methods 159
5.2.2 Load analysis results 164
5.3 Moment-curvature analysis 166
5.4 Safety assessment 172
5.4.1 Safety formats 172
5.4.2 Safety verification results 177
References 182
6. Conclusions 184
6.1 Aim and main achievements 184
6.2 Future research 189
Appendix A 191
Appendix B 201
Appendix C 210
Appendix D 215
Appendix E 223

List of Figures

Figure 1: C.so Grosseto viaduct (west view). 21

Figure 2: C.so Grosseto West – C.so Grosseto East and C.so Potenza – C.so Grosseto East routes..22

Figure 3: The construction site during building operations [2]........................22

Figure 4: Management records: (a) rust inhibitor treatment (October 2014), (b) debris removal from pier base (July 2016), (c) traffic restriction to 3.5 tons and 2.7 m height (April 2017), (d) closure of the viaduct (July 2017).........................23

Figure 5: Historical development of the Largo Grosseto interchange. 24

Figure 6: Geometry of the cross section at a pier (unit: m).............................25

Figure 7: Precast plant at the construction site [2]. 26

Figure 8: Layout of reinforcement in I-shaped and box cross-section............27

Figure 9: Demolition of the bridge using hydraulic crushers..........................28

Figure 10: End parts tested within the BRIDG|50 research project. 28

Figure 11: Dismantling operations: (a) cutting, (b) drilling, (c) lifting, (d) transportation. 29

Figure 12: In-service layout of the investigated structural members. 30

Figure 13: Effects of steel corrosion on pier cap. 37

Figure 14: Corrosion scenario at the end of the girders adjacent to pier cap 46. 38

Figure 15: Inadequate quality controls: (a) concrete segregation, (b) macro-voids, (c) insufficient concrete cover thickness. 38

Figure 16: Typical damages due to dismantling operations: top slab drilling and strands cutting. 39

Figure 17: Half-cell potential measurement. 40

Figure 18: Cumulative frequency distribution of half-cell potentials measured on: (a) B3-P47/46, (b) B8-P47/46, (c) B4-P47/46, (d) B9-P47/46, (e) B6-Ab/P47, (f) B6-P48/49 (g) B10-Ab/P47, (h) B5-P47/46 girder..42

Figure 19: Scheme of the Wenner technique. 43

Figure 20: Cumulative frequency distribution of electrical resistivities measured on: (a) B3-P47/46, (b) B8-P47/46, (c) B4-P47/46, (d) B9-P47/46, (e) B6-Ab/P47, (f) B6-P48/49 (g) B10-Ab/P47, (h) B5-P47/46 girder. 45

Figure 21: Electrical circuit of reinforced concrete system in CEPRA. 47

Figure 22: Cumulative frequency distribution of corrosion rate measured on: (a) B3-P47/46, (b) B8-P47/46, (c) B4-P47/46, (d) B9-P47/46, (e) B6-Ab/P47, (f) B6-P48/49 (g) B10-Ab/P47, (h) B5-P47/46 girder..48

Figure 23: Strands cutting in B5-P47/46 girder (bottom view). 51

Figure 24: Building stages of the steel reaction frame..................................54

Figure 25: Technical drawing of the load frame: steel frame base (black), supporting frames (blue), and loading system (red) (unit: cm). 54

Figure 26: General view of test setup: (a) three-point loading configuration, (b) four-point loading configuration. 55

Figure 27: Load-midspan deflection curves: (a) B3-P47/46, (b) B8-P47/46, (c) B4-P47/46, (d) B9-P47/46 girder..60

Figure 28: Detail of the failure zone: (a) B3-P47/46, (b) B8-P47/46, (c) B4-P47/46, (d) B9-P47/46 girder...61

Figure 29: Crack pattern after failure: (a) B3-P47/46, (b) B8-P47/46, (c) B4-P47/46, (d) B9-P47/46 girder...61

Figure 30: Load-tensile strain curves (cracking load): B3-P47/46, B8-P47/46, B4-P47/46, and B9-P47/46 girder. 62

Figure 31: Load-compressive strain curves: B3-P47/46, B8-P47/46, and B9-P47/46 girder..63

Figure 32: Load-tensile strain curves (decompression load): B3-P47/46, B8-P47/46, and B9-P47/46 girder. 63

Figure 33: Load-shear strain curves: (a) B8-P47/46, (b) B9-P47/46 girder....64

Figure 34: Load-midspan deflection curves: (a) B7-P47/46, (b) B6-Ab/P47, (c) B6-P48/49, (d) B10-Ab/P47, (e) B5-P47/46 girder. 66

Figure 35: Detail of the failure zone: (a) B7-P47/46, (b) B6-Ab/P47, (c) B6-P48/49, (d) B10-Ab/P47, (e) B5-P47/46 girder...68

Figure 36: Crack pattern after failure: (a) B7-P47/46, (b) B6-Ab/P47, (c) B6-P48/49, (d) B10-Ab/P47, (e) B5-P47/46 girder...68

Figure 37: Load-tensile strain curves (cracking load): B7-P47/46, B6-Ab/P47, B6-P48/49, and B10-Ab/P47 girder......69

Figure 38: Load-compressive strain curves: B7-P47/46, B6-Ab/P47, B6-P48/49, B10-Ab/P47, and B5-P47/46 girder. 70

Figure 39: Load-tensile strain curves (decompression load): B7-P47/46, B6-Ab/P47, B6-P48/49, and B10-Ab/P47 girder. 70

Figure 40: Cross-section strain (recorded by sg1, C-01, C-02, C-03, and T-01): (a) B6-Ab/P47, (b) B6-P48/49, (c) B10-Ab/P47, (d) B5-P47/46 girder. 71

Figure 41: Load-shear strain curves: (a) B7-P47/46, (b) B6-P48/49 girder....72

Figure 42: Working phases of curb cutting. 73

Figure 43: Load-midspan deflection curve of Bx2-Ab/P47 girder. 74

Figure 44: Cracks after the load test: (a) detail of the failure zone, (b) cracks pattern. 74

Figure 45: Load-tensile strain curves (cracking load) of Bx2-Ab/P47 girder.75

Figure 46: Load-compressive strain curves of Bx2-Ab/P47 girder. 75

Figure 47: Load-tensile strain curves (decompression load) of Bx2-Ab/P47 girder. 76

Figure 48: Cross-section strain of Bx2-Ab/P47 girder: (a) inner side, (b) exposed side. 76

Figure 49: Load-strand strain. 77

Figure 50: Load-shear strain curves of Bx2-Ab/P47 girder. 77

Figure 51: Cumulative distribution function of rebound hammer test results.83

Figure 52: Core data and conversion model identified with the least-square criterion. 86

Figure 53: Concrete coring. 89

Figure 54: Typical failure mode of core specimens. 92

Figure 55: Tensile splitting strength test. 94

Figure 56: Typical stress-strain diagrams for: (a) rebar, (b) strand. 96

Figure 57: Load-deflection analysis: (a) identification of stiffness drop, (f) determination of the cracking load. 116

Figure 58: Static scheme for completely crushed girders. 120

Figure 59: Saw-cut test: (a) strain gauge setup, (b) left side cut, (c) right side cut, (d) triangular prism shape. 121

Figure 60: Strain relief measured for B5-P47/46 girder. 122

Figure 61: Operative phases of strand-cutting method: (a) strand cleaning, (b) bonding of strain gauges, (c) wire cutting, (d) strands cut. 125

Figure 62: Percent loss of jacking stress from experimental tests. 128

Figure 63: Comparison between predicted and experimental prestress loss. 143

Figure 64: Simulation procedure. 145

Figure 65: Prestress loss histogram of the Monte Carlo simulation computed for the probability distribution function of: (a) girder concrete compressive strength, (b) girder concrete modulus of elasticity, (c) slab concrete compressive strength, (d) slab concrete modulus of elasticity, (e) strand tensile strength, (f) strand modulus of elasticity, (g) rebar modulus of elasticity, and (h) relative humidity. 148

Figure 66: Probability density function for predicted prestress loss. 149

Figure 67: Schematic representation of the bridge deck. 158

Figure 68: Relationships between the stiffness of longitudinal beams and transverse system: (a) transverse system without bending stiffness, (b) transverse system with infinite bending stiffness, and (c) longitudinal beams with infinite torsional stiffness. 159

Figure 69: Schematization of the transverse behavior according to the Courbon assumption. 159

Figure 70: Plane grid layout. 161

Figure 71: Transverse arrangement of load model 1 prescribed by NTC (unit: cm). 164

Figure 72: Layered section analysis. 167

Figure 73: Numerical and experimental load-midspan deflection curves of the three-point bending tests. 170

Figure 74: Numerical and experimental load-midspan deflection curves of the four-point bending tests. 171

Figure 75: Probability distribution functions of the safety margin, load, and resistance...174

Figure 76: Histograms of midspan section resistance for: (a) box, and (b) I-girder...180

List of Tables

Table 1: Weighted average of corrosion measurements................................49

Table 2: Load test protocol...52

Table 3: Number of sensors installed for each load test................................57

Table 4: Outcomes of the three-point bending tests.......................................64

Table 5: Outcomes of the four-point bending tests. 72

Table 6: Statistical parameters of the rebound index for each test region......80

Table 7: Statistical parameters of the rebound index for each girder............82

Table 8: NDT and compression strength test results at core locations..........84

Table 9: NDT results and compressive strength estimation based on NDT results...87

Table 10: Compression strength test results..90

Table 11: Tensile splitting strength test results. 94

Table 12: Uniaxial tensile test results..96

Table 13: Mechanical and geometric properties..113

Table 14: Input bending moments and effective prestressing stress estimated by cracking load method...114

Table 15: Input bending moments and effective prestressing stress estimated using the modified version of the cracking load method...................................116

Table 16: Input bending moments and effective prestressing stress estimated by the decompression load method...118

Table 17: Effective prestressing stress obtained by the saw-cut method. 122

Table 18: Effective prestressing stress obtained by the strand-cutting method. 125

Table 19: Input parameters for prestress loss prediction models. 142

Table 20: Statistical parameters of the normal distribution functions..........146

Table 21: Bending moments at midspan for box and I-girder based on Courbon, Engesser, and plane grid analysis (unit: kNm). 165

Table 22: Mean values of the mechanical properties used in the models. ...168

Table 23: Target reliability index β_T (EC-0). 176

Table 24: Target reliability index β_T (JCSS). 177

Table 25: Comparison between the maximum bending moment calculated according to NTC code and that of the original design (unit: kNm). 178

Table 26: Statistics of the resistance and bending moment variables considered in the reliability analysis...181

Chapter 1

Introduction

1.1 Background

As inhabitants of the Earth, we are experiencing global crises interconnected by the COVID-19 pandemic, the war in Ukraine, the food and energy crises, all against the background of a climate change emergency. Major supply-chain disruptions, rising inflation, and unsustainable debt are just some of the destructive consequences of these crises on the current global economy. According to the Sustainable Development Goals Report 2022 [1], maintaining high-quality infrastructure plays a key role in economic growth and prosperity for a country. Transport systems contribute directly or indirectly to the pursuit of sustainable development. While infrastructure promotes growth by facilitating access to education, healthcare, employment, and markets, its responsible management can reduce the unsustainable consumption of resources. As part of the transport infrastructure, bridges are essential elements as they connect different points that usually cannot be accessed, controlling and influencing the capacity of the traffic flow in the transport system. If a bridge is not functioning, the viability of the road is compromised by delays, the need for alternative routes, and increased travel distances [2]. Because of their importance, bridges need to be carefully planned and designed, looking for the right balance between current and future traffic demand, cost, and safety.

However, with the aging of the bridges, their structural integrity deteriorates in spite of increasing loads and traffic volumes. This deterioration is exacerbated by the harmful effects of environmental pollution, extensive use of de-icing salt, and the poor quality of construction materials. While the process of deterioration is accelerating, it is expected that bridges will remain operational throughout their lifetime. Therefore, although bridges are a strategic component of the transportation system with significant social and economic impacts, the rate of repair remains relatively slow, and maintenance programs are often limited. Policy choices and the allocation of funds to other priorities contribute to this deadlock, while the cost of bridge repairs continues to rise due to their aging and weakening. Maintaining structures in a functional state is also a complex task due to the wide variety of structural typologies. Different types of structures are characterized by different behaviors, mechanisms of deterioration, and require suitable maintenance operations. Moreover, bridge owners around the world are today dealing with a huge stock of structurally deficient bridges in need of modernization. Especially in Europe, a considerable number of bridges were built between 1945 and 1960 to replace the numerous bridges that were destroyed during the Second World War, and in the subsequent decade to build major motorway networks. A large scale of resources was mobilized to build a great number of new bridges, limiting maintenance to urgent repairs. Statistics from the European Integrated Research Project “Sustainable Bridges” show that of 220000 bridges owned by 17 different railways and representative of the 300000 railway bridges in Europe, almost 67% are more than 50 years old, while only 11% are less than 20 years old [3]. In the United States, approximately 40% of the total 618000 bridges require structural repair, rehabilitation, or replacement. Currently, 42% of the highway bridges in this country are over 50 years old. It has been estimated that at the current investment rate of $14.4 billion per year, it will require until 2071 to finish all necessary repairs [4]. In developing countries, the number of bridges is growing rapidly. In China, the total number of bridges reached 860000 by the end of 2013, ranking first in the world. It is expected to exceed one million by 2025. However, although the average service life of national bridges is only 23.8 years, national railway bridges classified as severely deteriorated account for 24.8% of the total number of bridges [5]. As it is economically and strategically impossible to replace all structurally deficient bridges in the short term, the average age of bridges and maintenance investment will increase exponentially in the future. This situation reflects the urgent need for comprehensive bridge management, including assessment, maintenance, and strengthening methods, to reduce costs and make our bridges safe under the required traffic conditions.

Various factors such as diverse climates, environmental influences, design and construction practices at different building site, lead to distinct challenges that impact the management of bridges within a specific country. Consequently, transport administrators in many countries have implemented appropriate bridge management procedures and practices to assess structural conditions and facilitate cost-effective decision-making processes. The bridge management committee of the International Association for Bridge Maintenance and Safety (IABMAS) has published a report on the bridge management systems adopted by 18 countries, encompassing the management of approximately 1 million structures [6]. According to the IABMAS report, all transportation agencies utilize condition information obtained from visual inspections to establish condition rating and prioritize the maintenance work. Therefore, there exists a lack of standardization in the field of bridge management. The policy governing the inspection and assessment of bridge conditions depends on the infrastructure owner. Although new standards and guidelines for assessing existing bridges have been developed in some countries (e.g. USA [7], Canada [8], UK [9], Germany [10], Switzerland [11], Netherlands [12] and Italy [13] are examples), in many cases, the assessment is usually performed by considering traditional codes intended for designing new bridges, and additional standards related to testing methods [14]. However, the design codes for new structures, which are based on a semi-probabilistic approach, make conservative assumptions regarding applied loads and corresponding structural responses. While these codes have ensured the safety of bridge designs over the years, their use for assessing existing structures may result in unnecessary and costly replacements or strengthening of numerous structures. Partial safety factors are defined to account for a wide range of uncertainties, which may not accurately represent the reality for an existing structure. To obtain a more accurate estimation of the actual load-carrying capacity and a realistic definition of safety level, it is crucial to determine the actual conservation state of the structural elements and the effective mechanical properties of the materials. Common strategies for structural assessment are based on successive detailed evaluations of the structural condition. However, the method employed by bridge authorities to assess the bridge conditions and plan repair and strengthening measures often ends with the calculation of a condition index based on visual inspections [15]. General guidelines have been established to determine the extent and severity of deterioration as part of the condition assessment. Non-destructive tests (NDTs) are not yet sufficiently integrated and regularly applied within the structural assessment process. There is a wide variety of methods available to gather information on the structural condition, but selecting the most effective is not always straightforward. Due to limited knowledge regarding the associated costs and time requirements, as well as difficulties in interpreting the data, bridge authorities often not consider NDT information into the structural assessment process. All of these remarks highlight that structural assessment necessitates a rational judgement to address numerous technical and economic issues throughout the entire process.

In such context, field measurements and full-scale experimental tests represent a strategic action to calibrate bridge assessment models and ensure a better understanding of the structural behavior of existing bridges. The use of results from full-scale loading tests allows to consider the degree of uncertainty that is representative of the bridge's in-service condition. Moreover, these tests provide a means to validate the practical applicability of assessment methods under realistic conditions. Given the diverse range of structural typologies, construction practices, environmental effects, and service lives, the knowledge gained from experimental tests conducted on decommissioned bridges is of significant value for each specific region. Storing high-quality disaggregated data on the structural performance of old bridges could provide valuable insights for similar bridges that are still in service. The establishment of a comprehensive database could augment statistical information on material properties and facilitate their incorporation into probabilistic strength assessments. Additionally, further theoretical and experimental research is required to develop rapid and cost-effective methods aimed at defining parameters essential for accurate predictions of the residual structural performance of existing structures. However, it is important to note that carrying out large-scale tests on existing bridges is both expensive and challenging, and therefore its applicability remains relatively limited.

The current state of bridge management necessitates the development of a cost-effective framework for structural assessment that includes methods capable of rapidly and reliably estimating the safety level. In light of this objective, the present study was undertaken, supported by the unique opportunity to validate methods and analytical models on full-scale prestressed concrete (PC) bridge girders. Among various structural typologies, PC bridges are prone to hidden effects that may not be readily detectable through simple investigations, requiring a comprehensive approach for their safety assessment. The performance of PC structures is significantly influenced by the bond between the steel and the surrounding concrete [16]. For an accurate assessment of existing PC bridges, the long-term effects leading to prestressing losses must also be taken into consideration. Furthermore, PC has been a dominant technique in the building of motorway and road bridges worldwide. The shortage of steel after the World War II made PC the most popular technique for bridge reconstruction during the 1950s. The production of precast beams under factory conditions resulted in cost-effective structures with minimal formwork requirements and rapid construction processes. Consequently, this facilitated the rapid urbanization of numerous major cities since the mid-1970s, where the growing volume of motorway traffic necessitated the development of long urban viaducts [17]. As a result, PC bridges constitute a significant portion of similar bridge assets in terms of structural type and age of construction, leading to an increased interest in assessing the structural performance of existing PC bridges in recent decades.

Prior to establishing the experimental program and planning subsequent work for this thesis, a comprehensive literature review was conducted to identify the current practice and needs in full-scale failure testing of PC bridges, focusing on aspects such as structural types, load test setups, prestressing loss assessment, material characterization, and ultimate load-carrying capacity. Additionally, a thorough literature review was conducted pertaining to various parts of the project, aiding in the formulation of more specific research questions.

1.2 Literature review

The Walnut Street Bridge [18], built in 1960 in East Hartford, was a simply supported multi-beam bridge. The deck consisted of 13 PC box girders with a span of 16.5 m. Due to severe deterioration, it was decided to completely replace the structure. A joint research program was set up to investigate the effect after 27 years of service on two beams. The average values of the concrete compressive strength and the modulus of elasticity were measured as 49 and 28300 MPa, respectively. The stress-strain curves of the strands were obtained, revealing a modulus of elasticity of 171000 MPa and an ultimate tensile strength of 1810 MPa. The prestressing force was determined by considering the crack reopening load during the loading test, resulting in an average strand stress of 1055 MPa at midspan. After testing, the strand-cutting method was applied to the exposed strand far from the yielding and transfer length, but with poor results. The beams were tested with load applied at third points to simulate HS-20 (1989 AASHTO) truck axle load. Both beams exhibited ductile behavior with ultimate bending capacities of 223 and 213 kN. The measured values greatly exceeded the flexural strength at factored load levels of 156 kN, required by the 1989 AASHTO specifications. Flexural cracking was not observed until loads of 129 and 158 kN were reached, well above the service load of 69.4 kN. Rao et al. [19] analyzed the fatigue behavior of two other beams from the same bridge. The beam subjected to cyclic loading increments, producing a strand stress range of $0.06f_{pu}$, exhibited excellent performance even after 1500000 cycles. However, the beam cycled with a strand stress range of $0.11f_{pu}$, simulating the effect of frequent overloading, experienced fatigue failure of the strand wires after 145000 cycles. The bridge girders were expected to perform with satisfactory fatigue strength if infrequent overloads occurred.

Azizinamini et al. [20] conducted an ultimate load test on a 25-year-old PC girder taken from a bridge near Lincoln. The girder, designed as a PC I-shaped cross-section, had a span of 16.7 m. According to the original design data, the strands were prestressed to 1206 MPa, which accounted for 70% of their ultimate strength. Material testing was performed on specimens obtained from undamaged areas after the ultimate test, and the obtained data aligned with the material properties specified in the design documents. The average compressive strength of the concrete was 34 MPa and the ultimate tensile stress of the strands was 1788 MPa. When the effective prestress obtained from the crack test was compared with the initial prestress, a total prestress loss of 20.7% was found. The ultimate load test was carried out with a four-point bending test setup with the applied loads at a distance of 1.8 m. The girder failed with crushing of the concrete in the top flange at a maximum load of 327.9 kN.

The ATH-144-0844 bridge was a PC bridge built in 1954 in Ohio [21]. The 6.7 m wide deck consisted of 22 inverted T-beams and concrete fill. In 1994, when it was scheduled for decommissioning due to misalignment and geometric issues, the bridge was in good structural condition. Each composite specimen removed, consisted of two adjacent inverted T-beams together with the concrete fill. The composite specimen was 0.61 m wide and 8.85 m long. A total of five composite samples were taken but only two were tested. After testing, compressive tests on the concrete samples from the inverted T-beam and the fill concrete gave an average concrete strength of 81 and 58 MPa, respectively. Tensile tests were conducted on the prestressing steel, revealing an ultimate strength of 1790 MPa. The loss of prestress was evaluated through the crack load, decompression load, and strand-cutting methods. These methods yielded prestress loss values ranging from 20% to 34% of the initial prestress of 1030 MPa. The specimens were subjected to a three-point bending test configuration until the compression concrete crushed. The results exhibited good agreement with the test data obtained from an original prototype beam casted in 1954, indicating that the beam’s performance had not deteriorated after 40 years.

Pessiki et al. [22] conducted an experimental investigation on two PC bridge I-beams after being in service for 28 years. These beams were extracted from the Shenango River Bridge in Pennsylvania, with a span length of 27.6 m. As the primary purpose of the experimental campaign was to determine prestressing losses, the slab was removed during demolition. A thorough inspection revealed excellent condition with no evidence of cracking prior to testing. Compressive strength tests carried out on concrete samples removed after completion of the ultimate load tests gave an average compressive strength of 58.2 MPa, greater than 65% of the original design strength. Modulus data taken during the compression tests gave an average value of 34100 MPa. Both beams were tested in a three-point bending test configuration. Failure occurred by crushing of the concrete in the compression zone at ultimate loads of 1115 and 1128 kN. The average prestress loss calculated starting from the decompression load was 18%, which was 60% of the loss predicted from the design specifications.

Eder et al. [23] tested two 50-year-old PC bridge girders 13.7 m long. The cross-section of the girders was I-shaped and connected to the deck slab by shear stirrups. The girders were post-tensioned with four bars, two of which were bent into a harped profile prior to tensioning. The external condition was judged to be good with the exception of longitudinal cracks from the quarter points along the harped bar on one girder. Compressive tests on concrete cores taken from untested girder on the same bridge, provided a compressive strength of 68 MPa. After the loading test, samples of the bar were removed and tested to determine the tensile strength properties. The bar was found to have an elastic modulus of 175 GPa and a tensile strength of 1000 MPa. The post-tensioning stress was calculated using the decompression load and was found to be 414 MPa. The loading test was conducted utilizing a four-point bending test configuration, with a shear span of about 5 m. The ultimate load capacity was indicated by the plateau load for one girder and the load at which the bar rupture occurred for the other. The girders failed at maximum applied loads of 346.5 and 335 kN, respectively. The theoretical nominal capacity showed that the deck slab was not effective in resisting the bending moment. In fact, the slab cracked and separated from the girders during the test. The measured ultimate strength was 20% higher than the live load based on AASHTO HS-20 truck loading, and even after 50 years, the structural performance had not been compromised.

The Sorell Causeway bridge was a 34-span PC road bridge built in Tasmania in 1957 with a span of 13 m [24]. The deck consisted of 14 simply supported T-beams, post-tensioned with two parabolic tendons containing 18 high-tensile steel wires. In 2002, due to the increasing size and frequency of longitudinal cracks in the web, it was decided to replace the bridge. During demolition, three beams with good external condition, moderate cracking and severe cracking respectively, were selected for detailed investigation. The load tests were carried out by applying two-point loads at the third points of each beam. The beam in good condition failed in bending at a load of 112 kN. The moderately and severely cracked beams failed in shear with maximum loads of 57 and 83 kN, respectively. Progressive failure of the strands in the tendons was recorded during each loading test. The presence of corrosion significantly reduced the ductility of the beams compared to the beam in apparently good condition, although the latter did not have a capacity greater than the design load.

The bridge No. 35-17-6.80 was a three-span structure with equal lengths of 14.6 m, located in Ohio [25]. The deck consisted of nine adjacent hollow-core box beams prestressed by twenty-seven strands in the bottom flange. Live load transfer between the beams was achieved by both tie rods and shear keys. The bridge was built in 1967 and after 43 years of service was considered to be in need of replacement. Prior to decommissioning, a full-scale load test of the bridge was planned to investigate the load transfer between girders with varying degrees of damage. Within a single span, the damage consisted of a cut on the bottom side of three beams, intercepting the first row of 14 strands. The load was applied over two spans using three independent steel frames with a hydraulic cylinder at the centre. A spreader beam was placed under each cylinder to distribute the load across more beams. Initially, the load was applied individually from each cylinder to study how the load was transferred transversely. In the second stage, all three cylinders were loaded simultaneously to determine the ultimate capacity of the span. The tests showed that the box girder behaved as a system. The undamaged span had an ultimate capacity of 2077 kN and the damaged span had a total applied load of 1633 kN, much higher than the service load.

During the construction of several new bridges in Utah, seven PC bridge girders were collected from Interstate 215 to determine the effective prestressing after 42 years of service and the ultimate shear capacity [26]. The bridge was built in 1968 as a four-span bridge with spans ranging from 7.1 m to 20.4 m. The investigated girders were 7.1 m long, I-shaped, with a composite slab. Compressive tests on concrete samples showed an average compressive strength of 48.9 MPa. According to the original design, the prestressing force at jacking was 964 kN and the estimated prestress loss was 19%. The strands were tested with tensile test obtaining an ultimate stress of 1780 MPa. A group of five girders were tested in a three-point bending test configuration to determine the effective prestress using the decompression load method. The average effective prestressing force for all the girders was 727.3 kN, corresponding to 25% of the losses. This value was compared with calculated values using the AASHTO LRFD, corresponding to 17% of losses. In addition, shear capacity tests were carried out on two girders at 122 cm from the centre of the support. The ultimate shear capacity was determined to be 727.7 and 1163.2 kN. A parametric study using a detailed finite-element model showed that the differences in shear capacity were mainly due to the concrete compressive strength of the concrete.

Four PC girders were collected from Interstate 15 in Utah [27]. The road bridge was built in 1960 and consisted of two adjacent three-span bridges. In 2004, the space between the two bridges was used to accommodate additional lanes. During decommissioning in 2011, four I-girders, adopted for the expansion, were salvaged from a span of 11.1 m. The girders were prestressed with 11 straight strands in the bottom flange and 2 in the top flange, with an ultimate strength of 1862 MPa. The original design gave an effective prestressing after losses of 1132 MPa. The shear reinforcement extended into the deck concrete to develop composite behavior. The specified compressive strength for the girder concrete in the original design was 34.5 MPa at 28 days. Compressive tests on concrete cylinders cored from the deck and girder gave an average compressive strength of 58.6 and 77.9 MPa, respectively. The average prestressing stress estimated using the decompression load method in a three-point bending test configuration was 1010 MPa. This value was compared with both the general and refined AASHTO LRFD methods, which gave values 4.9 and 8.4% higher than the measured stress. After estimating the prestressing loss, the girders were tested to failure with a point load at different locations to investigate shear, flexure-shear, and flexure failures. Assuming d, the depth from the top of the slab to the bottom of the girder, the tests were carried out with the load applied at distances of 1d, 2d, 4d from the centre of the support and the midspan. Each of the tests showed a similar failure with concrete crushing in the slab, except for the 1d test which failed with shear cracks leading from the support to the load and sliding of the prestressing strands.

Pepe et al. [28] reported load tests on three PC beams recovered during the demolition of the Sorell Causeway Bridge in 2002, after increasing corrosion was observed. The bridge was the first PC bridge in Australia when it was completed in 1957. It has been continuously exposed to an aggressive marine environment throughout its life. The bridge consisted of 34 spans 13 m long, each consisting of 14 post-tensioned T-beams. Post-tensioning was applied by two 18-wire tendons installed in parabolic ducts. The beams were selected to have severe cracking, moderate cracking and good surface condition, respectively. Unpublished project reports provided information on the concrete and prestressing steel strength, which were reported to be 34 MPa and 1670 MPa, respectively. However, subsequent tests conducted on the beams revealed average concrete compressive and steel tensile strengths of 61 MPa and 1870 MPa, respectively. Each beam was tested using a four-point system with loads applied at third points along the length of the beam. During the load test, progressive failure of the prestressing wires occurred without reaching the expected design capacity. The beam with the best surface condition exhibited an ultimate moment of 483 kNm and failed in flexural mode. In contrast, the other two beams failed in a brittle manner, characterized by large diagonal cracks and ultimate moments of 333 kNm and 243 kNm, respectively.

The Pesio Viaduct [29], built in Italy in 1965, was a 26-span bridge composed of simply supported PC box-girders. Each span comprised five 35 m long girders connected by transverse reinforced concrete beams. After 40 years of service, a set of girders was removed for the modernization of the A6 Torino-Savona motorway. An experimental campaign was commissioned to test 9 PC box-girders characterized by different states of deterioration according to visual inspections. The post-tensioning reinforcement consisted of 5+5 tendons placed in the two lateral webs. The design documents indicated a characteristic tensile strength for the prestressing reinforcement of 1800 MPa. The characteristic compressive strength for the precast concrete and top slab concrete was 45 and 25 MPa, respectively. The effective residual stress in the prestressing steel was determined using the decompression load method. The percentage loss with respect to the initial prestressing stress of 1106 MPa assumed in the original design ranged from 28% to 35%. The beams were tested to failure using a four-point bending test. The maximum failure load was 1503 kN, recorded with the crushing of the top compressed chord. The beams characterized by the most severe corrosion of the prestressing and ordinary reinforcements showed a 35% reduction in the ultimate load corresponding to the tensile steel failure or shear-failure along the connection between the vertical webs and the bottom flange. The maximum failure load was 2.54 times greater than the design value given in the original design documents.

The Kiruna Bridge in Sweden was a continuous five-spans bridge built in 1959 [30]. Due to subsidence caused by nearby mine workings, it was decided for the demolition in 2014. In this context, a test program was planned to evaluate the load-carrying capacity of the girders and strengthening methods using carbon fibre reinforced polymers (CFRP). The decks consisted of three post-tensioned girders connected to the top slab, ranging in length from 18 to 26.5 m, and a free distance of 5 m between them. Construction drawings specified a concrete quality higher than 40 MPa and a tensile strength for the post-tensioned reinforcement of 1700 MPa. Compressive tests on concrete samples taken from unloaded decks, gave an average compressive strength of 62.2 MPa. Uniaxial tensile tests on post-tensioned cables recovered during demolition gave an average tensile strength of 1734 MPa. Residual force in the post-tensioned cables was determined by decompression load, saw-cut and theoretical methods, with a variability of 35%. The loading system consisted of two transverse steel beams positioned to apply loads in the midspans of each girder and loaded to obtain failures in one of the outer girders and then in the inner girder. The loads for the two failures were 13400 kN and 12700 kN, respectively. Both girders failed in a mixed bending-shear mode, with extensive concrete cracking and yielding of the reinforcement, and subsequent failure of the stirrups crossing a diagonal crack in the girder.

Liu et al. [31] carried out destructive tests on four PC hollow beams that had been in service for 20 years in a freeze-thaw region. The bridge was built in 1995 for the G1 Expressway in China. The beams were prestressed by 14 strands with a strength of 1860 MPa and a tensile stress of 1395 MPa. The compressive strength of the concrete was 40 MPa. After the loading tests, the concrete with low stress and reinforcement were sampled and tested, resulting in a concrete compressive strength of 44.9 MPa and a tensile strength of 1937 MPa for the prestressed reinforcement. Before conducting the loading test, the corrosion potential of the beams was measured. The results indicated that corrosion activity was observed only at the end zone of the beams, while the remaining portions showed no signs of corrosion. The loading tests were performed in a four-point bending test configuration with a span of 15.6 m and a distance between the two loading points of 2.0 m and 5.2 m, respectively, for each pair of beams. In the first loading configuration, failure was achieved by the concrete crushing at the top edge with an average ultimate load of 284.0 kN. In the other configuration, slippage of the prestressed reinforcement and subsequent shear-compression failure was observed with an average ultimate load of 282.9 kN. Slippage of the strands not only induced brittle failure with a reduction in load carrying capacity, but also changed the location of the failure.

Wang et al. [32], based on the China expressway reconstruction and expansion project, selected two hollow PC slab bridges with spans of 10 m and 13 m, to check whether the bearing capacity met the load standard after 22 years of service. In the load tests, two load points were used at a distance of 2 m for the 10 m span and 3 m for the 13 m span. At the ultimate loads of 207.5 and 227.5 kN, the concrete was crushed in the compression zone. According to JTG/J21-2011 specifications, the bending resistance was twice the standard load; the shear resistance did not meet the standard load. However, it was considered that after the expansion project, the traffic lane of the existing bridge was mainly used as an express lane, resulting in a reduced impact on its usage. An integral cast-in-place slab was also considered to improve the shear capacity.

Jeon et al. [33] presented experimental data on two 45-year-old PC bridge girders in South Korea. The bridge was built in 1975 in a mountainous area and has not been exposed to the marine environment. The superstructure consisted of five PC I-girders with a span of 25 m. The girders were prestressed by 6 tendons with 12 steel wires each. Given the absence of a comprehensive repair and maintenance history, a detailed visual inspection was conducted. Due to severe cracking of the slab, traces of water flow and efflorescence were found along the surface of the girder. Cracking was also noted in several locations. To determine the material properties of the concrete, the girder was cut every 1 m after the loading test and a total of 120 specimens were taken through the concrete coring. Overall, the average compressive strength was 37.1 MPa, higher than the design strength of 35 MPa. The average ultimate strength and elastic modulus of the steel wires were 1549 MPa and 200 GPa, respectively. To estimate the prestress loss, the cracking load and strain change from wire-cutting methods were included in the test program. The estimated prestress loss was 57% for the cracking moment and 48% for the wire-cutting method, much higher than the 25% reported in the design assumptions. The bending test was carried out in a three-point bending configuration with a single actuator located at midspan. Of the two girders, one was loaded until concrete crushing at the concrete slab and the other was tested with multiple load steps inducing steel wire cuts. The maximum load and displacement recorded for the girder tested under monotonic loading were 920.4 kN and 387 mm, respectively. The other girder exhibited a reduction of 14.5% in strength and 16.7% in displacement, as evidenced by the load-displacement curve, which exhibited a flattening trend before reaching the point of concrete crushing.

Liu et al. [34] investigated the effect of fire on the residual capacity of two 20 m spans of hollow slab girders removed from a fire-damaged bridge in southern China. The bridge had four spans and each span consisted of 15 PC hollow slab girders. All the girders were 20 m long and were prestressed by 14 prestressing strands. In 2018, a truck carrying thermoplastic polyurethane elastomer and cotton caught fire, causing extensive damage to the girders. Two PC hollow slab girders with varying degrees of damage were taken. One girder was near the centre of the fire and had concrete spalling resulting in steel exposure, the other girder was at the edge of the fire and had less damage. The nominal compressive strength of the concrete was 50 MPa. The ultimate strength of the prestressing steel was 1860 MPa and the effective prestress was 1300 MPa. Investigations, including inspection and relaxation tests, were carried out to determine the effects of the fire. According to the inspection result, the highest temperature reached was estimated to be over 800 °C. The strand-cutting method was used to determine the effective post-fire prestress. The residual prestress of the exposed strands was 717.2 MPa, corresponding to a loss of 44.8% compared to the initial prestress given in the design documents. The girders were tested in a four-point bending test configuration, with loading stopped when the concrete in the compression zone was crushed. For the girder with more severe damage, the displacement of the loading point near the fire centre was significantly greater than the other loading point and the failure load was approximately 400 kN. Prior to concrete crushing near the damaged area, steel fractures were heard during the load test. However, the other girder did not experience a complete fracture and the failure load was approximately 412.5 kN. The residual bearing capacity of the two girders was found to be similar due to the comparable maximum temperature experienced by the prestressed strands. To determine the capacity loss of the girders due to the fire, the bearing capacity of the original girders at ambient temperature was calculated. The residual capacities of the two girders were 17.6 and 15.1% lower than the capacities before the fire accident.

The Alveo Vecchio viaduct was an Italian motorway bridge built in 1968 and decommissioned in 2005 after the failure of a pier caused by a landslide [35]. The viaduct had three spans and each span consisted of four 32.5 m long PC girders. According to the design documentation, the girders were prestressed by 14 post-tensioned parabolic cables with an initial jacking tension of 1250 MPa and an ultimate strength of 1700 MPa. The design calculations were based on a concrete compressive strength of 40 MPa. Prior to the load test, an extensive campaign of NDT and laboratory tests was carried out to characterize the material properties.

Pull-out and compression tests on concrete girders gave an average compressive strength of 50 and 31.9 MPa, respectively. Tensile tests on prestressing steel gave an ultimate tensile strength of 1742.7 MPa. The strand-cutting method was used on individual wires for residual prestressing, resulting in an average residual stress of 619 MPa. The viaduct was subjected to limited use of de-icing salts and no signs of corrosion were observed during visual inspection. The loading test was carried out with a load unit of 3x4 steel ballast weights of 100 kN placed by a crane. Several loading phases were planned, followed by a stop criterion based on a maximum midspan deflection of 300 mm. The stop criterion was reached with a load of 9300 kN, resulting in an estimated resisting moment almost four times greater than the bending moment specified in the design documentation. Visible torsion was evident from the longitudinally deformed shape of each girder, probably due to load redistribution, curb, different crack propagation or stiffness variation.

1.3 Scientific approach and scope of the thesis

The scientific study was motivated by the need to enhance assessment procedures for existing bridges and acquire a comprehensive understanding of their structural behavior. Through an extensive review of literature on current experience about large-scale experiments, various research findings were identified and summarized as follows:

- the structures investigated have an average age of 35 years, with only two cases exceeding 45 years;

- the prevalent approach entails measuring the load-deflection curve, midspan strains, and qualitatively assessing the failure type. No mention is made of strand sliding, slab behavior, or strains along the shear span;

- only two studies utilize distinct static schemes to induce different resistance mechanisms;

- deterioration assessment primarily relies on visual inspections, with corrosion potential measurements being conducted in only one case;

- the original design documents are not always available and therefore it is not possible to estimate the variation of mechanical properties and prestress loss;

- destructive tests are extensively employed to estimate the mechanical properties of concrete without reference to NDT;
- residual prestress is typically estimated through destructive methods, resulting in high variability between experimental and theoretical values.

These experiments revealed an approach mainly based on traditional standard procedures and a lack of recommendations for more informative structural assessment. The adopted strategies primarily focused on determining ultimate load and failure mode, without interest in defining practical methods that could assist engineers in making rational decisions based on research outcomes. On the basis of these findings, an extensive experimental program and subsequent works were designed. To overcome the difficulties related to loading, measurement, and limited accessibility to the investigated structural elements, it was decided to dismantle the structural elements and store them in a large testing site within the BRIDGE|50 research project framework. This facilitated the standardization of a diagnostic test protocol and monitoring layout during the loading tests. A specifically built test steel frame was utilized for a better control over the loading tests, accommodating different static schemes ranging from three-point bending to four-point bending configurations. Upon establishing the aforementioned research findings, the following objectives were outlined to be accomplished within the scope of this thesis:

- evaluation of durability issues using NDT techniques;
- characterization of concrete’s mechanical properties through a combination of destructive and NDT methods;
- estimation of the residual prestressing with NDT;
- analysis of the structural behavior of full-scale PC girders under varying damage and loading configurations;
- comparison of different safety formats through deterministic and probabilistic analysis within a multi-level approach.

The systematic execution of non-destructive and destructive tests was adopted to validate the feasibility and effectiveness of these methods for assessing existing bridges under real conditions.

References

[1] The Sustainable Development Goals Report. United Nations Publications, New York, USA, 2022.

[2] Barker, R. M. and Puckett, J. A. Design of Highway Bridges – An LRFD Approach, 2013.

[3] Bell, B. European Railway Bridge Demography. Sustainable Bridges: Assessment for Future Traffic Demands and Longer Lives, Sixth Framework Programme, 2003-2007.

[4] American Road and Transportation Builder's Association, Bridge Report, 2020.

[5] Zhou, J. and Zheng, D. (2017). Safety of Highway Bridges in China. *Strategic Study of CAE*, 19(6).

[6] Mirzaei, Z., Adey, B., Klatter, L. and Thompson, P. D. Overview of existing bridge management systems, 2014.

[7] AASHTO Manual for Bridge Evaluation, 2nd edn (MBE), American Association of State Highway and Transportation Officials, Washington, DC, 2011.

[8] CAN/CSA-S6-06: Canadian Highway Bridges Design Code, Canadian Standards Association, 2006.

[9] Highways Agency: Design Manual for Roads and Bridges, Highway Structures: Inspection and Maintenance - Assessment, Vol. 3, Sec. 4, UK, 2006.

[10] Bundesministerium für Verkehr, Bau und Stadtentwicklung- Abteilung Strassenbau, Richtlinie zur Nachrechnung von Strassenbrücken im Bestand (Nachrechnungsrichtlinie), 2011.

[11] SIA 269 − 269/8: Grundlagen der Erhaltung von Tragwerken, Schweizerischer Ingenieur- und Architekten Verein, 2011.

[12] Netherlands Normalisatie Instituut: NEN 8700 (nl) - Assessment of existing structures in case of reconstruction and disapproval – basic rules, 2011.

[13] Guidelines on Risk Classification and Management, Safety Assessment and Monitoring of Existing Bridges; Ministry of Infrastructure, CSLP: Rome, Italy, 2020.

[14] BRIME (2001). Bridge management in Europe. Final report, Bridge Management in Europe (BRIME) – 4th framework programme.

[15] Niederleithinger, E., Helmerich, R., Casas, J. R. (2007). New methods for inspection and condition assessment. Sustainable Bridges – Assessment for Future Traffic Demands and Longer Lives.

[16] Recupero, A., Spinella, N. (2019). Experimental tests on corroded prestressed concrete beams subjected to transverse load. Structural Concrete, 20, 2220-2229.

[17] Hewson, N. R. (2003). Prestressed concrete bridges: design and construction. Thomas Telford Publishing, London.

[18] Shenoy, C. V., Frantz, G. C. (1991). Structural Tests of 27-Year-Old Prestressed Concrete Bridge Beams. *PCI Journal*.

[19] Rao, C., Frantz, G. C. (1996). Fatigue Tests of 27-Year-Old Prestressed Concrete Bridge Box Beams. *PCI Journal*.

[20] Azizinamini, A., Keeler, B. J., Rohde, J., Mehrabi, A. B. (1996). Application of a New Nondestructive Evaluation Technique to a 25-Year-Old Prestressed Concrete Girder. *PCI Journal*.

[21] Halsey, T., Miller, R. (1996). Destructive Testing of Two Forty-Year-Old Prestressed Concrete Bridge Beams. *PCI Journal*.

[22] Pessiki, S., Kaczinski, M., Wescott, H. H. (1996). Evaluation of Effective Prestress Force in 28-Year-Old Prestressed Concrete Bridge Beams. *PCI Journal*.

[23] Eder, R. W., Miller, R. A., Baseheart, T. M., Swanson, J. A. (2005). Testing of Two 50-Year-Old Precast Post-Tensioned Concrete Bridge Girders. *PCI Journal*.

[24] Pepè, T. M., Melchers, R. E. (2011). The effects of corrosion on 45-year-old pre-stressed concrete bridge beams. *Structure and Infrastructure Engineering*, 7:1-2, 101-108.

[25] Huffman, J. M. (2012). Destructive Testing of a Full-Scale 43 Year Old Adjacent Prestressed Concrete Box Beam Bridge: Middle and West Spans [Master's thesis, Ohio University]. *OhioLINK Electronic Theses and Dissertations Center*.

[26] Osborn, G. P., Barr, P. J., Petty, D. A., Halling, M. W., Brackus, T. R. (2012). Residual Prestress Forces and Shear Capacity of Salvaged Prestressed Concrete Bridge Girders. *Journal of bridge engineering*, 17, 302-309.

[27] Barr, P., Higgs, A., Halling, M. (2013). Forensic Testing of Prestress Concrete Girders after Forty Years of Service. Final Report.

[28] Pepe, T. M., Melchers, R. E. (2013). Performance of 45-year-old corroded prestressed concrete beams. *Structures and Buildings*, 166(10), 547-559.

[29] Guglia, M., Taliano, M. (2014). Experimental analysis of the effective pre-stress in large-span bridge box girders after 40 years of service life. *Engineering Structures*, 66, 146-158.

[30] Bagge, N. (2017). Structural Assessment Procedures for Existing Concrete Bridges. Experiences from failure tests of the Kiruna Bridge. *PhD Thesis*, Luleå University of Technology.

[31] Liu, J., Jia, Y. (2019). Destructive testing of twenty-year-old prestressed concrete bridge beams in freezing-thawing region. *The civil engineering journal*, 3, 344-356.

[32] Wang, B., Xing, D., Chen, C., Tian, Z., Xu, G. (2021). Experimental Study on Residual Bearing Capacity of Existing Prestressed Concrete Hollow Slab Beam. *IOP Conference Series: Earth and Environmental Science*, 632.

[33] Jeon, C. H., Sim, C., Shim, C. S. (2021). The effect of wire rupture on flexural behavior of 45-year-old post-tensioned concrete bridge girders. *Engineering structures*, 245.

[34] Liu, Z., Xie, H., Han, B., Li, P., Jiang, Z., Yu, J. (2022). Experimental study on residual bearing capacity of full-size fire-damaged prestressed concrete girders. *Structures*, 45, 1788-1802.

[35] Tonelli, D., Rossi, F., Brighenti, F., Verzobio, A., Bonelli, A., Zonta, D. (2022). Prestressed concrete bridge tested to failure: the Alveo Vecchio viaduct case study. *Journal of Civil Structural Health Monitoring*.

Chapter 2

Corso Grosseto viaduct

2.1 History

The C.so Grosseto viaduct, located in Turin, Italy, was a multilevel road interchange built in a dense context of residential buildings and road network (Figure 1). The infrastructure developed along two main lines in the north-western part of Turin, namely the C.so Grosseto West - C.so Grosseto East (GWE) and C.so Potenza - C.so Grosseto East (PGE) routes (Figure 2).

Figure 1: C.so Grosseto viaduct (west view).

Figure 2: C.so Grosseto West – C.so Grosseto East and C.so Potenza – C.so Grosseto East routes.

It was built in 1970 to meet the high traffic demand following the rapid development of Italian industry and the consequent increase in the population of northern Italy. Turin and the surrounding urban centres grew rapidly in number of inhabitants, from 720000 in 1951 to 1125000 in 1967. In order to solve the problem of traffic in the city, the municipality at the time ordered the construction of a series of overpasses and underpasses at the most important hubs [1]. In the case of the C.so Grosseto viaduct, the structural typologies adopted were statically determinate schemes, constituted by PC elements, a typical solution consolidated during the post-war reconstruction for their fast and economic building operations. Due to the size of the structure, the girders were cast in steel moulds in plants near the construction site and moved by crane (Figure 3).

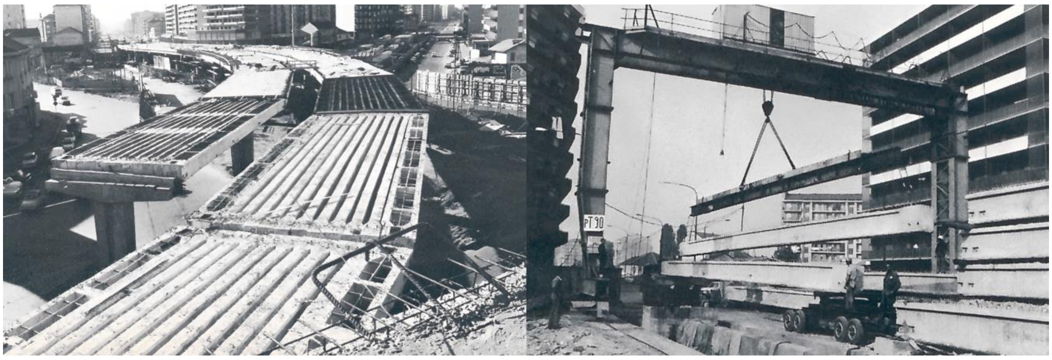

Figure 3: The construction site during building operations [2].

The building process consisted of the construction of the lower part of the deck, post-tensioning of the pier caps prior to the laying of the girders, placement of the girders, casting of the top slab and diaphragms, secondary post-tensioning of the pier caps prior to the application of non-structural loads and finishing of the deck. The C.so Grosseto viaduct was designed in accordance with the design live loads specified in the Italian standards Circ. Min. LL.PP. 14/02/1962 n. 384 [3]. It classified the roads in 1st category, intended for the transit of civil and military cargoes, and in 2nd category, if intended for the transit of civil cargoes only. Accordingly, the equivalent of a column of trucks corresponding to 12 tonnes and an isolated military cargo of 74.5 tonnes were assumed, with a transverse length of 3.00 m and 3.50 m, respectively. The magnitude of the sustained load on each longitudinal member was estimated assuming the orthotropic plate behavior defined by the Guyon-Massonnet-Bares method [4]. Located in a freeze-thaw region of northern Italy, it has experienced high temperatures in summer and temperatures several degrees below zero in winter. Over the years, exposure to aggressive atmospheric agents and the massive use of de-icing salts have led to problems of durability and consequent conservative maintenance. Unfortunately, the repair and management history was not properly recorded. However, since 2009, maintenance records reported an increasing frequency of debris removal. In April 2017, transit for heavy vehicles was restricted and, three months later, the complete closure of the road interchange was ordered (Figure 4).

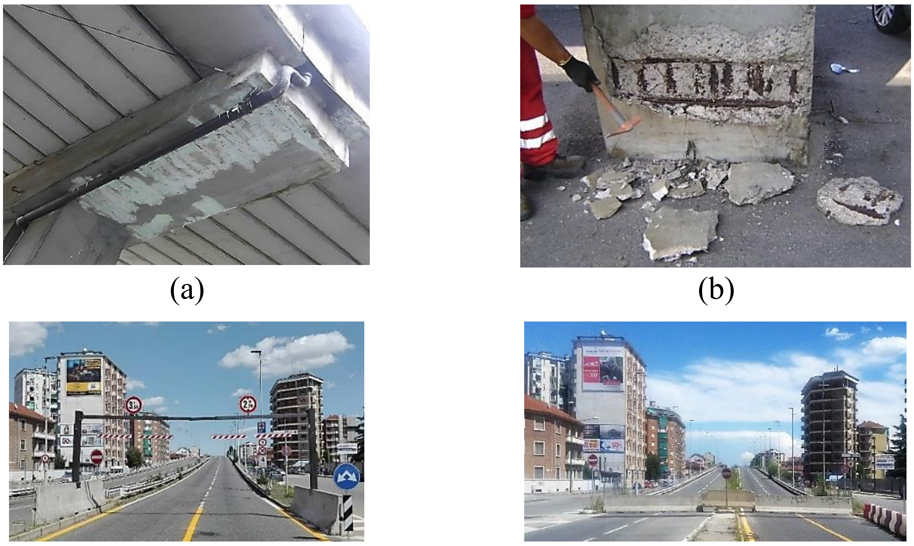

(a) (b)

(c) (d)

Figure 4: Management records: (a) rust inhibitor treatment (October 2014), (b) debris removal from pier base (July 2016), (c) traffic restriction to 3.5 tons and 2.7 m height (April 2017), (d) closure of the viaduct (July 2017).

In September 2018, the demolition of the viaduct began for an urban redevelopment project commissioned by the Piedmont Region and managed by S.C.R. Piemonte S.p.a., an Italian contracting authority for public works. The modernization of the infrastructure system consisted of a new underground railway line, integrated into the existing railway infrastructure. The functionality of the viaduct was replaced by a new four-lane road underpass and a more efficient surface road intersection. The urban redevelopment also allowed the renewal of all the sub-services. The Largo Grosseto interchange has followed the development of Turin over the years, meeting different mobility needs characterized by the dramatic increase in transport demand during the economic boom, and the need for a more sustainable transport system today (Figure 5). The demolition of the viaduct also provided the opportunity to activate the BRIDGE|50 research project (bridge50.org) [5-6], a research agreement between universities, public authorities, and private companies, with the aim of investigating the residual structural performance of a 50-year-old structure that is widespread in the Italian motorway heritage in terms of structural type and age.

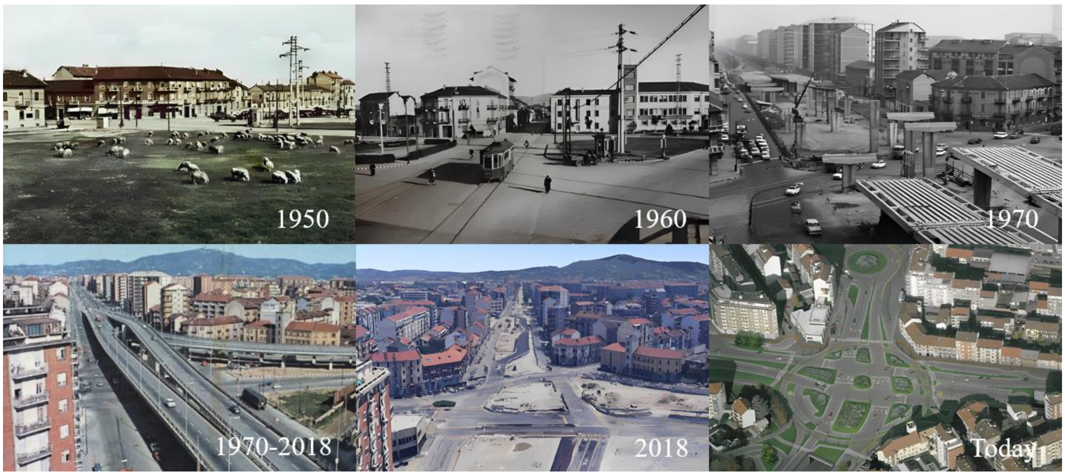

Figure 5: Historical development of the Largo Grosseto interchange.

2.2 Geometry

The C.so Grosseto viaduct was an 80-span structure with a total length of 1.4 km. The decks were inclined longitudinally to achieve a maximum vertical clearance of 12.4 m for the GWE route and 5.9 m for the PGE route. Each of these two lines was connected by two structurally independent decks, one for each carriageway, with spans ranging from 16.0 m to 30.0 m and a total of 87 piers. The 8.3 m wide superstructure consisted of ten inner PC I-girders, and two edge PC box girders per span. The longitudinal girders were connected with a cast-in-place 14.0 cm thick reinforced concrete (RC) slab at the top and two transverse diaphragms at 1/3 and 2/3 of the span. The I-girders had a lower flange width of 58.0 cm and a total height of 90.0 cm. The box girders were 96.0 cm high and 100.0 cm wide. The girders were simply supported on laminated elastomeric rubber pads at the PC pier caps and abutments. The decks were supported on RC piers founded on spread footings. Figure 6 shows a typical cross-section of the viaduct at one pier.

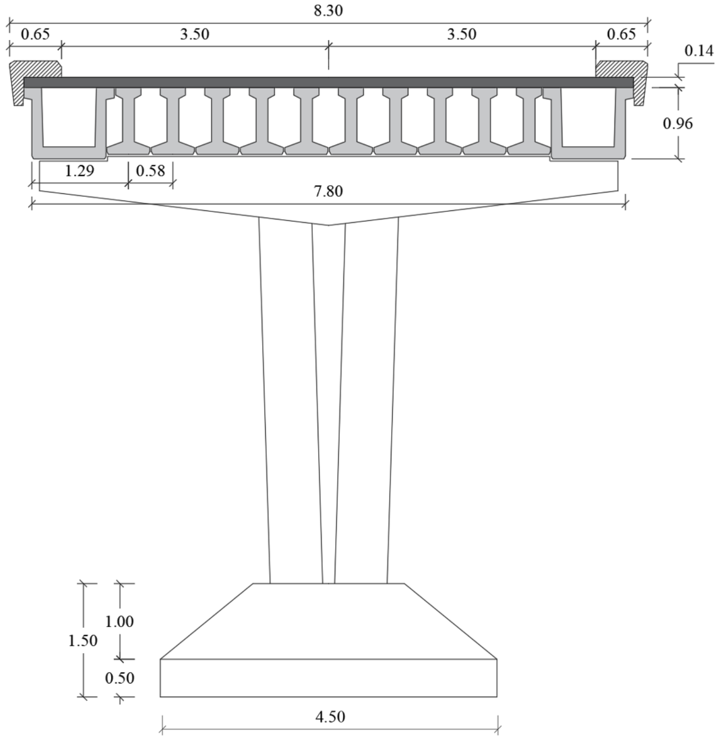

Figure 6: Geometry of the cross section at a pier (unit: m).

2.3 Material

Based on the original design document [7], the structural elements were designed considering the allowable stress design method. The I-girders were designed to have an ultimate load capacity of 823.9 kNm, while the box girders were designed for a higher ultimate load capacity of 1638.7 kNm. The minimum estimated compressive strength of the concrete in the girders was 32.1 MPa (f_{ck} > 26.6 MPa), and the reinforcing steel had generally $f_y = 215.8$ MPa. The steel quality of the prestressing strands was determined to be $f_{p(1)k}/f_{ptk}$ = 1474/1638. Archival research into the laboratory tests provided the test certificates issued in the 1970s by the Testing Laboratory of the Politecnico di Torino. These documents reported a 28-day concrete compressive strength of 50.3 MPa, averaged over 4 standardized cubic samples taken from precast girders. The concrete compressive strength of the slab was 40.5 MPa, averaged over 7 samples. Mechanical tests on 20 samples of 12.5 mm nominal diameter strands gave an average yield strength of 1486.0 MPa and an ultimate strength of 1722.2 MPa.

2.4 Girder reinforcing

Both types of girders were designed with 7-wire straight strands with a nominal diameter of 12.5 mm. However, mild reinforcement was used to hold the shear stirrups in place during casting. The I-girders were prestressed with 17 strands in the bottom flange and 3 strands in the top flange. The box girders were designed to be roughly twice as resistant as the I-girders, by doubling the cross-section and the number of strands in the top and bottom flanges. The original design indicated that after losses, the prestressing strands would have an effective prestress of 836.3 MPa, a 40% reduction from the initial jacking stress of 1400.7 MPa. The girders were prestressed after steam curing with a 24-hour operating cycle in the site plant (Figure 7). To introduce prestressing forces at predetermined distances, three strands of the I-girder were unbonded in grouted ducts from the end to 5.0 m, and two strands from the end to 3.0 m. For the box girder, four strands were unbonded up to 5.0 m, four strands up to 3.5 m, and four strands up to 1.3 m. The minimum specified cover concrete for the prestressing strands was 45 mm.

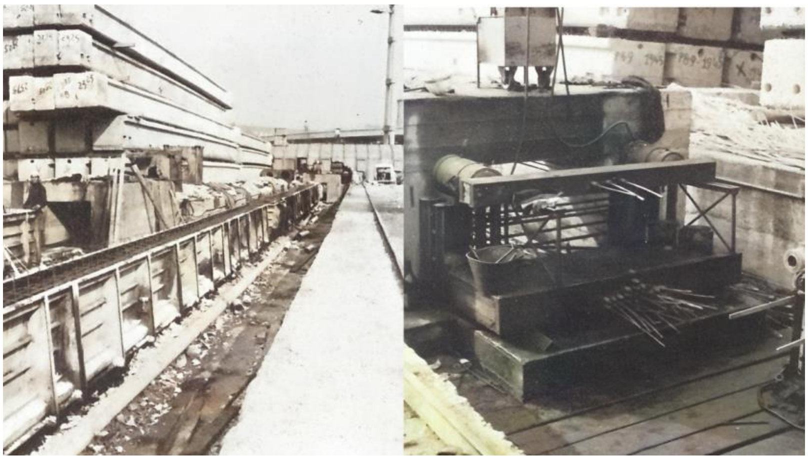

Figure 7: Precast plant at the construction site [2].

Shear reinforcement was provided using $\phi 8$ mm stirrups spaced at 17.0 cm from the end of the girder to 1.30 m, and 25.0 cm for the remaining span. The stirrup arrangement was symmetrical to the centre of the beam. The bars extended into the top slab to develop composite behavior with the girders. The slab was reinforced with $\phi 8$ mm square mesh of 20.0 cm at the top and bottom edges. The reinforcement configuration is detailed in Figure 8.

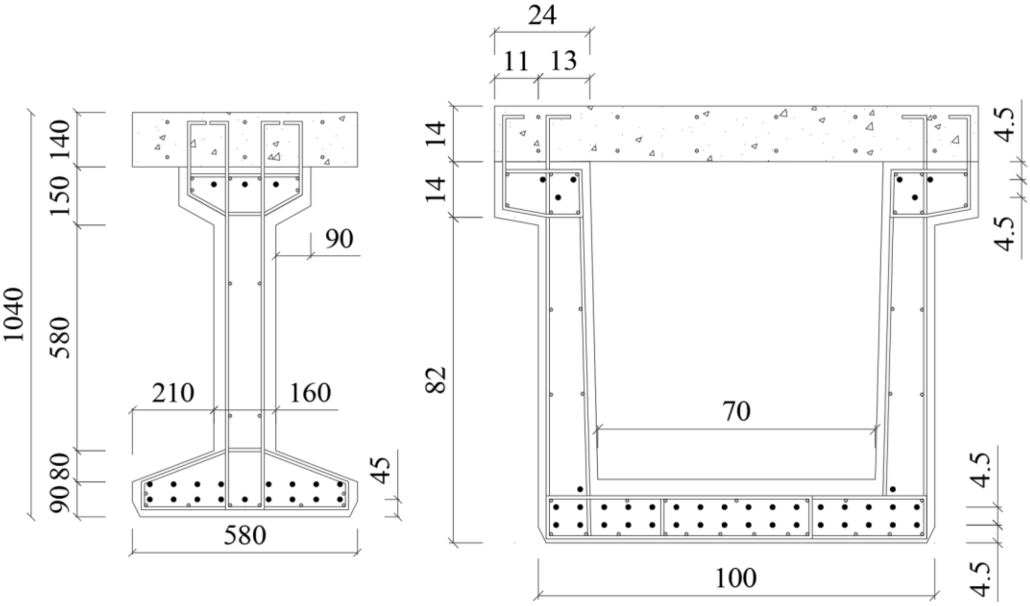

Figure 8: Layout of reinforcement in I-shaped and box cross-section.

2.5 Demolition operation

The demolition work took place during the initial phase of the new project, which included the demolition of the GWE viaduct, the relocation of the subservices, and the construction of the bulkheads of the railway tunnel. Being a strategic infrastructure system, a proper planning was required to mitigate the environmental impact and ensure regular traffic flow on the roadway at the base of the structure, also including night hours. Regular technical meetings with stakeholders and constant communication with citizens facilitated the application of environmental impact measures [8]. The first phase started in May 2018 and ended in October 2018, with a mixed demolition using diamond disc/wire cutting and excavators equipped with hydraulic crushers (Figure 9).

Figure 9: Demolition of the bridge using hydraulic crushers.

Demolition by cutting was used for the spans that were considered critical due to their location in areas with greatest traffic flow and their proximity to buildings and the electric tram network. Demolition using hydraulic crushers was preferred in other areas in order to reduce working time. This method of demolition, without prior handling of the structural members on the ground, was carried out after the construction of a sand embankment approximately 30 cm thick, in order to reduce the acoustic and vibrational effects associated with the falling of the concrete debris. During the demolition work, the use of nebulised water directed by suitable lance was used to reduce dust by up to 90%. In addition, an HDPE sheet supported by mobile cranes was used to contain the projection of concrete debris from the construction site towards neighbouring buildings.

The final decommissioning involved some of the central spans along the PGE route and the reaming spans to the east and south direction, with the exception of the two end spans, which were preserved for the BRIDGE|50 research project (Figure 10). The dismantling of these structural members began on 29 May 2019 and was completed after 12 days, involving precision cutting, movement by a 500-tonne mobile crane and exceptional transport by truck.

Figure 10: End parts tested within the BRIDG|50 research project.

The bridge dismantling operations can be described with the following execution phases (Figure 11):

- Wire/diamond cutting of the deck slab and the connecting transverse diaphragms.

- Drilling of the deck with a drilling machine at the top and a manual drill at the bottom to allow the insertion of the lifting ropes, useful for the subsequent lifting of the cut elements. A different drilling technique was used for the lower surface to avoid cutting of the prestressing strands.

- Slinging of the individual portions of the deck sectioned with ropes.

- Handling and subsequent transport by truck to the testing site for the experimental campaign. Each transport was characterized by the movement of three PC I-beams or a single PC box girder or pier cap. A maximum weight of 40 tonnes was allowed for the transportation truck used.

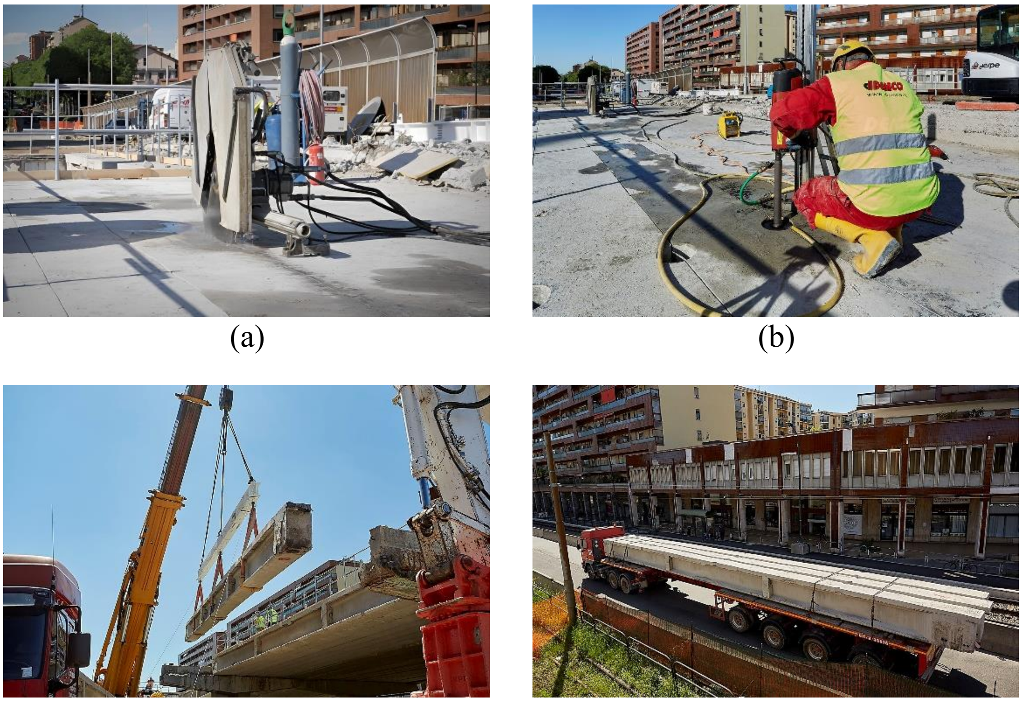

(a) (b)

(c) (d)

Figure 11: Dismantling operations: (a) cutting, (b) drilling, (c) lifting, (d) transportation.

A specific procedure was employed for lifting the pier caps. These elements were disconnected from the piers by cutting with a diamond disc, while being supported by a mobile crane.

A total of 31 structural elements, including 25 I-beams, 4 box girders, and 2 pier caps, were dismantled and stored in a testing site of approximately 6000 m^2 in Turin. A detailed layout of the preserved structural elements in the original deck configuration is shown in Figure 12, where the elements recovered for the BRIDGE|50 research project are shown in green, and the elements investigated in this thesis are shown in red.

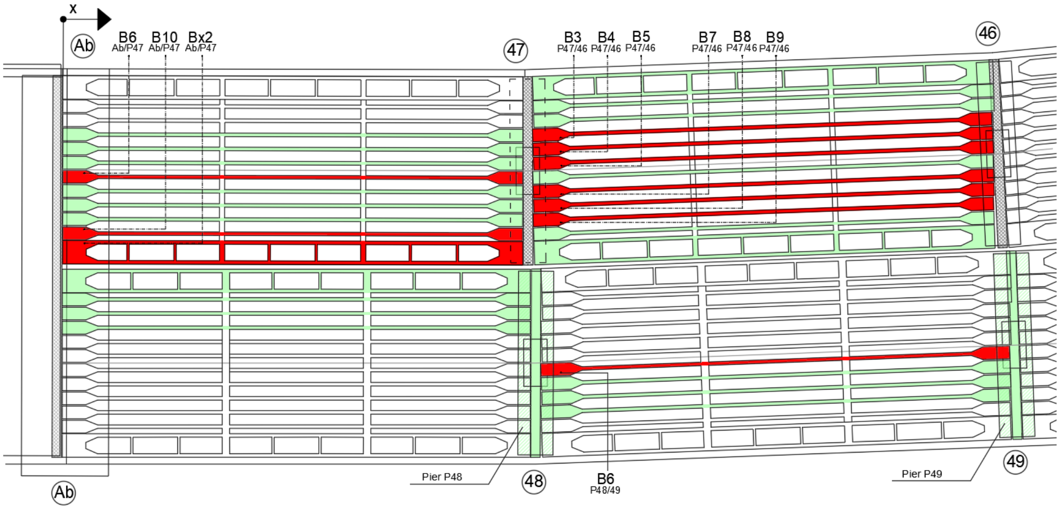

Figure 12: In-service layout of the investigated structural members.

All elements were identified with a proper identification code relating to their original position on the viaduct. Furthermore, in order to maintain the same structural scheme in-service, the storage of the girders was carried out by placing them on RC New Jersey elements. The deck girders were placed at a sufficient distance from each other to facilitate detailed laboratory investigations on each side.

2.6 BRIDGE|50 research project

At a time when monitoring the residual capacity and durability of old bridges is becoming a relevant part of a management agency's responsibilities, data on the performance of old structural elements are needed to assist these agencies in decision-making policies. Understanding the structural behavior of existing bridges is therefore crucial to optimize the management of the bridge stock. In this spirit, the BRIDGE|50 research project was signed on 18 December 2018, a research agreement between Politecnico di Torino, Politecnico di Milano, S.C.R. Piemonte, Lombardi Engineering, Piedmont Region, City of Turin, Metropolitan City of Turin, TNE Torino Nuova Economia, ATI Itinera & C.M.B., ATI Despe & Perino Piero, and Quaranta Group. This agreement concerns the safety assessment and residual lifetime evaluation of existing bridges by providing experimental data on the long-term performance of structural member and by developing a survey framework with validated diagnostic methods.

An extensive experimental programme was designed to assess the residual structural performance of the girders, including NDT, full-scale load tests, dynamic tests, laboratory tests, traditional and innovative techniques for diagnosis from both chemical and mechanical point of view. The experimental programme can be summarised in the following steps:

- preliminary activities prior to the demolition of the viaduct, including visual inspections [9], concrete coring and carbonation tests on pier samples, dynamic tests prior to the demolition of the decks to characterize the global dynamic behavior [10];

- NDT at the testing site, including inspection, degradation mapping, profometer test, rebound hammer test, ultrasonic test and electrochemical methods for corrosion measurements;

- static and dynamic loading tests on the bridge girders;

- stress-relief tests on concrete and steel wires for the estimation of the residual prestressing forces;

- material testing of concrete, reinforcing and prestressing steel;

- calibration of numerical models for safety assessment and development of life-cycle design frameworks able to take into account the effects of material aging and deterioration phenomena;

- summarization and dissemination of the research results to inform the authorities involved in the management and inspection of existing structures.

The data collected during the first phases, integrated with the original drawings, provided a basis for the planning of the load tests, such as the layout of the measurement sensors.

The work described in this thesis was undertaken to provide experimental verification of the performance of PC girders, including static load test results, failure mode, prestressing force, and composite action. For the dynamic test results, reference is made to published work [10-12].

References

[1] Savino, P., Anghileri, M., Chiara, M., Salza, B., Quaranta, L. (2020). Corso Grosseto viaduct: Historical and technical overview. In *Proceedings of the Tenth International Conference on Bridge Maintenance, Safety and Management (IABMAS 2020)*, Sapporo, Japan, 28 June–2 July.

[2] Impresa Pessina 1976. 25 Anni di Costruzioni Pessina, rassegna delle opere significative realizzate da un'impresa italiana in venticinque anni di attività. Arti Grafiche Amilcare Pizzi S.p.A., Cinisello Balsamo, Milano.

[3] Italian Ministry of Public Works (1962) Ministerial circular n. 384 of 14/02/1962—rules related to loads for the calculation of road bridges, Rome.

[4] Massonnet, C. (1962). Compléments à la méthode de calcul des ponts à poutres multiples. Annales de l'ITBTP N° 169. Janvier.

[5] Biondini, F., Manto, S., Beltrami, C., Tondolo, F., Chiara, M., Salza, B., et al. (2020). BRIDGE|50 research project: Residual structural performance of a 50-year-old bridge. In *Proceedings of the Tenth International Conference on Bridge Maintenance, Safety and Management (IABMAS 2020)*, Sapporo, Japan, 28 June–2 July.

[6] Biondini, F., Tondolo, F., Manto, S., Beltrami, C., Chiara, M., Salza, B., et al. (2021). Residual structural performance of existing PC bridges: Recent advances of the BRIDGE|50 research project. *First Conference of the European Association on Quality Control of Bridges and Structures (EUROSTRUCT 2021)*, Padua, Italy, 29 August–1 September.

[7] Ing. Massaro. Progetto esecutivo–Interscambio stradale Largo Grosseto; Repository of Turin Municipality; Ufficio tecnico lavori pubblici Città di Torino–Ripartizione IV: Turin, Italy, 1970.

[8] Anghileri, M., Biondini, F., Rosati, G., Savino, P., et al. (2020). Deconstruction of the Corso Grosseto viaduct and setup of a testing site for full scale load tests. *In Proceedings of the Tenth International Conference on Bridge Maintenance, Safety and Management (IABMAS 2020)*, Sapporo, Japan, 28 June–2 July.

[9] Beltrami, C., Bianchi, S., Cervio, M., Anghileri, M., Felicetti, R., Quattrone, A., Chiara, M., Salza, B., Masala, D. (2020). Bridge visual inspections: Experience of local authorities and the case study of the Corso Grosseto viaduct. *In Proceedings of the Tenth International Conference on Bridge Maintenance, Safety and Management (IABMAS 2020)*, Sapporo, Japan, 28 June–2 July.

[10] Quattrone, A., Sabia, D., Tondolo, F., Capacci, L., Lencioni, A., Legramandi, C. (2020). Dynamic tests and modal identification of Corso Grosseto viaduct decks before the dismounting. *In Proceedings of the Tenth International Conference on Bridge Maintenance, Safety and Management (IABMAS 2020)*, Sapporo, Japan, 28 June–2 July.

[11] Sabia, D., Quattrone, A., Tondolo, F., Savino, P. (2021). Dynamic identification of damaged PC bridge beams. *In Proceedings of the First Conference of the European Association on Quality Control of Bridges and Structures (EUROSTRUCT 2021)*, Padua, Italy, 29 August–1 September 2021.

[12] Sabia, D., Quattrone, A., Tondolo, F., Savino, P. (2022). Experimental evaluation of the effect of controlled damages on the dynamic response of PC bridge beams. *In Proceedings of the 11th International Conference on Bridge Maintenance, Safety and Management (IABMAS 2022)*, Barcelona, Spain, 11–15 July 2022.

Chapter 3

Full-scale tests on PC girders

3.1 Introduction

The safety assessment of existing bridges may be required for several reasons, mainly when they are subject to changes such as deterioration, mechanical damage, repair, or new traffic load requirements. The assessment of existing bridges can be seen as an adaptive process that refines and updates the current state of knowledge. Based on the findings, it may be decided to conduct more detailed surveys, refining the gathered information and enabling a more sophisticated analysis. According to many national codes, the assessment of the bearing capacity of an existing bridge is usually based on an examination of the existing project documentation and a preliminary inspection of its condition. At this stage, the characteristics of the bridge and the condition of the structural members are identified and critically analyzed to determine the current level of deterioration and its impact on structural safety. Supplementary investigations can be carried out at higher levels of accuracy and complexity, to provide more accurate data on material properties and current condition, which can be used as input for more advanced analysis. Finally, at the enhanced evaluation level, the actual material properties and behavior of the bridge, can be determined directly through load testing. However, the level of refinement can be improved not only by more accurate structural analyses and data collection methods, but also by the use of appropriate safety formats. Depending on the level of knowledge and related uncertainties, the structural assessment can be conducted using a purely heuristic approach based on experience, deterministic and semi-probabilistic safety formats, or probabilistic analyses. In some cases, simple checks based on information obtained from original documentation and visual inspection may be sufficient to demonstrate structural safety. Conversely, employing a semi-probabilistic method can be beneficial for establishing a standardized level of safety. In other situations, this approach may result in excessive strengthening measures, and the use of a less conservative probabilistic approach may be required.

However, due to economic constraints, the step-by-step methodology for routine evaluation is usually limited to the first level of knowledge. In this case, it is not possible to take samples from the structure, and the material properties have to be estimated indirectly. For concrete bridges, one starting point is the strength class specified in the original design. However, the ongoing effects of hydration and deterioration may have changed the resistance value, and a reassessment is required. On the other hand, taking material samples is a time-consuming and destructive process. As a result, only a few results are obtained, and these may not be representative of the whole structure. The true resistance of the structural elements may be misinterpreted or, conversely, overly conservative mechanical properties and resistance models may be used.

Based on all these considerations, a proper diagnostic campaign was planned and detailed in the present Chapter, including non-destructive tests, laboratory tests, and loading tests. Several parameters relevant for the assessment of similar structures still in-service were collected at different levels of details, concerning the structural typology, the state of deterioration, the performance of the structural members, and the mechanical properties.

3.2 Non-destructive assessment of deterioration

The first step of the experimental program was the preliminary assessment of the state of conservation by checking the effects of deterioration on the structural elements. As mentioned earlier, the first level of assessment usually assumes the safety of the bridge based on the results of visual inspections. However, visual inspections are limited to surface observations at a relatively late stage, when the degree of corrosion is sufficient to cause surface cracking, delamination, and rust staining, or when cracking is already present due to other mechanisms (cracking load, thermal effects, support settlement). If the volume expansion of the corroded steel is not sufficient to split stresses, some defects will remain undetected at this level. Since visual inspection alone is not sufficient to determine adequate knowledge of the actual state of deterioration, a comprehensive diagnostic campaign has been properly planned, including appropriate criteria, methods and procedures to collect meaningful data on physical and chemical properties.

3.2.1 Visual inspection

The visual inspection campaign, which took place after the deconstruction, was organized into three operative phases involving geometric surveys, photographic surveys and deterioration mapping of each structural member. In the first phase, the initial information provided by the original drawings were ascertained and upgraded. Standard measuring instruments were utilized for the geometric survey, while a magnetic cover-meter was employed to ascertain the arrangement of reinforcement. The inspected areas, relating to the bottom and side surfaces, confirmed the reinforcement layout of the original drawings. With respect to the cast-in-place slab, the reinforcement layout was determined visually as it was exposed by the cutting process conducted to isolate individual girders. A variable step was found for the stirrups, resulting in an average value of 250 mm. A concrete cover of 45 mm was confirmed for the prestressing strands, while a high variability was observed for the ordinary reinforcement, with a minimum value of 10 mm. Photographic surveys of the elements showed that their condition varied according to the different type of structure. In particular, significant signs of deterioration were observed on the pier caps, with extensive delamination of the concrete and consequent exposure of severely corroded reinforcement (Figure 13). Such significant signs were associated with the lack of adequate drainage systems and were exacerbated by the presence of de-icing salts, which are widely used on bridges in the northern regions of Italy.

Figure 13: Effects of steel corrosion on pier cap.

In addition, deficiencies in the water drainage from the deck at the structural joint greatly accelerated the deterioration of the end portions of the structural members exposed to wetting. Figure 14 shows a corrosion scenario for the last four adjacent beams of deck 47/46. Progressive deterioration can be highlighted from the innermost I-beam to the outermost box beam, characterized by delamination of the concrete cover in the more exposed girders.

Figure 14: Corrosion scenario at the end of the girders adjacent to pier cap 46.

In addition to the exposure conditions that led to the macroscopic deterioration problems, the detailed investigation of areas that were difficult to examine with the bridge in service also revealed inadequate quality control during the construction phases. Evidence of concrete segregation, mainly concentrated at the ends of the girders, suggested a poor concrete vibration during casting (Figure 15a). This phenomenon, together with the congestion of reinforcing bars in the same area, caused the presence of macro voids (Figure 15b). In addition, inadequate concrete cover thickness for the steel reinforcement and consequent corrosion initiation were also detected (Figure 15c).

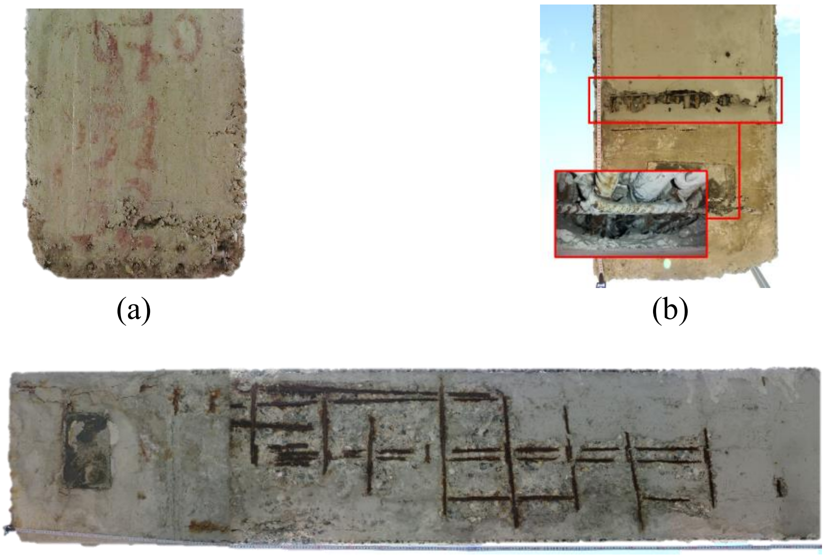

(a)

(b)

(c)

Figure 15: Inadequate quality controls: (a) concrete segregation, (b) macro-voids, (c) insufficient concrete cover thickness.

The results of the visual inspection campaign were used to classify the structural members into three different categories: undamaged, damaged by corrosion, and damaged by dismantling operations. The latter category included damage resulting from coring operations which caused the perforation of the upper slab and/or cutting of the prestressing strands in the lower flange (Figure 16). Based on these three classes, the load test schedule was planned, starting with undamaged beams to be used as benchmarks for subsequent load tests.

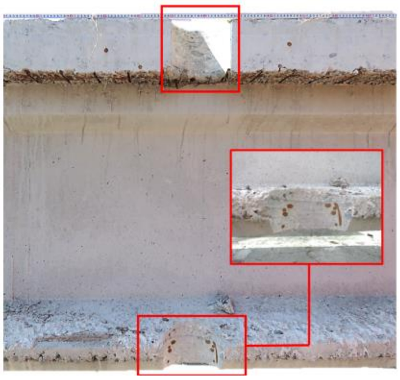

Figure 16: Typical damages due to dismantling operations: top slab drilling and strands cutting.

During the mapping phase, each sign of degradation was recorded in terms of extent, location and properly reported in digital format. All cracks were carefully marked, and the widths measured using a crack meter with spacing of 2.0 cm. An overview of the survey sheets relating to the beams investigated in this thesis has been reported in *Appendix A*. In particular, the cracks observed on all faces of the beams were listed in terms of length and average width. The orientation given for each face was related to the configuration of the testing site. As expected, the most cracked surface corresponds to the eastern side of the box girder, which was the most exposed to the environment during its service life. In this map, the cracks appeared mainly parallel to the stirrups with an average width of 0.4 mm. In general, the cracks detected in the I-beams were in the area close to the supports, with an average width of less than 1 mm. Therefore, it was assumed that these cracks would not affect the load carrying capacity and the beams were classified as undamaged. Beam B6-P49/48 had two strands cut for dismantling operations on either side of the lower flange at distances of 3.7, 9.6, and 15.5 m from the end section respectively. The B10-Ab/P47 had two strands cut on the west side at distances of 3.8 and 15.5 m respectively. Accordingly, both beams were classified as damaged due to dismantling operations.

3.2.2 Corrosion measurements

In order to obtain reliable information on the extent and rate of deterioration, and to obtain durability parameters, NDT tests were carried out prior to the loading tests. Corrosion of steel in concrete is one of the major durability problems, especially when the passive state of the steel is disrupted by carbonation and/or chlorides ingress. The rate of corrosion directly affects the amount of remaining service life of a corroding structure and a number of diagnostic techniques, namely half-cell potential, concrete resistivity, and corrosion current density, are usually used to monitor it [1].

Since corrosion is the result of an electrochemical process, which involves metal atoms releasing electrons and forming ions, a potential difference is created between the uncorroded (cathode) and corroded (anode) areas. The most commonly used electrochemical technique for determining corrosion activity is the half-cell potential measurement [2, 3]. The measurement is based on the electrical and electrolytic continuity between the embedded rebars, the reference electrode on the concrete surface and the voltmeter (Figure 17).

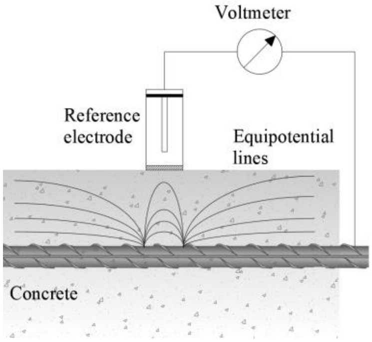

Figure 17: Half-cell potential measurement.

The numerical value of the measured potential difference between the half-cell rebar and the reference electrode is related to the state of corrosion of the steel in the concrete. According to ASTM C876 standard [4], a potential more negative than -350 mV against the Cu/CuSO4 reference electrode (CSE) indicates a 90% probability that steel corrosion is occurring at the time of measurement, and a negative value less than -200 mV/CSE indicates a 90% probability that there is no corrosion risk. However, depending on concrete moisture content, temperature, chloride content, carbonation and cover thickness, different potential ranges for active corrosion could be obtained in different structures [5, 6]. In order to consider such influences, a RILEM recommendation gives typical potential ranges for different conditions [3].

Before evaluating the corrosion condition of the reinforcement and identifying the anodic (corroding) and cathodic (passive) parts of the beams, a coordinate system on the surfaces of the specimens was considered to correlate the measurement points with the geometries of the elements. As the aim of the present work was to evaluate the corrosion condition of the strands, a constant grid spacing of 1.0 m in the longitudinal direction and 0.2 m in the transverse direction was assumed on the bottom face for each girder. For a statistical evaluation of the potential readings, suitable to provide a representative value of the magnitude of affected area for each structural element, the half-cell potential data were plotted on a cumulative frequency diagram (Figure 18).

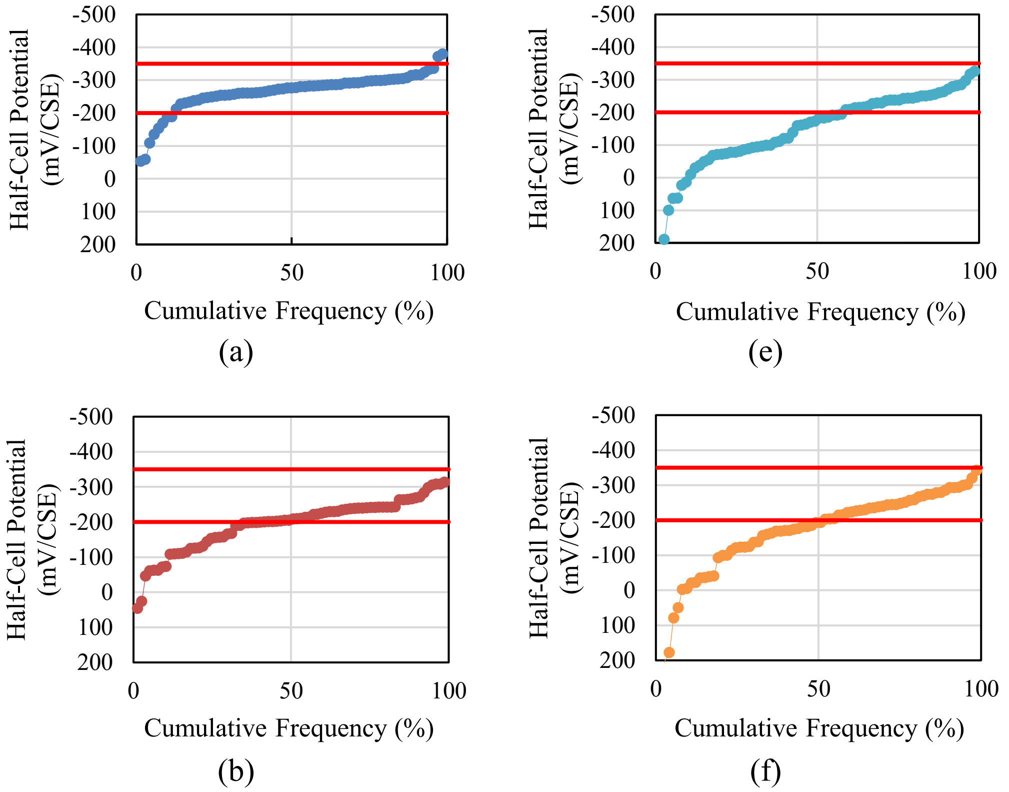

(a)

(e)

(b)

(f)

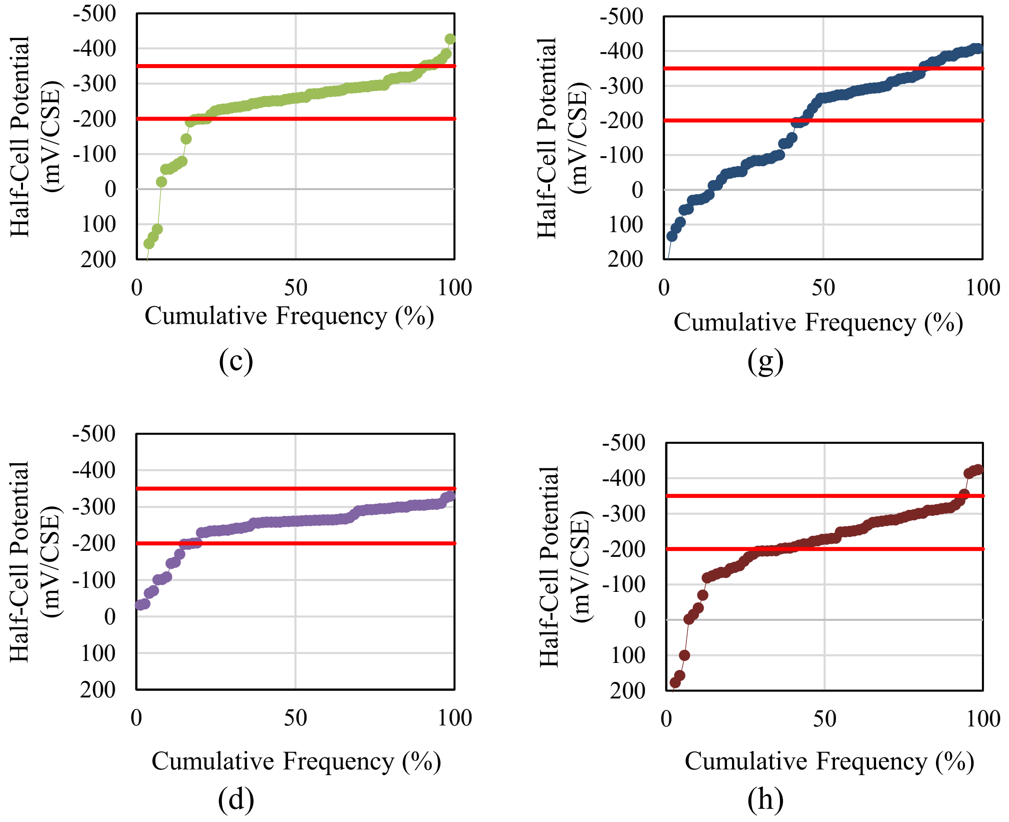

Figure 18: Cumulative frequency distribution of half-cell potentials measured on: (a) B3-P47/46, (b) B8-P47/46, (c) B4-P47/46, (d) B9-P47/46, (e) B6-Ab/P47, (f) B6-P48/49 (g) B10-Ab/P47, (h) B5-P47/46 girder.

It is interesting to note two different types of curves associated with the beams shown in Figure 18. Specifically, the B3-P47/46, B4-P47/46 and B9-P47/46 curves have the highest number of readings in the potential range between -200 and -350 mV/CSE, indicating an intermediate corrosion risk with possible carbonated concrete. The other set of beams have almost half the readings in these ranges with a slope change shifted to -100 mV/CSE, corresponding to more passive zones. However, in some cases there are readings more negative than -400 mV/CSE, associated with severe corrosion in chloride-contaminated concrete. As the spatial variation of the potential readings is lost in the statistical representation, the equipotential contour maps of the above curves are shown in *Appendix B*. The statistical variability shown by the cumulative frequency plots is confirmed within the contour maps. For B4-P47/46, B10-Ab/P47 and B5-P47/46, the presence of potentials more negative than -400 mV/CSE has been confirmed near the support zones, probably related to the contamination with de-icing salts.

However, half-cell potentials provide a qualitative information on corrosion activity without reference to the severity of the corrosion problem. A wide variation in corrosion rate can be found for similar potential values. Depassivated steel reinforcement may corrode at an advanced rate or so slowly that it will not be a problem within the design life of a structure. Therefore, potential measurements shouldn’t be used as absolute criteria to determine the corrosion condition of steel in concrete and complementary data are required [7]. A major influence on potential measurements is the moisture content of the surface layer of the concrete. It is generally accepted that the corrosion rate in dry concrete is low due to the high electrical resistivity, and in wet concrete, the corrosion rate could be also low due to the slow transport of oxygen. At an intermediate moisture content, the corrosion rate can be high due to relatively low resistivity and high oxygen transport [8]. Furthermore, in structures with chloride-induced corrosion, concretes with lower resistivity facilitate the transport of chlorides and the depassivation of reinforcements. From another point of view, in the presence of carbonated structures, the precipitation of calcium carbonate in the pores, leads to a significant increase in resistivity and also to more positive potentials [9]. As the electrochemical process involves the concrete as an electrolyte between the two electrodes, the electrical resistivity of the concrete plays an important role in controlling the transfer velocity of ion between the cathode and anode, and must be combined with corrosion potential measurements [10].

The electrical resistivity of concrete is typically measured using the Wenner four-probe method [11]. An alternating current is impressed between the two outer probes and the resulting voltage drop of the electric field is measured across the two inner probes (Figure 19). The concrete resistivity can then be calculated by multiplying the measured ohmic resistance by a geometric conversion factor.

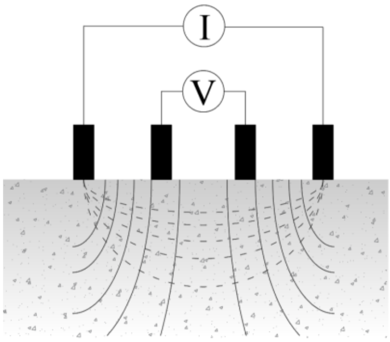

Figure 19: Scheme of the Wenner technique.

It is generally recognized that the resistivity range from 100 ohm·m to 200 ohm·m represents a transition regime below which severe corrosion is possible and above which corrosion is only rarely observed [10]. The resistivity measurements were taken at the same sample points as the potential mapping, in order to correlate the concrete resistivity surveys with the half-cell potential surveys. Figure 20 shows the collected resistivities plotted on cumulative frequency diagrams. The resistivity values have been limited to 10 kohm·m to appreciate differences compared to the 1000 ohm·m limit, beyond which active and passive steel cannot be distinguished as the risk of corrosion is negligible [12]. Visual representations of the resistivity contour plot are given in *Appendix B*.

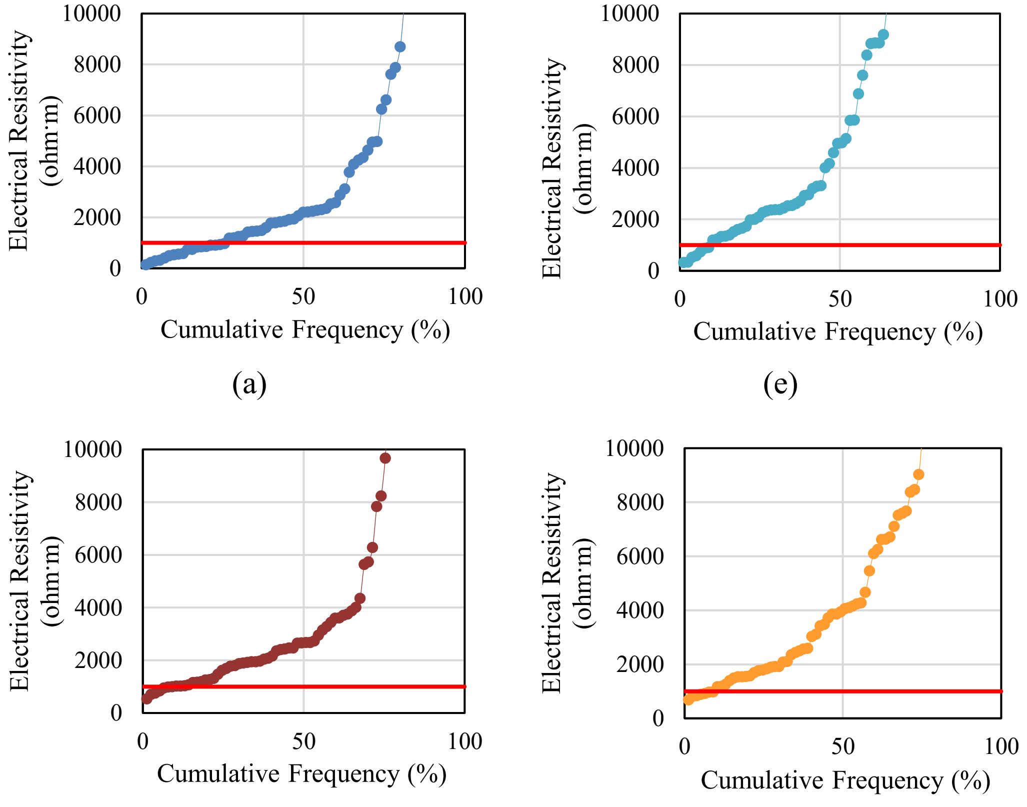

(a) (e)

(b) (f)

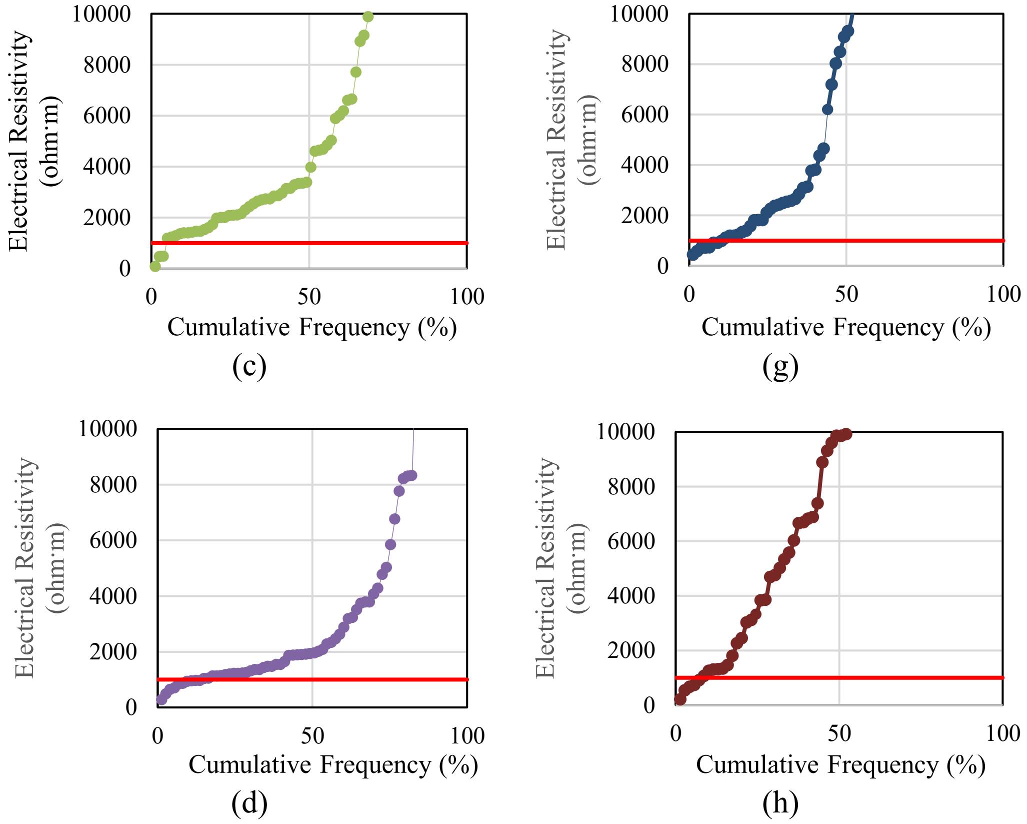

(c) (g)

(d) (h)

Figure 20: Cumulative frequency distribution of electrical resistivities measured on: (a) B3-P47/46, (b) B8-P47/46, (c) B4-P47/46, (d) B9-P47/46, (e) B6-Ab/P47, (f) B6-P48/49 (g) B10-Ab/P47, (h) B5-P47/46 girder.

The cumulative probability plot shows a high concrete resistivity with approximately 10% of the points below the 1000 ohm·m threshold. Only for B3-P47/46 was recorded the 25% of the points below the 1000 ohm·m threshold, but well above the severe corrosion range. In addition, except for B5-P47/46, two characteristic distributions can be observed: a first line with a maximum resistivity between 2000 and 4000 ohm·m associated with 40-60% of the points, and a second line with increasing values. In view of the results obtained, the influence of the concrete quality and the environmental conditions should be taken into account. The evidence of pore compaction found during visual inspection, could have led at the intrinsic resistive inhomogeneities due to the different moisture content of the concrete. On a microscopic scale, this means an open pore structure and a higher connectivity of the pores to the CO_2 ingress. Therefore, the carbonation densifies the concrete and its depth becomes a relevant parameter to estimate: if it extends beyond the concrete cover, its resistivity controls the rate of any active corrosion, otherwise it is controlled by the resistivity of the concrete [10]. In addition, changes in temperature have an important effect on the concrete resistivity. A decrease in temperature results in an increase in the measured resistivity of the concrete and vice versa. Therefore, as the measurements were taken in January with an average temperature of 10 °C, a decrease of 3% to 5% per degree should be considered in the warmer periods [9].

The carbonation depth was determined chemically during the material characterization phase of the experimental campaign. After the concrete core drilling, phenolphthalein indicator solution was sprayed on the surface. A total of thirty-three carbonation depth samples were taken from beams B3-P47/46, B8-P47/46, B4-P47/46 and B9-P47/46 beam, showing an average value of 2.7 cm and a standard deviation of 0.7 cm. When the carbonation depth is related to the average concrete cover, it can be seen that the carbonation has reached the reinforcement but is well below the 4.5 cm of the strands level. These results are consistent with the depassivation of the reinforcement as indicated by the negative half-cell potentials and the high resistivity values.

As described above, concrete resistivity measurements can be considered as an additional descriptor of the tendency of a system to develop corrosion but are not sufficient to assess the rate of deterioration. The amount of electronic current generated by the anodic reaction and consumed by the cathodic regions of the corroding steel can provide a useful quantitative indication of corrosion activity. Therefore, to confirm the passive state of the strands, the instantaneous corrosion rate was estimated on the same sample points as defined above. The corrosion rate is determined electrochemically using the theory of polarization resistance developed by Stern and Geary in 1957 [13]. The linear polarization technique requires the steel to be polarized by an electric current and is based on the assumption that the polarization curve is linear close to the corrosion potential. The slope between the change in potential and the resulting current is defined as the polarization resistance. The polarization resistance is related to the corrosion current by the Stern and Geary formula [14]. Several analytical models have been proposed in the literature to explain the effect of corroded steel, assuming an appropriate equivalent electrical model. The device used to measure the polarization resistance in this thesis is based on a recently developed technique called Connectionless Electrical Pulse Response Analysis (CEPRA) [15, 16]. The method is based on using a four-probe Wenner array configuration and assuming a steel-concrete system with double layer capacitance at the steel-concrete interface, concrete resistances and polarization resistance (Figure 21). The outer probes are used to apply a current pulse, while the potential differences between the two inner probes are monitored. The polarization resistance, from which the corrosion rate is determined, is obtained by fitting the measured voltage response to the theoretical transient of the circuit over time.

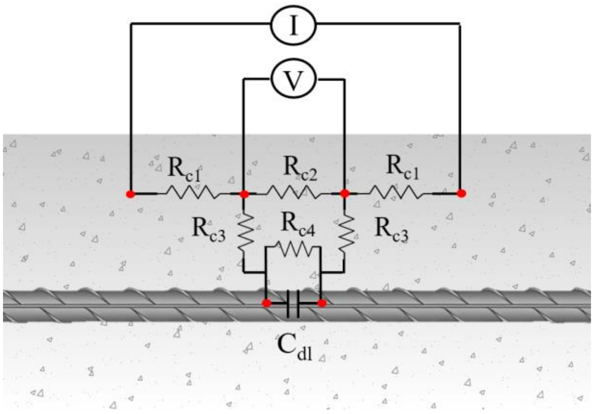

Figure 21: Electrical circuit of reinforced concrete system in CEPRA.

From a practical point of view, corrosion rate values below 0.1 μA/cm^2 indicate negligible corrosion associated with steel reinforcement classified as passive, the range between 0.1-0.5 μA/cm^2 can be considered the transition region between passive and active corrosion, and values above 1 μA/cm^2 represent a high corrosion rate [17]. According to the half-cell potentials and resistivities measurements, each structural member was treated statistically to obtain a representative condition (Figure 22). The pattern of the corrosion current is shown in *Appendix B*.

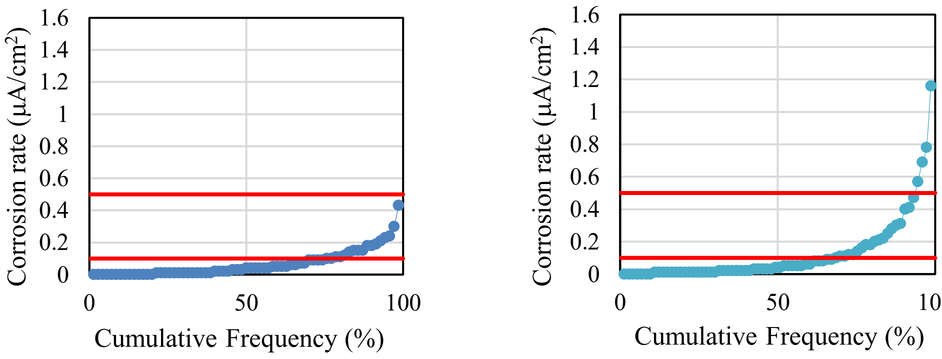

(a) (e)

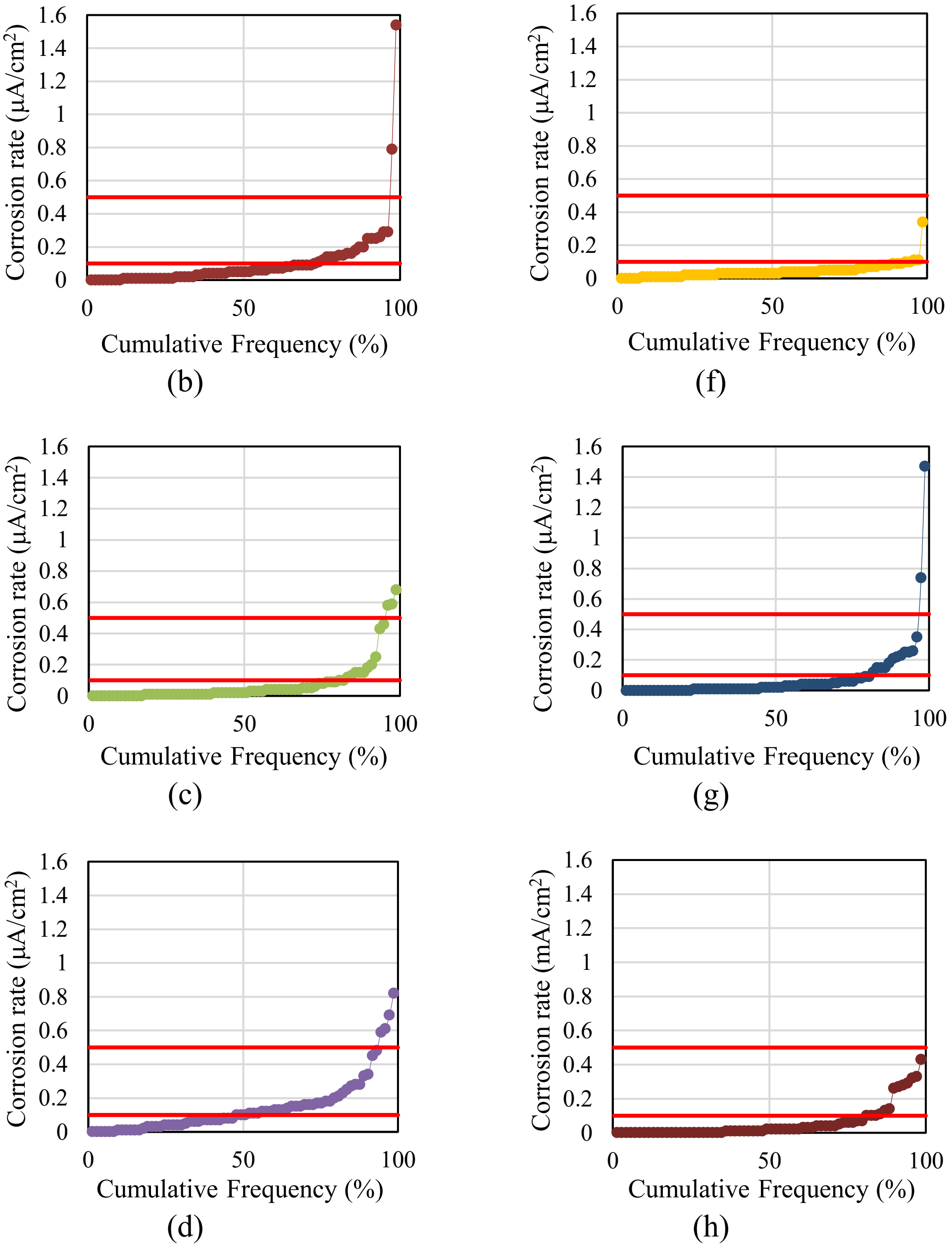

(b) (f) (c) (g) (d) (h)

Figure 22: Cumulative frequency distribution of corrosion rate measured on: (a) B3-P47/46, (b) B8-P47/46, (c) B4-P47/46, (d) B9-P47/46, (e) B6-Ab/P47, (f) B6-P48/49 (g) B10-Ab/P47, (h) B5-P47/46 girder.

The corrosion rate was found to be below the limit of 0.1 μA/cm^2 in 65-80% of the sample points and was therefore negligible. The B6-P48/49 beam presented the highest number of sample points in the passive state, equal to 97%, while the B9-P47/47 beam presented the lowest number, equal to 48%. The remaining points showed relatively low levels of corrosion, except for a few isolated points where the corrosion rate was higher than 0.5 μA/cm^2. This tendency agrees well with the intermediate value observed for the half-cell potentials and with the high variability of the electrical resistivity measured.

The representative values of the structural elements are given in Table 1. The effective contribution of the data has been taken into account by calculating the weighted average with reference to the thresholds specified above for each parameter.

Table 1: Weighted average of corrosion measurements.

Beam ID	**Half-cell potential (mV/CSE)**	**Electrical resistivity (ohm·m)**	**Corrosion rate (μA·cm^2)**
B3-P47/46	-263.3	7423.5	0.06
B8-P47/46	-192.7	6955.5	0.10
B4-P47/46	-223.8	10496.9	0.08
B9-P47/46	-243.3	6368.6	0.14
B7-P47/46	-	-	-
B6-Ab/P47	-148.7	10711.7	0.12
B6-P48/49	-166.5	7361.4	0.04
B10-Ab/P47	-194.3	18060.7	0.08
B5-P47/46	-208.7	15355.5	0.06
Bx2-Ab/P47	-	-	-

Overall, the electrochemical measurements revealed a generally passive state of the reinforcement, with the exception of a few areas where the presence of chloride ions or the lower resistivity, probably associated with a localized increase in porosity, resulted in a low corrosion rate. However, the carbonation depth was found to be lower than the concrete cover of the strands, thus attributing the low corrosion activity detected to the rebar. Destructive tests carried out as part of the experimental campaign allowed to remove the concrete cover and confirmed the good state of preservation of the strands, with no signs of rust. It is worth mentioning that the concrete cover of the prestressing strands was found to be in compliance with the minimum value requirements for the durability of prestressing steel according to the Eurocode 2 (EC2) provisions [18], taking into account the structural class S4 and the exposure class XD1/XS1.

Finally, it should be mentioned that the electrochemical measurements show daily and seasonal variations due to changes in temperature and relative humidity. However, the aim of the present work was not to predict the evolution of structural degradation, but to assess the condition and influences on the structural behavior at the time when the measurements were carried out. Therefore, measurements over a long period of time were not required.

3.3 Full-scale load tests

Static load tests are usually performed to measure the corresponding deformations and to verify whether the actual working condition of the new bridge meets design assumptions. Load tests can also be conducted during the service life if the structural integrity of the bridge is compromised. Moreover, the experimental data from the load test are also useful for calibrating numerical models of the viaduct, representative of the in-service performance. Basically, two types of static load tests can be used: diagnostic load tests and proof load tests [19]. Diagnostic load tests are used to update structural models with respect to observed response under service load. In contrast, proof load tests are intended to verify whether a bridge can withstand prescribed loads without significant non-linear effects. Diagnostic load tests are suitable for in-service bridges, where only the linear elastic response can be observed. However, the response of a structure to in-service loads is not fully representative of its behavior at higher loads due to non-linearity, stress redistribution, and interactions between elements. Testing elements up to failure provides more detailed information about non-linear behavior and the maximum bearing capacity of the bridge. However, its application is relatively rare because the bridge must be decommissioned after the test is completed.

Within the BRIDGE|50 framework, there was the unique opportunity to study the response of existing PC bridge girders during a load protocol up to failure. Based on the main objective of collecting as much informative data as possible by performing load tests, a proper design was implemented, including appropriate sensors, their location, and the load test setup.

3.3.1 Loading tests plan

The planning of the research project was designed to test beams with a range of degradation, from those in good condition to those exhibiting controlled damages. Finally, beams damaged by corrosion will be also tested in order to correlate the extent of deterioration observed with the residual bearing capacity. The first part of the experimental testing campaign, included in this thesis, involved B3, B4, B5, B7, B8 and B9 girders belonging to P47/46 span, B6 belonging to P48/49 span and B6, B10 and Bx2 belonging to Ab/P47 span. As detailed in Section 3.2.1, all beams were classified undamaged except for B6-P49/48 and B10-Ab/P47 which showed damages induced by the lifting operations. To study the contribution of the cast in situ slab to the composite behavior with I-beams, the B9-P47/46 beam was tested after the removal of the slab by saw cut. Finally, to investigate the flexural behavior change due to a reduction of about 50% of the prestressed reinforcement comparable to a high level of corrosion, controlled damage was induced to B5-P47/46 beam. The damage was created by cutting a total of eight strands in the bottom flange at a distance of 60.0 cm on either side of the girder midspan (Figure 23).

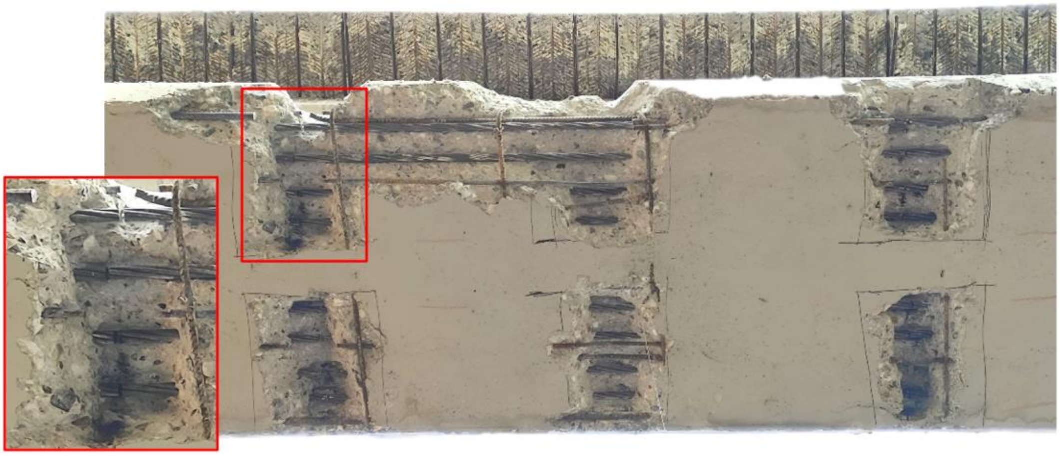

Figure 23: Strands cutting in B5-P47/46 girder (bottom view).

Several test setups and loading procedures were planned to examine various phenomena. To investigate the bending resistance of the girders under the combined influence of shear and flexure, a three-point bending test configuration was adopted. In addition, the four-point bending test configuration was also considered, where loads were applied with appropriate shear span to induce a constant bending moment region and approach shear failure. In this thesis has been reported the experimental tests referred to flexural failure. The loading process was planned with two distinct phases. The first loading phase aimed to achieve stabilized crack opening, while the second loading phase, following the unloading of the first phase, enabled the determination of decompression load and the ultimate load capacity. For B9-P47/46 beam, a monotonic load test was specifically planned to analyse the structural behavior up to failure, excluding the influence of the initial loading phase. The PC box girder was subjected to loading in three phases. The first phase involved one cycle of loading after cracking, followed by one cycle with stabilized cracks. Finally, the girder was subjected to a load until failure, allowing for a comprehensive investigation of its structural performance. The specifies of the load test protocol are reported in Table 2.

Table 2: Load test protocol.

Beam ID	Type	Class	Test setup	Loading phases
B3-P47/46	Composite	Undamaged	3 p.b.t	2
B8-P47/46	Composite	Undamaged	3 p.b.t	2
B4-P47/46	Composite	Undamaged	3 p.b.t	1
B9-P47/46	I-beam	Undamaged	3 p.b.t	2
B7-P47/46	Composite	Undamaged	4 p.b.t	2
B6-Ab/P47	Composite	Undamaged	4 p.b.t.	2
B6-P48/49	Composite	Damaged by dismantling	4 p.b.t.	2

B10-Ab/P47	Composite	Damaged by dismantling	4 p.b.t.	2
B5-P47/46	Composite	Controlled damage	4 p.b.t.	2
Bx2-Ab/P47	Composite/box beam	Undamaged	4 p.b.t.	3

Due to the extent of the project, external contractors were required to move the girders, and effective coordination among them was a crucial part of the planning process. This work also included risk analysis to ensure a safe working environment.

3.3.2 Loading frame

One of the aims of this research study was to establish a diagnostic test protocol capable of effectively recording the performance of PC girders under both service and ultimate conditions. To meet this requirement, a loading frame was specifically designed and supplied by the Interdepartmental Center for the Safety of Infrastructures and Constructions (SISCON) of Politecnico di Torino. The large-scale experimental testing ensured a robust and reliable assessment of the structural behavior of the girders, allowing for systematic field loading and easy access for sensor installation.

The load frame was a semi-permanent steel structure suitable for testing structural elements with span up to 30.0 m. The supporting base consisted of two main steel longitudinal beams, each composed of five bolted I-shaped sections. These segments were built by welding a 2.0 m high web to 1.0 m wide flanges with plate stiffeners at 1.0 m intervals. The longitudinal beams are connected transversally by five 1.5 m long I-beams (Figure 24).

Figure 24: Building stages of the steel reaction frame.

The specimens under testing are located on the supporting frames (blue color in Figure 25), where specifically designed bridge bearings replicate the statically determinate static scheme. The hinge and roller bolted to the supporting frames have a support plate of 400 × 400 mm and allow ±4° of rotation; the roller allows ±150 mm of longitudinal displacement [20].

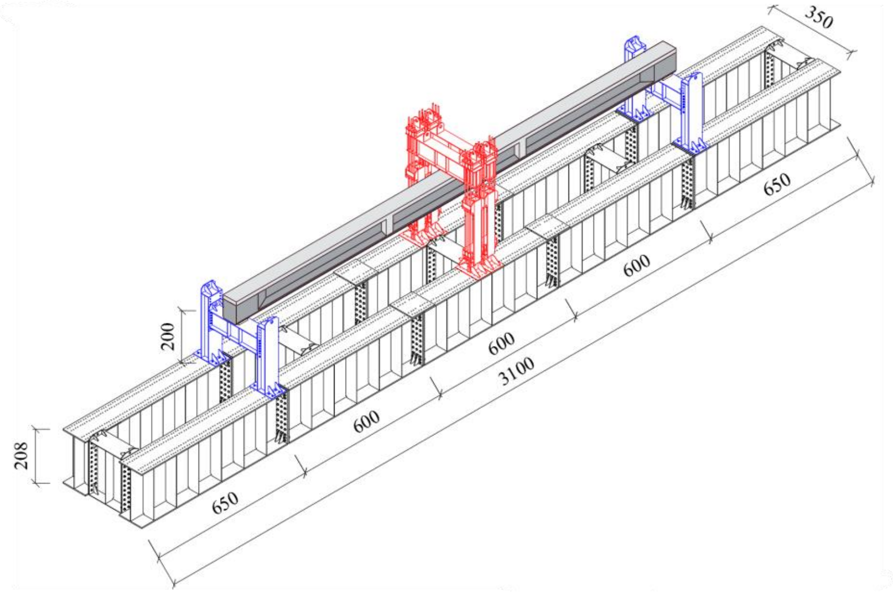

Figure 25: Technical drawing of the load frame: steel frame base (black), supporting frames (blue), and loading system (red) (unit: cm).

A system of four hydraulic jacks is used to apply external loads to the girders. Each jack, hosted into a steel reaction member hinged to the main longitudinal beam, acts on a thrust plate (red color in Figure 25). The reaction force generated is then transferred by six 32 mm steel bars on the opposite plate, which act on a transverse steel beam. The transverse steel beam is used to transfer the load from each pair of hydraulic jacks to the specimen under testing. The capacity of one jack is 1.2 MN, with a stroke length of 750 mm. The loading system is activated by the use of a hydraulic pump with loading rate controlled by the pump pressure. Both the supporting frame and the loading system can be bolted along the longitudinal beams at 10 cm intervals, to test structural members with different spans under three or four-point bending test configurations. The span length adopted in the present work was 19.0 m and the two pairs of hydraulic jacks were positioned 0.3 and 3.0 m away from the midspan, to perform loading tests with three and four-point configuration, respectively. Figure 26 shows a general view of the two setups.

(a) (b)

Figure 26: General view of test setup: (a) three-point loading configuration, (b) four-point loading configuration.

3.3.3 Measurement system

A measurement plan was designed to record the structural response of the girders and to control the loads applied during the tests. The layout of the monitoring system was defined to measure key parameters providing a comprehensive understanding of the structural behavior of the girders. The pilot locations were determined according to the load test setup and subsequently tailored considering both the already performed load tests and the specific specimen under testing. This section summarizes the equipment used to measure the parameters reported in this thesis and detailed below:

- load: measured with load cells placed between the actuators and the thrust plate to measure the acting forces applied to the girder and check the symmetrical loading condition;

- vertical displacement: measured with linear displacement transducers between a fixed frame and the top slab adjacent to the supports;

- horizontal displacement: measured longitudinally with linear displacement transducers between a fixed frame and the cross-section at the ends of the girders;

- deflection: measured with three draw-wire sensors and six linear displacement transducers linked to the lower side of the girders with Invar alloy wires;

- concrete bending strain: measured with linear variable displacement transducers (LVDTs) installed on aluminium frames to obtain average strain referred to a measurement base of 400 mm for I-girders and 500 mm for box girder. The LVDTs were located longitudinally to measure the tensile and compressive strains of the concrete around the midspan. Vertically aligned LVDTs were intended to measure the strain distribution in a cross section of the girder. Furthermore, two electrical strain gauges were installed on the top and bottom flange to compare the LVDTs measurements. All the strain gauges had 120-ohm resistance and measuring lengths of 20 mm;

- concrete shear strain: measured along the shear span with LVDTs installed on supporting frames oriented at 45° and measurement base of 700 mm;

- strand slip: measured with linear displacement transducers between unbounded strands and a frame fixed to the concrete cross-section;

- relative slip between cast-in-place slab and precast beam: measured with linear displacement transducers. It was installed in the shear span for the specimens tested with four-point bending test setup;

- longitudinal strand strain: measured with a strain gauge installed on a single wire at a distance of 1.3 m from the midspan. The strain gauge had 120 ohm resistance and measuring length of 2 mm. This was used for the box beam load test.

Different LVDT stroke lengths were set depending on the expected direction of displacement. The following notation was used to identify the location at which the sensors were placed, followed by a progressive number, indicated here with “xx”:

- V-xx: vertical displacements at the supports;
- H-xx: horizontal displacements at the supports;
- D-xx: vertical displacement to the lower side of the girder;
- C-xx: concrete strain at the top or web around the midspan;
- T-xx: concrete tensile strain at the bottom flange around the midspan;
- SG-xxC/T: concrete strain on the top slab "C" and the bottom flange "T";
- SH-xxA/B: concrete shear strain distinguished by "A" negative and "B" positive slope;
- STR-xx: strand sliding;
- SL-xx: slab sliding;
- LST-xx: longitudinal strand strain.

The detailed layout of the instrumentation installed for each load test is shown in *Appendix C*. The schemes refer to the monitoring system installed on one side of the beams. Due to the different environmental exposures during the service life of the two webs of the box girder, it was decided to duplicate the monitoring system to control both sides. The number of sensors installed for each individual position and load test is given in Table 3.

Table 3: Number of sensors installed for each load test.

Beam	**Position**										**Tot. sensors**
	V	**H**	**D**	**C**	**T**	**SG**	**SH**	**STR**	**SL**	**LST**	
B3-P47/46	2	-	9	4	7	-	20	2	-	-	44
B8-P47/46	2	-	9	4	7	-	20	2	-	-	44

B4-P47/46	2	2	9	4	7	-	16	2	-	-	42
B9-P47/46	2	2	9	2	6	-	20	2	-	-	43
B7-P47/46	2	2	9	2	6	2	20	2	1	-	46
B6-Ab/P47	2	1	9	6	6	2	16	2	1	-	45
B6-P48/49	2	1	9	6	6	2	16	2	1	-	45
B10-Ab/P47	2	1	9	6	6	2	16	2	1	-	45
B5-P47/46	2	1	9	6	6	2	16	2	1	-	45
Bx2-Ab/P47	2	-	9	6	6	3	16	2	1	1	46

During all phases of measurement, the sensors were connected by wire to six data acquisition systems where data were collected at a sampling frequency of 10 Hz and stored on a computer. After each load test the cracks were carefully marked and then reported in digital format using a digital camera. In addition to the monitoring during the loading test, other parameters were recorded during the diagnostic tests. Details of the equipment used are given in the inherent sections.

3.3.4 Three-point bending test results

Several measurements and observations were made using the monitoring system described above. The parameters observed provided information on the stiffness, resistance mechanism, and interaction between the precast I-beam and the cast-in-place slab. For a better presentation of the results, these were differentiated into three-point bending tests, four-point bending tests, and the box girder test. The most representative data are reported and discussed below. Dashed curves indicate unreliable measurements due to unforeseen technical issues. The diagrams were obtained in relation to the load transferred by an actuator; therefore, the total load can be obtained by multiplying this value by four. It is worth noting that the total action present on the beam must include the weight of the loading frame (estimated to be 11.82 kN per actuator) and the dead load of the specimen. The B3-P47/46, B8-P47/46, B4-P47/46, and B9-P47/46 girder, were subjected to static loading at rates 1.7, 3.0, 2.7, and 1.8 kN/min, respectively. All recordings are listed in *Appendix D* for each girder.

Figure 27 illustrates the load-deflection curves obtained from the midspan measurement point. Each beam exhibited a consistent trend characterized by two distinct slopes. Initially, during the early loading stages, the load-deflection curve followed a linear trend, emphasizing the elastic behavior of the tested beams. As the load approached the cracking point, the deflection increased due to a reduction in stiffness. During the first loading phase, the B9-P47/46 girder showed a lower flexural stiffness, which can be attributed to the removal of the top slab. At the end of the first loading cycle, the internal damage induced to the beams led to a residual deflection of approximately 12 mm after unloading. In the subsequent loading cycle, the presence of prestressing exhibited a beneficial effect, as no evident signs of stiffness reduction were observed. During the second loading cycle, the crack propagation phase continued until failure. The B3-P47/46 specimen reached its maximum capacity before collapsing under a load of 78.2 kN, which is associated to an applied bending moment of 1438.9 kNm. The maximum applied loads for B8-P47/46 was 81.1 kN, corresponding to a bending moment of 1492.2 kNm. The B4-P47/46 specimen was loaded up to failure occurred at 71.4 kN, corresponding to a bending moment of 1313.8 kNm. The B9-P47/46 PC beam collapsed after reaching a maximum load of 64.6 kN, corresponding to a bending moment of 1188.6 kNm. At the ultimate load, B3-P47/46, B8-P47/46, B4-P47/46, and B9-P47/46 exhibited maximum midspan deflections of 167 mm, 150 mm, 135 mm, and 145 mm respectively. The curve of the B3-P47/46 beam shows a load reduction at 75 kN related to a holding time required for the visual inspection phase of the cracking pattern. The drop recorded in the response of the B4-P47/46 beam at 72 kN can be associated with a first crushing of the cast-in-place slab.

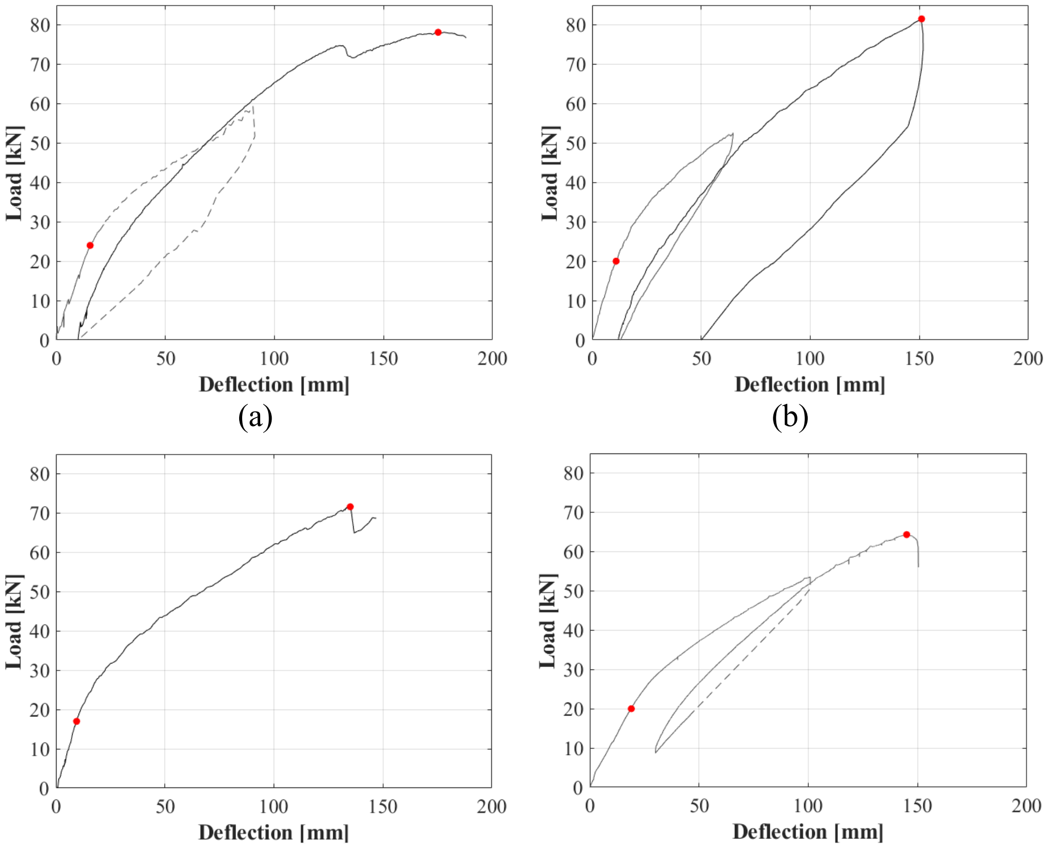

(a) (b)

(c) (d)

Figure 27: Load-midspan deflection curves: (a) B3-P47/46, (b) B8-P47/46, (c) B4-P47/46, (d) B9-P47/46 girder.

All girders collapsed in a non-ductile mode with a bending failure mechanism due to concrete crushing in the top compression zone. In all four tests, crushing of the slab occurred near the loading system rather than in the region of maximum bending moment, probably due to the confining effect of the transverse steel beams. Indeed, a diagonal crack initiated in the highly compressed zone, starting from the lower flange of the same steel beam, as illustrated in Figure 28.

(a) (b)

(c) (d)

Figure 28: Detail of the failure zone: (a) B3-P47/46, (b) B8-P47/46, (c) B4-P47/46, (d) B9-P47/46 girder.

The distribution of the crack pattern after failure is shown in Figure 29. Looking at the mapping of the composite specimens, it can be seen a similar distribution characterized by diagonal cracks due to the influence of shear. Referring to the B8-P47/46 girder, the higher load achieved during the load test resulted in wider crack distribution compared to other beams. For B9-P47/46 girder, the loss of the positive contribution given by the cast-in-place slab anticipates failure without involving the shear resistance. Therefore, mainly vertical cracks are visible near the midspan.

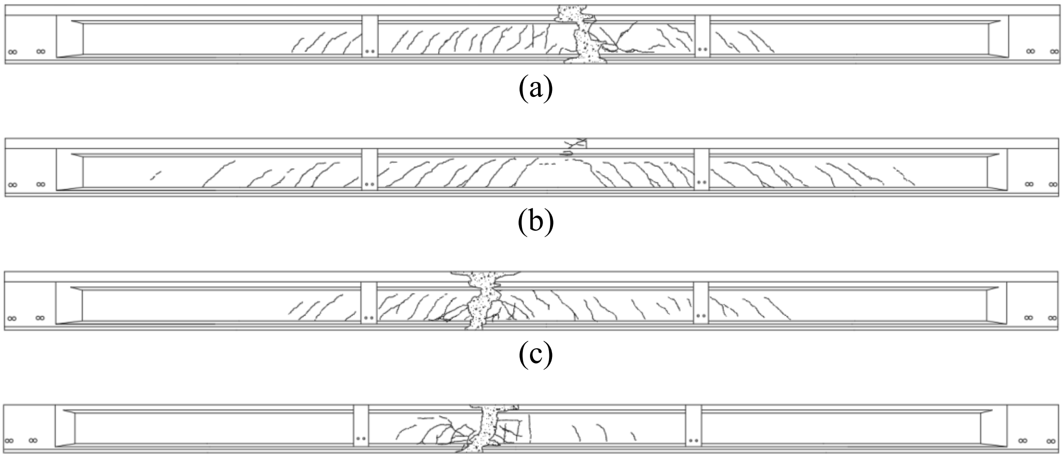

(a)

(b)

(c)

(d)

Figure 29: Crack pattern after failure: (a) B3-P47/46, (b) B8-P47/46, (c) B4-P47/46, (d) B9-P47/46 girder.

During the loading process, the average strains on the concrete in the midspan zone and along the shear spans were taken as representative of the resistance mechanism. The load-tensile strain curves are shown in Figure 30. For clearness, only recordings referred to the minimum cracking load for each beam have been reported. To highlight the change in slope of the curves, it has been considered the first loading cycle up to 35 kN. Each curve shows a linear relationship between the load and strains before cracking. At a load of 22.7 kN, the B3-P47/46 girder cracked, with a strain of 100 με. Similarly, at a load of 17.7 kN, the B8-P47/46 girder cracked, with a strain of 77.2 με. The B4-P47/46 girder cracked as the load reached 16.2 kN, with a strain of 175.9 με. Lastly, the B9-P47/46 girder cracked with a load of 18.7 kN, resulting in a strain of 194.6 με.

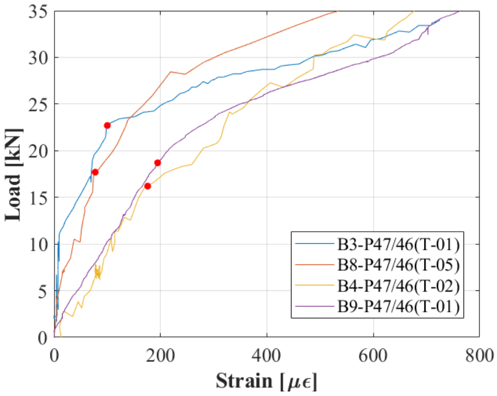

Figure 30: Load-tensile strain curves (cracking load): B3-P47/46, B8-P47/46, B4-P47/46, and B9-P47/46 girder.

Considering that the failure mechanism of all the girders was attributed to the crushing of the top compressive concrete, the measurement of concrete strain in the compression zone becomes a valuable source of information regarding the structural response of the girders under ultimate load conditions. Therefore, the maximum strains recorded at the top slab for girders B3-P46/47 and B8-P46/47, and at the top flange for B9-P46/47 girder, are shown in Figure 31. The concrete strain in the top slab of the composite cross sections was significantly greater than that of the I-beam under the ultimate load. The maximum compressive strain reached for B3-P46/47 was -4132 με, while B8-P46/47 exhibited a maximum strain of -4275 με, and B9-P46/47 showed a maximum strain of -1716 με. When the loading process was close to the ultimate load, a flattening of the curve was observed due to the sharp growth of vertical cracks and a rapid change of the neutral axis. Abnormal behavior occurred with curve B8-P47/46, which was characterized by constant strain with increasing load, likely due to locking of the LVDT support frame.

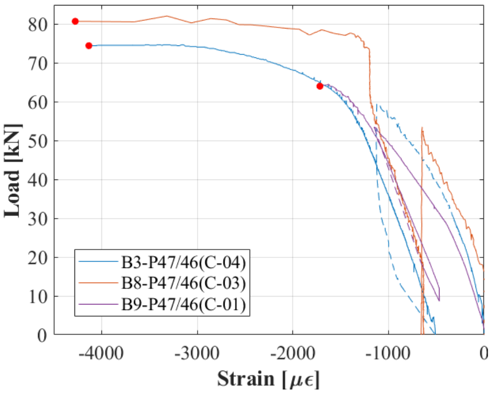

Figure 31: Load-compressive strain curves: B3-P47/46, B8-P47/46, and B9-P47/46 girder.

Another important parameter recorded during the load tests with double loading cycles was the decompression load. During reloading, the cracks remain closed due to the prestressing force and only tensile strains are recorded. Once the applied load is sufficient to reopen the cracks, it is no longer transmitted through the cracks and a sharp change in slope is observed. The load corresponding to the loss of the primary strain rate was taken as the decompression load. Figure 32 shows the load-strain curves for the girders loaded in two phases. Since the strain was related to the measurement base of the LVDTs support, it should be considered as the average strain due to crack opening and the concrete strain between cracks. The change in slope for B3-P47/46 occurred at 11.8 kN, for B8-P47/46 at 12.5 kN, and for B9-P47/46 at 14.8 kN.

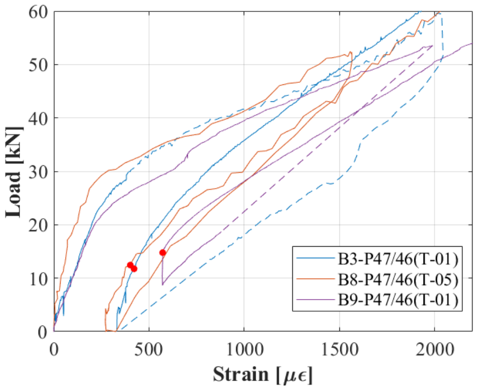

Figure 32: Load-tensile strain curves (decompression load): B3-P47/46, B8-P47/46, and B9-P47/46 girder.

To understand the interaction between shear and bending in the resistance mechanism, Figure 33 shows the average tensile strains recorded by the LVDTs along the shear span. As an example, the measurements of the composite B8-P47/46 girder were compared with those of the precast B9-P47/46 girder during the second and the whole loading phases, respectively. The color of the curves refers to the position of the LVDTs. Instead, dashed lines were used to distinguish the left shear span from the right one. In both cases, a decrease in strain can be seen in the transition from the midspan to the support zone. Furthermore, a slight similarity can be seen by comparing the recordings of the left side (dashed lines) with the corresponding ones on the right (solid lines). As expected, when approaching the maximum load, different resistance mechanisms were activated in the two types of resistant sections. Diagonal cracks were found at about 40 kN in both cases. However, the shear strains of B9-P47/46 were significantly lower than that of the composite section near the ultimate load, which was also confirmed by the cracking pattern shown in Figure 29.

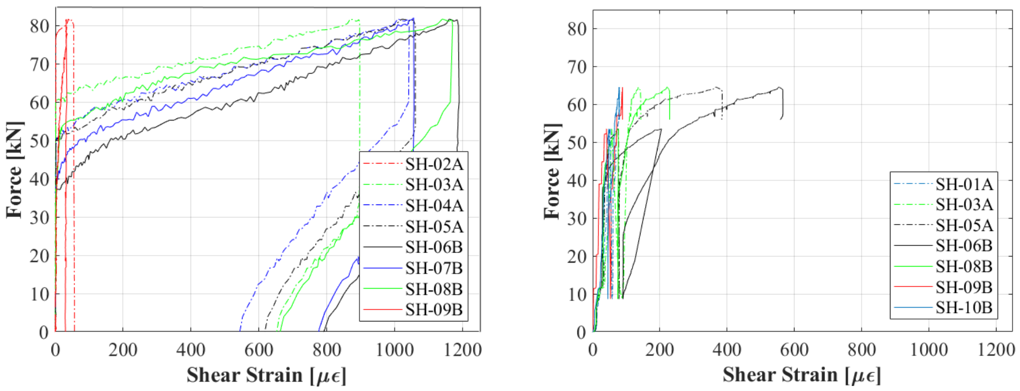

(a) (b)

Figure 33: Load-shear strain curves: (a) B8-P47/46, (b) B9-P47/46 girder.

Table 4 summarizes the most important parameters resulting only from applied loads. In order to obtain values comparable to the results of the four-point bending test, all parameters were related to the bending moment value. In addition, the inherent LVDT positions were adopted for the cracking (M_{cr}) and decompression (M_d) bending moment.

Table 4: Outcomes of the three-point bending tests.

Beam	**M_{cr} [kNm]**	**M_d [kNm]**	**M_u [kNm]**
B3-P47/46	376.8	195.9	1438.9

B8-P47/46	322.1	227.5	1492.2
B4-P47/46	281.9	-	1313.8
B9-P47/46	317.9	251.6	1188.6

If the bending moment of 217.5 kNm due to the weight of the load system and the bending moment of 342.3 kNm due to the self-weight under testing conditions are added to the lowest bending capacity of the composite I-beams, the total bending moment in the critical section is 1873.6 kNm. Thus, it provides a margin of approximately 2.3 times the design load capacity of 823.9 kNm.

3.3.4 Four-point bending test results

In order to determine the bearing capacity under flexural-shear loading, the shear span was reduced from 9.2 m to 6.5 m for each pair of actuators (see schemes in *Appendix C*). Based on experience from the previous three-point bending tests, none of the girders completely collapsed, as the tests were stopped for safety reasons when signs of crushing on the top compression fiber appeared. The load-deflection curves obtained from the four-point bending tests are reported in Figure 34. The diagrams show that the loading process can be divided into three stages: the elastic stage prior to cracking, the cracking stage, and the failure stage. In the first stage, the girders exhibit a linear behavior before cracking. As the applied load increases, concrete cracking in the pure bending region increases and the position of the neutral axis shifts upward. A trend almost parallel to the initial stage occurs during the reloading phase. Due to a more gradual rise of the neutral axis over the cross section in the cracked state, the change in slope when the cracks reopen is smoother than that at the cracking point. The transition from the elastic to the cracked stage of the load-midspan deflection curve for the B5-P47/46 girder was not abrupt as extensive damage was induced in the midspan region prior to the load test. The load-deflection diagram also indicates that the overall stiffness was significantly affected by the induced damage. The B7-P47/46 girder failed at an ultimate load of 120.1 kN, corresponding to a bending moment of 1561.3 kNm. The B6-Ab/P47 girder failed at an ultimate load of 126.5 kN, corresponding to a bending moment of 1644.5 kNm. The B6-P48/49 girder achieved a maximum load of 105.6 kN with an inherent bending moment of 1372.8 kNm. The B10-Ab/P47 girder failed at an ultimate load of 124.0 kN and subsequent bending moment of 1612.0 kNm. The B5-P47/46 girder failed at an ultimate load of 72.4 kN and inherent bending moment of 941.2 kNm. The vertical midspan displacement of the above girders at the ultimate load were 179.9 mm, 191.3 mm, 184.3 mm, 205.5 mm, and 163.4 mm, respectively.

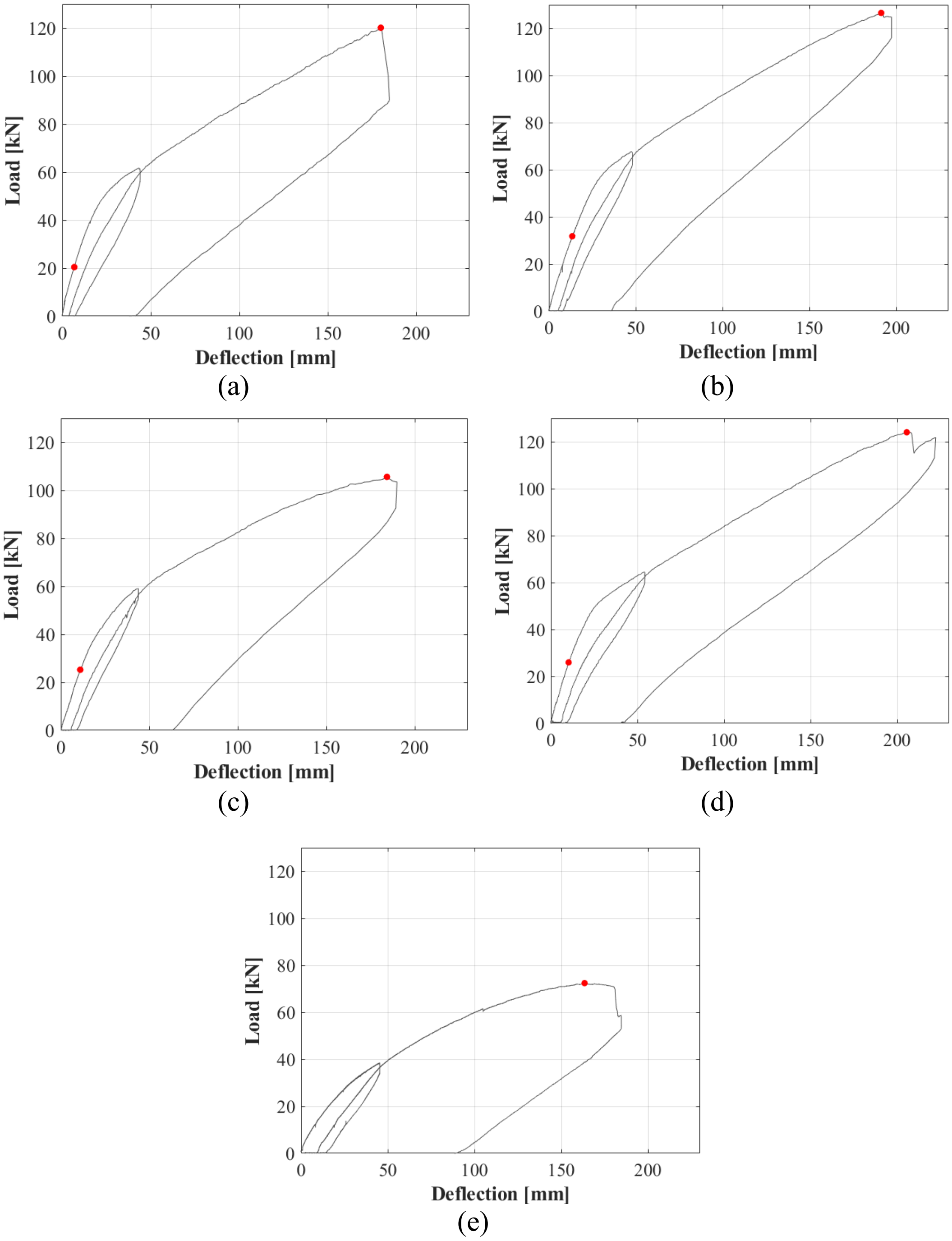

(a) (b) (c) (d) (e)

Figure 34: Load-midspan deflection curves: (a) B7-P47/46, (b) B6-Ab/P47, (c) B6-P48/49, (d) B10-Ab/P47, (e) B5-P47/46 girder.

Since the B6-Ab/P47 girder had the highest ultimate load, it was used as a benchmark to compare the strength of the damaged girders. Girder B6-P48/49, which had strands cut in the midspan equal to a 23.5% reduction in strands in the lower flange, showed a 16.5% decrease in strength. Girder B5-P47/46, which had eight strands cut, equivalent to a 47.1% reduction in strands in the bottom flange, showed a 42.8% reduction in strength. However, no significant changes were recorded for B10-Ab/P47 girder, indicating a negligible effect of wire cutting outside the pure bending region on flexural behavior. The total bending capacity of the most damaged girder, including the bending moment due to the weight of the load system of 153.7 kNm and the bending moment due to the self-weight of 342.3 kNm under testing conditions, was 1437.2 kNm. This provides a margin of approximately 1.7 times the design load capacity of 823.9 kNm, despite the 47.1% reduction in strands at midspan.

Each girder exhibited failure similar to the three-point flexural test, characterized by the compressive failure of the cast-in-place concrete slab, but with different crack patterns. This type of failure occurred in all beams in the region between the two loads except for B6-Ab/P47 girder that failed near a load point (Fig. 35).

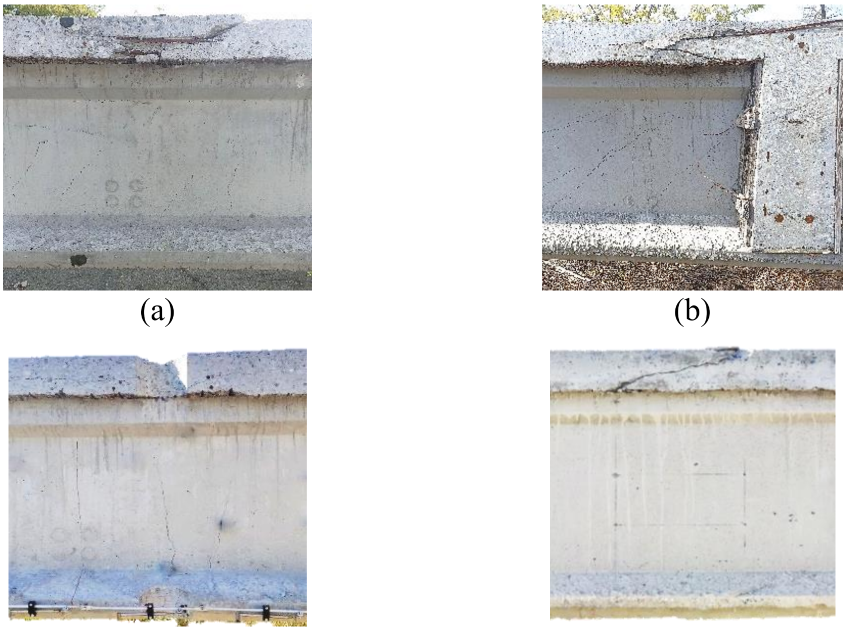

(a) (b)

(c) (d)

(e)

Figure 35: Detail of the failure zone: (a) B7-P47/46, (b) B6-Ab/P47, (c) B6-P48/49, (d) B10-Ab/P47, (e) B5-P47/46 girder.

The crack patterns of the girders after load tests are shown in Figure 36. Two distinct patterns can be evidenced among the girders. Cracks formed outside the constant moment region extended diagonally from the bottom to the top flange for girders without strand cuts at midspan. Only a few cracks were detected in the pure bending region of the B7-P47/46 girder. Vertical cracks consistent with the flexural regime were found in this region for girders with reduced resistance at midspan.

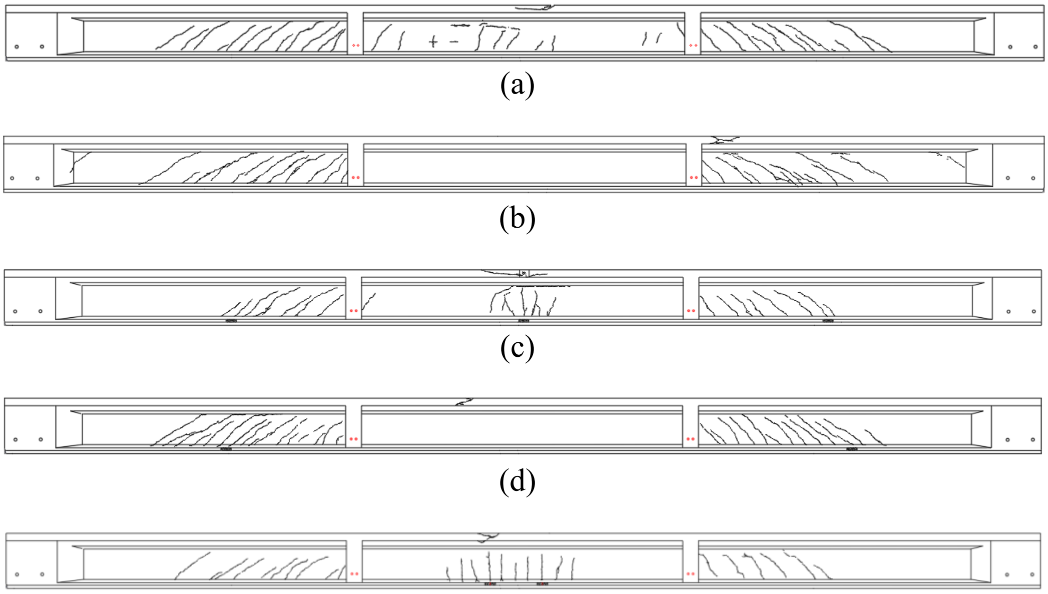

(a)

(b)

(c)

(d)

(e)

Figure 36: Crack pattern after failure: (a) B7-P47/46, (b) B6-Ab/P47, (c) B6-P48/49, (d) B10-Ab/P47, (e) B5-P47/46 girder.

Figure 37 shows the load-tensile strain curves at the bottom edge of the tested girders. For clarity, only recordings related to the minimum cracking load for each beam are reported. For B5-P47/46 girders, the curve was omitted as it was widely damaged at midspan before the load test. However, all available data can be found in *Appendix D*. To highlight the change in slope of the curves, it has been considered the first loading cycle up to 35 kN. Each curve shows a linear relationship between the load and strain before cracking. At a load of 15.0 kN, the B7-P47/46 girder cracked, with a strain of 25.1 με. Similarly, when the load reached 25.5 kN, the B6-Ab/P47 girder cracked, showing a strain of 135.3 με. At a load of 17.2 kN, the B6-P48/49 girder cracked, yielding a strain of 57.5 με. Lastly, the B10-Ab/P47 girder cracked as the load reached 21.5 kN, with a strain of 82.1 με. After cracking, the non-linear phenomenon began, and the neutral axis moved upward, causing a change in slope.

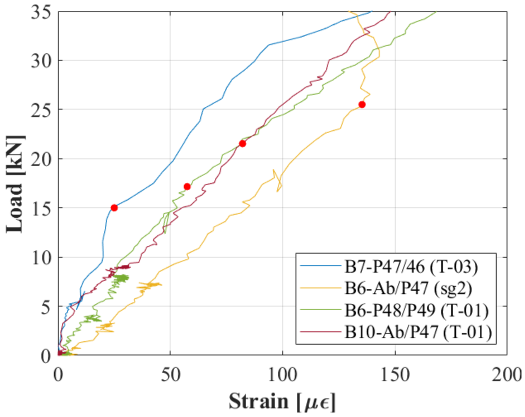

Figure 37: Load-tensile strain curves (cracking load): B7-P47/46, B6-Ab/P47, B6-P48/49, and B10-Ab/P47 girder.

Figure 38 depicts the compressive strain curves of the cast-in-place slab of the tested beams. For girders without prior damage, a linear increase in concrete strain is seen before the cracking. When the load exceeds the cracking point, the linear increase disappears, and the strain increment is higher than the linear one. However, only for the B7-P47/46 girder, the strain gauge was installed near the crushing zone, and a compressive ultimate strain of -2242 με was recorded. The strain gauge for B6-Ab/P47, B6-P48/49, B10-Ab/P47, and B5-P47/46, was far from the crushing zone. As a result, the maximum compressive strain recorded was -1385 με, -1080 με, -1675 με, and -1290 με, respectively.

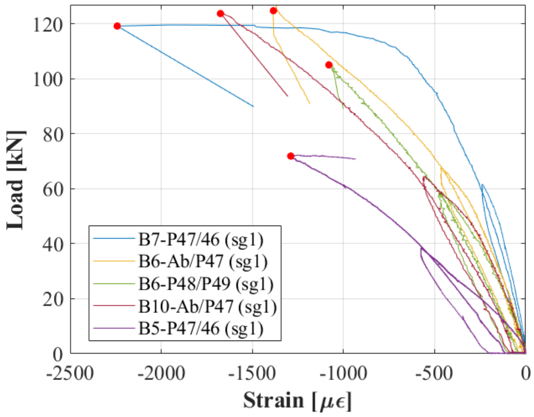

Figure 38: Load-compressive strain curves: B7-P47/46, B6-Ab/P47, B6-P48/49, B10-Ab/P47, and B5-P47/46 girder.

The decompression load was determined by examining the load-tensile strain curves during the reloading phase (Fig. 39). These curves typically exhibit a bilinear response. In the first branch, the increase in load was accompanied by a proportional decrease in precompression. The increase in the load applied in the second branch is no longer accompanied by a proportional increase in strain, as the load was no longer transferred across the cracks at the beam surface. The load corresponding to the transition point was taken as the decompression load. The strain rate for B7-P47/46 changed at 9.1 kN, for B6-Ab/P47 at 17.0 kN, for B6-P48/49 at 15.6 kN, and for B10-Ab/P47 at 15.9 kN. The decompression load for B5-P47/46 girder could not be determined due to pre-existing damage.

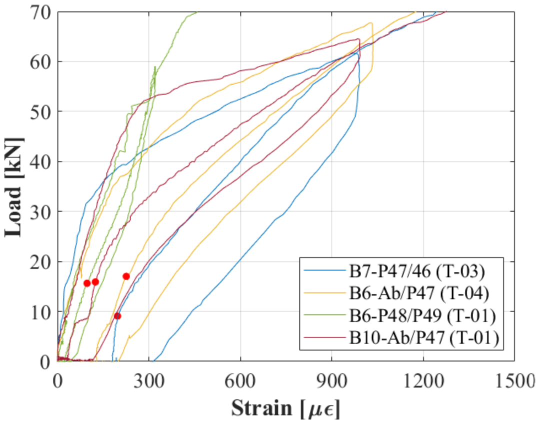

Figure 39: Load-tensile strain curves (decompression load): B7-P47/46, B6-Ab/P47, B6-P48/49, and B10-Ab/P47 girder.

The following Figure 40 shows the strain distribution along the cross section at various loads. According to the graphs, the cross section of the girders before cracking basically conformed to the hypothesis of plane section at various load levels. At this stage, the ratio between the height of the compressive zone and the effective height of B6-Ab/P47, B6-P48/49, B10-Ab/P47, and B5-P47/46 girder was about 0.46, 0.52, 0.62, and 0.49, respectively. When cracking occurred, the neutral axis shifted up the cross section and the strain distributions become non-linear. When the applied load reached the ultimate value, the ratio decreased to 0.30, 0.27, 0.24, and 0.23, respectively.

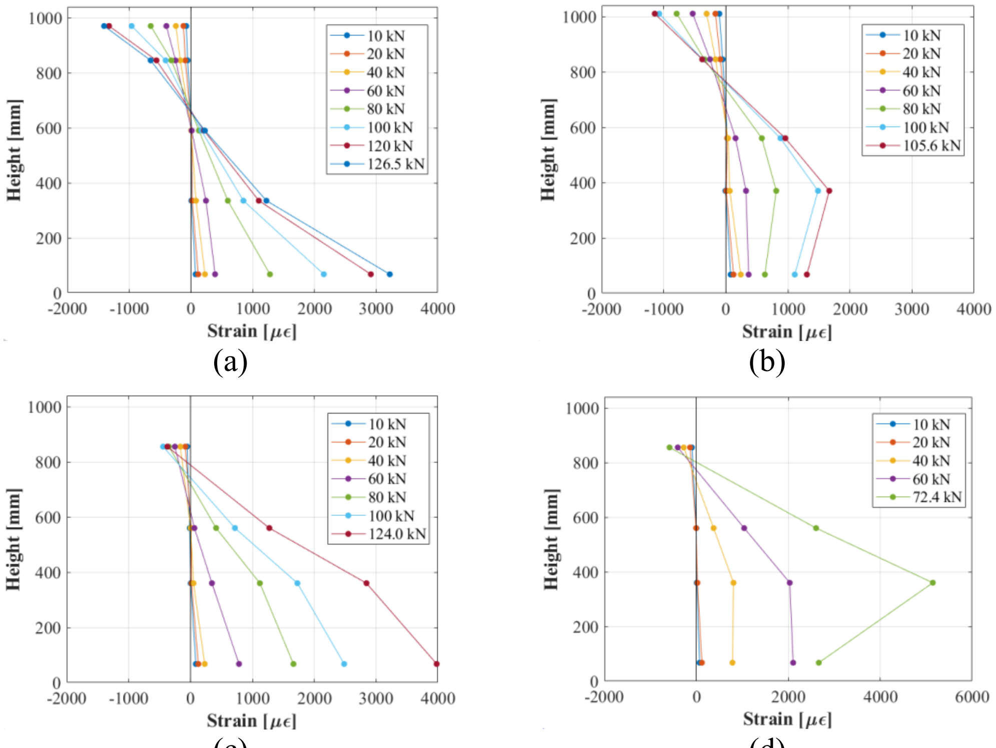

(a) (b)

(c) (d)

Figure 40: Cross-section strain (recorded by sg1, C-01, C-02, C-03, and T-01): (a) B6-Ab/P47, (b) B6-P48/49, (c) B10-Ab/P47, (d) B5-P47/46 girder.

As examples of shear behavior in an undamaged girder and a girder with induced damaged, Figure 41 shows the diagonal strains recorded for B7-P47/46 and B6-P48/49 girder. The color of the curve indicates the location of the LVDT. Instead, a dotted line is used for B6-P48/49 plot to differentiate between left shear span (dashed lines) and right shear span (solid lines). When the girders were loaded to 60 kN, diagonal cracks become visible in the web between the load points and the supports. However, when the maximum load was approached, different resistance mechanisms were activated in the two girders. The shear strains of B6-P48/49 were significantly lower than that of the undamaged girder due to the lower shear stress. In both cases, major shear cracking was observed near the loading points. As expected, the four-point bending setup involved higher levels of shear strain than the previous three-point bending test.

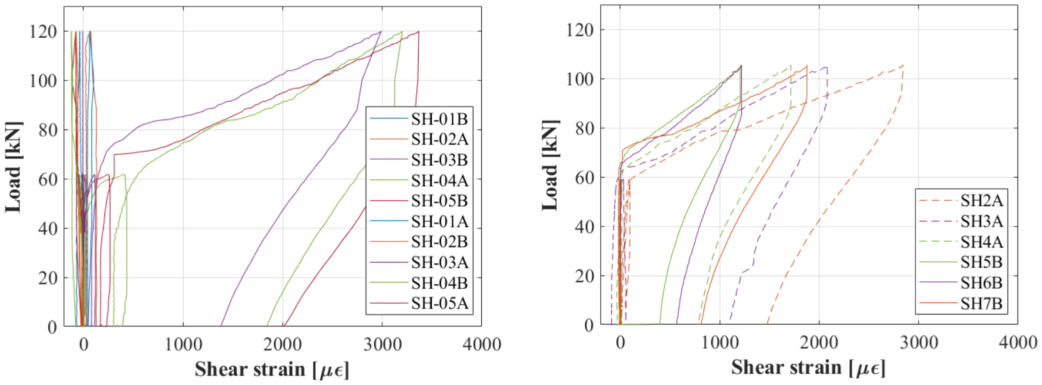

(a) (b)

Figure 41: Load-shear strain curves: (a) B7-P47/46, (b) B6-P48/49 girder.

Table 5 shows the main parameters obtained from the applied loads alone. As previously stated, to obtain the actual value of actions applied to the girders, the self-weight and the weight of the loading system must be taken into account.

Table 5: Outcomes of the four-point bending tests.

Beam	**M_{cr} [kNm]**	**M_d [kNm]**	**M_u [kNm]**
B7-P47/46	195.0	118.3	1561.3
B6-Ab/P47	331.5	221.0	1644.5
B6-P48/49	223.6	202.8	1372.8
B10-Ab/P47	279.5	206.7	1612.0
B5-P47/46	-	-	941.2

3.3.5 Four-point bending test of PC box girder

Durgin the loading test of the box girder, a preventive regularization of the top surface was carried out using a diamond blade to mitigate potential undesirable torsional loads due to the presence of the curb (Fig. 42).

Figure 42: Working phases of curb cutting.

In the following, only the most significative data for the representation of the structural response are presented. Additional recordings are provided in *Appendix D*. Figure 43 shows the load-midspan deflection diagram during the three loading phases. It can be seen the elastic stage, cracks initiation and propagation stage, and the failure point. During reloading cycles, a branch almost parallel to the initial stage shows the beneficial effects of the prestress reinforcements. However, residual displacements of 3.6 mm and 8.1 mm highlight the residual damages during the first and the second cycle, respectively. Also in this case, the presence of over-reinforcement led to the crushing of the compressed concrete in the top slab. The maximum failure load, observed for the box girder was equal to 241.5 kN, corresponding to a bending moment of 3139.5 kNm. The deflection at the ultimate load was 155.4 mm. The bending capacity of the box girders resulted about two times that of the I-girders. This agrees well with the assumption on the original design to assume a box girder the double of the I-girder for the purpose of distributing the load on the deck. Therefore, by adding the bending moment of 217.5 kNm from the weight of the load system and the bending moment of 652.7 kNm from the self-weight in testing conditions, the total bending moment in the critical section resulted 3792.2 kNm. Thus, it provides a margin of approximately 2.3 times the design load capacity of 1638.7 kNm.

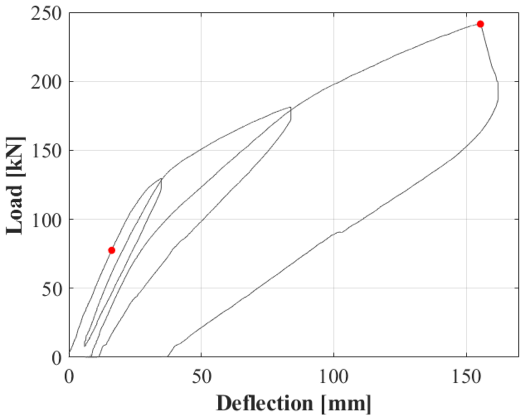

Figure 43: Load-midspan deflection curve of Bx2-Ab/P47 girder.

The PC box girder failed due to concrete crushing of the top slab between the two loading points (Fig. 44a). After the load test, the crack pattern of the girder was characterized by diagonal cracks along the shear span (Fig. 44b). No visible cracks were present in the constant moment region, highlighting the weakness of the cast-in-place slab compared to the precast I-girder.

(a)

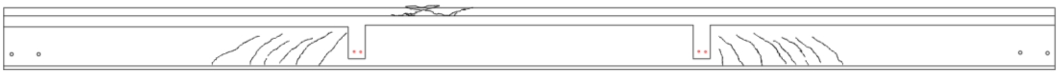

(b)

Figure 44: Cracks after the load test: (a) detail of the failure zone, (b) cracks pattern.

Figure 45 shows the tensile strain measured at the bottom edge by two parallel LVDTs: T-03 installed on the inner side, and T-04 installed on the most exposed side of the in-service configuration. To highlight the strain rate variation, the first loading cycle up to 130 kN has been reported. The T-04 LVDT experienced a variation at 55.1 kN, highlighting the opening of the first crack with a strain of 149.0 με. At the same load, a slight variation was recorded also for the T-03 LVDT. However, due to the low strain recorded on this side, it was possible that cracks opened earlier on the T-04 side.

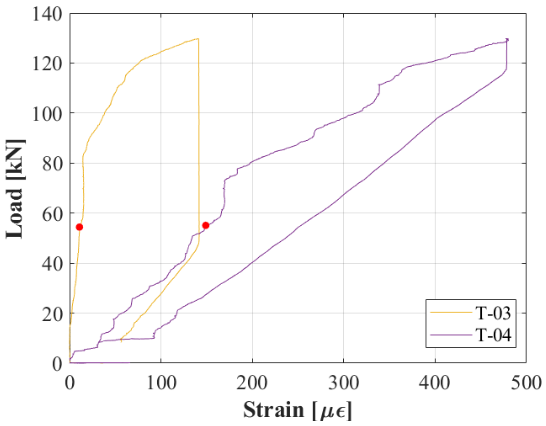

Figure 45: Load-tensile strain curves (cracking load) of Bx2-Ab/P47 girder.

Figure 46 depicts the compressive strain curves obtained from the strain gauge installed on the cast-in-place slab and the corresponding LVDT on the top flange of the girder. A linear increase in concrete strain is observed before cracking occurs. In the cracking phase, the linear increase disappears, and the strain rate is higher than linear. However, it can be appreciated the higher increment in the upper slab compared to the precast girder. At the ultimate load, strains of -1129 με, and -661 με was recorded on the cast-in-place slab and top flange, respectively.

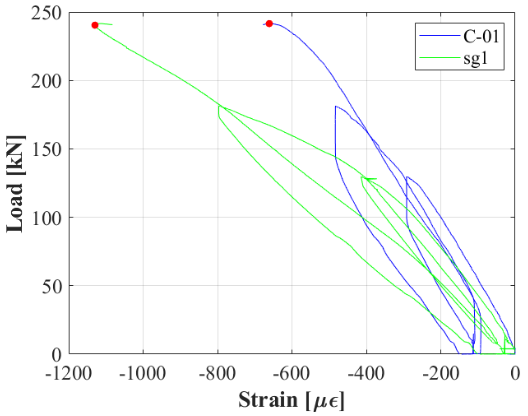

Figure 46: Load-compressive strain curves of Bx2-Ab/P47 girder.

The decompression load was determined from the load-tensile strain curve of the T-04 LVDT, during the reloading phase (Fig. 47). The first and second loading cycles up to 180 kN were reported to visualize the bilinear response at the crack opening. The load corresponding to the transition point was found at 26.0 kN.

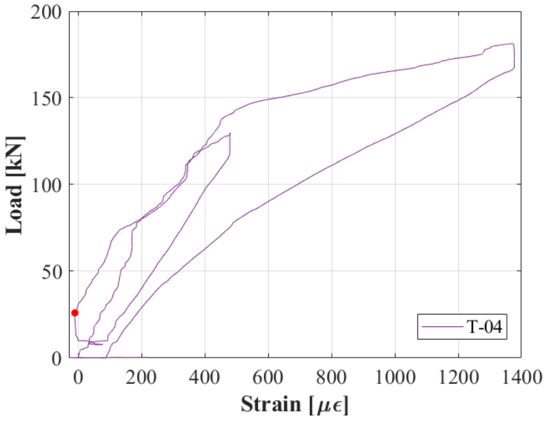

Figure 47: Load-tensile strain curves (decompression load) of Bx2-Ab/P47 girder.

Due to the different exposure and consequent conservation state of the two surfaces on both sides, a difference in the resistant mechanism could be found during the load test. Therefore, in Figure 48 the strain distribution along the cross sections on both sides was compared. According to the graphs, the instrumented cross sections before cracking show a plane section deformation at multiple load levels. At this stage, the ratio between the height of the compressive zone and the effective height of the inner side (Fig. 48a) and the exposed side (Fig.48b) of the girder were about 0.63, and 0.52, respectively. When cracking occurred, the neutral axis shifted upwards in the cross section and the strain distributions become non-linear. When the applied load reached the ultimate value, the ratio decreased to 0.40, and 0.28, respectively. Therefore, higher strains were recorded on the most exposed side.

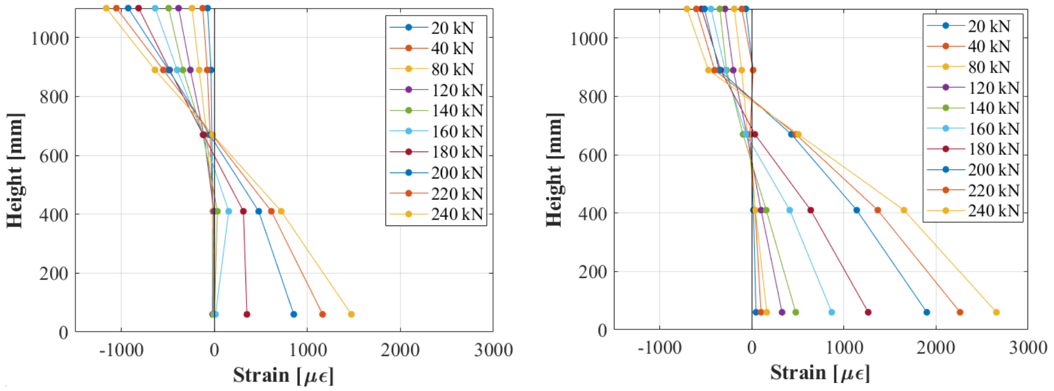

(a) (b)

Figure 48: Cross-section strain of Bx2-Ab/P47 girder: (a) inner side, (b) exposed side.

Figure 49 shows the recordings from the strain gauge on the steel strands. This graph shows the strain resulting from the applied load; it does not include the inherent prestressing strains, self-weight strains, and strains caused by the weight of the loading system. During the first unloading, a trend parallel to the linear branch is maintained. After the second load cycle, the strain value became negative at zero applied load. This could be attributed to local slip of the strand after cracking.

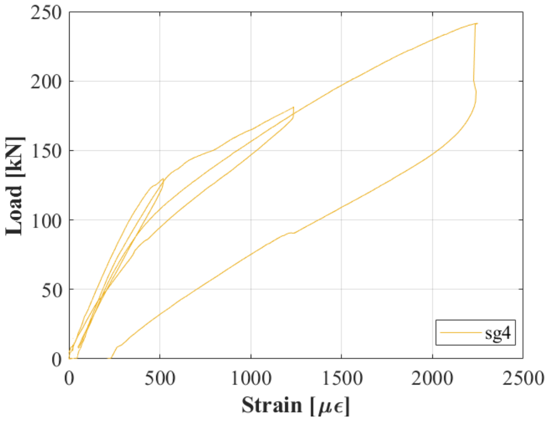

Figure 49: Load-strand strain.

Finally, a comparison was also made among the shear strains. Figure 50 shows two LVDTs on the inner side (dashed line) and their correspondent on the opposite side (solid line). In general, diagonal cracks opened at 150 kN except for SH-05B which experienced a first opening at 125 kN. However, a good correspondence was found among the shear strains of the two opposite sides.

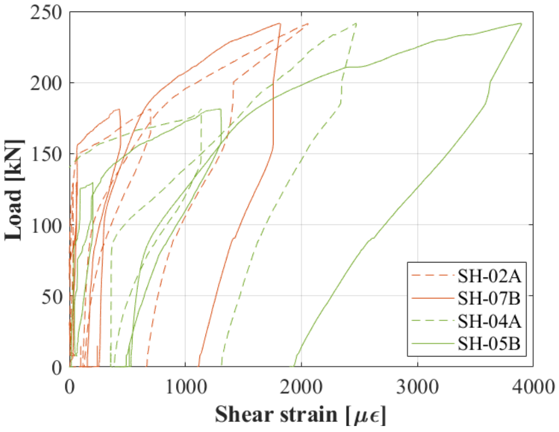

Figure 50: Load-shear strain curves of Bx2-Ab/P47 girder.

3.4 Material tests

Resistance models used for the structural assessment can be defined by data collected from NDT, semi-destructive or destructive tests, as well as monitoring of the structural behavior, or at initial level of assessment from design drawings, and national codes. Intermediate assessment can be carried out using resistance models calibrated with NDT or semi-destructive test data, while advanced assessment requires probabilistic models that take into account statistical variation of parameters. In general, mechanical properties determined by material testing of specimens provide the most reliable assessment at the current age of the structure. However, destructive tests are relatively expensive and time-consuming, and often only a limited number of test data are available. Determining overall structural capacity from a few measurements is not a suitable approach because the material properties of old structures may be affected by different degrees of deterioration depending on the location being analysed. Therefore, indirect measurements using NDT or semi-destructive methods often provide a basis for a reliable assessment, identifying homogeneous areas in terms of concrete properties and minimizing the number of samples required.

Following the preliminary assessment described in Section 3.2, rebound hammer tests were carried out to characterize the concrete without disruption of the surfaces. After completion of the loading tests, an extensive destructive test campaign was planned to evaluate the quality of the concrete and steel by direct methods. A detailed plan was developed to consider the type, number and location of tests. The location of the specimens was chosen to be in areas of minimum stress experienced during the loading tests, where there were no observable signs of damage. As the top slab was produced using continuous casting, it was assumed that samples extracted from this area belonged statistically and qualitatively to the same concrete population. As a result, a smaller number of samples were collected in comparison to the I-girders. However, for practical application, it should be extracted a larger number of samples from the cast-in-place slab when compared to the I-girders. This is because the latter are manufactured under controlled conditions, resulting in reduced variability in the concrete quality. At the same time, since the ordinary reinforcement was not intended for load-bearing purposes in the original design, only a restricted number of samples were collected. Obviously, as the choice on test sites led to values that are more or less representative of the whole population, in the case of existing structures, this choice is based on the objective of the investigation.

3.4.1 Rebound hammer test

The rebound hammer (RH) test is a NDT test that consists of causing the impact of a standardized mass against the surface of the material being tested. After impact, the known initial kinetic energy is partially absorbed by the concrete and the remainder returns to the mass, which moves of a distance proportional to the remaining available energy. Rebound is related to the compressive strength of the concrete surface, as it is greater the higher the surface hardness or density of the concrete. This measure is expressed as a percentage of the rebound height over the distance travelled by the moving mass between the moment it is released and the moment it hits the concrete surface. This percentage is called the rebound index R. Similar to other NDT tests, this technique has inherent limitations. In particular, there is an inherent uncertainty because the rebound index is affected by a number of factors, such as surface moisture, carbonation, surface texture, age, and aggregate type [21]. In order to mitigate the influence of some of the causes affecting the measurement results, it is necessary to carry out several test measurements at the same test area, at a sufficient distance from each other. The RH tests on the concrete surface were carried out according to the European standard (EN 12504-2) [22], avoiding the reinforcement effect, high porosity, and significant irregularities. The RH tests were carried out on all elements after the surface had been properly smoothed with an abrasive stone. For each element, the rebound index was measured in three test areas at 1/6, 1/2, and 5/6 of the span length. In order to obtain values representative of the average conditions of the concrete, without the influence of variations in compaction due to the direction of pouring, measurements were taken in the centre of the web. At each location, readings were taken at 16 grid points spaced 5 cm apart. The maximum and minimum values were then eliminated from each set of local readings and the representative rebound index for each grid was calculated as the mean of the remaining 14 values. The test area was defined by assuming concrete homogeneity in each of them. Therefore, the mean (R) and the standard deviation (s) were considered representative of the concrete strength population in a test area, including the accuracy of the measurement and the material variability. In addition, the coefficient of variation (CoV) was also calculated to compare the level of data dispersion at different scales, considering the test region, individual girders, and grouped elements. Table 6 shows the parameters obtained when each test region is considered as an independent population.

Table 6: Statistical parameters of the rebound index for each test region.

Beam	**Region**	***R***	***s***	**CoV [%]**
B3-P47/46	1	42.9	1.9	4.44
	2	42.6	1.7	4.04
	3	38.4	1.2	3.07
B8-P47/46	1	42.5	2.1	4.93
	2	41.4	1.2	2.84
	3	42.8	2.2	5.16
B4-P47/46	1	39.4	1.1	2.66
	2	38.3	1.0	2.69
	3	39.0	1.2	3.06
B9-P47/46	1	41.9	2.3	5.56
	2	40.5	1.6	4.04
	3	40.4	2.7	6.66
B7-P47/46	1	47.1	1.4	2.98
	2	45.9	1.8	3.94
	3	40.5	2.0	4.92
B6-Ab/P47	1	43.6	1.8	4.04
	2	42.4	3.0	6.94

	3	40.4	2.4	5.89
B6-P48/49	1	47.6	1.5	3.15
	2	45.6	2.2	4.73
	3	45.0	2.1	4.60
B10-Ab/P47	1	46.5	2.0	4.36
	2	43.8	1.8	4.16
	3	42.2	1.5	3.60
B5-P47/46	1	34.5	1.9	5.56
	2	36.0	1.2	3.32
	3	37.1	1.6	4.18
Bx2-Ab/P47	1	41.7	1.6	3.78
	2	42.5	2.3	5.32
	3	41.1	1.6	3.95

The mean values of the rebound index obtained along the girders showed a very small scatter, with the exception of B6-P48/49 which had a maximum difference of 6.6 units between the maximum and minimum values. Furthermore, similar variability was found in each test region with low CoV, ranging from 2.66 to 6.94%. Table 7 shows the results obtained by considering each girder as a homogeneous region.

Table 7: Statistical parameters of the rebound index for each girder.

Beam	***R***	***s***	**CoV [%]**
B3-P47/46	41.3	2.6	6.33
B8-P47/46	42.2	2.0	4.67
B4-P47/46	38.9	1.2	3.06
B9-P47/46	40.9	2.4	5.75
B7-P47/46	44.5	3.4	7.57
B6-Ab/P47	42.1	2.8	6.54
B6-P48/49	46.1	2.2	4.82
B10-Ab/P47	44.2	2.5	5.72
B5-P47/46	35.9	1.9	5.34
Bx2-Ab/P47	41.8	1.9	4.64

Each girder appeared to have relatively close characteristics in terms of mean, standard deviation, and CoV. Only the B5-P47/46 girder had a slightly lower rebound index than the others. Nevertheless, the CoV calculated based on the average values of the rebound index and the standard deviation of the girders was 6.59%, resulting similar to the variability observed within each girder. This value led to the assumption that all the girders were statistically homogeneous. Assuming that all data belong to the same population, concrete properties can be described by a unique distribution. Therefore, by ranking all the test results from the lowest to the highest value, the following cumulative distribution function (CDF) of the RH test results was obtained (Figure 51). The CDF shows that the rebound index of all the girders ranges between 32 and 50 units with a median value of 42.

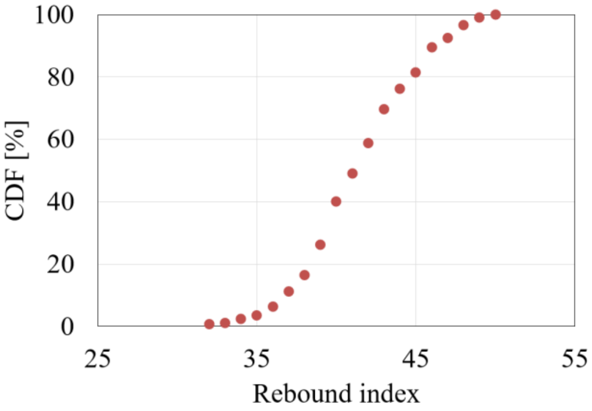

Figure 51: Cumulative distribution function of rebound hammer test results.

NDT tests could be used not only for qualitatively assessment of concrete homogeneity but also for a quantitative assessment of strength. A considerable amount of research has been devoted for decades to analysing the relationships between NDT test results and estimates of concrete strength. An impressive number of studies in literature have proposed a variety of conversion models that correlate concrete properties and NDT measurements. However, the wide variety of concrete compositions, the presence of influencing factors, and measurement errors have led to a lack of accuracy when these models are used to predict concrete strength in different contexts [23-24]. It is now widely accepted that an efficient approach should relate the interpretation of these measurements to reliable and representative test results provided by destructive testing. The use of field tests does not eliminate the need for core sampling, but it can reduce the number of cores required by providing a better understanding of the strength variation in the structure and greater confidence that the cores taken reflect the conditions being investigated. Thus, the real challenge is to reduce the number of destructive tests and determine how many specimens can be considered sufficient without compromising the quality of the assessment [25-27]. There are no common rules for determining the relationship between the amount of NDT information available after testing, the method of processing NDT results, and the level of accuracy of concrete strength estimates [28]. Identifying the appropriate conversion model is equivalent to minimizing the gap between the field test results and the strength of the corresponding cores at selected locations. In general, there are two main approaches for determining model parameters: employing statistical regression to fit a specific model or calibrating a prior model. It should be emphasised that the identification of the conversion model through a prior model is more robust compared to a specific fitted model when there is a limited number of cores, and the range of strengths is the same. Conversely, specific models exhibit greater efficiency when there is a larger number of cores available for statistical regression. The European standard EN 13791, in both its 2007 [29] and 2019 [30] versions, provided a procedure for the evaluation of in-situ concrete strength from NDT measurements. The main changes in the improved version (EN 13791-2019) relate to the adoption of conditional coring to select the sampling position, the reduction of the number of cores from 18 to 8 when an indirect test method is used, and the adoption of only linear regression of a specific model as the method for identifying the conversion model. Two approaches are provided for assessing the in-situ compressive strength by combining NDT and core results, namely the indirect test method with calibration and without calibration. Furthermore, it provides an approach to estimate the characteristic in-situ compressive strength when direct testing method is used. Moreover, a recent RILEM publication [31] proposed a guideline for the improvement of the in-situ compressive strength assessment introducing a target accuracy consistent with predefined objectives.

In order to establish a correlation model between the rebound index and concrete compressive strength of cores, a total of 8 conditioned cores were taken from the same locations as the RH tests. The test areas were distributed over 4 girders, with 2 locations examined on each girder. For proper evaluation, cores should have been taken to cover the full range of rebound index values (region 1 of B5-P47/46 and region 1 of B6-P47/48) as this may increase the range of strength variation covered by the regression. However, due to the schedule of the research project, it was necessary to collect the cores in a progressive order. All the results obtained during the destructive testing campaign are detailed in the next section. Compression tests were carried out in accordance with EN 12390-3 [32] and EN 12504-1 [33] procedures. All the extracted cores had a length to diameter ratio (L/d_m) of approximately 2.0. Table 8 summarizes the results of the compression test on cores taken from the region where both the RH test and the compression test were carried out.

Table 8: NDT and compression strength test results at core locations.

Beam	**Region**	***R***	**Core ID**	**d_m [mm]**	**L [mm]**	**f_c [MPa]**
B3-P47/46	1	42.9	T3_4	74.3	150.2	35.2

	3	38.4	T3_2	74.3	150.9	28.9
B8-P47/46	1	42.5	T8_1	74.3	151.9	29.5
	2	41.4	T8_3	74.3	150.3	27.7
B4-P47/46	1	39.4	T4_4	74.4	151.7	25.8
	3	39.0	T4_2	74.4	151.6	24.0
B9-P47/46	1	41.9	T9_3	74.4	152.1	34.8
	3	40.4	T9_2	74.3	151.6	32.5

The calibration was performed according to the recommendations of the European standard EN 13791:2019 [30] and RILEM TC249-ISC [31]. The comparison of the rebound indices (R) and the strength values (f_c) did not show any clear non-linearity and therefore a linear model was defined to fit the eight pairs of values:

$$f_c = a + b \cdot R \tag{1}$$

where a and b represent the model parameters to be identified. In order to minimize the residual between the estimated ($f_{c,est\,i}$) and measured strengths (f_{ci}), regression analysis based on the least-square criterion was used:

$$SSE = \sum_{i=1}^{n} \left(f_{ci} - f_{c,est\,i}\right)^2 = \sum_{i=1}^{n} e_i^2 \tag{2}$$

where SSE represents the sum of squared errors e_i between the observations and the regression line on n test points. By minimizing the SSE, the slope coefficient and the intercept can be expressed as:

$$b = \frac{n \sum_{i=1}^{n} R_i f_{ci} - \sum_{i=1}^{n} R_i \sum_{i=1}^{n} f_{ci}}{n \sum_{i=1}^{n} R_i^2 - (\sum_{i=1}^{n} R_i)^2} \tag{3}$$

$$a = \frac{\sum_{i=1}^{n} f_{ci} - b \sum_{i=1}^{n} R_i}{n} \tag{4}$$

The accuracy of the model was evaluated using the root mean square error (*RMSE*) as an indicator:

$$RMSE = \sqrt{\sum_{i=1}^{n} \frac{\left(f_{ci} - f_{c,est\ i}\right)^2}{n}} \tag{5}$$

The conversion model was identified from the eight pairs of strengths and rebound indices, which led to:

$$f_{c,est} = -35.9 + 1.61 \cdot R \tag{6}$$

The calculated value of the fitting error was $RMSE_{fit}$ = 2.8 MPa. The conversion model and the experimental results are plotted in Figure 52.

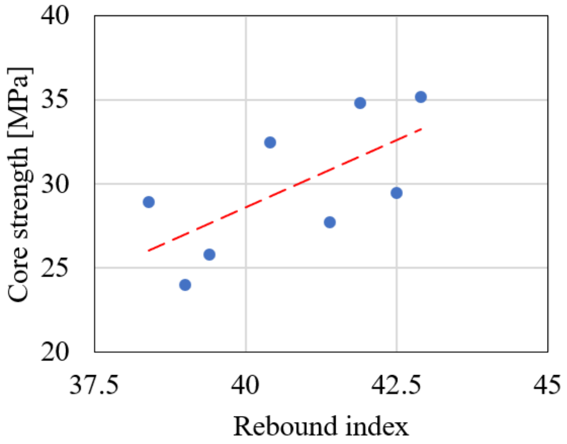

Figure 52: Core data and conversion model identified with the least-square criterion.

Due to the limited number of conditioned cores, it was not possible to validate the model on new data. Therefore, the leave-one-out cross-validation [34] was performed by splitting a single data and obtaining a conservative estimate of the model performance. A total of eight models were identified, each consisting of seven strength and rebound index pairs. The additional pairs removed from the original set, allowed for testing the model on new data. The eight differences between measured and estimated strengths resulted in an average prediction error of $RMSE_{pred}$ = 8.4 MPa, which corresponds to the accuracy for estimating each local strength from the rebound indices. This value was significantly higher than the fitting error. However, it is important to mention that the regression models developed for cross-validation were based on a number of points lower than those proposed to achieve good accuracy. Ali-Benyahia et al. [35] investigated the effect of the number of cores on the model accuracy. The results showed that from 9 cores, *RMSE* stabilizes around 3 MPa. Similarly, Boussahoua et al. [26] found that beyond 9 cores, the prediction errors stabilize around 6.5 MPa. Therefore, due to the limited number of conditioned cores, it is not possible to determine whether increasing the number of cores will reduce the error.

Once the conversion model was identified, the compressive strength was calculated at each location where NDT test results were available. The model was used only within the range of values used for fitting, avoiding any process of extrapolation in accordance with RILEM recommendations. This resulted in mean, standard deviation, and CoV values of 30.6 MPa, 2.2 MPa, and 7.04% respectively. The results obtained are summarised in Table 9.

Table 9: NDT results and compressive strength estimation based on NDT results.

Beam	**Region**	***R***	$f_{c,est}$ ***[MPa]***
B3-P47/46	1	42.9	33.3
	2	42.6	32.8
	3	38.4	26.0
B8-P47/46	1	42.5	32.6
	2	41.4	30.9
	3	42.8	33.1
B4-P47/46	1	39.4	27.6
	3	39.0	27.0
B9-P47/46	1	41.9	31.7

	2	40.5	29.4
	3	40.4	29.3
B7-P47/46	3	40.5	29.4
B6-Ab/P47	2	42.4	32.5
	3	40.4	29.3
B10-Ab/P47	3	42.2	32.2
Bx2-Ab/P47	1	41.7	31.4
	2	42.5	32.6
	3	41.1	30.4

3.4.2 Uniaxial concrete compressive tests

The most reliable determination of in-situ compressive strength is achieved by destructive testing. The destructive method consists of taking core samples from structural members to be used in laboratory tests. The drilling, core preparation, and compressive strength tests were carried out in accordance with the European standards EN 12390-3 [32] and EN 12504-1 [33]. In order to determine the mechanical properties of the concrete in the girders, two independent laboratories, belonging to the Politecnico di Torino and the Politecnico di Milano, carried out tests on concrete samples taken from the specimens after the loading tests. Cores were taken from the structural members, avoiding cracked areas, highly stressed sections, and reinforcements. Furthermore, cores were also drilled both perpendicular and parallel to the longitudinal axis of the members (Fig. 53).

Figure 53: Concrete coring.

After drilling, the extracted cores were marked with the indication of their specimen number and location. In the core ID, the first letter refers to the laboratory ("T" for Politecnico di Torino and "M" for Politecnico di Milano). Cores drilled from the cast-in-place slab were marked with the letter "s". Prior to compression testing, each core was rectified by cutting off the ends. As the preliminary NDT showed that the concrete in different sections was of similar composition and quality, random sampling was carried out over the entire girders. A total of 23 concrete core samples were taken for the I-girders and 6 for the concrete slab. The cores subjected to compression testing were of different diameters and lengths (the ratio of length to diameter varied from 1 to 2). In order to homogenize the dimensional parameters, the strength values obtained were converted to the equivalent in-situ cylindrical strength. In addition, when comparing the strength of concrete cores and properly cast specimens, the effect of the disturbance caused by the mechanical action of sampling should be taken into account. Therefore, the corrected strengths ($f_{c,corr}$) were also obtained by multiplying the core strengths by the disturbance coefficient given in the "Guidelines for the evaluation of the characteristics of concrete in-situ" issued by the Italian Superior Council of Public Works [21]. The results of the uniaxial compression test for cylindrical specimens, including the densities, are shown in Table 10.

Table 10: Compression strength test results.

Beam	**Core ID**	d_m **[mm]**	L **[mm]**	**L/d$_m$**	**Density [kg/m^3]**	f_c **[MPa]**	E **[MPa]**	$f_{c,corr}$ **[MPa]**
B3-P47/46	M3_1	74.0	152.0	2.05	2306.8	30.5	-	32.7
	M3_2	74.0	154.0	2.08	2340.2	24.2	-	26.2
	M3_3	74.0	152.0	2.05	2319.0	29.8	-	31.6
	M3_4	143.0	150.0	1.05	2270.6	23.3	-	25.2
	T3_2	74.3	150.9	2.03	2344.8	28.9	21634.0	30.8
	T3_3	74.3	151.6	2.04	2268.7	34.0	19198.0	35.5
	T3_4	74.3	150.2	2.02	2250.1	35.2	22637.0	36.6
	T3_1(s)	74.3	151.1	2.03	2186.1	27.5	14573.0	29.4
B8-P47/46	M8_1	94.0	103.0	1.10	2333.5	30.9	-	32.6
	M8_2	94.0	94.0	1.00	2325.5	32.7	-	34.3
	M8_3	94.0	95.0	1.01	2311.6	22.4	-	24.3
	M8_4	94.0	94.0	1.00	2386.8	38.0	-	38.6
	M8_5	143.0	150.0	1.05	2302.1	29.6	-	31.4
	M8_6	74.0	150.0	2.03	2346.8	38.1	-	38.7
	T8_1	74.3	151.9	2.04	2317.2	29.5	24291.0	31.3
	T8_2	74.3	150.9	2.03	2328.5	26.4	25062.0	28.4
	T8_3	74.3	150.3	2.02	2313.5	27.7	21062.0	29.6

	T8_4	74.3	152.1	2.05	2281.8	31.6	17920.0	33.3
	T8_1(s)	74.2	134.2	1.81	2222.7	25.1	18166.0	27.1
B4-P47/46	T4_2	74.3	150.5	2.03	2277.6	24.0	25571.0	26.0
	T4_3	74.2	150.5	2.03	2304.4	22.2	24273.0	24.1
	T4_4	74.4	151.7	2.04	2288.4	25.8	23509.0	27.8
	T4_1(s)	74.3	150.6	2.03	2100.2	25.5	14066.0	27.4
B9-P47/46	T9_1	74.3	151.6	2.04	2351.2	34.6	23441.0	36.0
	T9_2	74.3	151.7	2.04	2374.5	32.5	28543.0	34.1
	T9_3	74.4	152.1	2.04	2291.8	34.8	20489.0	36.2
	T9_1(s)	105.5	211.6	2.01	2297.1	25.0	25483.4	27.0
	T9_2(s)	111.9	219.3	1.96	2168.1	24.8	23303.1	26.8
	T9_3(s)	111.7	214.8	1.92	2264.4	24.6	17761.0	26.6

Assuming that the whole group of elements was made of the same quality of concrete, i.e. a single strength class, the average compressive strength of the I-girders was 31.5 MPa with a standard deviation of 4.4 MPa and a CoV of 13.86%. The same values for the cast-in-place slab were 27.4 MPa, 0.9 MPa and 3.42%. The mean compressive strength of cylindrical specimens taken from the I-girders was 15.6% higher than the original design strength and 32.5% lower than the values given in the material certificates, tested at the time of bridge construction. At the same time, the mean compressive strength of core specimens taken from the slab was 22.8% lower than the strength given in the material certificates. In general, the failure mode of the core specimens was typical and met the requirements of the EN 12390-3 standard [32] (Fig. 54).

Figure 54: Typical failure mode of core specimens.

As the information correlated with mechanical properties is representative of local regions and may be subject to significant uncertainty, it should be considered as a characteristic value or with probabilistic models. According to EN 13791 standard [30], the characteristic in-situ compressive strength can be determined as:

$$f_{ck} = min\begin{pmatrix} f_{c,m(n)is} - k_n \cdot s \\ f_{c,is,lowest} + M \end{pmatrix} \tag{7}$$

where $f_{c,m(n)is}$ is the mean in-situ compressive strength, $f_{c,is,lowest}$ is the lowest in-situ compressive strength, k_n is a coefficient which depends on the number of test results (1.75 for test equal to 23), s is the standard deviation, and M is the value of margin (4 for $f_{c,is,lowest} \geq 20$ MPa). Therefore, the critical condition for determining the characteristic in-situ compressive strength is determined by the mean in-situ compressive strength, resulting in a characteristic value of 23.9 MPa, which is 11.3% lower than the compressive strength assumed in the design drawings. The mean value of the elastic modulus for the I-girder was 22894.6 MPa with a standard deviation of 2738.7 MPa and a CoV of 11.96%. The same values for the cast-in-place slab were 18892.1 MPa, 4216.1 MPa and 22.32%. Based on the experimentally obtained concrete compressive strengths and the calculated mean value, the concrete modulus of elasticity was also determined empirically by using the following equations taken from different international codes:

$$E_{cm} = 22000 \left(\frac{f_{cm}}{10}\right)^{0.3} \quad (\mathrm{EN}\ 1992-1-1)[18] \tag{8}$$

$$E_c = 4700 \sqrt{f_{cm}} \quad (\mathrm{ACI}\ 318-14)[36] \tag{9}$$

$$E_c = 0.043 w_c^{1.5} (f'_c)^{0.5} \quad (\mathrm{AASHTO-LRFD})[37] \tag{10}$$

where w_c is the density (2314.6 and 2206.4 kg/m^3 for the I-girder and slab, respectively). The elastic modulus estimated by the above equations resulted higher than 26.3, 13.3, and 14.9% of the experimental value for the I-girder, and higher than 36.5, 23.2, and 19.0% for the slab. However, none of the previous equations takes into account other relevant factors that influence the value of the elastic modulus, such as the aggregate properties. Therefore, the Comité Euro-International du Beton-Fédération Internationale de la Précontrainte (CEB-FIP) Model Code [38], introduced the empirical coefficient α_e to take into account the used aggregate:

$$E_c = 21500 \alpha_E \left(\frac{f_{cm}}{10}\right)^{1/3} \quad (\mathrm{MC2010})[38] \tag{11}$$

where α_e is 0.7 for sandstone aggregates. Substituting the average compressive strengths obtained for the I-girders and the slab, the modulus of elasticity was 22061.8 MPa and 21059.8 MPa respectively. An accurate estimate was obtained for the precast concrete, but an overestimate of 10.3% was obtained for the slab, probably related to the higher variance found in the experimental data.

3.4.3 Tensile splitting strength test

To determine the tensile strength of the concrete, additional 15 cores were drilled and tested using the tensile splitting strength tests according to the EN 12390-6 standard [39]. The test consists of applying a compressive force to two plane plates which transfer the load along the length of the specimen through narrow strips. The resulting orthogonal tensile force causes the specimens to fail in tension (Fig. 55). All the preliminary procedures relating to surface rectification and specimens marking were also carried out.

Figure 55: Tensile splitting strength test.

Table 11 summarizes the main results obtained from the tensile splitting strength tests. Assuming that the whole group of elements was composed by the same quality of concrete, i.e. a single strength class, the average tensile strength of the I-girders was 3.5 MPa with a standard deviation of 0.5 MPa and a CoV of 15%. The same values for the cast-in-place slab were 2.4 MPa, 0.6 MPa and 25%, respectively.

Table 11: Tensile splitting strength test results.

Beam	**Core ID**	d_m **[mm]**	L **[mm]**	**L/d$_m$**	**Density [kg/m^3]**	f_{ct} **[MPa]**
B3-P47/46	M3_1	74.0	150.0	2.0	2294.1	3.7
	M3_2	74.0	149.0	2.0	2356.3	3.6
	M3_3	74.0	150.0	2.0	2303.4	3.0
	M3_4	143.0	169.0	1.2	2306.4	3.2
	M3_1(s)	74.0	155.0	2.1	2277.1	1.8
	M3_2(s)	74.0	78.0	1.1	2244.6	3.0
	T1_1	94.10	152.5	1.6	2270.7	3.4

B8-P47/46	M8_1	94.0	103.0	1.1	2386.7	2.7
	M8_2	143.0	173.0	1.2	2350.2	4.0
	M8_3	94.0	110.0	1.2	2316.0	2.7
	T8_4	74.4	200.4	2.7	2312.8	3.2
B4-P47/46	M4_1	94.0	98.0	1.04	2337.9	3.8
	M4_2	94.0	95.0	1.01	2381.4	3.6
	T4_5	74.3	169.4	2.3	2261.8	4.0
B9-P47/46	T9_4	74.3	159.6	2.1	2290.0	4.6

Based on the concrete compressive strengths obtained experimentally and the corresponding mean value, the concrete tensile strength was also determined empirically by using the following equations:

$$f_{ct} = 0.3\,(f_{cm})^{2/3} \quad (\mathrm{EN\ 1992-1-1})[36] \text{ and } (\mathrm{MC2010})[39] \tag{12}$$

$$f_{ct} = 0.55\,(f_{cm})^{1/2} \quad (\mathrm{ACI\ 318-14})[37] \text{ and } (\mathrm{AASHTO-LRFD})[38] \tag{13}$$

The tensile strength estimated by the above equations resulted lower than 17.0, and 13.4% of the experimental value for the I-girder, and higher than 12.0, and 16.6% for the slab.

3.4.4 Reinforcing steel tensile tests

After the full-scale load tests, samples of strands and rebars were carefully removed from the end of the girders where stresses remained in the elastic range during the tests. A total of ten rebars, 8 mm in diameter and 500 mm long, were collected for tensile testing. In addition, nineteen strands, 12.5 mm in diameter and 1200 mm long were collected to characterize the mechanical properties of the prestressing steel. Complete stress-strain curves were measured under uniaxial tension using a computer-controlled Walter+bai ag (LFSV-600) testing machine. The load, crosshead displacement, and strains were recorded digitally during the test using an interactive computer program, which also programmed and controlled the test procedure in accordance with ISO 6892-1 standard [40]. The gage length of the rebars was 100 mm and that of the strands was 600 mm. Figure 56 shows two typical tensile test results obtained for rebars and strands respectively.

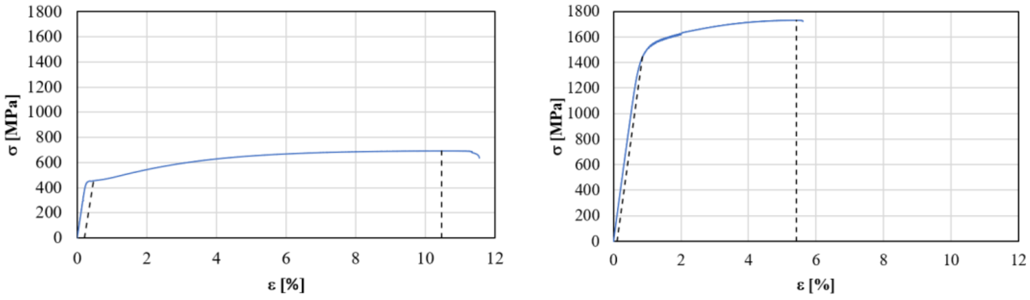

(a) (b)

Figure 56: Typical stress-strain diagrams for: (a) rebar, (b) strand.

The dashed lines show the deviations from proportionality of 0.2% for the rebar and 0.1% for the strand used to determine the yield stress $f_{y,0.2}$ and $f_{p0.1}$ respectively. The vertical dashed lines refer to the elongation at maximum load A_{gt}. As expected, a lower ductility was found for the prestressing steel, with also a less pronounced transition from the elastic to the plastic phase. The mechanical properties of the steel reinforcements are summarized in Table 12, where the strains are referred to the gage lengths detailed above, and the stresses are related to the nominal cross-sections. In the last column a note has been reported if strands presented evident signs due to demolition operations.

Table 12: Uniaxial tensile test results.

Beam	**Sample ID**	D **[mm]**	A_0 **[mm²]**	$f_{y,0.2}$ ($f_{p,0.1}$) **[MPa]**	E **[GPa]**	A_{gt} **[%]**	f_t **[MPa]**	**Dam.**
B3-P47/46	R3_1	8	50.3	487.1	393.3	10.0	728.7	-
	R3_2	8	50.3	469.3	393.3	11.7	715.6	-
	S3_1	12.5	93	1624.8	190.2	3.6	1776.1	No

	S3_2	12.5	93	1574.4	207.2	1.6	1687.5	Yes
B4-P47/46	S4_1	12.5	93	1557.0	194.5	2.4	1769.3	No
	S4_2	12.5	93	1540.9	185.1	4.4	1781.7	No
	S4_3	12.5	93	1532.3	272.1	1.4	1697.9	Yes
	S4_4	12.5	93	1519.4	215.0	2.5	1745.6	No
	S4_5	12.5	93	1528.0	200.0	2.4	1738.5	No
	S4_6	12.5	93	1539.8	202.1	1.1	1645.2	Yes
B9-P47/46	S9_1	12.5	93	1604.3	197.8	3.9	1862.5	No
	S9_2	12.5	93	1447.3	193.6	5.4	1731.6	No
	S9_3	12.5	93	1607.5	202.6	2.4	1828.3	No
	S9_4	12.5	93	1451.6	215.4	3.0	1688.0	No
	S9_5	12.5	93	1492.5	207.1	1.0	1645.2	Yes
	S9_6	12.5	93	1439.8	190.1	3.6	1700.6	No
B7-P47/46	R7_1	8	50.3	469.5	212.1	11.0	734.0	-
	R7_2	8	50.3	447.6	119.3	10.3	642.5	-
	R7_3	8	50.3	411.8	88.2	11.3	636.8	-
	R7_4	8	50.3	413.8	117.1	11.4	635.0	-
	R7_5	8	50.3	465.5	212.5	10.9	737.5	-
	R7_6	8	50.3	447.6	149.2	10.9	690.4	-

R7_7	8	50.3	423.8	148.3	11.1	639.3	-
R7_8	8	50.3	453.6	185.1	11.2	691.6	-
S7_1	12.5	93	1594.6	206.6	4.4	1839.2	No
S7_2	12.5	93	1554.8	205.1	5.4	1864.6	No
S7_3	12.5	93	1546.2	203.6	2.3	1811.7	No
S7_4	12.5	93	1550.5	211.0	3.4	1830.2	No
S7_5	12.5	93	1569.9	206.5	4.3	1836.1	No

Samples that appeared to have been affected by evident signs of the demolition process were discarded to ensure that the results were as representative as possible of the actual mechanical properties. Therefore, the mean, standard deviation, and CoV of the yield strength $f_{y,0.2}$ of steel rebar were 449.0 MPa, 24.2 MPa, and 5.4%, respectively. The same values for the ultimate strength f_t resulted in 685.1 MPa, 41.0 MPa, and 6.0%. For the elastic modulus, it was obtained an average value of 201.8 GPa with a standard deviation of 103.1 GPa and consequent CoV of 51.1%. The elastic modulus measurements showed a high variability compared to the other mechanical properties. A possible reason could be related to the potential deformation induced during the demolition process. This factor, combined with varying degrees of corrosion, could have affected the elastic phase of the samples in different ways. Based on the strand specimens, the mean, standard deviation, and CoV of the yield strength $f_{p,0.1}$ were 1542.4 MPa, 56.2 MPa, and 3.6% respectively. The same values for the tensile strength f_t were 1786.9 MPa, 44.3 MPa, and 3.1% respectively. The mean value of the elastic modulus E was 201.1 GPa with a standard deviation of 8.9 GPa and a CoV of 4.42%. The elongation at rupture showed a mean value of 3.6% with a standard deviation of 1.0% and a CoV of 29.0%. The results indicated that the mechanical properties of the strands were similar for all specimens except for the elongation at rupture which showed a higher variability. Due to the good conditions of the prestressing reinforcement, an explanation could be related to the possible influence induced by the demolition operations.

References

[1] Ahmad, S. (2003). Reinforcement corrosion in concrete structures, its monitoring and service life prediction-a review. *Cement & Concrete Composites*, 25, 459-471.

[2] Won Song, H., Saraswathy, V. (2007). Corrosion Monitoring of Reinforced Concrete Structures - A Review. *International Journal of Electrochemical Science*, 2, 1-28.

[3] Elsener, B., Andrade, C., Gulikers, J., Polder, R., Raupach, M. (2003). Recommendations on half-cell potential measurements-potential mapping on reinforced concrete structures. *Materials and Structures*, 36(7), 461-471.

[4] ASTM C876-91. (1991). Starndard test method for half-cell potentials of uncoated reinforcing steel in concrete, *Annual Book of ASTM Standards*.

[5] Elsener, B. (2001). Half-cell potential mapping to assess repair work on RC structures. *Construction and Building Materials*, 15(2-3), 133-139.

[6] Bertolini, L., Elsener, B., Pedeferri, P., Redaelli, E., Polder, R. (2013). Corrosion of Steel in Concrete: Prevention, Diagnosis, Repair (2nd ed.). Weinheim, Germany: Wiley VCH.

[7] Sagües, A. (1993). Corrosion measurement techniques for steel in concrete. *Corrosion 91*. Paper No. 353.

[8] Ahlström, J. Corrosion of steel in concrete at various moisture and chloride levels. Rapport 2015:133.

[9] Polder, R., Andrade, C., Elsener, B., Vennesland, Ø., Gulikers, J., Weidert, R., Raupach, M. (2000). RILEM 154-EMC: Electrochemical techniques for measuring metallic corrosion. *Materials and Structures*, 33, 603–611.

[10] Millard, S.G. (1991). Reinforced concrete resistivity measurement techniques. *Proceedings of the Institution of Civil Engineers*, 91, 71-88.

[11] Wenner, F. (1916). A method of measuring earh resistivity. *Bulletin of US Bureau of Standards*, 12, 469-478.

[12] Broomfield, J.P. (2007). Corrosion of Steel in Concrete: Understanding, investigation and repair (2nd ed.). New York.

[13] Andrade, C., González, J.A. (1978). Quantitative measurements of corrosion rate of reinforcing steels embedded in concrete using polarization resistance measurements. *Materials and Corrosion*, 29, 515-519.

[14] Stern, M., Geary, A.L. (1957). Electrochemical polarization I. A theoretical analysis of the shape of polarization curves. *Journal of the Electrochemical Society*, 104(56).

[15] Ghods, P., Alizadeh, A., Salehi, M. (2017). U. S. Patent No. 20170227481A1.

[16] Fahim, A., Ghods, P., Alizadeh, R., Salehi, M., Decarufel, S. (2019). CEPRA: A new test method for rebar corrosion rate measurement. *ASTM Selected Technical Papers*, 1609, 59-80.

[17] Andrade, C., Alonso, C., Gulikers, J., Polder, R., Cigna, R., Vennesland, Ø., Salta, M., Raharinaivo, A., Elsenser, B. (2004). Test methods for on-site corrosion rate measurement of steel reinforcement in concrete by means of the polarization resistance method. *Materials and Structures*, 37, 623-643.

[18] European Committee for Standardization (2005) Eurocode 2: Design of Concrete Structures - Part. 1-1: General Rules and Rules for Buildings (EN 1992-1-1:2004). Brussels, Belgium.

[19] Alampalli, S., Frangopol, D.M., Grimson, J., Halling, M.W., Kosnik, D.E., Lantsoght, E.O.L., Yang, D., Zhou, E. (2021). Bridge Load Testing: State-of-the-Practice. *Journal of Bridge Engineering*, 26(3).

[20] Savino, P., Tondolo, F., Sabia, D., Quattrone, A., Biondini, F., Rosati, G., Anghileri, M., Chiaia, B. (2023). Large-Scale Experimental Static Testing on 50-Year-Old Prestressed Concrete Bridge Girders. *Applied Sciences*, 13(834).

[21] Consiglio Superiore dei Lavori Pubblici, Servizio Tecnico Centrale. (2017). Linee guida per la valutazione delle caratteristiche del calcestruzzo in opera.

[22] EN 12504-2, Testing concrete in structures - Part 2: Non-destructive testing – Determination of rebound number, September 2021.

[23] Breysse, D., Fernàndez, J.L.M. (2014). Assessing concrete strength with rebound hammer: review of key issues and ideas for more reliable conclusions. *Materials and Structures*, 47, 1589-1604.

[24] Alwash, M., Breysse, D., Sbartaï, Z.M. (2017). Using Monte-Carlo simulations to evaluate the efficiency of different strategies for nondestructive assessment of concrete strength. *Materials and Structures*, 50:90.

[25] Ali-Benyahia, K., Kenai, S., Ghrici, M., Sbartaï, Elachachi, S.M. (2023). Analysis of the accuracy of in-situ concrete characteristic compressive strength assessment in real structures using destructive and non-destructive testing methods. *Construction and Building Materials*, 366(2023).

[26] Boussahoua, Y., Kenai, S., Sbartai, Z.M., Breysse, D., Ali-Benyahia, K. (2023). Influence of the number of cores on concrete strength assessment by nondestructive tests in old existing structures. *Asian Journal of Civil Engineering*.

[27] Youcef, B., Said, K., Khoudja, A.B. (2018). Prediction of concrete strength by non-destructive testing in old structures: Effect of core number on the reliability of prediction. *2nd International Congress on Materials & Structural Stability (CMSS-2017)*, 149.

[28] Breysse, D., Balayssac, J.P., Biondi, S., Borosnyói, A., Candigliota, E., Chiauzzi, L., Garnier, V., Grantham, M., Gunes, O., Luprano, V., et al. (2017). Non destructive assessment of in situ concrete strength:

comparison of approaches through an international benchmark. *Materials and Structures*, 50: 133.

[29] EN 13791 (2007). Assessment of in-situ compressive strength in structures and precast concrete components, CEN, Brussels.

[30] EN 13791 (2019). Assessment of in-situ compressive strength in structures and precast concrete components, CEN.

[31] Breysse, D., Balayssac, J.P., Biondi, S., Corbett, D., Goncalves, A., Grantham, M., Luprano, V.A.M., Masi, A., et al. (2019). Recommendation of RILEM TC249-ISC on non destructive in situ strength assessment of concrete. *Materials and Structures*, 52:71.

[32] EN 12390-3, Testing hardened concrete - Part 3: Compressive strength of test specimens, August 2003.

[33] EN 12504-1, Testing concrete in structures – Part 1: Cored specimens – Taking, examining and testing in compression, February 2021.

[34] Lachenbruch, P.A, Mickey, M.R. (1968). Estimation of error rates in discriminant analysis. *Technometrics*, 10, 101-111.

[35] Ali-Benyahia, K., Sbartaï, A., Breysse, D., Kenai, S., Mohamed, G. (2017). Analysis of the single and combined non-destructive test approaches for on-site concrete strength assessment: General statements based on a real case-study. *Case Studies in Construction Materials*, 6, 109-119.

[36] ACI Committee 318. 2014. Building Code Requirements for Structural Concrete (ACI 318-14) and Commentary (ACI 318R-14). *American Concrete Institute*, Farmington Hills.

[37] AASHTO LRFD BRIDGE. 2012. Design specification. American Association of State Highway and Transportation Officials, Washington, DC.

[38] Walraven, J.C., van der Horst, A.Q.C. (2013). FIB model code for concrete structures 2010. Internation Federation for Structural Concrete (fib), Lausanne.

[39] EN 12390-6, Testing hardened concrete – Part 6: Tensile splitting strength of test specimens, December 2009.

[40] ISO 6892-1, Metallic materials – Tensile testing – Part 1: Method of test at room temperature, November 2019.

Chapter 4

Assessment of prestress loss in 50-year-old PC bridge girders

4.1 Introduction

Prestressing is a widely employed technique in the construction industry aimed at enhancing the behavioral characteristics and performance of reinforced concrete structures, mitigating the risk of potential cracking and augmenting their overall strength, durability, and efficiency under live loads. Nevertheless, the effectiveness of the applied prestress decreases over time due to various time-dependent phenomena. The estimation of prestress losses is of paramount importance in the design process as it aids to ensure that the stresses occurring in the girder under service loads will not exceed the prescribed limits of concrete tensile stress and prevent the occurrence of excessive deflections. Conversely, overestimation of prestress losses can lead to inadequate camber, causing cracks in the top fiber and resulting in an uneconomical design. Accurate prediction of prestress losses requires accurate prediction of the long-term properties of the concrete and prestressing strands, which is a very complex process due to the interdependent factors involved such as concrete creep and shrinkage, relaxation in prestressing steel, degradation processes, and environmental parameters. Relaxation is affected by the shortening of the prestressing reinforcement due to concrete creep and shrinkage. The phenomenon of concrete creep, in turn, is constantly altered due to stress variations associated with the prestressing reinforcement. Furthermore, concrete creep and shrinkage are partially restrained by the prestressing. Therefore, errors in predicting long-term losses may be due to the inaccuracy of long-term material models, inaccuracy of material properties, and simplification of the analysis method. For bridge in-service, knowledge of the residual prestress is critical to assess durability, quantify remaining service life, and implement retrofitting measures. The potential cracking induced by prestress loss not only reduces section stiffness and increases bridge deflection, but also accelerates the concrete deterioration and corrosion of the prestressing reinforcement. These result in a reduction of both serviceability and ultimate capacity. To assess the safety of existing PC structures, it is necessary to determine the level of the prestressing present in their structural components. Assessing the stress state of in-service PC structures is a rather difficult task and engineers are often faced with a lack of actual design information and environmental conditions.

Several analytical models for prestress loss prediction have been proposed in design codes and technical documents from around the world. These can be classified into three classes according to their level of refinement: the one-step method, the refined calculation method, and the incremental time-step method. In the one-step calculation method, all factors considered in relation to the prestress losses, including concrete creep, concrete shrinkage, and relaxation of prestressing reinforcement, are included in a prediction expression, such as the equation described in the EC2 [1]. In the refined calculation method, the prestress losses due to concrete creep, concrete shrinkage, and prestressing steel relaxation are calculated separately and then summed to determine the total losses. This method is used for the estimation of time-dependent losses, such as in AASHTO-LRFD [2] and ACI 318 [3]. For the time-step methods, to account for the continuous interactions between long-term effects with time, the loading time of the structure is divided into a set of discrete time intervals and the prestress level is estimated at each time interval.

A series of experimental studies have been carried out to measure prestress losses in PC girders and compare them with design code estimates. The studies include several laboratory tests on old girders removed from existing bridges, and experimental research involving the fabrication, testing, and field monitoring of PC specimens. Shenoy and Frantz [4] tested two 27-year-old PC box beams. The measured prestress losses were half those predicted by the current PCI method using actual material properties. Similarly, Azizinamini et al. [5] evaluated the prestress loss on a 25-year-old PC I-girder. Comparison with the current PCI and AASHTO (1989) specifications showed that the maximum overestimation of the predicted values was 27.6%. Halsey & Miller [6] found a good agreement between prestress loss measured on two 40-year-old PC beams and AASHTO (1989) Code estimates. Pessiki et al. [7] conducted an experimental study to determine effective prestress force in two PC beams that were removed from a bridge after 28 years in-service. Measured prestress loss resulted in approximately 60% of the loss predicted according to AASHTO (1992) specifications. In Labia et al. [8], two 20-year-old PC box girders were removed from an existing bridge and tested. Losses were calculated using methods in the ACI, AASHTO (1992), and PCI specifications. However, all the predicted losses were lower than the measured loss, with a maximum difference of 43.6%. A possible cause was attributed to the underestimation of creep and shrinkage loss in analytical models. The National Cooperative Highway Research Program (NCHRP) [9] measured prestress losses in seven instrumented girders collected from four different states in the USA. The measured prestress losses were compared with prestress losses estimated using refined AASHTO LRFD-98 and PCI specifications. All prediction methods were applied using the specified concrete strength and corresponding estimated material properties. The measured long-term prestress losses were modified to reflect the losses at time infinity rather than those obtained at 385 to 490 days. Both methods provided conservative estimates of the prestress loss, with an average overestimate of 3.2% for the PCI method and 34.5% for the AASHTO specifications. Kukay et al. [10] monitored the behavior of four PC girders for almost one year since the time of casting. The measured prestress losses were compared with those calculated using the AASHTO LRFD-04 specifications and the method proposed by NCHRP [9]. Overall trends indicated that the predicted losses with actual compressive strengths were 10% un-conservative than the field values. Kukay et al. [11] presented research results on the testing of eight PC girders that had been in service for 40 years. On average, the AASHTO LRFD-04 and 07 detailed methods overestimated the measured prestress force by 12%. Osborn et al. [12] evaluated the prestress loss in five PC bridge girders that had been in service for 42 years. The measured effective prestress was compared with calculated values according to the AASHTO LRFD-09 specifications. The AASHTO refined method provided the most accurate results, being 10% higher than the average measured prestress force. Caro et al. [13] analyzed the changes in prestress losses for PC prismatic specimens over a period of one year from casting. Experimental prestress losses due to elastic shortening, creep, and shrinkage were compared with theoretical values derived from different code methods. The prestress loss due to elastic shortening did not show significant variation across the different methods. The most accurate prediction for the total prestress loss aligned with AASHTO LRFD-12, although it overestimated the creep loss and underestimated the elastic shortening. The Model Code 2010 and EC2 methods effectively predicted prestress losses due to concrete creep but underestimated the predicted loss resulting from concrete shrinkage. Garber et al. [14] investigated the influence of different concrete materials and construction techniques on prestress loss. To this end, 30 full-scale PC girders were constructed and instrumented with a monitoring system embedded in the specimens. To investigate the accuracy of the prestress loss estimation methods, the measured short and long-term prestress losses for each specimen were compared with those determined using the methods suggested by ACI Committee 423. Both the refined and incremental time step AASHTO LRFD-12 methods provided the most accurate prestress loss with overestimates of 32.9% and 22.5% respectively. Garber et al. [15] built an experimental database of 27 research studies (published between 1970 and 2013) to investigate different short- and long-term loss estimation methods. The use of the approximate and time-step methods according to AASHTO LRFD-12 gave the most accurate results, with conservative estimates on average 13.0% and 11.5% higher than the measured prestress loss. Guo et al. [16] investigated the long-term prestress losses in post-tensioned concrete beams by casting eight post-tensioned concrete beams and monitoring them for more than one year. The measured time-varying prestress losses were compared with the predicted values using different prediction models, finding the greater prediction accuracy for the NCHRP method. Ye et al. [17] presented a monitoring campaign aimed at determining the early-age prestress loss of four PC beams of a newly constructed railway bridge. Prestress loss predictions were calculated using European and American standards and then compared with measured values. It was found that code predictions of prestress loss using measured material properties gave reasonable agreement with the field measurement, with a slight underestimation for early-age prestress losses and almost negligible two to three years after beam casting. The time-step methods provided a better prediction of prestress loss evolution over time compared to the simplified method.

As observed, the predictions based on the design codes, although quite satisfactory, have generally exceeded the measured prestress loss. To obtain the best results from analytical methods, it is necessary to know the environmental and loading conditions to which the girder has been subjected over time, as well as the time-dependent phenomena. Nevertheless, the generation of scientifically and systematically collected data on the current level of prestressing in existing bridges represents the most reliable method for reducing the level of uncertainty in the determination of long-term performance. Thus, reliable and non-destructive diagnostic techniques are required to determine the residual value of the prestressing force for in-service structures. Currently, many possible methods have been proposed by researchers over the years for the in-situ assessment of the effective prestress force. These methods can be classified according to their impact on the investigated construction as either destructive or non-destructive. As destructive approaches inevitably cause damage which affect the structural integrity, they are not suitable for application to in-service bridges, but can only be useful for experimental activities. Of these methods, cracking test, decompression load, and strand-cutting methods are techniques that have been more traditionally used to directly determine the residual prestress force. In the present work, non-destructive methods are considered techniques that produce negligible impact on the structure and can be properly repaired. Non-destructive testing has always been an important issue and a promising field to get the in-service residual prestress force, and research is currently ongoing. Azizinamini et al. [5] developed a non-destructive method consisting of studying the stress state around a pre-cracked drilled hole and determining the side pressure required to close the crack. However, the relationship between the applied pressure and the unknown stress in the lower flange of the beam is based on a factor determined by numerical simulation and is strictly dependent on the case study. Civjan et al. [18] proposed a prototype instrument for estimating stress levels in exposed prestressed strands by applying a lateral force and measuring the resulting displacement. Owens [19] proposed the concrete stress relief core method for determining residual prestress by tacking out a concrete core and measuring the elastic stress relief using electrical strain gauges installed near the hole boundary. Kesavan et al. [20] improved the stress-relief core method by fixing waterproof strain gages in the center of the intended core, aligned in the direction of maximum stress. A cumbersome procedure was required for connecting and disconnecting the strain gages, as the lead wires could not be kept connected to the instrument during core drilling. Zhong et al. [21] proposed a method to monitor the stress release process using ultrasonic waves. It is based on the estimation of the acoustoelastic coefficient, which expresses the relationship between ultrasonic wave velocities and stress levels in materials. However, all the above methods have the drawback of requiring calibration data covering the specific conditions and technology. Another experimental method widely studied in the literature is the determination of prestress losses taking into account the natural frequencies of the structures. Nevertheless, the influence of prestressing on the dynamics of PC girders is still under discussion. In this context, significant experimental studies have been carried out to investigate the influence of the prestressing force value on the natural frequency of the prestressed member, without any definitive evidence to emphasize this behavior. Whilst some references in the literature state that the prestressing force has no effect on the vibration frequencies, other experimental tests show an increase in the natural frequencies as the value of the prestressing increases. The application of higher level of prestressing resulted in a decrease in the frequency of vibration. [22-25]. In addition, the relevance of the dynamic properties changes also depends on many other aspects that sometimes produce counterbalancing effects, making it difficult to identify a clear relationship between the dynamic properties and the level of prestressing. As a result, the use of natural frequencies as an appropriate parameter for determining prestress loss is uncertain. Additional techniques have also been used to determine the prestress loss over time by instrumenting the internal tendons of PC girders using load cells, elasto-magnetic (EM) sensors or strain sensors. Caro et al. [13] carried out an experimental study to evaluate the prestress loss in prestressed concrete prismatic specimens over a period of one year after casting. The force supported by the prestressing reinforcement was measured directly using a hollow force transducer. EM sensing is a non-contact measurement method based on the principle of the inherent magnetic-elastic effect in the ferromagnetic material. The calibration of the results is carried out in the laboratory between tensile force and magnetic permeability. Chen and Zhang [26] investigated the application of EM sensing in bonded tendons to determine the possible influence of plastic duct and cement grout on the measurement results. Since these are non-metallic materials, they have no influence on the measurement results of the EM sensor. In practice, of the abovementioned techniques, strain-based methods by embedding vibrating wire strain gauges (VWG) in concrete have been used extensively in field applications as a reference [11, 14, 27-28]. However, as they provide local measurements, recent studies have replaced VWGs with fiber-optic sensors. Webb et al. [29] used fiber-optic cables to study creep and shrinkage in 30 m long prestressed bridge girders. However, the cables were found to be highly susceptible to breakage during casting, transport and installation of the beams. After the beams were cast, it was found that half of the total number of fiber-optic cables originally installed remained intact; after transport and erection on site, this figure had fallen to just under a third, and 314 days after installation, only 14% of the cables provided readings. On the other hand, Jaber and Glisic [30] used long-gauge fiber optic sensor to monitor prestress loss in a post-tensioned pedestrian bridge. Reliable results were collected over a three-year period starting after post-tensioning. Ye et al. [17] used fiber optic arrays to monitor early-age concrete behavior for a newly constructed railway bridge. Close agreement was found between design code predictions and field measurements within three years after beam casting. Furthermore, in order to ensure the full composite action between the reinforcement and the fiber optic sensor as well as the proper functioning of the sensor, Kim et al. [31] developed a new strand by replacing the steel core of the normal PC strand with a carbon-fiber-reinforced polymer containing an optical fiber sensor embedded in the inner center. The developed smart strand was then used to measure the variation of prestressing force distribution during tensioning and anchoring of actual post-tensioned girder bridges [32]. However, it is important to note that strain-based methods are unable to detect prestress loss due to strand relaxation, as this phenomenon results in a loss of stress without a corresponding change in strain. In addition, because the methods used to monitor prestress loss over time require the sensors to be embedded at the time of casting, their applicability is limited to new structures.

Consequently, an optimal technique for in-situ quantification of residual prestressing forces, for the purpose of practical engineering implementation, should be based on mechanical models. Since the implementation of these techniques does not require calibration data covering the specific conditions, they can be directly applied to different configurations without prior laboratory calibration. To this end, Bonopera and Chang [33] proposed an analytical model for determining the residual prestressing force in simply supported PC girders. The model is based on the compression-softening theory and consists in defining the magnification factor between the analytical and measured vertical deflection due to an applied vertical load. However, it is not directly applicable to the on-site evaluation of residual prestressing due to the need to perform a load test. A promising technique has been proposed by Kukay et al. [34], called the “saw-cut method”. This approach is based on observing the change in strain in the area where the stress is relieved by sawing. The applied saw-cuts across the entire bottom flange and isolates a block on the tensile face of the prestressed beam. The reduction in stress in the block should then be related to the effective prestress remaining in the beam. Several tests were carried out to achieve near-zero strain by varying the depth, width and length of two parallel cuts, and it was found that the most important parameter was the depth of cuts. A comparison between non-destructive and destructive tests showed that the non-destructive test was more conservative than their destructive counterparts. On average, the residual prestress force obtained from the non-destructive test was 94% of that obtained from the destructive tests. More recently, Bagge et al. [35] and Kralovanec et al. [36] analyzed the prestress loss in a 55-year-old and 62-year-old post-tensioned bridges, respectively. In both studies, the saw-cut method was supported by numerical simulation. Since full isolation of the concrete block was not possible due to the small concrete cover, the stress relief was calculated by comparing the results of the saw-cut test and the stress relief of the numerical simulation.

Overall, the thorough literature review identified two significant research gaps in the field of prestress losses in aging PC bridges. These gaps pertain to the need for practical techniques to acquire valuable prestress loss data and the lack of systematic field studies focused on the measurement of prestress loss in aging PC bridges. As a result, the current state of knowledge concerning the progression of prestress loss in existing bridges after a significant period of service is limited. Therefore, the 50-year-old girders that were the subject of this thesis, provided an excellent opportunity to evaluate the long-term loss of prestress after 50 years of service life. To achieve this objective, this part of the research aims to optimize the saw-cut method and extend its applicability to in-service structures. The results of the non-destructive tests have been compared with those obtained from well-established destructive methods. In addition, the reliability of numerical models provided by current codes in estimating the residual prestressing of structural members after 50 years of service has been evaluated. Moreover, this study proposes an enhanced formulation of the one-step EC2 method, specifically tailored to account for the staged construction of composite PC girders and cast-in-place slabs. The experimental findings of this research are expected to provide valuable insights for highway authorities responsible for managing infrastructure networks. The knowledge gained from this study will contribute to a deeper understanding of prestress loss in aging bridges, thus enabling better-informed decision regarding the maintenance and performance enhancement of such critical infrastructure elements.

4.2 Experimental program for prestress loss assessment

The calculation of service loading, shear capacity and cracking loads in PC beams are all affected by the assumed loss of prestressing force. Therefore, an accurate evaluation of the long-term prestressing loss is essential for the overall structural health and performance of PC girders. To this end, a suitable experimental program was designed to determine the effective prestressing force after 50 years of service through both destructive and non-destructive testing. The experimental program included a systematic evaluation of prestress losses, carried out in three distinct phases. In the first phase, the cracking load and the decompression load were determined during the full-scale load tests. The second phase of the assessment consisted in the application of the saw-cut method. Finally, in the third phase, the strand-cutting method was applied to the same location as in the second phase of assessment. A description of each of these methods and a comparison of their results is given below. The experimental program is expected to extend the current knowledge of the non-destructive saw-cut method and its wider application to the quantification of the residual prestress of in-service bridge structures.

4.2.1 Residual prestress from cracking load test

The cracking test was carried out on the prestressed girders to determine the available compressive stress in the bottom flange and hence the effective prestressing force in the strands. This is a destructive test in which the girder is subjected to a load sufficient to induce a flexural crack. At the moment of crack initiation, the stress in the bottom fiber was equal to the concrete tensile strength. Since the beam weight and the applied loads were known, the prestressing force at this time could be calculated by imposing equilibrium at the bottom fiber:

$$\sigma_{cp} + \sigma_{cg} + \sigma_{cq} = f_{ctm} \tag{14}$$

where σ_{cp} is the stress due to the prestressing force, σ_{cg} is the stress due to dead load, and σ_{cq} is the stress due to the applied load that caused the flexural crack. The equation may be rewritten as follows:

$$\frac{N_p}{A_g} + \frac{N_p \cdot e}{I_g} y_g + \frac{M_{sw}}{I_g} y_g + \frac{M_q}{I_c} y_c = f_{ctm} \tag{15}$$

where N_p is the effective prestressing force in the girder, M_{sw} is the bending moment due to the dead load, M_q is the bending moment due to the applied load, A_g is the cross-sectional area, I_g is the moment of inertia of the girder, e is the eccentricity of the prestressing force, y_g is the neutral axis position of the girder, y_c is the neutral axis position of the composite section, I_c is the moment of inertia of the composite section, and f_{ctm} is the tensile strength of the concrete. In computing the effective prestress, it was assumed that the entire dead load was carried by the I-shaped girders. The applied load was carried by the entire composite section. It was assumed that all strands were subjected to the same effective prestressing force, so this calculation gave an average loss in each strand. The calculated strand stresses were modified by eliminating the bending contribution attributed to the dead load. Several methods have been used in the literature to detect the first crack opening, such as visual observation, strain gauges and LVDTs. However, in order to standardize the assessment among the girders, the tensile strains recorded by the LVDTs installed in the bottom flange during the load tests were used. To avoid the influence of near cracks opening, the recordings from the LVDTs that detected the crack initiation for the first time were used. Table 13 shows all the parameters involved in Eq. 15. The modulus of elasticity of the concrete in the precast girders B3-P47/46, B8-P47/46, B4-P47/46, and B9-P47/46, refers to the average value estimated from the compressive tests. For the other girders, the average compressive strength was estimated from the non-destructive tests (Table 9) and then the modulus of elasticity was calculated from Eq. 11. As B6-P48/49 had rebound indices outside the range of Eq. 6 and concrete strength could not be derived, the modulus of elasticity was assumed to be the average of all the compressive test results. The modulus of elasticity of the cast-in-place slab and the steel reinforcement were assumed to be the average of the destructive test results. Girder B5-P47/46 was excluded from this test as it was used to simulate controlled damage prior to the loading test and was then extensively damaged at midspan.

Table 13: Mechanical and geometric properties.

Beam ID	E_{cm} [MPa]	A_g [cm^2]	I_g [mm^4]	y_g [mm]	I_c [mm^4]	y_c [mm]
B3-P47/46	21156.3	2438.5	2.326E+10	383.3	4.316E+10	521.4
B8-P47/46	22083.8	2427.4	2.312E+10	383.8	4.231E+10	517.9
B4-P47/46	24451.0	2403.0	2.281E+10	385.2	4.042E+10	509.6
B9-P47/46	24157.7	2405.8	2.285E+10	385.0	-	-
B7-P47/46	21560.2	2433.5	2.320E+10	383.5	4.278E+10	519.9

B6-Ab/P47	21920.8	2429.3	2.314E+10	383.7	4.246E+10	518.5
B6-P48/49	22962.2	2417.8	2.300E+10	384.4	4.157E+10	514.7
B10-Ab/P47	22224.0	2425.8	2.310E+10	383.9	4.219E+10	517.3
Bx2-Ab/P47	22054.0	4623.8	5.971E+10	388.5	9.529E+10	546.6

Since the effective prestressing force in Eq. 15 is directly influenced by the concrete tensile strength, and the results of the tensile splitting tests were subject to significant uncertainty, these were considered by taking into account the mean and standard deviation of 3.5 and 0.5 MPa, respectively. Therefore, the experimental results of the cracking load method have been summarized in Table 14, where $\sigma_{p,\mu-\sigma}$, $\sigma_{p,\mu}$, and $\sigma_{p,\mu+\sigma}$ represent the effective prestressing stress computed for a tensile strength of 3.0, 3.5, and 4.0 MPa, respectively.

Table 14: Input bending moments and effective prestressing stress estimated by cracking load method.

Beam ID	**M_{sw} [kNm]**	**M_q [kNm]**	**$\sigma_{p,\mu-\sigma}$ [MPa]**	**$\sigma_{p,\mu}$ [MPa]**	**$\sigma_{p,\mu+\sigma}$ [MPa]**
B3-P47/46	300.2	573.0	599.5	563.1	526.6
B8-P47/46	304.5	537.2	578.6	542.4	506.2
B4-P47/46	302.9	487.6	546.3	510.7	475.1
B9-P47/46	223.2	518.8	646.7	611.0	575.4
B7-P47/46	304.9	348.7	520.2	483.9	447.5
B6-Ab/P47	301.7	485.2	682.1	645.9	609.7
B6-P48/49	301.7	377.3	556.1	520.1	484.2

B10-Ab/P47	301.7	433.2	620.7	584.6	548.4
Bx2-Ab/P47	591.6	870.0	424.3	385.0	345.7

The findings presented in Table 14 reveal crucial insights regarding the prestress of the girders, particularly when considering the mean value of concrete tensile strength. The prestress at the bottom of the girders was observed to have a mean value of 557.7 MPa, with a standard deviation of 72.4 MPa, and a CoV of 13.0%. Notably, the box girder exhibited a lower prestressing level compared to the I-shaped girders. One remarkable observation from Table 14 is that a variation in tensile strength of about 14.3%, equivalent to 0.5 MPa deviation from the mean value, resulted in an average variation of approximately 6.0% in effective prestress. This observation highlights the relatively moderate sensitivity of prestress to changes in tensile strength.

Since cracks in small areas of the girder length can be induced by localized higher stresses and/or lower concrete tensile strengths, they may not be representative of the average response of the specimen. Therefore, the first flexural cracking was also detected from the load-deflection response. The evaluation based on the load-deflection measurements was indicative of the global response of the specimen and was not influenced by the local variation in specimen condition. According to the procedure proposed in [37], the load-deflection data were discretized into displacement steps. The discretization allowed to calculate the stiffness for each displacement step. By plotting the flexural stiffness versus displacements, it can be seen that the flexural stiffness varied within a well-defined band, indicating the uncracked flexural response. When the concrete cracked, the flexural stiffness decreased and the point just before the deviation was considered to be the end of the linear behavior. The deflection corresponding to the first flexural cracking was used to determine the flexural cracking load from the load-deflection response. An example of the procedure is shown in Figure 57 for girder B3-P47/46.

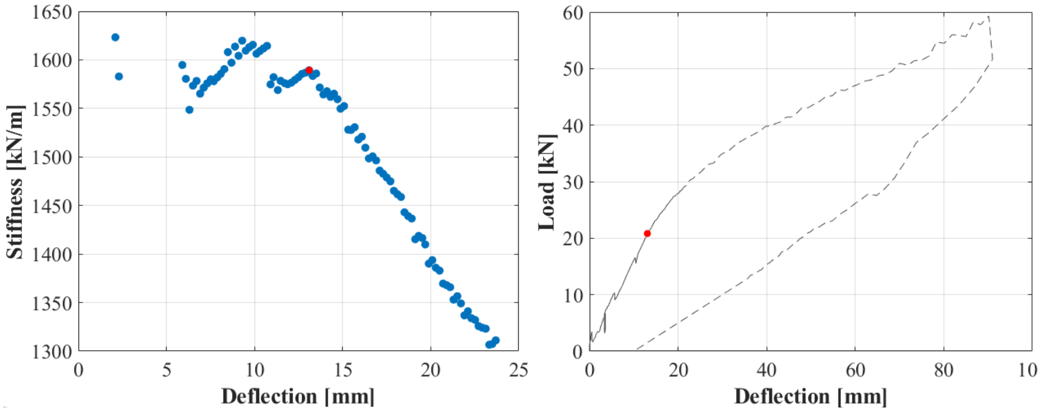

(a) (b)

Figure 57: Load-deflection analysis: (a) identification of stiffness drop, (f) determination of the cracking load.

In this procedure, the bending moment due to the applied load and the dead load have been related to midspan. Table 15 summarizes the values of bending moments adopted in Eq. 15 and the effective prestressing stress obtained for the modified version of the cracking load method.

Table 15: Input bending moments and effective prestressing stress estimated using the modified version of the cracking load method.

Beam ID	**M_{sw} [kNm]**	**M_q [kNm]**	**$\sigma_{p,\mu-\sigma}$ [MPa]**	**$\sigma_{p,\mu}$ [MPa]**	**$\sigma_{p,\mu+\sigma}$ [MPa]**
B3-P47/46	305.0	600.6	628.8	592.3	555.9
B8-P47/46	305.0	542.7	583.9	547.7	511.6
B4-P47/46	305.0	543.0	598.3	562.7	527.1
B9-P47/46	225.7	549.1	685.7	650.1	614.4
B7-P47/46	305.0	382.1	560.4	524.1	487.8
B6-Ab/P47	305.0	569.7	787.1	750.9	714.7

B6-P48/49	305.0	458.1	656.8	620.8	584.9
B10-Ab/P47	305.0	470.6	669.1	633.0	596.8
Bx2-Ab/P47	593.3	866.2	423.4	384.1	344.7

The observed increase in cracking load determined an increase in the estimated effective prestress, giving a mean of 610.2 MPa, a standard deviation of 95.1 MPa, and a CoV of 15.6%. This method was preferable due to the reduced subjectivity in determining the cracking load and the greater consistency between the mechanical properties, considered as average values for the whole specimen, and the cracking load estimated from the load-deflection curves. However, the problem with using the cracking load method to estimate prestress losses is that it is highly dependent on the value of the concrete tensile strength. Therefore, the decompression load method was also used in the experimental campaign as a more accurate method of measuring prestress loss.

4.2.2 Residual prestress from decompression load test

After cracks initiation during the first loading phase, the beams were unloaded until the crack closed due to the prestressing contribution. Girder B4-P47/46 was excluded from the decompression load test as it was subjected to monotonic loading. During the reloading phase, the reopening of the crack at the bottom surface was carefully monitored to determine the decompression load from the load-strain curves. From a theoretical perspective, crack reopening occurs when the compressive stress in the lower fibre of the beam is overcome by the effect of the applied load and the stress at the crack location becomes zero. In such condition, the sum of the flexural stress due to applied load, self-weight, and the contribution given by the prestressed force at the location of the flexural crack is zero. Based on the above discussion, the calculation of the effective prestressing force in a prestressed girder can be determined using the following equation:

$$\frac{N_p}{A_g}+\frac{N_p\cdot e}{I_g}y_g+\frac{M_{sw}}{I_g}y_g+\frac{M_q}{I_c}y_c=0 \tag{16}$$

where M_q is the bending moment due to the decompression load. Although similar to the previous technique of using the cracking load to estimate prestress loss, this approach has the advantage of not requiring knowledge of the concrete tensile strength and is therefore considered more reliable. By reloading the girders, the load associated with the opening of the flexural crack was determined using the same LVDTs as previously employed to detect the cracking load. For girder B6-Ab/P47, the strain gauge readings were utilized in the cracking load method, whereas the LVDT at position B-04T was considered in the decompression load method. Figures 32 and 39 show the plot of the load-strain curves used to determine the decompression load. At an applied load corresponding to the decompression load, the load-strain curves show a drastic change in slope from the initial linear branch corresponding to crack opening and a consequent dramatic reduction in stiffness. Once the decompression load of each beam had been determined, the effective prestress can be calculated directly being the unique unknown. The results of the decompression load tests are summarized in Table 16. In this test, also B4-P47/46 girder was excluded as it was tested with a single monotonic loading phase.

Table 16: Input bending moments and effective prestressing stress estimated by the decompression load method.

Beam ID	M_{sw} [kNm]	M_q [kNm]	σ_p [MPa]
B3-P47/46	300.2	392.1	603.7
B8-P47/46	304.5	442.6	653.5
B9-P47/46	223.2	452.5	699.2
B7-P47/46	304.9	272.0	575.5
B6-Ab/P47	304.9	374.7	687.1
B6-P48/49	301.7	356.5	666.8
B10-Ab/P47	301.7	360.4	669.4
Bx2-Ab/P47	591.6	491.7	445.8

The results shown in Table 16 indicate a residual prestress with a mean value of 650.7 MPa, a standard deviation of 41.7 MPa, and a CoV of 6.4%. The mean value of the prestressing stress was 14.3% and 6.2% higher than the mean value obtained by the cracking load and modified cracking load methods, respectively. A lower value of prestressing stress in the box girder was also confirmed by the decompression load method. The reason for the discrepancy between the losses obtained using the cracking load and the decompression load methods was probably due to the value of concrete tensile strength assumed in the calculations for the cracking load method. It can be seen that the percentage difference between the modified cracking load method and the decompression load method is within the range of variation of the concrete tensile strength, and therefore the two methods can be assumed comparable.

4.2.3 Residual prestress from saw-cut method

For the non-destructive determination of the residual prestress, the saw-cut method proposed by Kukay [34] was used in the present study to determine the available prestress in the 50-year-old girders. Unlike the methods described above, which require that a bridge must first be decommissioned, this approach allows the residual prestress to be quantified directly on girders still in-service. In the previously proposed method, the evolution of the longitudinal strain at the surface as a concrete block is progressively isolated, depends on the depth of the transverse saw-cuts on both sides of the strain measurement point. Therefore, if the reinforcement is too close to the concrete surface, it is not possible to make sufficiently deep saw-cuts and the concrete block cannot be fully isolated. As a result, Bagge et al. [35] and Kralovanec et al. [36] adopted a revised form of the saw-cut method supported by numerical simulation. Thus, by modelling the test procedure with a FE analysis, an iterative procedure is performed to find the residual prestressing force corresponding to the behavior observed during the tests. However, in such an approach, the reliability of the results is highly dependent on the accuracy of the simulated responses and a standardization of the method is not possible. Furthermore, in order to simulate the test procedure, it was necessary to isolate the concrete block progressively and correlate the increments in saw-cut depth with the corresponding strain. This introduces further uncertainty into the test results due to the depth measurements. For this purpose, an optimized procedure has been proposed by performing the saw-cut test with inclined cuts and isolating a triangular prism. In this way, the standardized block can be completely isolated without the problem of intercepting the steel reinforcement and eliminating the dependence on the depth of cuts. The prestressing force can then be calculated using the Navier formula, taking into account all the factors that contributes to the strains at the point investigated:

$$\frac{N_p}{A_g} + \frac{N_p \cdot e}{I_g} y_g + \frac{M_{sw}}{I_g} y_g = \sigma_c \tag{17}$$

where y_g is the distance to the neutral axis of the monitored surface, and σ_c is the longitudinal concrete stress at the surface, determined by the measured strain relief $\varepsilon_{c.meas}$, using the Hooke's law:

$$\sigma_c = E_c \cdot \varepsilon_{c,meas} \tag{18}$$

Due to the variability of concrete mechanical properties, it should be preferable to take samples close to the test point to estimate the local modulus of elasticity. However, in the absence of this information, the average value estimated for each girder during the material characterization experimental campaign, as described in Section 4.2.1, was considered. The non-destructive technique was carried out after the load test due to the research project scheduling. After the load tests, the girders were positioned over the new jersey supports on two or four points, depending on whether or not the failure load had completely separated the girders into two rigid blocks. As the girders B3-P47/46, B4-P47/46, and B9-P47/46 were completely crushed at midspan after the load tests, the actual static scheme was taken into account by considering the positioning on new jersey supports according to the following scheme:

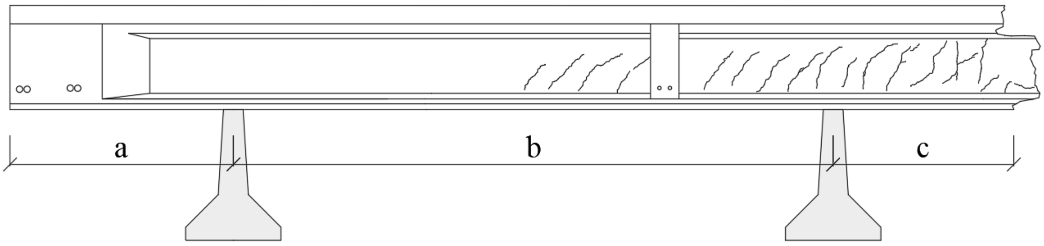

Figure 58: Static scheme for completely crushed girders.

For those girders that did not separate into two different blocks after the load tests, the static scheme shown in Fig. 58 should be referred to the whole span. For the girder B5-P47/46, the saw-cut method was carried out at midspan prior to the load test. The test locations for the girders were selected to be distant from both the failure zone and the anchorage zone, in order to ensure full active prestress.

In the experimental tests, electromagnetic concrete cover measurements were first used to determine the absence of stirrups near the surface to be investigated, and then a smooth surface was prepared before installing a strain gauge. In the proposed approach, it was not required to monitor the depth of the saw-cuts as full stress relief was achieved in the isolated block. Therefore, linear foil strain gauges with a measuring grid length of 20.0 mm were used to record the strain. The linear foil strain gauges were installed at the centre of the axial distance between the saw-cuts. Transversely, they were placed at the centre of the vertical edge of the bottom flange. The tests were then carried out by making two vertical cuts 70.0 mm apart at an angle of 45° from the vertical surface. This resulted in a triangular prism with a depth of 35.0 mm. Figure 59 shows the operational phases during the saw-cut test.

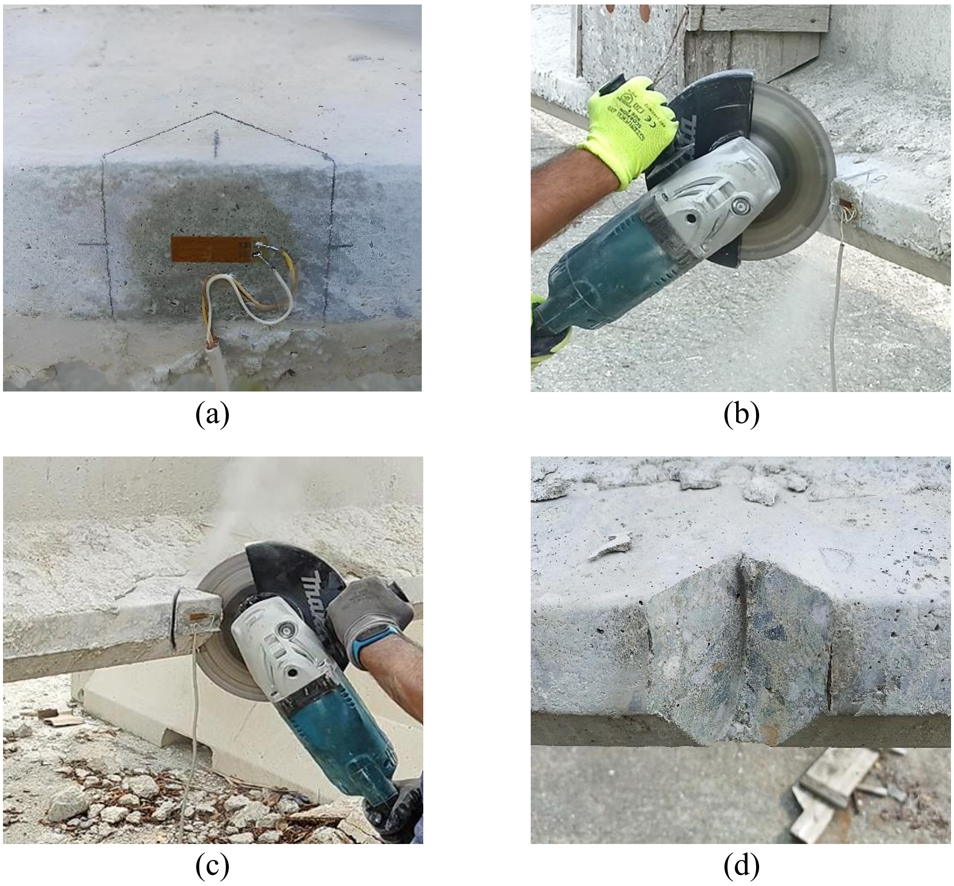
(a) (b)

(c) (d)

Figure 59: Saw-cut test: (a) strain gauge setup, (b) left side cut, (c) right side cut, (d) triangular prism shape.

Figure 60 shows the recorded strain relief data for girder B5-P47/46 at midspan. The diagram exhibits a first branch, which spans approximately 50.0

seconds, corresponding to the execution of the first cut. This was followed by a steady state period of approximately 2.0 minutes to ensure that the relaxation resulting from the first cut had stabilized. Full strain relief was then induced by performing the second cut, which facilitated full isolation of the prismatic specimen. Subsequently, a waiting period of approximately 100.0 seconds was observed to ensure strain stabilization following the execution of the saw-cut method.

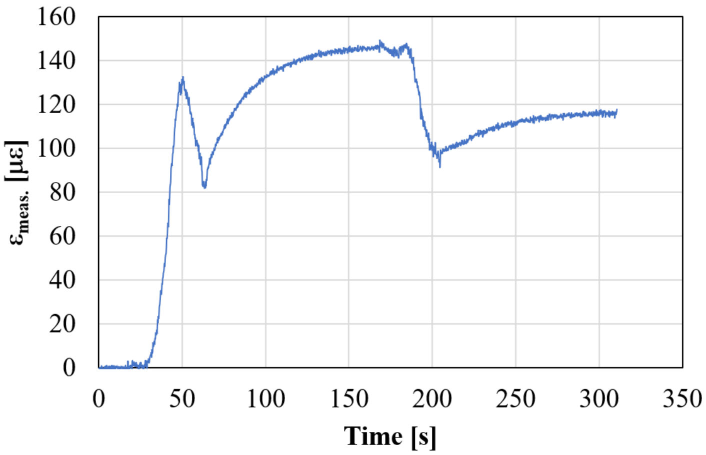

Figure 60: Strain relief measured for B5-P47/46 girder.

The parameters relating to the test configurations, the recorded strain values, and the effective prestress calculated by excluding the contribution of the dead load are summarized in Table 17. The distance z_i refers to the location of the test points from the end of the girders. In the case of a girder separated into two blocks after the loading tests, the parameters denoted by *a*, *b*, and *c*, as illustrated in Fig. 58, allow differentiation between the distinct components.

Table 17: Effective prestressing stress obtained by the saw-cut method.

Beam ID	**a [cm]**	**b [cm]**	**c [cm]**	**z_i [cm]**	**$\varepsilon_{c,meas}$ [με]**	**σ_p [MPa]**	**$\mu_{\sigma p}$ [MPa]**	**$s_{\sigma p}$ [MPa]**
B3-P47/46	33.5	651.5	345.0	226.0	146.3	379.8	435.6	55.8
				746.5	309.6	491.4		

B4-P47/46	127.5	584.0	137.5	233.5	246.6	690.9	756.4	75.0
				294.5	252.6	716.9		
	145.5	899.0	34.5	233.5	291.1	861.5		
B9-P47/46	130.0	570.0	136.0	303.5	336.6	929.7	765.2	117.2
				613.5	354.2	666.2		
	118.0	913.0	54.0	303.5	237.1	699.5		
B7-P47/46	66.5	1780.0	111.5	300.0	189.9	638.8	489.0	87.4
				500.0	88.8	423.7		
				750.0	130.8	458.1		
				1350.0	136.8	435.5		
B6-Ab/P47	87.5	1751.0	111.5	300.0	264.6	815.6	687.1	81.1
				600.0	283.6	686.7		
				900.0	204.0	594.9		
				1650.0	206.4	651.3		
B5-P47/46	102.5	1782.0	70.5	977.5	118.2	455.1	-	-

In contrast to the aforementioned methodologies, the saw-cut method allowed the estimation of the residual prestress along the length of the girders. A total of 17 tests were carried out on six girders, with distances from the end cross-section ranging from 226.0 cm to 977.5 cm. The evaluation of the obtained results was based on the actual number of active strands, as provided by the original drawings. For instance, in the case of the B3-P47/46 girder, a noticeable deviation from proportionality between the measured strains and the estimated residual prestress was observed. This difference can be primarily attributed to a reduction of approximately 30% in the number of effective prestressing strands between the points located at 746.5 cm and 226.0 cm along the length of the girder. Variations were also identified between the same testing locations of a specimen, with the exception of girder B7-P47/46, which exhibited consistent levels of prestress across its inner points. In general, discrepancies within the same specimen, apart from those inherent to the execution of the experimental test, could be related to actual variations in prestress that occurred over time due to local effects. Overall, the saw-cut method provided prestressing stress values comparable to those obtained using the modified version of the cracking load method and the decompression load method, resulting in an average value of 623.3 MPa, a standard deviation of 157.5 MPa, and a CoV of 25.3%.

4.2.4 Residual prestress from strand-cutting method

As strand cutting is the most destructive technique, it was carried out at the end of the experimental program. After the saw-cut test, some strands were exposed over a short length at the same location as the saw-cut test. This location was well beyond the transfer length and far from the failure zone so that the prestress at this location would be fully active. The strand-cutting method is based on measuring the change in strain as the strand is cut. The strain gauges were bonded to a single wire and aligned along the wire axis. Care was taken to avoid damaging the strain gauges by relaxing the strands during cutting. The strands were cut with a cutting disc while data were collected simultaneously (Fig. 61).

(a) (b)

(c) (d)

Figure 61: Operative phases of strand-cutting method: (a) strand cleaning, (b) bonding of strain gauges, (c) wire cutting, (d) strands cut.

Based on the measured change in strand strain and the average modulus of elasticity estimated on the same strands collected after the strand-cutting method, the effective prestress was determined using Hooke's law:

$$\sigma_p = E_p \cdot \varepsilon_{p,meas} \tag{19}$$

where σ_p is the prestressing stress, E_p is the modulus of elasticity, and $\varepsilon_{p,meas}$ is the recorded strain change. Finally, the calculated strand stresses were modified to eliminate the bending contribution due to the dead load according to the static scheme on new jersey supports. Thus, the recorded strain change, the parameters used to account for the dead load contribution, and the estimated effective prestress are reported in Table 18.

Table 18: Effective prestressing stress obtained by the strand-cutting method.

Beam ID	a [cm]	b [cm]	c [cm]	$\varepsilon_{p,meas}$ [με]	σ_p [MPa]	$\mu_{\sigma p}$ [MPa]	$s_{\sigma p}$ [MPa]
B3-P47/46	33.5	651.5	345.0	-2673.8	540.8	580.9	33.1
				-2753.2	557.1		
	112.0	535.0	226.0	-3096.3	622.7		
				-3003.1	603.9		

B8-P47/46	95.5	1772.0	95.5	-1681.2	320.6	351.5	120.2
				-2509.1	487.3		
				-2543.7	496.5		
				-1139.7	210.9		
				-1294.4	241.9		
B4-P47/46	127.5	584.0	137.5	-2584.2	517.3	554.6	35.2
				-2750.3	551.5		
	145.5	899.0	34.5	-2699.1	537.7		
				-3071.2	611.8		
B9-P47/46	130.0	570.0	136.0	-2680.7	537.5	588.2	67.1
				-3415.8	686.2		
				-2889.2	580.4		
	118.0	913.0	54.0	-3193.6	637.3		
				-2504.7	499.4		
B7-P47/46	66.5	1780.0	111.5	-3524.4	694.4	634.2	127.9
				-2346.8	455.4		
				-3702.2	722.0		

				-2386.7	454.0		
				-3811.2	741.7		
				-3811.2	737.9		
B5-P47/46	102.5	1782.0	70.5	-2813.1	530.0	559.6	29.7
				-3108.2	589.3		

The prestress values observed in each beam exhibited significant variability, with a minimum value of 351.5 MPa and a maximum value of 634.2 MPa. However, the residual prestress estimated for B8-P47/46 showed unreasonably low values with a corresponding CoV of 34.2%. It is possible that the process of removing concrete to expose the strand induced localized damages that can impact the accuracy of the estimates obtained. Therefore, neglecting the aforementioned values, the mean prestress for all girders was 590.8 MPa, while the standard deviation and CoV were 84.7, and 14.3%, respectively. The value obtained is comparable to the residual prestress estimated by the other methods, being 12.1%, 3.8%, and 1.7% higher than the results obtained by the cracking load method, the modified version of the cracking load method, and the saw-cut method, respectively. The observed value shows a reduction of 2.6% when compared to the result obtained by the decompression load method.

4.2.5 Comparison of experimental results on prestress loss

Based on the original design data, the strands were pretensioned to 95% of their characteristic stress $f_{p(1)k}$ corresponding to 1% strain. The characteristic stress specified in the design drawings was 1474.4 MPa, corresponding to a maximum jacking stress of 1400.8 MPa. The effective prestress at the infinite time was calculated taking into account the contribution of elastic shortening, creep, shrinkage, and strand relaxation, which gave a prestress reduction of 564.5 MPa. The total losses were therefore 40.3% of the applied jacking stress, resulting in an effective prestress of 836.3 MPa.

The total prestress losses that occurred between the fabrication of the girders and the time of the experimental campaign were obtained as the difference between the initial tensioning stress and the effective prestress measured from the aforementioned methods. Higher losses indicate smaller residual prestress forces that result in a more conservative approach. A comparison of the experimental results and the prestress loss provided by the design drawings has been presented in Fig. 62.

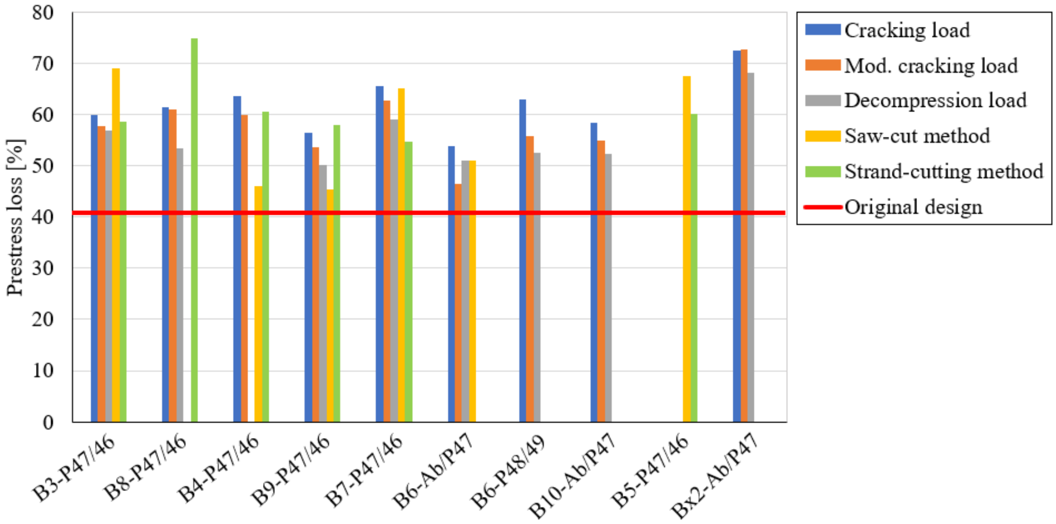

Figure 62: Percent loss of jacking stress from experimental tests.

Comparing the average effective prestress values obtained from the experimental tests with the initial prestress, the total prestress loss ranged from 53.5% for the decompression method to 61.1% for the strand cutting method. However, the modified version of the cracking load method, the decompression load method and the saw-cut method gave consistent results for the loss range of 56.4, 53.5, and 55.5%, respectively. It should be noted that the strand cutting technique is a direct measurement approach to assessing the residual prestress in a strand. Therefore, a direct comparison with the prestress loss assessments obtained by the other methods is not effective, since the latter refer to average prestress values. In general, the experimental tests gave more conservative results (i.e. higher prestress loss) than the analytical values specified in the original design. The results shown in Fig. 62 indicate that the prestressing losses measured by destructive testing are 2.9% more conservative than those measured by the saw-cut method. The design values overestimated the residual prestress by 28.5% and 31.3% compared to the average results obtained by the saw-cut method and the destructive tests respectively.

4.3 Analytical prediction of prestress loss

The research studies proposed in the literature have been related to the evaluation of the current provisions for calculating prestressing losses in laboratory test specimens, and relatively few have been related to girders retrieved from existing bridge structures. Therefore, research is needed to evaluate the suitability of the current code provisions for estimating prestress losses in full-scale structural members subsequent to their exposure to real in-service conditions.

Over time, the level of prestress in a concrete member will vary due to the influence of inherent concrete behavior mechanisms such as creep and shrinkage, stress relaxation of the prestressing strands, and external factors such as deck placement. As the concrete shrinks, the contraction of the prestressing steel results in a consequent loss of tensile force. Consequently, the degree of creep exhibited by the concrete is reduced compared to when it is subjected to constant compression. In addition, as the concrete undergoes creep and shrinkage, the prestressing strands exhibit a reduced degree of relaxation compared to when they are stressed and held in a stretched state between two fixed points. Conversely, the occurrence of stress gains is attributed to the elongation of the strand, typically as a result of a positive bending moment induced by an external load and/or differential shrinkage between the precast PC girder and the cast-in-place concrete deck. In general, prestressing losses can be classified as instantaneous loss, which includes elastic shortening, and long-term prestressing loss, which includes creep and shrinkage of concrete and relaxation of steel. The magnitude of the elastic shortening loss depends on the modulus of elasticity of the concrete. The relaxation loss of steel depends on the nature of the prestressing strands and is typically minimal for low-relaxation prestressing strands. The amount of prestressing loss due to creep and shrinkage is related to the stiffness of the aggregate used, the compressive strength of the concrete, the configuration and dimensions of the PC elements, as well as the ambient temperature and relative humidity. Due to the complexity resulting from the number of variables involved and the modelling of the interaction between the shrinkage and creep of the concrete, the relaxation of the prestressing strands, and the interaction between the precast PC girder and the cast-in-place slab, several models with different levels of accuracy have been proposed in current codes.

4.3.1 Prestress loss according to Eurocode's model

For structures with prestressing strands, prestress losses are distinguished in instantaneous losses and time-dependent losses. Immediate losses occur between the time of prestressing and the transfer of prestress to the concrete. After initial tensioning, the first prestress loss observed is anchorage seating loss. Anchorage seating loss occurs when the strands are initially tensioned and seated prior to casting. During the prestressing phase, an anchor displacement of a could result in a uniform prestress loss of:

$$\Delta\sigma_p = \frac{a \cdot E_p}{L} \tag{20}$$

where L is the length of the prefabrication bench. Prefabricators typically overstress the strands so that the strand stress after seating loss is the desired initial prestress. Before the prestressing is transferred to the concrete, a reduction in stress occurs due to an acceleration of strand relaxation caused by the heat treatment curing. EC2 suggests that the loss due to relaxation is based on the 1000-hour values for the three different classes of relaxation given in the code. Therefore, the equivalent time, t_{eq}, is estimated to take into account the maximum temperature reached in the steam curing thermal cycle. The loss of prestress due to relaxation, $\Delta\sigma_{p,r}$, for class 2 wires or strands has been defined as the percentage ratio of the variation of the prestressing stress to the initial prestressing stress σ_{pi}:

$$\frac{\Delta\sigma_{p,r}}{\sigma_{pi}} = 6.6\,\rho_{1000}\,e^{9.1\mu}\left(\frac{t_0 + t_{eq}}{1000}\right)^{0.75\,(1-\mu)}\,10^{-6} \tag{21}$$

where ρ_{1000} is the relaxation loss at 1000 hours after tensioning and at a mean temperature of 20 °C, μ is the ratio between the initial prestress and the characteristic tensile strength of the prestressing steel, and t_0 is the time after tensioning. When the prestressed strands are released from the anchorages, the transfer of prestress to the concrete results in an elastic shortening of the concrete and a prestress loss of:

$$\Delta\sigma_{p,e} = \left(\frac{P_0}{A_g} + \frac{P_0 \cdot e_p}{I_g} y_g\right)\frac{E_p}{E_c} \tag{22}$$

where P_0 is the prestress force at the end of the thermal curing.

The time dependent losses are calculated by considering the reduction of strain due to the creep and shrinkage of concrete, and the reduction of stress due to the relaxation under tension. The assumptions of plane cross-section, linear behavior, perfect bond between concrete and steel are used in the calculation. Furthermore, the strain compatibility is imposed between strands and concrete at the same level:

$$\Delta\varepsilon_c(t,t_0) = \Delta\varepsilon_p(t,t_0) \tag{23}$$

Therefore, the concrete strain due to shrinkage and creep can be expressed as:

$$\Delta\varepsilon_c(t,t_0) = \varepsilon_{cs} + \varepsilon_{cc} \tag{24}$$

where ε_{cs} is the concrete shrinkage strain, and ε_{cc} is the concrete strain due to creep. For an applied constant stress σ at time t_0, the total strain at time t is the result of an elastic contribution and a strain increment due to the creep:

$$\varepsilon_{cc}(t,t_0) = \sigma\left[\frac{1}{E_c(t_0)} + \frac{\varphi(t,t_0)}{E_{c,28}}\right] \tag{25}$$

with $\varphi(t, t_0)$ creep coefficient and $E_{c,28}$ modulus of elasticity of the concrete at 28 days. In the case of continuous variation of concrete stress, as in the case of concrete at the strand level due to long-term losses, concrete creep should be taken into account by time integration of Eq. 25. However, in the case of asymptotic stress, it is widely accepted to assume the integral part equivalent at an ageing coefficient $\chi(t,t_0)$ according to:

$$\varepsilon_{cc}(t,t_0) = \Delta\sigma(t,t_0)\left[\frac{1}{E_c(t_0)} + \chi(t,t_0)\frac{\varphi(t,t_0)}{E_{c,28}}\right] \tag{26}$$

The aging coefficient was introduced by Bažant [38] to allow the effective modulus to be calculated in one step. This phenomenon, where the stress varies slightly and the elastic modulus is assumed to be constant, is taken into account by defining the age-adjusted effective modulus of elasticity of concrete:

$$E_{c,eff} = \frac{E_c(t_0)}{1+\varphi(t,t_0)} \tag{27}$$

Therefore, the concrete strain due to the initial stress $\sigma_c(t_0)$, and its variation with time $\Delta\sigma_c$, can be expressed in Eq. 24 as:

$$\Delta\varepsilon_c = \varepsilon_{cs} + \sigma_c(t_0)\frac{\varphi(t,t_0)}{E_c} + \frac{\Delta\sigma_c}{E_c}[1 + \chi\,\varphi(t,t_0)] \tag{28}$$

Imposing the equilibrium between the prestress loss due to creep, shrinkage and relaxation, $\Delta\sigma_{p,c+s+r}$, and the variation of concrete stress at strands level, results:

$$\Delta\sigma_c = -\frac{\Delta\sigma_{p,c+s+r}}{A_c}\left(1 + \frac{A_c}{I_c}z_{cp}^2\right) \tag{29}$$

where A_c is the area of the concrete section, I_c is the second moment of area of the concrete section, and z_{cp} is the distance between the centre of gravity of the concrete section and the strands. All of these quantities are based on the cross-section of the beam only and do not relate to the behavior of the composite section. Considering the assumption of the strain compatibility expressed by Eq. 23, the variation of prestress within the strands results:

$$\Delta\sigma_{p,c+s+r} = \Delta\varepsilon_c E_p + \Delta\sigma_{relax}(t,t_0) \tag{30}$$

Substituting Eq. 29 into Eq. 28, and then Eq. 28 into Eq. 30, gives the prestress loss in the strands due to creep, shrinkage and relaxation at time t:

$$\Delta\sigma_{p,c+s+r} = \frac{\varepsilon_{cs}E_p + \sigma_c(t_0)\dfrac{E_p\,\varphi(t,t_0)}{E_c} + \Delta\sigma_{relax}(t,t_0)}{1 + \dfrac{E_p}{E_c}\dfrac{A_p}{A_c}\left(1 + \dfrac{A_c}{I_c}z_{cp}^2\right)[1 + \chi\,\varphi(t,t_0)]} \tag{31}$$

The stress reduction resulting from actual relaxation is lower than that experienced during pure relaxation for the initial stress, because the applied deformation on the prestressing strands is not a constant value, but rather varies in response to the deformation of the concrete. As the deformation of the concrete decreases, the relaxation loss is less than that of pure relaxation, which is assumed to be the 80% in the EC2 [1]. In Eq. 31, the ageing coefficient is assumed to be 0.8.

The total shrinkage strain is composed by the drying shrinkage strain, ε_{cd}, and the autogenous shrinkage strain, ε_{ca}:

$$\varepsilon_{cs} = \varepsilon_{cd} + \varepsilon_{ca} \tag{32}$$

The drying shrinkage strain is influenced by the water migration within the hardened concrete and is characterized by the following time-dependent function:

$$\varepsilon_{cd}(t) = \beta_{ds}(t, t_s)\ k_h\ \varepsilon_{cd,0} \tag{33}$$

where k_h is a coefficient to take into account the area exposed to drying, β_{ds} is a coefficient depending on the age of the concrete at the moment considered and the age of the concrete at the beginning of drying shrinkage, and $\varepsilon_{cd,0}$ is the basic drying shrinkage strain calculated from:

$$\varepsilon_{cd,0} = 0.85\left[(220 + 110\ \alpha_{ds1})\ exp\left(-\alpha_{ds2}\ \frac{f_{cm}}{10}\right)\right] 10^{-6}\beta_{RH} \tag{34}$$

with α_{ds1} and α_{ds2}, two coefficients that depend on the type of cement, and β_{RH}, a coefficient that takes into account the ambient relative humidity. The autogenous shrinkage strain is expressed as a linear function of the concrete strength according to the following equation:

$$\varepsilon_{ca}(\infty) = 2.5(f_{ck} - 10)\ 10^{-6} \tag{35}$$

The development of autogenous shrinkage strain over time is represented by the coefficient $\beta_{as}(t)$ and results:

$$\varepsilon_{ca}(t) = \beta_{as}(t)\ \varepsilon_{ca}(\infty) \tag{36}$$

The creep coefficient is calculated from:

$$\varphi(t, t_0) = \varphi_0\ \beta_c(t, t_0) \tag{37}$$

where φ_0 is the notional creep coefficient and $\beta_c(t, t_0)$ is a coefficient describing the evolution of creep with time. The notional creep coefficient depends mainly on the modulus of elasticity of the concrete, and the moisture content. It is therefore estimated according to:

$$\varphi_0 = \varphi_{RH}\ \beta(f_{cm})\ \beta(t_0) \tag{38}$$

where φ_{RH} is a factor to account for the effect of relative humidity, $\beta(f_{cm})$ is a factor to account for the effect of concrete strength, and $\beta(t_0)$ takes into account the effect of concrete age at loading.

For further information concerning unexplained coefficients, the reader is referred to EC2 [1].

4.3.2 Prestress loss according to AASHTO's refined model

The AASHTO LRFD bridge design specifications [2] are based on the NCHRP project [9], which was established to improve the accuracy of the specification on the prestress loss estimation. The total prestress loss is divided into short-term and long-term components:

$$\Delta f_{pT} = \Delta f_{pES} + \Delta f_{pLT} \tag{39}$$

where the short-term component Δf_{pES} refers to the elastic shortening loss due to concrete strain, and the long-term component Δf_{pLT} refers to the sum of time-dependent prestress losses between transfer and deck placement (shrinkage of girder concrete, Δf_{pSR}, creep of girder concrete, Δf_{pCR}, and relaxation of prestressing strands, Δf_{pR1}), and from the time of deck placement to the final time (shrinkage of girder concrete, Δf_{pSD}, creep of girder concrete, Δf_{pCD}, relaxation of prestressing strands, Δf_{pR2}, and gain due to shrinkage of deck, Δf_{pSS}):

$$\Delta f_{pLT} = \left(\Delta f_{pSR} + \Delta f_{pCR} + \Delta f_{pR1}\right)_{id} + \left(\Delta f_{pSD} + \Delta f_{pCD} + \Delta f_{pR2} - \Delta f_{pSS}\right)_{df} \tag{40}$$

This separation was made to account for the effects of the non-composite section up to deck casting and the composite section after the deck placement.

In order to calculate the elastic shortening loss, the relative shortening of the member at the level of the prestressing strands, ε_c, due to the concrete compressive stress, f_{cgp}, is defined as:

$$\varepsilon_c = \frac{f_{cgp}}{E_{ci}} = \varepsilon_p \tag{41}$$

where the concrete compressive stress is given by the self-equilibrating loads according to:

$$f_{cgp} = \left(f_{pbt} - \Delta f_{pES}\right) A_p \left(\frac{1}{A_g} + \frac{e_p^2}{I_g}\right) - \frac{M_{sw} e_p}{I_g} \tag{42}$$

By substituting Eq. 42 into Eq. 41, the change in strain can then be used to find the prestress loss due to elastic shortening:

$$\Delta f_{pES} = E_p \varepsilon_p = \frac{E_p}{E_{ci}} f_{cgp} \tag{43}$$

where E_{ci} is the modulus of elasticity of the concrete at the time of release. By solving Eq. 43 for Δf_{pES}, the elastic shortening loss can be calculated from:

$$\Delta f_{pES} = \frac{A_p f_{pbt}\left(I_g + e_p^2 A_g\right) - e_p M_{sw} A_g}{A_p\left(I_g + e_p^2 A_g\right) + \dfrac{A_g I_g E_{ci}}{E_p}} \tag{44}$$

where f_{pbt} is the strand stress before transfer.

In order to take into account the time-dependent interaction between concrete and bonded steel, transformed section coefficients have been defined according to the following procedure. As the presence of steel in the member restrains the shrinkage and creep of the concrete, the strain in the prestressing strand, ε_p, caused by concrete strain has been defined as:

$$\varepsilon_p = \varepsilon_b - \varepsilon_{\Delta P} \tag{45}$$

where ε_b is the concrete strain in the section without strands, and $\varepsilon_{\Delta p}$ is the strain in the concrete due to the resistance provided by the prestressing strands. Substituting the effective contributions into Eq. 45 gives:

$$\frac{\Delta P_p}{A_p E_p} = \varepsilon_b - \left(\frac{\Delta P_p}{E''_{ci} A_g} + \frac{\Delta P_p}{E''_{ci}} \frac{e_p^2}{I_g}\right) \tag{46}$$

where E''_{ci} is the age-adjusted effective modulus of elasticity of the concrete. Solving for the generic loss Δf_p and introducing the transformed section coefficient K, Eq. 46 can be rewritten as:

$$\Delta f_p = \frac{\Delta P_p}{A_p} = \varepsilon_b K E_p \tag{47}$$

where the transformed section coefficient results:

$$K = \frac{1}{1 + \frac{E_p}{E_{ci}}\frac{A_p}{A_g}\left(1 + \frac{A_g e_p^2}{I_g}\right)\left(1 + \chi\psi(t_f, t_i)\right)} \tag{48}$$

where $\psi(t_f, t_i)$ is the girder creep coefficient at the final time due to the load applied at transfer and χ is the ageing coefficient assumed to be 0.7.

According to the procedure described above, the shrinkage loss between the time of release and the time of deck placement was defined as:

$$\Delta f_{pSR} = \varepsilon_{bid} K_{id} E_p \tag{49}$$

where ε_{bid} is the concrete shrinkage strain, and K_{id} is the transformed section coefficient, both defined for the period between transfer and deck placement.

Accordingly, the girder creep loss was defined as:

$$\Delta f_{pCR} = \frac{f_{cgp}}{E_{ci}} \psi_b(t_d, t_i) K_{id} E_p \tag{50}$$

where $\psi_b(t_d, t_i)$ is the girder creep coefficient at the time of deck placement due to the load applied at transfer.

The prestress loss due to shrinkage of the girder concrete from the time of deck placement to the final time is calculated from:

$$\Delta f_{pSD} = \varepsilon_{bdf} K_{df} E_p \tag{51}$$

where ε_{bdf} is the shrinkage strain of the girder between the time of deck placement and the final time, and K_{df} is the transformed section coefficient after deck placement, related to the composite section.

The prestress loss due to creep of the girder from the time of deck placement to the final time is due to the prestressing force, self-weight, deck loads, and any other superimposed dead loads at the time of deck placement. Therefore, the creep loss has been divided into two components, the prestress loss caused by the continued creep of the concrete due to the initial prestressing force and self-weight, and the prestress loss caused by the stress change in the concrete due to the prestress loss prior to deck placement and any superimposed dead loads:

$$\Delta f_{pCD} = \frac{E_p}{E_{ci}} f_{cgp} K_{df} \left[\psi_b(t_f, t_i) - \psi_b(t_d, t_i)\right] + \frac{E_p}{E_{ci}} \Delta f_{cd} \psi_b(t_f, t_d) K_{df} \tag{52}$$

where $\psi_b(t_f,t_d)$ is the creep coefficient of the girder at the final time due to the load applied at deck placement, and Δf_{cd} is the change in concrete stress at the strand centroid, expressed by:

$$\Delta f_{cd} = \frac{P_\Delta}{A_g} + \frac{P_\Delta e_p^2}{I_g} - \frac{M_{sd} e_{pc}}{I_c} \tag{53}$$

where M_{sd} is the moment due to the deck weight and other superimposed dead loads, e_{pc} is the eccentricity of the prestressing force with respect to the centroid of the composite section, I_c is the moment of inertia of the composite section, and P_Δ is the total long-term prestress losses prior to deck placement, calculated from:

$$P_\Delta = -\left(\Delta f_{pSR} + \Delta f_{pCR} + \Delta f_{pR1}\right) A_p \tag{54}$$

The shrinkage strain is estimated using the expression below:

$$\varepsilon_{sh} = k_s k_{hs} k_f k_{td} 0.48 \cdot 10^{-3} \tag{55}$$

where k_{hs} is the humidity factor for shrinkage, k_s is the factor for the effect of the volume-to-surface ratio, k_f is the factor for the effect of concrete strength, and k_{td} is the time development factor.

Creep is found in a similar way using the expression below:

$$\psi(t, t_i) = 1.9 k_s k_{hc} k_f k_{td} t_i^{-0.118} \tag{56}$$

where k_{hc} is the humidity factor for creep, and t_i is the age of the concrete at loading. Both Eqs. 55 and 56 are used to find the shrinkage strain and creep coefficient for the beam and deck concrete at different required time intervals.

At the time of deck placement, typically several months after the beam casting, it is assumed that most of the shrinkage of the girder concrete has already occurred and therefore the shrinkage of the deck concrete is resisted by the girder. This results in positive bending in the beam and a gain in strand stress equivalent to:

$$\Delta f_{pSS} = \frac{E_p}{E_{ci}} \Delta f_{cdf} K_{df} \left[1 + \psi_b\left(t_f, t_d\right)\right] \tag{57}$$

where the change in concrete stress at the centroid of the prestressing strands due to shrinkage of the deck concrete is calculated from:

$$\Delta f_{cdf} = \frac{\varepsilon_{ddf} A_d E_{cd}}{1 + \chi \psi_d\left(t_f, t_d\right)} \left(\frac{1}{A_c} - \frac{e_{pc} e_d}{I_c}\right) \tag{58}$$

where ε_{ddf} is the shrinkage strain of the deck concrete between placement and final time, A_d is the area of the deck concrete, E_{cd} is the modulus of elasticity of the deck concrete, $\psi_d(t_f, t_d)$ is the creep coefficient of the deck concrete at final time due to the load applied after deck placement, and e_d is the eccentricity of the deck with respect to the composite section. Equation 58 is a mechanics-based expression which assumes that the shrinkage of the deck concrete imposes a point load P_{sd} on the system at an eccentricity of e_d, defined by:

$$P_{sd} = \frac{\varepsilon_{ddf} A_d E_{cd}}{1 + \chi \psi_d\left(t_f, t_d\right)} \tag{59}$$

The expressions for the prestress loss due to strand relaxation before and after deck placement in the AASHTO LRFD procedure, are separate but of equal magnitude:

$$\Delta f_{pR1} = \Delta f_{pR2} = \frac{f_{pt}}{K_L} \left(\frac{f_{pt}}{f_{py}} - 0.55\right) \tag{60}$$

where f_{pt} is the stress in the prestressing strands immediately after transfer, K_L is a coefficient equal to 30 for low relaxation strands, and f_{py} is the yield stress of the prestressing strands. There is also an expression in the commentary that gives a time-dependent value for the relaxation loss:

$$\Delta f_{pR1} = \left[\frac{f_{pt}}{K_L'} \frac{log(24t)}{log(24t_i)} \left(\frac{f_{pt}}{f_{py}} - 0.55\right)\right] \left[1 - \frac{3\left(\Delta f_{pSR} + \Delta f_{pCR}\right)}{f_{pt}}\right] K_{id} \tag{61}$$

where K_L' is a factor accounting for the type of steel, equal to 45 for low relaxation steel, t is the time from transfer to deck placement, and t_i is the time from stressing to transfer. The expression was derived by Magura et al. [39] and refined to account for the steady decrease in strand prestressing due to the concrete creep and shrinkage and to include the transformed section coefficient K_{id}.

For further information concerning unexplained coefficients, the reader is referred to AASHTO LRFD [2].

4.3.3 Proposed model based on Eurocode’s formulation

The current EC2 formula for computing long-term losses (Eq. 31), is a one-step method that provides prestress loss by assuming a time step between strand releases to infinity. However, in the case of staged construction, the interaction between the precast PC girder and the cast-in-place concrete deck needs to be considered. When a deck slab is cast on a precast PC girder, the change in cross-section will generate restraint stresses, as the loaded girder tries to deflect further under creep, but this is resisted by the composite section. The additional dead load provided by the deck, induces stress redistribution as a result of a differential creep. During the curing of the concrete deck slab, it is assumed that the girders and deck are bonded to form a composite section. However, due to the time difference between the casting of the deck slab and the curing of the girders, a significant amount of concrete shrinkage would have occurred prior to the casting of the deck. Consequently, when considering the composite behavior, differential shrinkage emerges, leading to the development of compressive forces on the top of the concrete girder.

In view of the above considerations, a revised version of the EC2 formulation has been proposed, with the aim of predicting the long-term prestress loss more reasonably, without the need for a refined calculation using the time-step method. A similar form of the Eq. 31 has been obtained, referring to the loss before casting of the deck slab on the PC girder alone (t_d, t_0), and to the loss after casting of the deck slab applied to the composite section (t_f, t_d). For each stage of construction, the prestressing strands and concrete were assumed to be perfectly bonded, strain compatibility was satisfied, and the ageing coefficient was introduced to obtain the strain resulting from the initial stress and the subsequent continuously varying stress. Therefore, the resulting prestress loss was defined as:

$$\Delta\sigma_{p,c+s+r} = \Delta\sigma_{p,0d} + \Delta\sigma_{p,df} \tag{62}$$

where $\Delta\sigma_{p,0d}$ are the losses equivalent to the Eq. 31, estimated on the precast PC girder between the strand release and the deck placement:

$$\Delta\sigma_{p,0d} = \frac{\varepsilon_{cs}(t_d, t_0)E_p + \sigma_c(t_0)\dfrac{E_p\,\varphi(t_d, t_0)}{E_c} + \Delta\sigma_{relax}(t_d, t_0)}{1 + \dfrac{E_p}{E_c}\dfrac{A_p}{A_g}\left(1 + \dfrac{A_g}{I_g}z_{gp}^2\right)[1 + \chi\,\varphi(t_d, t_0)]} \tag{63}$$

and $\Delta\sigma_{p,fd}$ are the estimated losses on the composite section after deck placement.

Based on the strain compatibility relationship and the equilibrium equation between the change in prestressing and concrete stress (Eqs. 23-30), the losses after deck placement have been defined as:

$$\Delta\sigma_{p,df} = \frac{\varepsilon_{cs}(t_f,t_d)E_p+\sigma_c(t_0)\frac{E_p\left[\varphi(t_f,t_0)-\varphi(t_d,t_0)\right]}{E_c}+\Delta\sigma_c(t_f,t_d)\frac{E_p\left[1+\varphi(t_f,t_d)\right]}{E_c}+\Delta\sigma_{relax}(t_f,t_d)}{1+\frac{E_p}{E_c}\frac{A_p}{A_c}\left(1+\frac{A_c}{I_c}z_{cp}^2\right)\left[1+\chi\,\varphi(t_f,t_d)\right]} \tag{64}$$

where the geometric properties in the denominator refer to the composite cross section, ε_{cs} is the shrinkage of the girder after deck placement, $\Delta\sigma_{relax}$ is the strand relaxation after deck placement, $\sigma_c(t_0)$ is the concrete stress after strand release taken into account on the composite section with differential creep, and $\Delta\sigma_c(t_f, t_d)$ is the change in concrete stress at the strand centroid due to prestress loss before deck placement, superimposed load due to deck self-weight, and differential shrinkage of the deck, estimated from:

$$\begin{aligned}\Delta\sigma_c(t_f, t_d) = \Delta\sigma_{p,0d}A_p\left(\frac{1}{A_g} + \frac{1}{I_g}z_{gp}^2\right)\frac{\varphi(t_f, t_d)}{[1 + \varphi(t_f, t_d)]} - \frac{M_{swd}z_{cp}}{I_c} \\ + P_{shd}\left(\frac{1}{A_C} - \frac{e_d}{I_c}z_{cp}\right)\end{aligned} \tag{65}$$

The effect of the differential shrinkage of the deck is taken into account by applying a concentrated force P_{shd} at the centroid of the deck slab equal to:

$$P_{shd} = \frac{\varepsilon_{diff}A_dE_{cd}}{1 + \chi\varphi_d(t_f, t_d)} \tag{66}$$

where the differential shrinkage ε_{diff} is calculated by subtracting from the total shrinkage of the slab $\varepsilon_{ds}(t_f, t_d)$, the residual shrinkage of the girder after the beam is made composite $\varepsilon_{cs}(t_f, t_d)$:

$$\varepsilon_{diff} = \varepsilon_{ds}(t_f, t_d) - \varepsilon_{cs}(t_f, t_d) \tag{67}$$

The proposed modelling of prestress losses properly accounts for the interaction between the prestressing strand and the surrounding concrete by assuming no slip between the prestressing steel and the concrete. As a result, the steel restraint against concrete shrinkage and creep has been represented by the denominators of Eqs. 63-64. The creep and shrinkage strains required for loss estimation can be obtained using any of the concrete creep and shrinkage models proposed in the literature. However, in the following treatment, those proposed by EC2 have been used. The effects of differential shrinkage and creep strains resulting from the casting of the concrete deck after the prestressed concrete beams have undergone initial relaxation, creep, and shrinkage have also been included. The current EC2 and AASHTO's specifications assume a constant modulus of elasticity of concrete throughout the life of a structure. A realistic modulus of elasticity that varies with the age of the concrete should result in a more accurate estimation of prestress losses in concrete girders. Therefore, the EC2 formula was used to account for the modulus of elasticity associated with different stages of construction:

$$E_{cm}(t) = E_{cm}\left\{e^{s\left[1-\left(\frac{28}{t}\right)^{0.5}\right]}\right\}^{0.3} \tag{68}$$

where E_{cm} is the modulus of elasticity of concrete at an age of 28 days, and s is a coefficient that depends on the type of cement (0.38 for normal hardening cement). To take into account the effect of temperature on the maturity of the concrete, as for steam cured concrete, the time in days can be adjusted by estimating an equivalent time.

4.3.4 Analytical models comparison

The prediction models described above were used to estimate the prestress loss of the PC girders after 50 years of service. As the EC2 formulation does not include the composite behavior of the girders, two different simulations were performed, one neglecting the deck slab and the other assuming the composite transformed cross-section since the initial prestress stressing. Therefore, in both analyses, the effects due to the casting of the deck slab were ignored according to Eq. 31. However, in the AASHTO and the proposed model, the correct construction sequence has been taken into account. In the calculation process, all input parameters were assumed to be deterministic, with mean values detailed in Table 19. The material properties refer to the mean values of the destructive test results, and the ambient relative humidity refers to the mean values of monthly data recorded by the Turin Caselle weather station from 1980 to 2017. In the absence of any reference to the construction stages in the original drawings, a hypothetical time of 3 months was assumed between the prestressing of the PC girders and the casting of the deck.

Table 19: Input parameters for prestress loss prediction models.

Parameter	**Value**	**Unit**	**Source**
$f_{cm,girder}$	31.5	[MPa]	Experimental
$E_{cm,girder}$	22894.6	[MPa]	Experimental
$f_{cm,slab}$	27.4	[MPa]	Experimental
$E_{cm,slab}$	18892.1	[MPa]	Experimental
f_{ptm}	1786.9	[MPa]	Experimental
E_p	201.1	[GPa]	Experimental
E_s	201.8	[GPa]	Experimental
$\sigma_{p,jacking}$	1400.8	[MPa]	Original design
RH	72	[%]	Estimated
t_{slab}	90	[days]	Assumed

The performance of the models was evaluated by comparing the predicted prestress loss with the measured values outlined in Section 4.2. The experimental measurements were considered as mean values for each employed method. Figure 63 illustrates the comparison between the predictions of prestress loss based on average material properties and the experimental values. The comparative analysis between the theoretical models was facilitated by combining the different factors contributing to prestress loss, namely elastic shortening, shrinkage, creep, and relaxation effects.

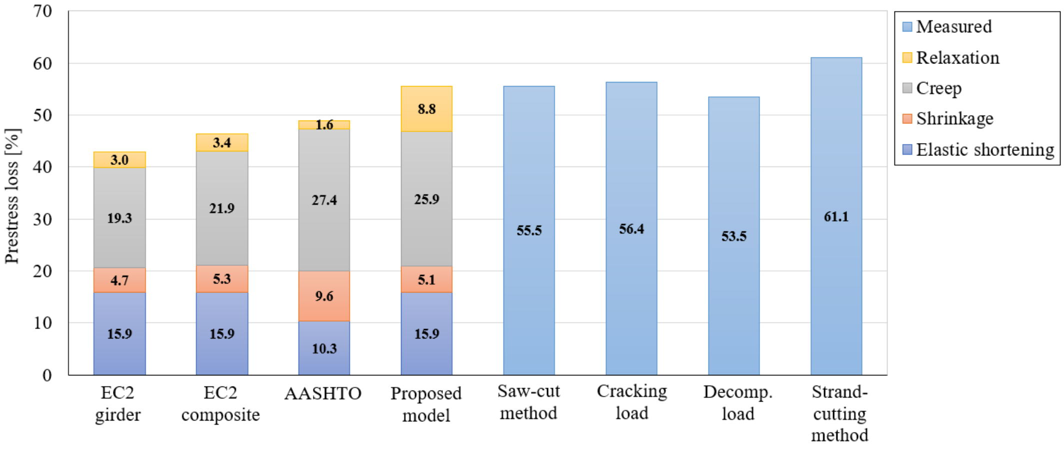

Figure 63: Comparison between predicted and experimental prestress loss.

As observed in Fig. 63, a first difference was found between the prestress loss due to elastic shortening estimated by EC2-based approaches and AASHTO's model. This discrepancy can be attributed to the neglection in the AASHTO method of losses occurring before prestress transfer, which are caused by anchor displacement and strand relaxation during the steam curing thermal cycle. Furthermore, the AASHTO method exhibited higher predictions for prestress loss due to concrete shrinkage but lower predictions for prestress loss caused by strand relaxation. It is important to mention that the primary objective of the research documented in NCHRP report [9], upon which the AASHTO method was based, was to extend the methodology for estimating prestress loss in high-strength concrete girders. Consequently, the baseline test specimen used to calibrate the shrinkage equations differed from the conditions of the presented case study. However, an agreement was observed between the prestress losses due to creep, as estimated by the proposed model and the AASHTO method. Both methodologies accounted for the distinct effects on the girder section up to deck casting and on the composite section after deck placement. Moreover, the proposed model indicated the highest prestress loss due to strand relaxation, which was calculated as the sum of the maximum relaxation contribution between prestress transfer to the deck placement and long-term relaxation.

Overall, the predicted prestress losses by the EC2 model with girder section, the EC2 model with composite section, the AASHTO model, and the proposed model, were determined to be 42.9%, 46.4%, 47.9%, and 55.5%, respectively. The prestress loss estimated by the proposed model was found to be adequate and comparable to the experimental results, except for the strand-cutting method. Both American and European code predictions exhibited unconservative estimates when compared to the experimental values. Specifically, the EC2 results highlighted improved accuracy when considering the composite section instead of the girder section alone. Moreover, the introduction of the proposed model assumption emphasized the significance of considering the actual construction process when predicting prestress losses. The proper evaluation of the cast-in-place slab proved to be crucial, not only in accounting for the effects of differential shrinkage and additional dead load, but also in the redistribution of stress within the cross-section.

4.3.5 Probabilistic analysis of prestress loss prediction

The accuracy of prestress loss predictions depends not only on the accuracy of the models, but also on the accuracy of the key input parameters. The aforementioned methods have been compared with a deterministic approach, assuming the mean values of the material parameters, thus neglecting the associated uncertainties. On the one hand, the use of more sophisticated models could lead to more accurate results, but on the other hand, more input parameters are required. However, when assessing existing structures, the availability of reliable information on the mechanical properties and the construction process of the structures is not always satisfactory. If a number of variables cannot be determined with certainty, significant errors may occur, and the effectiveness of refined models may be lost. The most rational way to obtain information on the reliability of the estimated prestress loss, is to consider the randomness of the uncertain parameters and treat them with probability distribution fitting. Questions also arise when parameters with little or no effect on the prestress loss are used. Parameters with limited variability can generally be assumed constant without significantly affecting the accuracy of the model. A method designed with these considerations can potentially offer advantages in terms of clarity, accessibility, and reduced susceptibility to error.

To this end, statistics and probability distributions have been derived for material, environmental, and construction phase data assumed as input to the proposed model for prestress loss prediction. As a first step, a sensitivity analysis was conducted to ascertain the stochastic variables with the greatest influence on code-based estimation of prestress loss. The most relevant variables were considered together as random variables for a probabilistic analysis of the prestress loss. The remaining quantities were assumed to be deterministic, with their mean values as shown in Table 19. Other uncertainties, such as geometry measurements or epistemic uncertainties related to the models, are not taken into account. Finally, the variation range of the prestress loss with a certain level of confidence was obtained to provide a basis for the rational determination in existing PC bridges. The probability distributions of the prestress loss were estimated by Monte Carlo simulation based on 10^4 samples. A script code was implemented in a MATLAB routine to perform the simulation process, according to the scheme in Fig. 64.

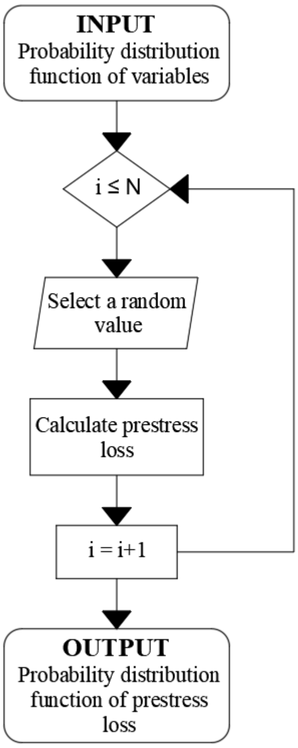

Figure 64: Simulation procedure.

The material properties database was based on the laboratory tests described in Section 3.4. Two different distributions were fitted to the concrete compressive strength and elastic modulus, assumed to be independent. Consequently, four distributions were obtained to model the concrete properties of both the girders and the slab. The parameters of the best fitting distribution were determined by the maximum likelihood estimation method by differentiating the likelihood that the data generated by the model were the actual observed data. The same procedure was used to derive the probability density function of the steel modulus of elasticity, the ultimate strength of the prestressing strands, and the ambient relative humidity. For simplicity, all the variables investigated were assumed to be normally distributed, despite minor deviations from normality occurred at some data points. Due to the lack of data on the time of deck casting, it was modelled with a uniform distribution with values between 30 to 180 days. *Appendix E* shows the histogram of the relative frequency, the probability distribution functions, and the Quantile-Quantile plot of the collected variables. The basic statistics of the distribution obtained in the analysis are presented in Table 20.

Table 20: Statistical parameters of the normal distribution functions.

Variable	**St. Dev.**	**Mean**	**Unit**	**CoV [%]**
$f_{c,girder}$	4.5	31.5	[MPa]	14.3
$E_{c,girder}$	2850.5	22894.6	[MPa]	12.5
$f_{c,slab}$	1.0	27.4	[MPa]	3.6
$E_{c,slab}$	4618.5	18892.1	[MPa]	24.4
f_{pt}	57.3	1786.9	[MPa]	3.2
E_p	9.2	201.1	[GPa]	4.6
E_s	108.7	201.8	[GPa]	53.9
RH	7.9	72.0	[%]	11.0

After quantifying all the random variables in terms of probability density functions, the sensitivity analysis was performed to define their influence on the prestress loss. A total of 10^4 random samples were generated for each variable. The prestress loss was then evaluated deterministically for each set of realizations for all variables. Finally, the histograms and probabilistic information of the prestress loss have been calculated. The sensitivity was evaluated by comparing the variation of the estimated prestress losses due to that of the input variables.

Therefore, the sensitivity S_{Pv} of the prestress loss P to the variable v was estimated from:

$$S_{Pv} = \frac{CoV_P}{CoV_v} \tag{69}$$

where CoV_P is the coefficient of variation of the estimated prestress losses, and CoV_v is the coefficient of variation of the 10^4 input variables. High values of S_{Pv} indicate high variation in prestress loss due to variation in the input parameter. The resulting prestress loss values from the Monte Carlo simulations for each input parameter are shown in Fig. 65. In addition to the histograms of the prestress losses, the statistics and the sensitivity coefficient are also reported.

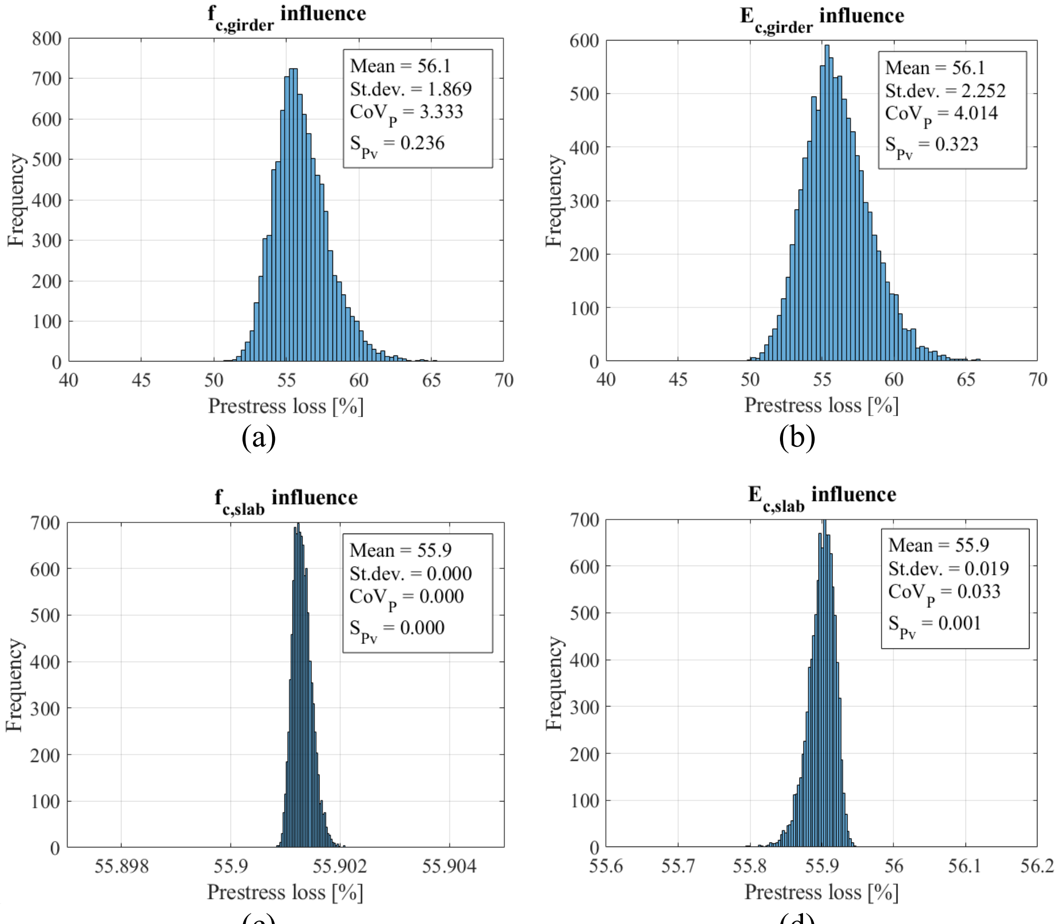

(a) (b)

(c) (d)

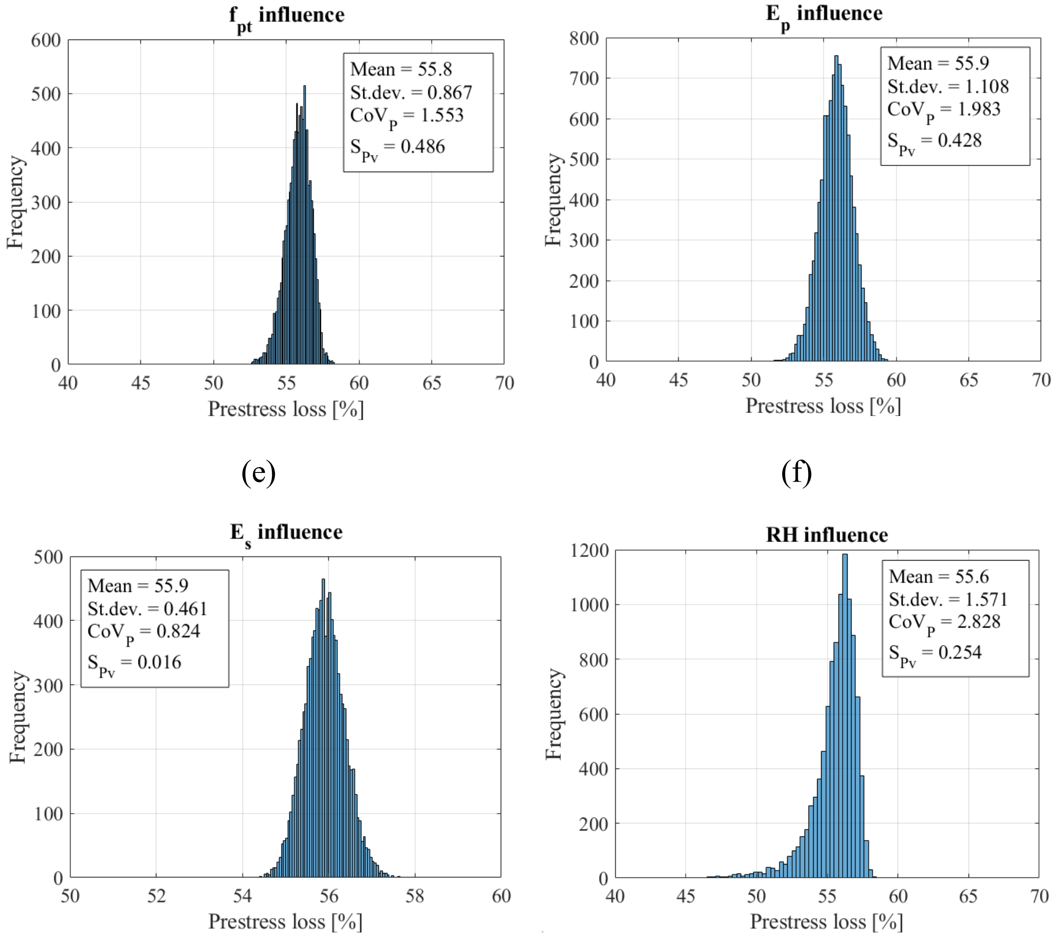

(e) (f)

(g) (h)

Figure 65: Prestress loss histogram of the Monte Carlo simulation computed for the probability distribution function of: (a) girder concrete compressive strength, (b) girder concrete modulus of elasticity, (c) slab concrete compressive strength, (d) slab concrete modulus of elasticity, (e) strand tensile strength, (f) strand modulus of elasticity, (g) rebar modulus of elasticity, and (h) relative humidity.

As can be seen from Fig. 65, the parameters that actually have the greatest influence on the prestress loss of PC elements are the mechanical properties of the concrete girder, the tensile strength of the strand, the modulus of elasticity of the strand, and the relative humidity. For these parameters, the coefficient of variation of the prestress loss takes values between 1.6% and 4.0%. Of all the parameters, the modulus of elasticity and tensile strength of the strand were found to have the greatest influence on the prediction of prestress loss compared to the other parameters. A similar influence was found for the relative humidity and the compressive strength of the concrete girder, which affect both concrete shrinkage and creep. The remaining parameters gave a coefficient of variation for prestress loss of less than unity, and consequently a very low coefficient of sensitivity. Therefore, the influence of these variables is negligible, and they have been considered as deterministic in the next analysis with their mean values.

Based on the results of the sensitivity analyses, the numerical analysis of the prestress loss was carried out simultaneously considering the most influential parameters with their distribution model and the time of deck casting with a uniform distribution between 30 and 180 days. The simulations were carried out using the Monte Carlo method for 10^4 sets of variables generated randomly according to the corresponding probability distribution function. The histogram of prestress loss obtained for all sets of variables and the distribution fit are shown in Fig. 66.

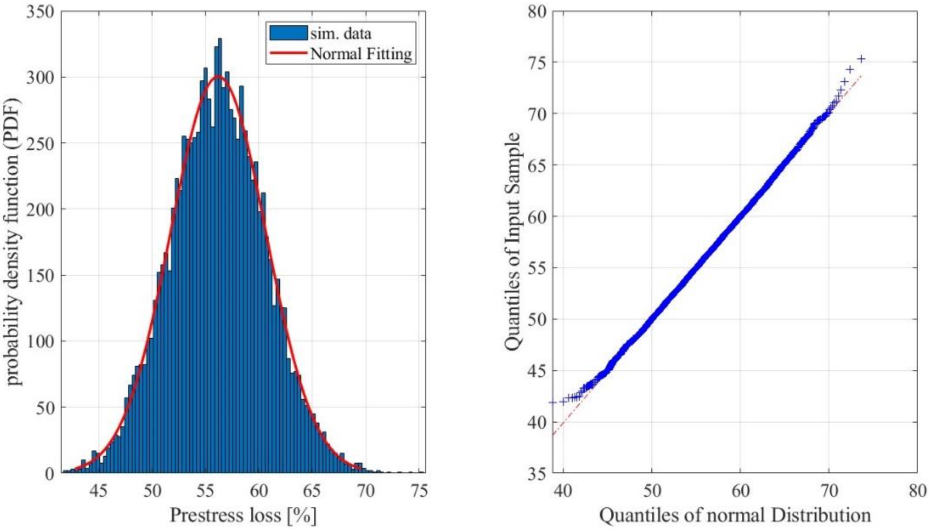

Figure 66: Probability density function for predicted prestress loss.

According to the Lilliefors test, the response obtained for prestress loss can be modelled by a normal distribution with a mean of 56.2% and a standard deviation of 4.48%. The distribution shown can be considered as representative of a range of PC girders with similar mechanical and geometric characteristics, which are widely distributed in the current infrastructure network.

From the comparison between the predicted mean value of the stochastic analysis and the experimental values measured by cracking load, decompression load, and saw-cut method, a good agreement was found. A slight overestimation was found for the strand-cutting method results, as this test provides a measure of prestress loss related to a single strand rather than the total prestressing force. However, all measured prestress losses were within the 95% confidence interval, having lower bound and upper bound of 48.8% and 63.6%, respectively. Considering the mean value of prestress loss measured by the strand-cutting method, the upper bound was 3.9% greater than the experimental value. On the other hand, considering the mean value of prestress loss measured with the decompression load method, which gave the lower value, the lower bound resulted 8.9% lower than the experimental value. It is noteworthy that the prestress loss predicted in the original design greatly underestimated the actual value, thus highlighting the adoption of an inadequate model for predicting long-term prestress loss.

Therefore, in practical engineering calculations, it is recommended to estimate the long-term prestress loss with a reasonable level of confidence and to select the upper bound of the confidence interval as the most unfavourable value of the long-term prestress loss from the perspective of ensuring serviceability.

References

[1] European Committee for Standardization (CEN). (2004). Eurocode 2: Design of concrete structures—Part 1–1: General rules and rules for buildings (EN 1992-1-1). Brussels: CEN.

[2] American Association of State Highway and Transportation Officials (AASHTO). (2020). AASHTO LRFD bridge design specifications (9th ed.). Washington, D.C.: AASHTO.

[3] ACI Committee 318. (2019). Building code requirements for structural concrete (ACI 318–19). Farmington Hills: American Concrete Institute (ACI).

[4] Shenoy, C.V.; Frantz, G.C. (1991). Structural Tests of 27-Year-Old Prestressed Concrete Bridge Beams. PCI Journal.

[5] Azizinamini, A.; Keeler, B.J.; Rohde, J.; Mehrabi, A.B. (1996). Application of a New Nondestructive Evaluation Technique to a 25-Year-Old Prestressed Concrete Girder. PCI Journal.

[6] Halsey, J.T.; Miller, R. (1996). Destructive Testing of Two Forty-Year-Old Prestressed Concrete Bridge Beams. PCI Journal.

[7] Pessiki, S.; Kaczinski, M.; Wescott, H.H. (1996). Evaluation of Effective Prestress Force in 28-Year-Old Prestressed Concrete Bridge Beams. PCI Journal.

[8] Labia, Y.; Saiidi, M.S.; Douglas, B. (1997). Full-Scale Testing and Analysis of 20-Year-Old Pretensioned Concrete Box Girders. ACI Structural Journal, 94-S43.

[9] Tadros, M.K., Al-Omaishi, N., Seguirant, S.J., and Gallt, J.G., (2003). "Prestress Losses in pretensioned high-strength concrete bridge girders." NCHRP Report 496, National Cooperative Highway Research Program, Transportation Research Board, National Research Council.

[10] Kukay, B.; Barr, P.J.; Halling, M.W. (2007). A comparison of time dependent prestress losses in a two-span, prestressed concrete bridge. Structure Congress: New Horizons and Better Practices, May 16-19, California, United States.

[11] Kukay, B.; Barr, P.J.; Halling, M.W.; Womack, K. (2010). Determination of the Residual Prestress Force of In-Service Girders using Non-Destructive Testing. Structure Congress, May 12-15, Florida, United States.

[12] Osborn, G.P.; Barr, P.J.; Petty, D.A.; Halling, M.W.; Brackus, T.R. (2012). Residual Prestress Forces and Shear Capacity of Salvaged Prestressed Concrete Bridge Girders. Journal of bridge engineering, 17(2): 302-309.

[13] Caro, L.A.; Martì-Vargas, J.R.; Serna, P. (2013). Prestress losses evaluation in prestressed concrete prismatic specimens. Engineering Structures, 48, 704-715.

[14] Garber, D.B.; Gallardo, J.M.; Deschenes, D.J.; Bayrak, O. (2015). Experimental Investigation of Prestress Losses in Full-Scale Bridge Girders. ACI Structural Journal, 112-S45.

[15] Garber, D.B.; Gallardo, J.M.; Deschenes, D.J.; Bayrak, O. (2016). Prestress Loss Database for Pretensioned Concrete Members. ACI Structural Journal, 113-S28.

[16] Guo, T.; Chen, Z.; Lu, S.; Yao, R. (2018). Monitoring and analysis of long-term prestress losses in post-tensioned concrete beams. Measurement, 122, 573-581.

[17] Ye, C.; Butler, L.J.; Elshafie, M.Z.E.B.; Middleton, C.R. (2020). Evaluating prestress losses in a prestressed concrete girder railway bridge using distributed and discrete fibre optic sensors. Construction and Building Materials, 247.

[18] Civjan, S.A.; Jirsa, J.O.; Carrasquillo, R.L.; Fowler, D.W. (1998). Instrument to Evaluate Remaining Prestress in Damaged Prestressed Concrete Bridge Girders. PCI Journal.

[19] Owens, A. (1993). In-situ stress determination used in structural assessment of concrete structures. Strain, 29(4), 115-124.

[20] Kesavan, K.; Ravisankar, K.; Parivallal, S.; Sreeshylam, P. (2005). Technique to assess the residual prestress in prestressed concrete members. Experimental Techniques, 29, 33-38.

[21] Zhong, B.; Zhu, J.; Morcous, G. (2020). Development of an NDT tool for in-situ assessment of prestress loss. Report SPR-P1(17) M074. Nebraska, Lincoln.

[22] Kerr, A. D. (1976). On the dynamic response of a prestressed beam. Journal of Sound and Vibration, 49(4), 569–573.

[23] Hop, T. (1991). The effect of degree of prestressing and age of concrete beams on frequency and damping of their free vibration. Materials and structures, 24(3), 210–220.

[24] Saiidi, M., Douglas, B., & Feng, S. (1994). Prestress force effect on vibration frequency of concrete bridges. Journal of Structural Engineering (United States), 120(7), 2233–2241.

[25] Breccolotti, M. (2018). On the Evaluation of Prestress Loss in PRC Beams by Means of Dynamic Techniques. International Journal of Concrete Structures and Materials, 12(1).

[26] Chen, Z.; Zhang, S. (2018). EM-Based Monitoring and Probabilistic Analysis of Prestress Loss of Bonded Tendons in PSC Beams. Advances in Civil Engineering.

[27] Baran, E.; Shield, C.K.; French, C. (2005). A comparison of Methods for Experimentally Determining Prestress Losses in Pretensioned Prestress Concrete Girders. In book: Special Publication on Historic Innovations in Prestressed Concrete: SP-231 (pp. 161-180). Publisher: ACI. Editors: Bruce Russell, Shawn Gross.

[28] Bymaster, J.C.; Dang, C.N.; Floyd, R.W.; Hale, W.M. (2015). Prestress losses in pretensioned concrete beams cast with lightweight self-consolidating concrete. Structures, 2, 50-57.

[29] Webb, G.T.; Vardanega, P.J.; Hoult, N.A.; Fidler, P.R.A.; Bennett, P.J.; Middleton, C.R. (2017). Analysis of Fiber-Optic Strain-Monitoring Data from a Prestressed Concrete Bridge. Journal of Bridge Engineering, 22(5).

[30] Jaber, H.A.; Glisic, B. (2017). Monitoring of prestress losses using long-gauge fiber optic sensors. Proc. SPIE 10170, Health Monitoring of Structural and Biological Systems 2017, 101702P, April 05.

[31] Kim, S.T.; Park, Y.S.; Yoo, C.H.; Shin, S.; Park, Y.H. (2021). Analysis of Long-Term Prestress Loss in Prestressed Concrete (PC) Structures Using Fiber Bragg Grating (FBG) Sensor-Embedded PC Strands. Applied Sciences, 11.

[32] Kim, S.H.; Park, S.Y.; Kim, S.T.; Jeon, S.J. (2022). Analysis of Short-Term Prestress Losses in Post-tensioned Structures Using Smart Strands. International Journal of Concrete Structures and Materials, 16:1.

[33] Bonopera, M.; Chang, K.C. (2021). Novel method for identifying residual prestress force in simply supported concrete girder-bridges. Advances in Structural Engineering, 24(14), 3238-3251.

[34] Kukay, B.M. (2008) Bridge instrumentation and the development of non-destructive and destructive techniques used to estimate residual tendon stress in prestressed girders. PhD thesis, Utah state university, Logan, Utah.

[35] Bagge, N.; Nilimaa, J.; Elfgren, L. (2017). In-situ methods to determine residual prestress forces in concrete bridges. Engineering Structures, 135, 41-52.

[36] Kralovanec, J.; Bahleda, F.; Moravcik, M. (2022) State of Prestressing Analysis of 62-Year-Old. Materials, 15.

[37] Garber, D.; Gallardo, J.; Deschenes, D.; Dunkman, D.; Bayrak, O. (2013). Effect of New Prestress Loss Estimates on Pretensioned Concrete Bridge

Girder Design. Technical Report FHWA/TX-12/0-6374-2, Austin, TX, USA: Texas Department of Transportation Research.

[38] Bazant, Z. (1972). Prediction of Concrete Creep Effects Using Age-Adjusted Effective Modulus Method. *Journal of the American Concrete Institute*, 212-217.

[39] Magura, D.D.; Sozen, M. A.; Siess, C.P. (1964). A Study of Stress Relaxation in Prestressing Reinforcment. *PCI Journal*, 13-57.

Chapter 5

Structural assessment

5.1 Introduction

The assessment of existing bridge structures is the most important component of the Bridge Management System framework. This is due to the provision of basic data on the actual condition of the bridge stock and its true behavior, which is essential for the decision-making process associated with the optimal strategy for bridge maintenance and rehabilitation. As a consequence, the bridge assessment process should include not only periodic inspections based on visual assessment of the bridge condition but also a comprehensive analysis of its reliability over the remaining lifetime, supported by testing and monitoring. Bridge assessment has become of paramount importance in recent years due to the increasing number of bridges in need of repair. The majority of these structures are exceeding their design life and are constantly exposed to increasingly severe events. For these reasons, there has been great interest in the development of approaches that can rapidly verify the safety conditions of the transportation network and perform a comprehensive classification of the entire bridge stock. In this context, a document entitled “Guidelines for risk classification, safety assessment and structural health monitoring of existing bridges” has recently been approved in Italy [1]. The primary objective of this document is to define the technical principles for the management of existing bridges. The present guidelines comply with the structural analysis provisions of the Italian Construction Code (NTC) [2] and are based on a multi-level approach coupled with a simplified risk analysis to establish an overall bridge attention class. On the basis of the attention class, a more or less accurate safety check is required. However, unlike the design of new structures, where conservative assumptions can be made with little additional costs, the assessment of existing bridges can have significant financial implications if a structure is classified as deficient with unnecessarily conservative measures. Thus, detailed approaches are required to provide a less conservative but reliable assessment of existing bridges.

The present work addressed this research topic and consisted of a multi-level assessment approach from deterministic numerical analyses to probabilistic analyses integrated by field test results and statistical uncertainty. At the first level of assessment, the resources provided by the original design, assumed as resistance, were compared with the loading effects resulting from the structural analysis, according to the current code provisions. At the enhanced levels, a theoretical model was developed to predict the actual bending capacity of the structural members, validated by comparing the analytical results with the load-deflection behavior of the full-scale tests in a deterministic approach. Finally, the structural model was integrated with a probabilistic analysis to verify whether the bearing capacity meets the current load requirements with a reliability analysis. The reliability of the structure was then estimated in terms of a reliability index (or failure probability) defined by taking into account the uncertainty associated with the material properties and the capacity model. The probabilistic assessment allows not only to model the different sources of uncertainty in a consistent way, but also to define, through a sensitivity analysis, which parameters need to be investigated in depth with further data collection. In this way, a targeted diagnostic campaign could be planned to characterize specific quantities, with a consequent reduction of uncertainty. In general, a structure may have several failure modes, geometries, structural elements, and degradation mechanisms that need to be considered in the structural analysis for the estimation of the reliability index. In the present analysis, all elements were assumed to be equivalent to the PC girders detailed in this thesis and therefore the reliability analysis was limited to the flexural capacity of the deck superstructure. In addition, for more accurate traffic load models, the actual traffic probability distribution calibrated on weigh-in-motion systems outcomes should be considered. Modelling bridge loads presents significant complexities owing to the necessity for site-specific long-term data, which is frequently inaccessible, and the requirement to forecast future loads. Therefore, in the present study, the required demand has been considered assuming prior probabilistic models.

5.2 Structural analysis

In the structural analysis of bridge decks, the estimation of live load effects is a three-dimensional problem involving the complex behavior of load paths between the slab, transverse diaphragms, and longitudinal beams. It is a spatial structure, usually schematized as a planar system of parallel and orthogonal beams (Fig. 67).

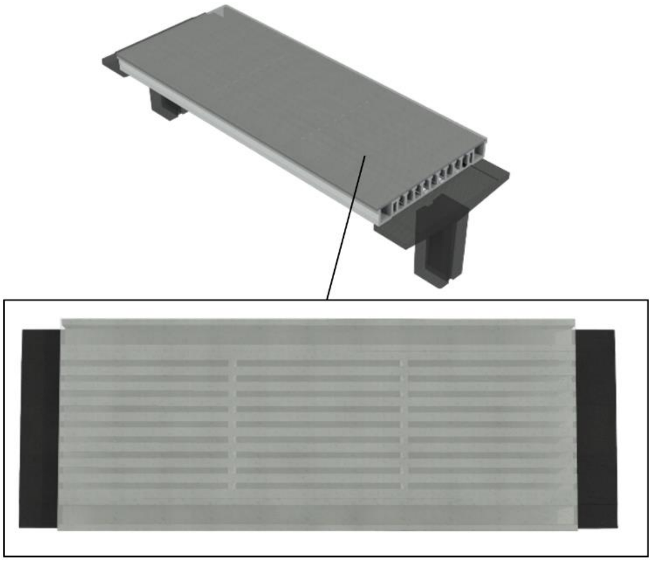

Figure 67: Schematic representation of the bridge deck.

In composite concrete deck beams, the transverse diaphragms and the top slab are essential for the live load distribution between adjacent beams. Depending on the relationship between the flexural stiffness of the transverse system and the torsional stiffness of the longitudinal beam, different limit cases can occur (Fig. 68).

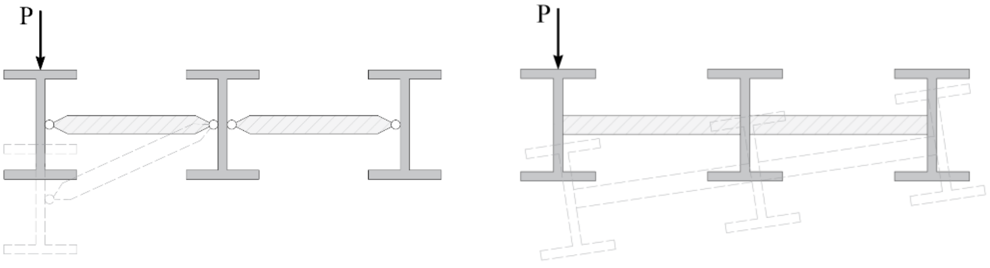

(a) (b)

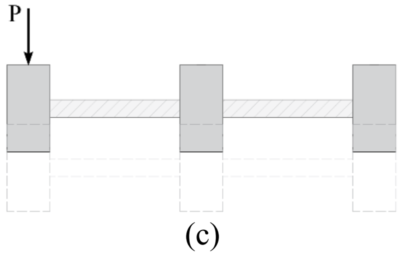

Figure 68: Relationships between the stiffness of longitudinal beams and transverse system: (a) transverse system without bending stiffness, (b) transverse system with infinite bending stiffness, and (c) longitudinal beams with infinite torsional stiffness.

In case of negligible bending stiffness of the transverse system, the entire load *P* is carried by the beam to which it is applied (Fig. 68a). In the case of infinite bending stiffness in transverse direction and negligible torsional stiffness for the longitudinal beams, the load is distributed linearly in the transverse direction according to the eccentricity of the beams in the deck (Fig. 68b). If the torsional stiffness of the longitudinal beams is also assumed to be infinite, the rotation of the deck is restrained, and the load is equally distributed between them (Fig. 68c).

5.2.1 Load distribution methods

To calculate the effects of load distribution on bridge girders, various load distribution methods with different degrees of approximation to the real behavior are used. Under the assumption of infinite bending stiffness and null torsional stiffness for the transverse system, a classic method is that of infinite transverse beams with infinite bending stiffness, commonly named the Courbon method. In this method, a general load *P* is distributed in transverse direction by solving the static scheme of a transverse beam assumed to be equivalent to a continuous beam on elastic bearings (Fig. 69).

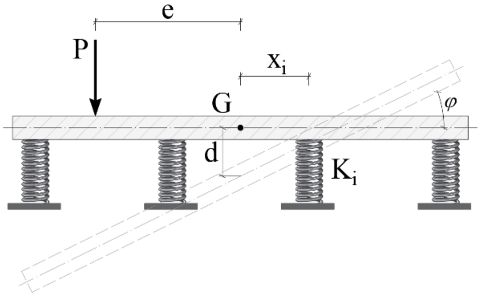

Figure 69: Schematization of the transverse behavior according to the Courbon assumption.

Consequently, the corresponding reactions in each spring are proportional to the displacement according to the relative stiffness. Considering K_i, the stiffness of the ith spring, the reaction r_i can be defined by:

$$r_i = K_i(d + \varphi x_i) \tag{70}$$

where d is the displacement of the transverse beam at the rotation center, φ is the rotation angle of the transverse beam, and x_i is the distance of the ith spring from the centre of spring stiffness G. The deformed configuration can then be determined by imposing the equilibrium to the rotation and in the vertical direction. The force resulting in the general spring is equivalent to the percentage of load P acting on the i beam, and is expressed by:

$$r_i = \frac{K_i}{\sum_{i=1}^{n} K_i} + \frac{K_i e x_i}{\sum_{i=1}^{n} K_i x_i^2} \tag{71}$$

where e is the eccentricity of the load P assumed to be equal to one. In the common case of constant spring stiffness, the distribution coefficients ρ_{ie} can be defined as a function of the number of beams n, and geometric quantities according to:

$$\rho_{ie} = \frac{1}{n} + e\frac{x_i}{\sum_{i=1}^{n} x_i^2} \tag{72}$$

Based on the above assumptions, the calculations are transformed from the girder scheme to that of multiple parallel beams, depending on the geometry and loading point.

In order to remove the Courbon assumption of infinite transverse beams with infinite bending stiffness and to take into account the actual number of transverse elements, another method widely used in the literature is the Engesser method. The present approach entails the implementation of a superimposition of effects between the scheme of continuous beams with auxiliary supports and a free scheme with nodal forces equivalent to the reaction forces of the first scheme. Thus, the nodal forces can be distributed without assuming infinite transverse beams. The problem is then reconducted to solve the scheme of a continuous beam and to distribute the nodal reaction with repartition coefficients according to Eq. 72. However, both methods do not take into account the real stiffness of the bridge deck members, considering the transverse system with infinite bending stiffness and the longitudinal beams with negligible torsional stiffness.

In the present work, the numerical methods introduced above have been compared with a detailed analysis, taking into account the actual bending and torsional contributions of all structural members under traffic loads. The numerical analysis was based on the well-established "displacements method", by imposing kinematically compatible displacements and solving the nodal equilibrium. In this approach, the bridge deck was idealized as equivalent to a system of longitudinal members representing the composite sections of precast beams and associated slab, and transverse members representing the composite section of diaphragms and associated slab. The load distribution problem was then reconducted to the plane grid analysis, with each member placed coincident with its respective axis. A general layout of the numerical elements employed in the analyses is shown in Fig. 70.

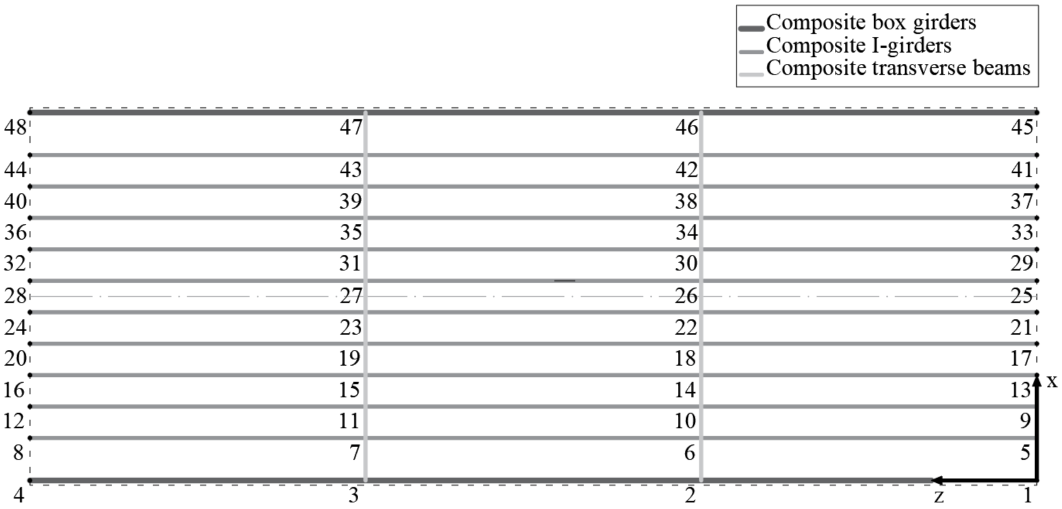

Figure 70: Plane grid layout.

The kinematic parameters that define the deformed configurations include the rotations relative to the *x* and *z* axes, as well as the displacement orthogonal to the plane, along the *y* axis. The bridge deck was then modelled using three different beam elements, each characterized by a proper stiffness matrix obtained by imposing the three generalised displacements at each node according to the local coordinate systems. Considering M, T, and M_t, as representing internal actions, and φ, v, and θ, as denoting rotation about the *x* axis, vertical displacement, and rotation about the *z* axis respectively, the following relationship can be written:

$$\begin{bmatrix} M_i \\ T_i \\ M_{t,i} \\ M_j \\ T_j \\ M_{t,j} \end{bmatrix} = \begin{bmatrix} \frac{4EI_x}{L} & -\frac{6EI_x}{L^2} & 0 & \frac{2EI_x}{L} & \frac{6EI_x}{L^2} & 0 \\ -\frac{6EI_x}{L^2} & \frac{12EI_x}{L^3} & 0 & -\frac{6EI_x}{L^2} & -\frac{12EI_x}{L^3} & 0 \\ 0 & 0 & \frac{GI_z}{L} & 0 & 0 & -\frac{GI_z}{L} \\ \frac{2EI_x}{L} & -\frac{6EI_x}{L^2} & 0 & \frac{4EI_x}{L} & \frac{6EI_x}{L^2} & 0 \\ \frac{6EI_x}{L^2} & -\frac{12EI_x}{L^3} & 0 & \frac{6EI_x}{L^2} & \frac{12EI_x}{L^3} & 0 \\ 0 & 0 & -\frac{GI_z}{L} & 0 & 0 & \frac{GI_z}{L} \end{bmatrix} \cdot \begin{bmatrix} \varphi_i \\ v_i \\ \theta_i \\ \varphi_j \\ v_j \\ \theta_j \end{bmatrix} \qquad (73)$$

where the local stiffness matrix is computed taking into account the length L of the element, the contributions of the bending stiffness EI_x and the torsional stiffness GI_z related to the transformed section properties of the composite beams. The length of the slab for the T-shaped cross sections of the transverse diaphragms was related to the distribution of the traffic load at an angle of 45° to the middle plane of the slab, according to:

$$B = b_0 + 2s_1 + s + \frac{l_x}{2} \qquad (74)$$

where b_0 is the length of the wheel contact surface, s_1 is the thickness of the pavement, s is the thickness of the slab, and l_x is the distance between the I-girders. The matrix relationship of Eq. 73 can be rewritten in the general form as:

$$\{S_e^*\} = [K_e]\{\delta_e^*\} \qquad (75)$$

where the subscript e denotes the generic element, and the superscript * denotes the local coordinates. In each node, the internal action must balance the applied actions according to:

$$\{S_e^*\} + \{f_e^*\} = [K_e]\{\delta_e^*\} \qquad (76)$$

where $\{f_e^*\}$ is the vector of nodal forces equivalent to the applied load. Before assembling the matrices of the whole system in the nodes where they converge, each vector must be transformed with respect to the global reference system. Equation 76 can therefore be rewritten in terms of the global coordinate system according to:

$$\{S_e\} + \{f_e\} = ([T]^T[K_e][T])\{\delta_e\} \tag{77}$$

where $[T]$ is the transformation matrix. To solve the whole structure, it is necessary to define for each node the equality of the kinematic variables of elements with the same node, and the equilibrium of the statics variables. This is done by expanding the vectors from the local dimension *6x1* to the global dimension *nx6*, where *n* is the total number of kinematic parameters defining the deformed configuration of the grid system. To this end, the assembling matrix $[A_e]^T$ has been defined, which is able to move the nodal parameters of each element to the corresponding node of competence. By multiplying each vector with the assembling matrix, Eq. 77 can be rewritten with the expanded form as:

$$\{S^e\} + \{f^e\} = ([A_e]^T[T]^T[K_e][T][A_e])\{\delta^e\} \tag{78}$$

The assembling operation is completed by summing the contribution given by each element in Eq. 78:

$$\sum_e(\{S^e\} + \{f^e\}) = \left(\sum_e[K^e]\right)\{\delta\} \tag{79}$$

where $[K^e]$ is the stiffness matrix of each element with respect to the global coordinate system, expanded to the n-dimension. Finally, the solver equation can be written as:

$$\{F\} = [K]\{\delta\} \tag{80}$$

where $\{F\}$ is the vector of nodal forces, $[K]$ is the global stiffness matrix, and $\{\delta\}$ is the global vector of the nodal displacements. The unknowns of the problem, represented by the vector of free displacements, can be determined by introducing constraint conditions. Equation 80 can then be partitioned in terms of free and constrained displacements, as:

$$\begin{bmatrix} K_{11} & K_{12} \\ K_{21} & K_{22} \end{bmatrix}\begin{bmatrix} \delta_1 \\ \delta_2 \end{bmatrix} = \begin{bmatrix} F_1 \\ F_2 \end{bmatrix} \tag{81}$$

where δ_1 refers to the unknown free displacements and δ_2 refers to the restrained displacements. Since the fixed displacements are zero, the free displacements can be obtained by:

$$\{\delta_1\} = [K_{11}]^{-1}\{F_1\} \tag{82}$$

Once all the kinematic parameters have been defined, the internal actions can be determined accordingly:

$$\{S\} = [K_{21}][K_{11}]^{-1}\{F_1\} - \{F_2\} \tag{83}$$

The main advantage of the plane grid analysis is that the internal forces are obtained directly without the need for stress integration as in classical FEM analysis. The parameters of the beams and transverse members were based on uncracked section and elastic behaviour. The procedure was implemented in a MATLAB script and resulted in a good alternative to the other simplified bridge deck analysis methods, allowing the distribution of traffic load in accordance with the stiffness, geometry and boundary conditions of the bridge deck.

5.2.2 Load analysis results

The traffic load distribution was obtained by positioning the traffic load models on the bridge deck to obtain the maximum value of the bending moment in the midspan section of the outer beams. For this purpose, two notional lanes of 3.0 m width were defined on the deck, bounded between the vehicle restraint systems. Figure 71 shows the loading scheme used in accordance with the NTC requirements. The Italian code defines six loading models according to the type of verification. In the case of the global verify, two types of traffic loads are prescribed using a set of concentrated loads and distributed loads according to the load model 1. The first load is composed of a tandem concentrated load with a total weight of 300 kN for each axle (F_{1k} = 150 kN), and a distributed load (q_{1k}) of 9 kN/m^2. The second lane is loaded by a tandem with a total weight of 200 kN for each axle (F_{2k} = 100 kN), and a distributed load (q_{2k}) of 3.5 kN/m^2.

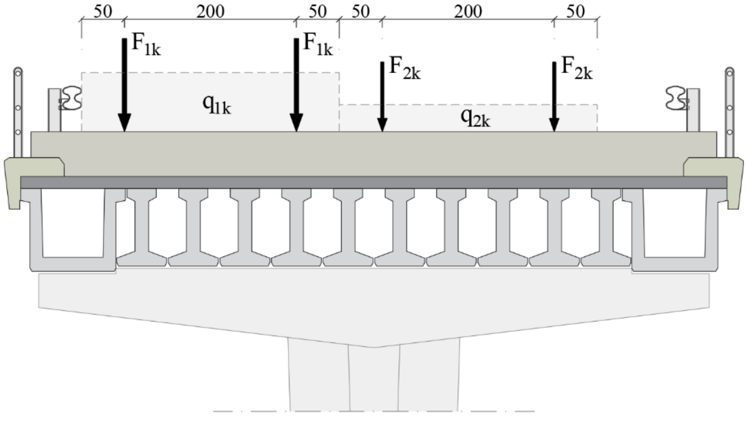

Figure 71: Transverse arrangement of load model 1 prescribed by NTC (unit: cm).

The permanent loads of the bridge were determined on the basis of the deck geometry and the characteristic densities of the construction materials. The values of the permanent loads considered in the assessment are outlined below:

- Self-weight of the I-girder – 5.00 kN/m;
- Self-weight of the box girder – 9.45 kN/m;
- Self-weight of the slab – 3.03 kN/m^2;
- Transverse diaphragm – 2.06 kN;
- Pavement – 1 kN/m^2;
- Kerb – 5.05 kN/m;
- Vehicle restraint system (VRS) – 0.49 kN/m;
- Parapet - 0.49 kN/m;

The transverse diaphragms were assumed as concentrated forces at third points, according to the deck girder layout.

The maximum bending moment in the box girder and in the I-girder due to permanent loads was 662.0 kNm and 355.1 kNm, respectively. These values were obtained without taking into account the kerb, VRS, and parapet loads, as these were distributed according to the load distribution methods. The results of the loads distribution for the outer and inner girders are shown in Table 21. As the stiffness of box girders was approximately twice that of I-girders, in the simplified methods these were assumed equivalent to double I-girders.

Table 21: Bending moments at midspan for box and I-girder based on Courbon, Engesser, and plane grid analysis (unit: kNm).

Load	**Box girder**			**I-girder**		
	Courbon	**Engesser**	**Grid analysis**	**Courbon**	**Engesser**	**Grid analysis**
Kerb	66.49	70.18	80.09	33.24	32.50	29.61
VRS + Parapet	12.92	13.63	15.56	6.46	6.31	5.75
$\mathbf{q_{1k}}$	385.55	376.99	276.61	166.80	163.09	99.76

q_{2k}	15.95	15.60	34.93	12.15	11.88	22.03
Tandem_1	836.70	743.09	546.05	361.98	483.73	470.13
Tandem_2	83.08	67.63	155.87	63.30	51.53	89.83

The results in Table 21 show slight differences between the three numerical medels. In particular, for the effect on the box girder due to the more eccentric traffic load models (subscript 1), an overestimation of the simplified approaches can be seen, compared to the plane grid analysis. On the other hand, in the case of traffic load models applied far from the box girders (subscript 2), the simplified approaches underestimate the actual bending moments. This phenomenon could be explained whit the assumption of a linear load distribution, as in the simplified approaches, resulted in a uniform distribution of the load between the girders when applied far from the outer girders. However, since in this case the load is resisted by the outer box girders due to their high torsional stiffness, this resulted in a higher level of bending moment. When the load is applied close to the box girders, these differences are limited as the resistance mechanism is mainly determined by the bending contribution.

5.3 Moment-curvature analysis

The moment-curvature method was used to predict the flexural behavior of the PC girders, taking into account the material non-linearities. The selection of the analytical model used to estimate the structural response was determined by the requirement for accuracy and simplicity, which are essential attributes for an operational tool to be widely implemented for the assessment of existing structures. The computer code was integrated with the prestressing loss prediction script to determine the moment-curvature diagram, and the prediction of the load-deflection response. It was designed to analyze the structural response of the I-girder alone or consider the contribution of the top slab to the composite section. Therefore, the following assumptions were established: perfect bond at the concrete-steel interface, plane section remaining plane after loading, composite behavior between the top slab and the I-girder, concrete softening branch and shear deformation neglected. The structural model of the PC girder was based on a layered discretization of the section and by defining the strain and stress at each layer according to the compatibility condition and constitutive relationships, as shown in Fig. 72.

According to the linear strain distribution over the section, the concrete strain at the ith layer can be expressed as:

$$\varepsilon_{ci} = \lambda + \mu \cdot y_i \tag{84}$$

where λ is the strain at the centroid of the section, μ is the curvature, and y_i is the location of the ith layer. The strain at the prestressing strands and steel reinforcement levels is determined according to the strain compatibility, also taking into account the long-term impressed strains. For a given curvature, the value of λ was determined by an iterative procedure aimed to satisfying the equilibrium of the horizontal forces:

$$\sum N = C_c - T_c - T_p \pm T_s = 0 \tag{85}$$

where C_c and T_c are the resultant concrete forces in compression and tension respectively, T_p is the resultant tension in the prestressing strands, and T_s is the resultant force in the steel reinforcement having the sign according to the strain compatibility. For simplicity, the resultant forces in the steel reinforcement have been omitted from Fig. 72.

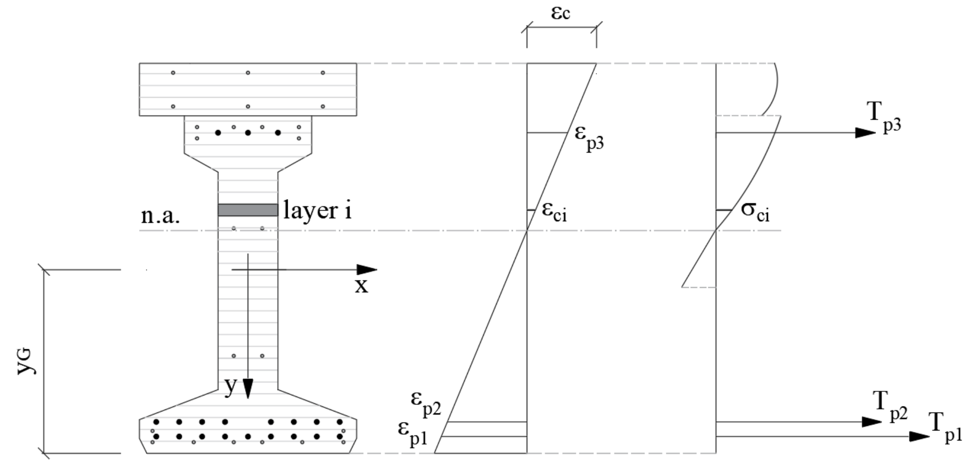

Figure 72: Layered section analysis.

Once the equilibrium stage is satisfied, the corresponding moment of resultant forces can be calculated for each deformed configuration:

$$M = \sum_{i=1}^{n} C_{ci} \left(y_G - y_i\right) + \sum_{l=1}^{m} T_{ci} \left(y_G - y_l\right) + \sum_{j=1}^{3} T_{pj} \left(y_G - y_{pj}\right) + \sum_{k=1}^{8} T_{sk} \left(y_G - y_{sk}\right) \quad (86)$$

where C_{ci} is the concrete compressive force at the centroid of the i^th^ layer with location y_i, T_{ci} is the concrete compressive force at the centroid of the l^th^ layer with location y_l, T_{pj} is the tensile force at the j^th^ level with location y_{pj}, and T_{sk} is the tensile force in the steel reinforcement at location y_{sk}.

The first stage of the resistance analysis was to calculate the moment-curvature relationship at discrete points along the beams. The midspan deflection due to an applied load can then be determined by the classical moment area method by integrating the corresponding curvatures along its half-length and summing the increment of tangential offsets given by the rotation of the segments used to discretize the beam [3].

For a reliable prediction of the structural behavior of existing structures, accurate modeling of the material properties is required. To this end, the mechanical properties based on measurements from laboratory tests were detailed in the section models. The stress-strain diagrams were related to the average measured properties and then considered as deterministic. Such an approximation is more plausible for the mechanical properties of the reinforcing steel, which generally have a lower scatter compared to the parameters describing the concrete. However, the aim of this section was to determine the reliability of the simplified model in detecting both the occurrence of cracking and the ultimate load of the girders. It was not intended to predict the structural behavior of each individual girder with its own properties. A summary of the parameters used to model the average stress-strain diagrams is given in Table 22.

Table 22: Mean values of the mechanical properties used in the models.

Properties	Value	Unit
$f_{cm,girder}$	31.5	MPa
$E_{cm,girder}$	22894.6	MPa

$f_{ctm,girder}$	3.5	MPa
$f_{cm,slab}$	27.4	MPa
$E_{cm,slab}$	18892.1	MPa
f_{p01k}	1542.4	MPa
f_{pt}	1786.9	MPa
E_p	201.1	GPa
ε_{pu}	30.8	‰
f_{ys}	449.0	MPa
f_{ts}	685.1	MPa
E_s	201.1	GPa
ε_{su}	109.8	%

The constitutive model for concrete in compression was established by calibrating the Sargin curve [4] to match the average stress-strain relationship derived from uniaxial compression tests on concrete cylinders. To describe the tensile behavior of concrete up to the tensile strength, a linear elastic stress-strain relationship was employed. The steel reinforcement, including both longitudinal reinforcing bars and the prestressed reinforcement, was characterized using an elastic hardening relationship based on the average values presented in Table 22.

Figure 73 shows a comparison between the numerical load-midspan deflection responses and the measured responses of the girders tested in the three-point bending test configuration. For the clarity of diagrams, the unloading and reloading branches have been removed from the experimental curves and the branches resulting from multiple loading steps have been combined into monotonic curves.

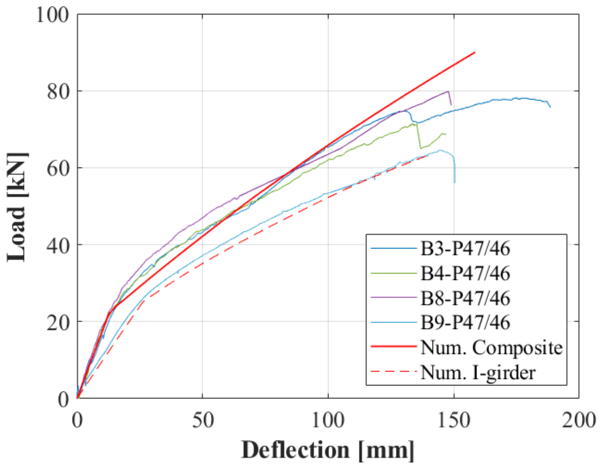

Figure 73: Numerical and experimental load-midspan deflection curves of the three-point bending tests.

Overall, a good correlation was observed between the load-deflection behavior of the B9-P47/46 I-girder and the analytical results throughout the loading test. As the elastic stiffness of the girder is strongly influenced by the elastic modulus of the concrete, this result shows that its constitutive law is effectively represented by the average values. This can be attributed to the greater care taken in the casting process employed for the PC girders, resulting in lower variability of the elastic modulus compared to the cast-in-place slab. Moreover, the comparison between the analytical and measured cracking load reveals a good estimation of the residual stress in the prestressing strands. Good agreement in predicting the structural behavior in the elastic phase was also found for the other girders. In both cases, the ultimate load was achieved by crushing the compression concrete with prestressing strands in the elastic phase. In terms of ultimate capacity, an overestimation of 11% was observed for the composite girders, corresponding to an estimated bending moment of 1656.0 kNm. For the actual value of the bending resistance, the dead load and the weight of the loading system must be taken into account. As the failure mechanism was governed by the top slab concrete, such a discrepancy between the numerical and experimental curves can be justified by its higher variability.

Figure 74 shows the comparisons between the numerical and analytical load-midspan deflection curves of the girders tested in four-point bending configurations. Since the aim of this section was to verify the effectiveness of the resistance model to be used in the reliability assessment of the bridge deck, only the girders in the actual conservation state were considered, and not those affected by artificially induced damage.

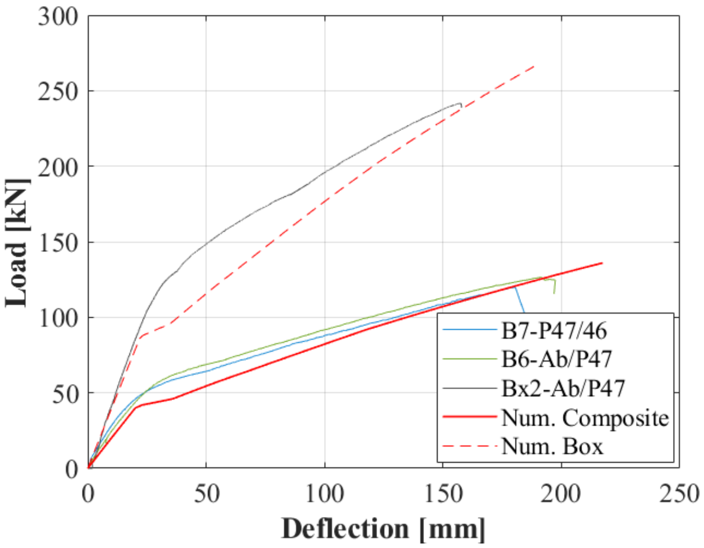

Figure 74: Numerical and experimental load-midspan deflection curves of the four-point bending tests.

According to the observations made for the three-point bending test results, the model showed a good ability to predict the structural behavior up to the cracking load. A weakness of the numerical model is observed in the prediction of the non-linear behavior in the post-cracking phase. This phenomenon could be related to the simplification of disregarding the positive contribution of the tension stiffening of the concrete to the resistance. Such underestimation was more accentuated in the four-point bending configuration as the areas affected by constant bending moment and subjected to cracking resulted higher than the three-point bending test configuration. However, at the ultimate load, the resistance is mainly provided by the compressed concrete and the discrepancy between the numerical and experimental curves decreases. Also in these cases, assuming the average concrete strength of the top slab led to an overestimation of the ultimate load. This was even more pronounced for the box girder where, in addition to the variability in the mechanical properties of the cast-in-place slab, there was also the variability in its thickness due to the cutting operations. However, even in these cases, the ultimate load was overpredicted, resulting 9.4% and 7.4% higher than the experimental values for the box girder and the I-girders, respectively. The predicted bending resistance for box and I-girders was 3458.0 kNm and 1768.0

kNm, respectively. The actual bending resistance will depend also on the weight of the loading system and the dead load.

These observations highlight the importance of having a comprehensive understanding of the constitutive law of the cast-in-place slab, which is the weak part in the composite girders. In this context, it can be stated that the numerical model predicts both the cracking and the ultimate loads in static tests with sufficient accuracy, and its variability can be related to the concrete uncertainty of the top slab. To consider the variability of materials, the safety of the bridge deck was assessed in the following section using a multi-level approach, moving from deterministic to semi-probabilistic and probabilistic analyses.

5.4 Safety assessment

The nonlinear behaviour of structures can be analysed by implementing governing equations based on fundamental physical principles. However, mathematical idealisation of physical laws, numerical errors in solution algorithms, uncertainties in input data, and spatial variability of mechanical properties can lead to discrepancies between predictions and the actual performance of structural members. In safety analysis, it is necessary to adequately characterise these uncertainties, and to quantify their impact on the structural response. For this reason, the safety assessment was carried out using a multi-level approach, starting from a first simplified level requiring only basic information to determine the current demand and the past resistance, and then moving to more refined levels taking into account the knowledge of the actual material properties with their mean values. The final stage involved a probabilistic approach, taking into account the available material test data with its statistical variability.

5.4.1 Safety formats

In the field of bridge engineering, the basis of the safety formats used for design or structural assessment is founded on the concept of limit states, defined as the boundary between the desired and undesired performance of the structure. A common method of defining structural safety is the partial safety factor method. For a given limit state, it can be expressed as:

$$\phi_R R \geq \gamma_{SD} S_D + \gamma_{SL} S_L + \cdots \tag{87}$$

where R is the member resistance (usually 5% fractile), ϕ_R is the partial factor of the resistance, and S_D, S_L are the dead and live load effects (usually 95% fractile) associated with the partial safety factors γ_{SD}, γ_{SL}. This allowed to take into account the uncertainties associated with the mechanical and geometrical parameters, the uncertainty of the resistance model and the uncertainty in the estimation of loads. However, the partial safety factors in the design codes are calibrated considering all the sources of uncertainty characteristic of the design and construction process of new structures. In the assessment of existing structures, all these uncertainties have been realised and different sources of uncertainty have arisen, such as the actual values of long-term properties, deterioration effects, undocumented changes, and different analytical models of the structural response. The uncertainties are no longer related to what will be realised, but to the limited knowledge of the actual realisation. To this end, the new Italian guidelines for the management of existing bridges [1] have introduced confidence factors to define the material properties according to the current state of knowledge. Furthermore, three different categories of bridges can be defined according to the "reference period", considered as the time for which the safety checks are satisfied:

- Adequate: applies to bridges that pass the safety check using the partial safety factors;
- Operational: applies to bridges that pass the safety check using the partial safety factors evaluated for the assumed reference period of 30 years;
- Passable: it refers to bridges that require intervention works. It may be possible to establish use restrictions and perform the safety verify with reduced safety factors with a reference period of 5 years.

However, for the assessment of existing bridges, the most reliable acceptance criterion is not simply to check that the minimum acceptable level of safety is achieved, but to take into account the actual performance of the structures through a structural reliability approach. The structural assessment of an existing structure has the advantage of knowing probabilistic information about materials and loads that must be incorporated into the analysis process. Thus, modelling the structure and its various influences with probabilistic analysis can be used for structural assessment when the bridge fails the safety check performed using the most conservative partial safety factor method.

In a probabilistic analysis, the resistance R of a structural member and the resultant stress S, are considered as random variables described by appropriate probability density functions. The safety assessment is then carried out to check whether the resistance is equal to or greater than the resultant stress, according to the following inequality:

$$S \leq R \tag{88}$$

The limit state, corresponding to the boundary between desired and undesired performance, is represented by the equality between the resistance and the load effect. However, as the safety assessment is affected by many sources of uncertainty, it is not possible to define an absolute safety, but it is required that the structures fulfil their function with a finite probability of failure P_f, defined by:

$$P_f = P(R < S) = P(g(R,\ S) < 0) \tag{89}$$

where $g(R, S)$ is the performance function (or limit state function). As R and S are random variables with f_r and f_s probability density functions, $g(R, S)$ is also a random variable with its own probability distribution function. Therefore, the probability of failure can be represented by the shaded area in Fig. 75.

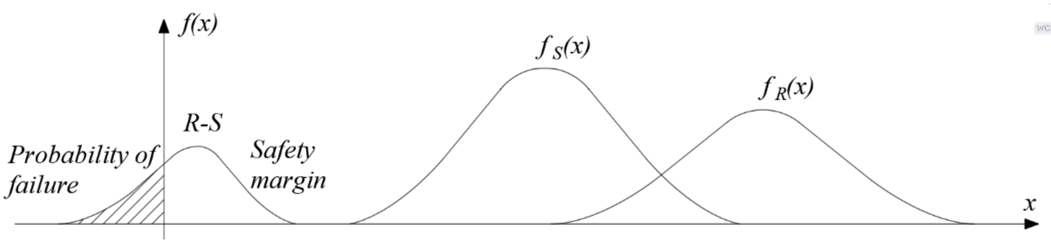

Figure 75: Probability distribution functions of the safety margin, load, and resistance.

The probability of failure is calculated by integrating the joint density function $f_{RS}(r, s)$ over the failure domain D, according to:

$$P_f = \int_D \int f_{RS}(r, s) dr ds \tag{90}$$

If R and S are independent, $f_{RS}(r, s) = f_R(r) f_S(s)$, Eq. 90 can be rewritten as follows:

$$P_f = \int_{-\infty}^{+\infty} F_R(x) f_S(x) dx \tag{91}$$

where $F_R(x)$ is the cumulative distribution function corresponding to the probability that the resistance R is less than a value x, and $f_S(x)$ is the probability that the load effect S takes the value between x and $x+\Delta x$ in the limit as $\Delta x \rightarrow 0$. Integration over all possible values of x gives the total probability of failure.

If R and S are statistically independent random variables and normally distributed with means μ_R and μ_S, and variances σ_R^2 and σ_S^2, the integral in Eq. 91 can be solved analytically. Introducing the new variable Z, called “safety margin”:

$$Z = R - S \tag{92}$$

and taking into account the well-defined rules for normal random variables:

$$\mu_Z = \mu_R - \mu_S \tag{93}$$

$$\sigma_Z^2 = \sigma_R^2 + \sigma_S^2 \tag{94}$$

Equation 89 can be rewritten as:

$$P_f = P(Z < 0) = \Phi\left(\frac{0 - \mu_Z}{\sigma_Z}\right) = \Phi(-\beta) \tag{95}$$

where Φ is the standard normal distribution function with zero mean and unit standard deviation, and β is the so-called “reliability index”, often referred to as the Cornell reliability index [5]. Substituting Eqs. 93 and 94 into Eq. 95, gives the reliability index:

$$\beta = \frac{\mu_R - \mu_S}{\sqrt{\sigma_R^2 + \sigma_S^2}} \tag{96}$$

If the standard deviations of the resistance and the load effect increase, the reliability index will decrease and therefore P_f will increase. Similarly, if the difference between their mean values is reduced, P_f increases. In order to quantify the structural reliability for the specific cases of linear limit state function, non-linear limit state function, and non-normal random variable, appropriate methods have been proposed in the literature [6].

An effective method of solving the multi-dimensional integration required in Eq. 89, when the basic variables are not normally distributed, is to use Monte Carlo simulation. In structural reliability analysis, this is done by sampling the random variables and checking the limit state function using the sampled set of values ($g(R_i, S_i)$). Given a number of simulations N, the probability of failure can then be approximated by:

$$P_f \approx \frac{1}{N}\sum_{i=1}^{N} I[g(R_i, S_i) \leq 0] \tag{97}$$

where $I[g(R_i, S_i) \leq 0]$ is a counter equal to *1* if the limit state function is violated. The generation of the basic random variables x_i can be obtained using the inverse transform method:

$$x_i = F_{x_i}^{-1}(r_i) \tag{98}$$

where F_{xi} is the cumulative distribution function of the basic variable X, and r_i is the random number generated, uniformly distributed. It is worth noting that the accuracy of P_f depends on the number of simulations, and the uncertainty in the estimate decreases as the number of simulations increases. Therefore, it can also be treated as a random variable with its own mean, standard deviation, and CoV. The plot of the progressive results of the estimated P_f and its variance will show a stability with a sufficient number of simulations. A key issue in the assessment of an existing structure is to compare the estimated probabilities of failure with the target nominal values to provide the required safety according to the risk acceptance criteria. The general equation in the probabilistic methods is:

$$\beta \geq \beta_T \tag{99}$$

where β_T is the target reliability index, usually determined by a multidisciplinary approach based on past performance of structures in service and socio-economic considerations. The Eurocodes [7] provide two sets of reliability indices for different reference periods and limit states. Furthermore, in the case of the ultimate limit state, different reliability classes are defined according to different failure consequences, low, medium, and high (RC-1, RC-2, and RC-3). The consequences of failure are related to loss of human life, economic, social and environmental impacts (Table 23).

Table 23: Target reliability index β_T (EC-0).

Limit State	**Reference period 1 year**			**Reference period 50 years**		
	RC-1	**RC-2**	**RC-3**	**RC-1**	**RC-2**	**RC-3**

Ultimate	4.2	4.7	5.2	3.3	3.8	4.3
Fatigue	-	-	-	-	1.5 - 3.8	-
Serviceability	-	2.9	-	-	1.5	-

Similarly, in the Probabilistic Model Code [8], the Joint Committee of Structural Safety (JCSS) proposed a set of target reliabilities according to the consequences of failure and different relative costs of safety measures (Table 24).

Table 24: Target reliability index β_T (JCSS).

Cost of safety measure	**Ultimate limit state**			**Serviceability limit state**
	Minor consequences	**Moderate consequences**	**Large consequences**	
Large	3.1	3.3	3.7	1.3
Normal	3.7	4.2	4.4	1.7
Small	4.2	4.4	4.7	2.3

However, both codes are intended for use in the design of new structures. As the cost of achieving a higher level of reliability for existing structures is usually higher than for new structures, the use of such a target level for the assessment of existing bridges may be overly conservative.

5.4.2 Safety verification results

As a first level of assessment, the resources provided by the original design were compared with the current code requirements. The action induced on the girders by the traffic loads prescribed by the regulations at the time of construction was taken as the minimum capacity guaranteed by the structure, and the action obtained using the traffic model provided by the current regulations was taken as the actual demand. An approximate safety factor against the current load regulations can then be estimated as the ratio between the bending moment capacity ($M_{design,1970}$) and the demand requirement (M_{NTC}). At the time of construction, the C.so Grosseto viaduct was designed in accordance with the Italian standards Circ. Min. LL.PP. 14/02/1962 n. 384 [9], considering the road in 1st category. In terms of traffic load models, the code provided the equivalent of a column of trucks corresponding to 12 tonnes and an isolated military cargo of 74.5 tonnes. Table 25 provides a comparison between the total bending moments due to the current traffic models, and the maximum bending moment provided by the original design. The maximum bending moment due to the NTC traffic load models is calculated by summing the contributions listed in Table 21.

Table 25: Comparison between the maximum bending moment calculated according to NTC code and that of the original design (unit: kNm).

Element	$M_{Courbon,NTC}$	$M_{Engesser,NTC}$	$M_{grid,NTC}$	$M_{design,1970}$
Box	1321.28	1203.31	1013.46	798.82
I-girder	604.23	710.23	681.75	380.82

Conservatively, using the maximum demand estimated by the Courbon method for the box girder and the Engesser method for the I-girder, the safety factors for the box and I-girder were 0.60 and 0.54, respectively. For the maximum bending moments estimated from the plane grid analysis, the safety factors for the box and I-girder were 0.79 and 0.56, respectively. These results demonstrate a significant increase in the effects of traffic loads associated with the current code provisions and highlight the need for a refined assessment of the actual capacity of the structural members. Therefore, as part of the successive improvements to the enhanced assessment approach, the structural performance of the deck girders has been further investigated taking into account the actual load carrying capacity using the resistance model and updated material properties.

In the second level of the assessment, safety was verified using the partial safety factor method. The safety check was carried out for the midspan sections of the most loaded girders according to Eq. 87. Using the partial safety factors defined in EC0 [7] and EC2 [10], the load effects given in Table 21 for the grid analysis and the moment resistance obtained by the moment-curvature method with the average mechanical properties, the check equation for the box and I-girders is as follows:

$$M_{Rd,box} = \frac{4218.9\ kNm}{1.3} \geq 1.35 \cdot (662.0 + 95.7 + 1013.5)\ kNm = M_{Ed,box}$$

$$M_{Rd,I-girder} = \frac{2201.1\ kNm}{1.3} \geq 1.35 \cdot (355.1 + 35.4 + 681.8)\ kNm$$
$$= M_{Ed,I-girder}$$

which leads to the following inequalities:

$$M_{Rd,box} = 3245.3 \text{ kNm} > 2391.1 \text{ kNm} = M_{Ed,box}$$

$$M_{Rd,I-girder} = 1693.2 \text{ kNm} > 1447.6 \text{ kNm} = M_{Ed,I-girder}$$

As it can be seen, using the partial safety factor method with the safety factors provided in the Eurocode, safety is verified for both box and I-girders with an ultimate bending moment greater than the design moment in the order of 26.3% and 14.5% respectively. From the comparison of the first and second levels of assessment, it can be deduced that despite the increase in the traffic load actions, a safety margin is preserved as a result of the overdesign of the cross-sections.

From a practical point of view, the safety check should be stopped at the second level of assessment as the structural members were found to be safe. However, as the material and load uncertainties were neglected at the second level of assessment, the third level probabilistic safety check was also carried out. The reliability of the box girder and the I-girder was then estimated using Monte Carlo simulation. A total of 10^4 simulations were performed to estimate the resistance distributions of the structural members. For PC girders, the basic variables that influence the resistance are the mechanical properties of the concrete, the reinforcement, and the dimensions of the cross-section. However, in the present analysis, since the dimensions were determined directly from the real geometry and the ultimate flexural response was governed by the strength of the top slab, the geometry and reinforcement properties were assumed to be deterministic with their mean values. In each simulation, the mechanical properties of the concrete for both the cast-in-place slab and the precast girders were randomly generated from the probability distributions based on the destructive test results (*Appendix E*). In addition to these models, the tensile strength of the precast concrete was also assumed with a probability distribution function with mean 3.5 MPa and standard deviation 0.546 MPa. Figure 76 shows the histograms of the ultimate bending resistance calculated at the midspan section of the box and I-girders. Following the procedure presented in the previous section, the probability distribution of the limit state function was first defined by fitting the simulation results of the box girders with a normal distribution and the resistance distribution of the I-girder with a Weibull distribution.

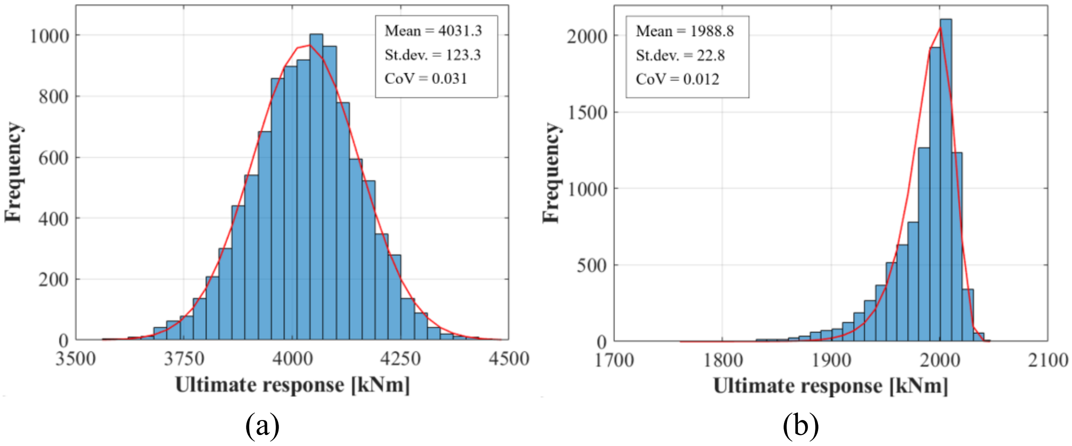

Figure 76: Histograms of midspan section resistance for: (a) box, and (b) I-girder.

In order to account for the uncertainties associated with the loads that a bridge will experience during its operational lifespan, it is essential that these uncertainties are accurately modelled using appropriate statistical distributions. The primary sources of permanent loads on a bridge are attributed to the self-weight of the bridge deck and the weight of non-structural components that remain permanently installed in the structure. The uncertainty associated with these loads arises from the variability in material density and the dimensions of individual bridge elements. To account for this uncertainty, permanent loads are usually modelled using a normal distribution with a CoV ranging from 0.05 to 0.1 [5, 7]. On the other hand, the traffic load experienced by the bridge is a stochastic process subject to temporal and spatial variations. Load models defined by codes aim to simulate load effects on bridge members that are representative of the lifetime of the bridge under a wide range of traffic conditions. As a result, these models tend to be very conservative. When real traffic flow information is not available, simplified probabilistic traffic load models based on assumptions about traffic composition and position can be used. In this work, the maximum traffic load effects have been estimated using the conventional traffic load model in the most unfavourable configuration, taking into account the characteristic values. Consequently, the parameters of the distribution corresponding to the traffic load effects are calculated considering that the characteristic load values defined in EC1 [11], correspond to the 95-th percentile of the probability distribution function of the traffic load. The mean values of the traffic load effects were then estimated assuming a normal distribution with a CoV of 0.15. The relatively high CoV values for traffic loads include not only the variability due to the load itself, but also account for dynamic amplification, girder distribution, and load modelling uncertainties [12]. Table 26 presents a summary of the statistical parameters utilized for reliability index estimations in this study.

Table 26: Statistics of the resistance and bending moment variables considered in the reliability analysis.

Stochastic variable	Box girder		I-girder	
	Mean value [kNm]	CoV [%]	Mean value [kNm]	CoV [%]
Bending resistance	4031.3	3.1	1988.8	1.2
Permanent load moment	757.7	10.0	390.5	10.0
Traffic load moment	812.9	15.0	546.9	15.0

Using Eq. 96 and the data from Table 26, the reliability indices corresponding to bending failure for the box and I-girder were calculated to be 12.9 and 11.2, respectively. By comparing these estimated reliability indices with the target values, it can be assumed that the structural members can be rated as safe.

The safety analysis conducted using the different safety formats discussed earlier showed that the bridge, which was initially considered deficient using the simplified approach, actually exhibits a good level of safety when the semi-probabilistic approach, accounting for effective resistance, is employed. Moreover, the measure of structural safety obtained from the probabilistic analysis allowed for the explicit consideration of existing statistical data, incorporating uncertainties related to material properties and applied loads.

References

[1] Linee guida per la classificazione e gestione del rischio, la valutazione della sicurezza ed il monitoraggio dei ponti esistenti. Rome, Italy: Italian High Council of Public Works; 2020 [in Italian].

[2] DM 17/01/2018. Aggiornamento delle «Norme tecniche per le costruzioni». Rome, Italy: Italian Ministry of Infrastructures and Transportation; 2018 [in Italian].

[3] Collins, M.P.; Mitchell, D. (1997). Prestressed concrete structures. Response publications, Canada.

[4] Sargin, M. (1971). Stress-Strain Relationship for Concrete and the Analysis of Structural Concrete Sections, Study 4, Solid Mechanics Division. University of Waterloo, Canada.

[5] Melchers, R.E.; Beck, A.T. (2018). Structural Reliability Analysis and Prediction. Third Edition. Hoboken, NJ: Wiley, 2018.

[6] Collins, K.R.; Nowak, A.S. (2000). Reliability of structures. Singapore: McGraw-Hill, 2000.

[7] EN1990 (2002): Eurocode 0 - Basis of structural design. CEN, Brussels.

[8] JCSS (2001). Probabilistic Model Code. Joint Committee on Structural Safety.

[9] Italian Ministry of Public Works (1962) Ministerial circular n. 384 of 14/02/1962—rules related to loads for the calculation of road bridges, Rome.

[10] EN1992-1-1 (2004): Eurocode 2 - Design of concrete structures - Part 1-1: General rules and rules for buildings. CEN, Brussels.

[11] EN1991-2 (2003): Eurocode 1 - Actions on structures - Part 2: Traffic loads on bridges . CEN, Brussels.

[12] Wiśniewski, D.F. (2007). Safety Formats for the Assessment of Concrete Bridges. [Doctoral thesis]. The University of Minho.

Chapter 6

Conclusions

6.1 Aim and main achievements

In the field of civil infrastructure, the management of the huge stock of existing bridges and other civil structures world-wide is an extremely complex issue involving technical, social, economic and political considerations. In recent decades, this issue has gained even more social attention due to the rapid deterioration of existing bridges. The main causes, which affect bridges at the end of their design life or beyond, can be related to increased traffic flows, environmental factors, widespread use of de-icing salts, limited maintenance programme, low quality of structural materials and constructive details. As a result, other to being structurally deficient due to deterioration, a bridge may be functionally obsolete if it is designed to satisfy lower traffic loads despite being in good technical condition. Therefore, structural assessment has become a crucial task in modern civil engineering. In general, it can be defined as a multi-step process, which refers not only to the level of refinement of the analytical models, but also to the planning of the diagnostic campaign and the inherent level of knowledge obtained. Before defining the analytical models and determining the safety level, it is essential to know the actual condition of the structure. However, the planning of a diagnostic campaign is subject to several constraints, such as limited economic resources, poor accessibility, which can limit the reliability of the estimated parameters and then the final rate assigned to the bridge. All these remarks show that the structural assessment requires a rational judgement to cover many technical and economic problems throughout the process. The structural assessment must be carried out at each stage by planning an adequate project of all the relevant operations necessary to obtain reliable estimates of the safety level in a cost-effective manner. However, if on the one hand, until recently, many countries are establishing guidelines for safety assessment based on different safety formats, there is a lack of an appropriate framework to establish reliable and feasible techniques aimed at achieving a predetermined and acceptable level of knowledge.

Therefore, the present research has been guided to respond to the following general requirement: "*to define a reliable and feasible framework for the structural assessment of existing prestressed concrete bridges*". The answers to this main requirement have been supported by the unique opportunity to validate methods and analytical models on full-scale PC girders. Therefore, a proper experimental programme has been established within the BRIDGE|50 research project to provide data on the performance of older girders and to aid management agencies in decision-making policies regarding older structures. Based on these purposes, the following research areas have been covered:

- **Assessment of durability problems using NDT:** the preliminary assessment of the conservation state was based on the well-established visual inspection, which aims to register visual signs of deterioration. However, visual inspection can only detect corrosion if the increase in volume of the corroding steel has resulted in concrete cracking and delamination. Therefore, the extent of corrosion was assessed by combining half-cell potential mapping, concrete resistivity, carbonation depth, and corrosion current density measurements. The combined NDT tools were shown to provide a good overview of the structural condition in terms of extent and rate of deterioration. The results highlighted a good condition of the prestressing strands after 50 years of service, which was also confirmed by direct inspection of the steel after removal of the concrete cover. The practical application of the corrosion monitoring techniques, being fast and low invasive, can be integrated into the preliminary assessment of existing structures, at least in the most exposed areas. Providing data only on the load-bearing capacity of components, without objective information on the conservation state, could result in less useful information for similar existing structures. For a comprehensive assessment, such a test method should be consolidated as a standard within the experimental activity and more systematic study of both residual strength and NDT for corrosion evaluation should be promoted.

- **Characterization of the mechanical properties of concrete based on both NDT and limited destructive testing:** reliable input parameters are the fundamental prerequisite for a proper assessment process. However, due to technical and economic limitations in performing destructive tests on existing structures, only a limited amount of test data is generally available. Therefore, an indirect testing method was evaluated by combining NDT and uniaxial compression test results. A correlation model between the rebound index and concrete compressive strength was then calibrated on samples taken from limited areas. The mean value of the compressive strength estimated from the conversion model and the rebound indices was found to be in agreement with that obtained from the compression tests. Consequently, the adoption of such an integrated approach in the structural assessment of existing bridges could provide a relevant amount of information for the mechanical characterization of the concrete, allowing the investigation of larger areas and reducing statistical uncertainties.
- **Full-scale load testing of PC girders:** one of the aims of the thesis was to define a robust and systematic approach for the experimental investigation of the structural behavior of full-scale PC girders in both serviceability and ultimate conditions. Accordingly, the planning, design, and implementation of such complex experimental research was detailed in terms of both loading and measurement systems. Despite the simplification to disregard the actual behavior of the deck as a system, such an approach allowed to perform full-scale load tests in a controlled and reliable manner, without the problems of traffic disruption and difficulties in accessing the bridge elements. The execution of the full-scale load tests allowed to build up a huge informative database on the structural performance of the PC girders, which have experienced 50 years of service. Several aspects were investigated, such as cracking and ultimate strength, stiffness, failure mode, composite behavior between the I-girder and the top slab, different load test setups including both three and four-point bending tests, structural behavior of elements with artificially induced damage, and structural behavior of a box girder. Together with information from NDT and destructive tests, it could provide a relevant basis for practitioners and highway authorities to assess the safety of other similar existing bridges.
- **Evaluation of residual prestressing force in existing PC bridges using diagnostic tests:** prestressed concrete girders have been widely used in the construction of infrastructure assets. However, over time, the effective prestress in the structures is reduced due to time-dependent phenomena.

Consequently, an accurate estimation of the residual prestressing force becomes crucial, primarily for serviceability verification. To this end, a comprehensive experimental programme was designed to determine the prestress loss in 50-year-old PC girders using the cracking load method, the decompression load method, and the strand-cutting method. In addition, an optimized version of the saw-cut method was proposed to standardize the procedure and extend its applicability to in-service structures. Through comparative analysis, the experimental results revealed varying degrees of total prestress loss, ranging from 53.5% for the decompression method to 61.1% for the strand-cutting method. However, the cracking, decompression and saw-cut methods showed consistent results, with an average prestress loss of 55.1%. These findings highlighted the reliability and suitability of the saw-cut method as an effective approach for assessing residual prestress in existing PC bridges.

- **Prediction of prestress loss using numerical models:** prestress losses in concrete members are influenced by multiple factors, including, creep, shrinkage, stress relaxation of prestressing strands, and external factors such as deck placement. In this study, the theoretical models proposed by the EC2 and AASHTO codes have been examined to accurately capture these complexities, considering the different levels of accuracy in each model. In addition, an enhanced version of the EC2 formulation has been proposed which allows the influence of the subsequent casting of the top slab to be taken into account. This new approach enables a more refined representation of prestress losses from the jacking stress to the casting of the top slab and the long-term losses thereafter. The performance of the models was evaluated by a comparative analysis, accounting for elastic shortening, concrete shrinkage, creep, and strand relaxation effects. Discrepancies were observed in the predictions of prestress loss between the EC2-based approaches and the AASHTO model. Specifically, the AASHTO method showed higher estimates of prestress loss due to concrete shrinkage and lower predictions for losses due to strand relaxation. The proposed model, designed to reflect the actual construction process, gives the highest prestress loss estimate due to strand relaxation, considering both prestress transfer to deck placement and long-term relaxation. The prestress loss predicted by the proposed model demonstrated adequate agreement with experimental results, with the exception of the strand-cutting method. In contrast, both American and European code predictions exhibited unconservative estimates when compared to the experimental values. Overall, these findings emphasize the importance of accurate and comprehensive models for estimating prestress losses in concrete members considering real construction process.

Finally, for a rational prediction of the prestressing losses, a probabilistic approach was also applied, considering the probability distribution of the input parameters. The results show that all prestressing losses measured in the experimental tests fall within the 95% confidence interval.

- **Comparison of different safety formats ranging from deterministic to probabilistic analyses within a multilevel assessment process:** the safety assessment was carried out using a multi-level approach ranging from deterministic to probabilistic formats. In the first level of assessment, the traffic load effects provided by the code at the time of construction were assumed as the minimum resistance provided by the elements and compared with the current traffic load prescriptions. In subsequent stages, the actual bending capacity was taken into account by means of moment-curvature analysis. The analytical model, validated against the experimental results, provided sufficiently accurate predictions of the structural behavior and was then used for the semi-probabilistic and probabilistic analyses at the second and third levels of assessment, respectively. At the second level of assessment, the actual resistance was estimated taking into account the average values of the material properties provided by the destructive tests and the partial safety factors defined by the Eurocodes. At the third level of assessment, the safety check was performed in the form of a reliability index, taking into account the uncertainties associated with the material properties and loads. Using the deterministic approach, the structural members were found to have insufficient load-carrying capacity. This was due to the increase in the current design load compared to previous regulations. However, when the actual resistance of the member was introduced in subsequent levels, the members passed the safety check. The probabilistic assessment resulted in the most effective formats, as it allowed to consistently model the different sources of uncertainty, neglecting the adoption of partial safety coefficients. It also allows to carry out sensitivity analyses and to properly plan the diagnostic campaign in order to collect samples related to the most uncertain variables with the major influence on the reliability index.

Finally, it can be concluded from the work presented that the acquisition of experimental data on the structural behavior of older bridges is a key step for the statistical characterization of infrastructure assets and its application to large-scale approaches. Promoting experimental research on structural members after they have experienced real life conditions and increasing the informative database with both durability and structural performance results could be useful to support the updating of reliable service life models for our existing structures. Under such conditions, detailed information on the current state of deterioration of the infrastructure heritage could be defined on a national scale, differentiated by structural typology, age, and exposure conditions. Accordingly, the level of safety could be increased by predicting deterioration and planning rational maintenance. The framework of the diagnostic campaign proposed in this thesis, could be useful not only as a strategy in the experimental activity in terms of planning, execution and evaluation of the tests, but also as a reliable tool for management agencies to carry out a large-scale safety assessment of the infrastructure network.

6.2 Future research

From the experience gained during the experimental activities and analyses detailed in this thesis, several aspects have been identified that merit further research and are discussed below.

The structural assessment of full-scale girders after 50 years of service has mainly focused on flexural or shear-flexural failure modes, assuming a fully adherent reinforcement, and composite behavior between the precast girders and the cast-in-place slab, as highlighted by the experimental evidence. The next stage of the research project could focus on the study of the degradation phenomenon due to corrosion and its influence on the structural performance of the PC girders. To this end, girders deteriorated by natural or artificial corrosion could be evaluated and tested with reference to the diagnostic campaign presented in this thesis. Several aspects could be studied, such as the constitutive law of the corroded steel reinforcement, the concrete-steel bond, the influence on the residual prestress, and the change in the failure mode. The study will allow us to verify the applicability of NDTs under different deterioration rates, validate theoretical models, and support the development of durability models. In these cases, the multi-level assessment for the safety check could be carried out by considering the lowest resistance contribution to the load-carrying capacity. Furthermore, the shear-induced failure mechanism could be studied by reducing the shear span in the loading test configuration.

For the assessment of existing PC bridges, the estimation of residual prestress is fundamental to the serviceability analysis. Since theoretical models for predicting residual prestress have a range of uncertainties associated with the input parameters, it would be useful to derive such information directly from in-situ measurements by NDT. The study reported in this thesis demonstrates that the saw-cut method is a valuable procedure for practical application on existing bridges. The proposed method allowed us to estimate the effective prestress in a standardized manner and with a low impact on the structural members. However, further investigations including more complex cases (i.e. statically indeterminate schemes, parabolic alignment) need to be carried out.

For a comprehensive study of bridge rehabilitation problems, future works could include not only assessment and evaluation techniques of their technical condition but also strengthening techniques. For the PC girders investigated, the load test results showed that the ultimate capacity was related to the crushing of the deck slab. Therefore, a possible strategy could be its replacement with high-performance concrete. In this way, a ductile failure mode could be achieved as well as an extended service life by meeting higher traffic load requirements.

With the continuous advancement of science and technology, bridge assessment will evolve in a scientific and standardized direction, providing important technical support to management agencies. A great contribution could be made by the development of digital twin bridges, which start their life at the design stage and are updated throughout their life by monitoring or in-situ measurements. With the structural condition recorded over time, effective deterioration models could be calibrated to represent the evolution of deterioration, such as to plan optimized maintenance works. By incorporating economic information, both deterioration and cost trends could be continuously monitored. In this way, the most effective maintenance options can be defined, as well as a priority list for the entire bridge stock.

Appendix A

Overview of the cracks mapping

Table A.1: Cracks mapping of B3-P47/46.

View	Crack nr.	Length [mm]	Width [mm]
East	1	60	0.13
	2	60	0.15
	3	120	0.29
South	1	150	5.07
	2	80	0.40
	3	200	0.17
West	1	260	1.13
Bottom	1	200	0.95
	2	70	0.18
	3	140	0.26

	4	100	0.37
	5	60	0.68
	6	340	0.55
	7	50	0.11

Table A.2: Cracks mapping of B8-P47/46.

View	**Crack nr.**	**Length [mm]**	**Width [mm]**
East	1	120	0.16
South	1	40	0.30
	2	560	0.13
	3	120	0.97
West	1	40	0.23
	1'	60	0.40
	2	160	0.14
	3	540	0.10
	4	160	0.20
	5	120	0.70
	6	100	0.10

	7	260	0.16
Bottom	1	140	1.35

Table A.3: Cracks mapping of B4-P47/46.

View	**Crack nr.**	**Length [mm]**	**Width [mm]**
East	1	220	0.51
South	1	400	0.14
	2	540	0.13
	3	140	0.10
	4	420	8.25
	5	40	0.27
West	1	240	1.95
	2	140	1.54
	3	260	0.33
	4	400	0.11
	5	100	0.47
	6	120	0.61
Bottom	1	80	0.13

	2	140	0.19
	3	260	0.31
	4	60	0.16
	5	140	0.17
	6	120	0.22
	7	180	2.09
	8	40	0.27
	9	140	0.18
	10	80	0.22

Table A.4: Cracks mapping of B9-P47/46.

View	**Crack nr.**	**Length [mm]**	**Width [mm]**
Bottom	1	60	0.23

Table A.5: Cracks mapping of B7-P47/46.

View	**Crack nr.**	**Length [mm]**	**Width [mm]**
North	1	140	0.10
South	1	40	0.30

West	1	260	0.10

Table A.6: Cracks mapping of B6-Ab/P47.

View	Crack nr.	Length [mm]	Width [mm]
East	1	220	0.10
South	1	100	0.20
West	1	300	0.13

Table A.7: Cracks mapping of B6-P49/48.

View	Crack nr.	Length [mm]	Width [mm]
North	1	560	0.16
West	1	200	0.15
Bottom	1	80	0.14
	2	40	1.10
	3	120	0.81
	4	80	0.12
	5	40	0.12
	6	40	0.12

	7	70	0.16
	8	80	0.13

Table A.8: Cracks mapping of B10-Ab/P47.

View	Crack nr.	Length [mm]	Width [mm]
Bottom	1	80	0.12
	2	140	0.17
	3	120	0.16
	4	100	0.14
	5	120	0.21
	6	80	0.19

Table A.9: Cracks mapping of B5-P47/46.

View	Crack nr.	Length [mm]	Width [mm]
East	1	260	0.15
	2	460	1.61
	3	60	0.30
South	1	260	0.31

	2	180	0.23
	3	500	0.14
	4	120	0.54
	5	80	0.10
	6	20	0.90
West	1	100	0.10
	2	420	0.10
	3	120	0.14
	4	260	0.31
	5	160	0.40
	6	360	1.09
	7	280	0.23
Bottom	1	60	1.20
	2	240	1.12
	3	160	0.23
	4	200	0.53
	5	60	0.29
	6	60	4.88

	7	60	0.50
	8	100	1.47
	9	260	0.33

Table A.10: Cracks mapping of Bx2-Ab/P47.

View	**Crack nr.**	**Length [mm]**	**Width [mm]**
North	1	200	0.17
	2	260	0.14
East	1	700	0.34
	2	220	0.16
	3	160	0.19
	4	140	0.30
	5	100	0.18
	6	120	0.19
	7	120	0.71
	8	40	0.55
	9	740	0.17
	10	440	0.14

	11	180	0.14
	12	480	0.16
	13	200	0.14
	14	140	0.13
	15	220	0.13
	16	240	0.24
	17	220	0.29
	18	80	0.20
	19	120	0.24
	20	80	1.10
	21	160	0.44
	22	100	1.93
	23	140	0.75
	24	440	1.12
	25	140	0.66
	26	180	0.56
South	1	260	0.21
West	1	420	0.10

	2	320	0.17
Bottom	1	260	0.40
	2	100	0.78
	3	320	1.04
	4	140	0.63
	5	340	0.52
	6	100	0.54
	7	60	1.08
	8	80	0.43
	9	80	0.27
	10	440	0.58
	11	100	0.38
	12	300	0.83
	13	80	0.48
	14	280	0.64
	15	100	0.44
	16	200	0.11

Appendix B

Electrochemical measurements

Corrosion potential (mV/CSE)

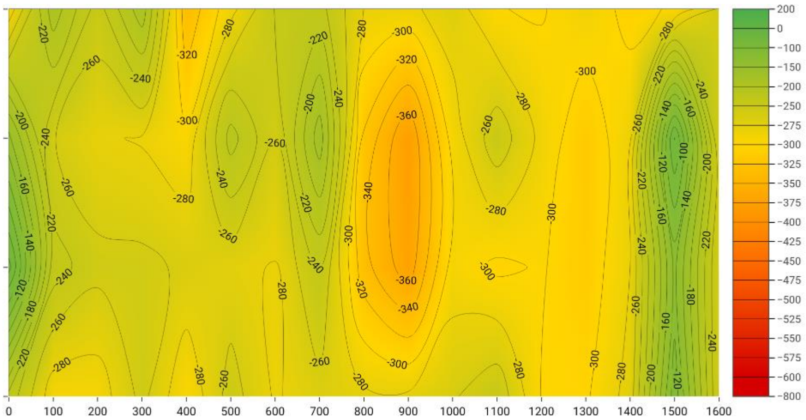

Concrete Resistivity (ohm.m)

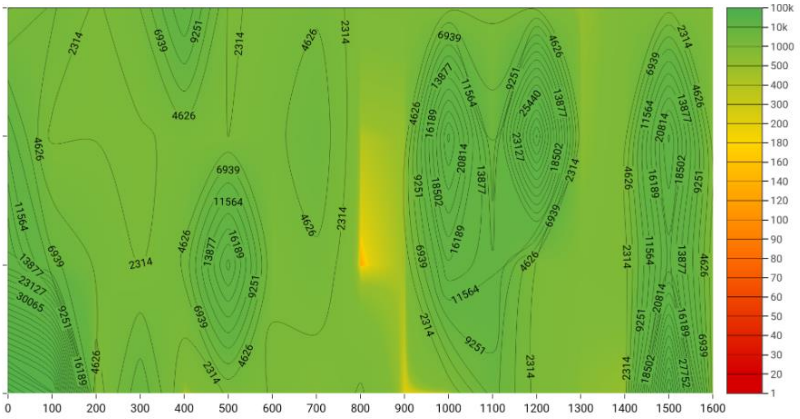

Corrosion Rate (μA/cm^2)

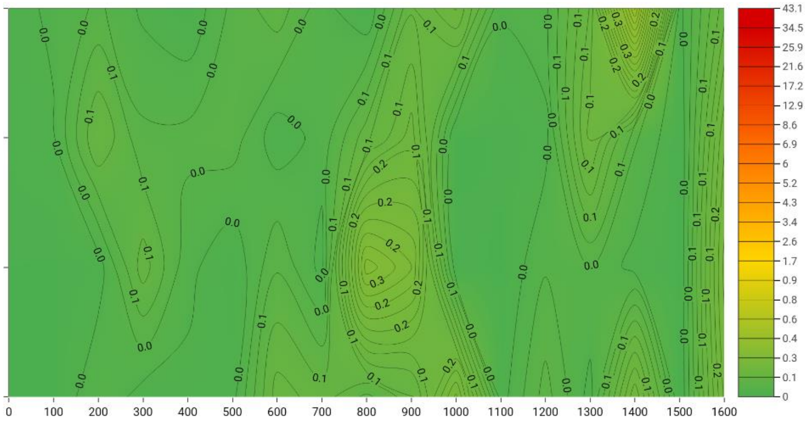

Figure B.1: Corrosion measurements B3-P47/46 girder.

Corrosion potential (mV/CSE)

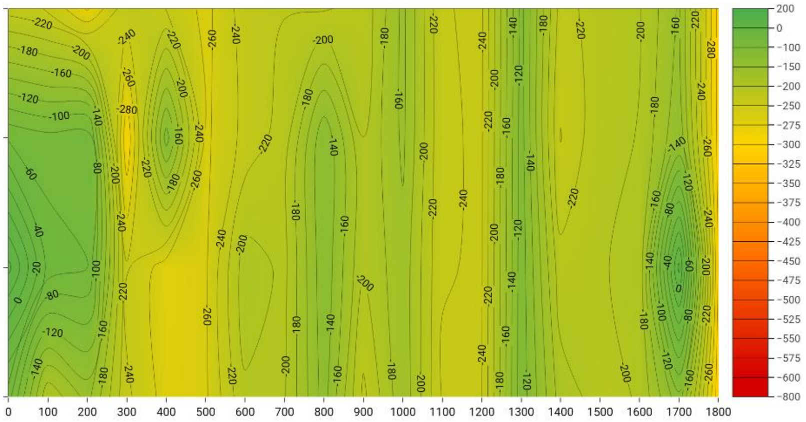

Concrete Resistivity (ohm.m)

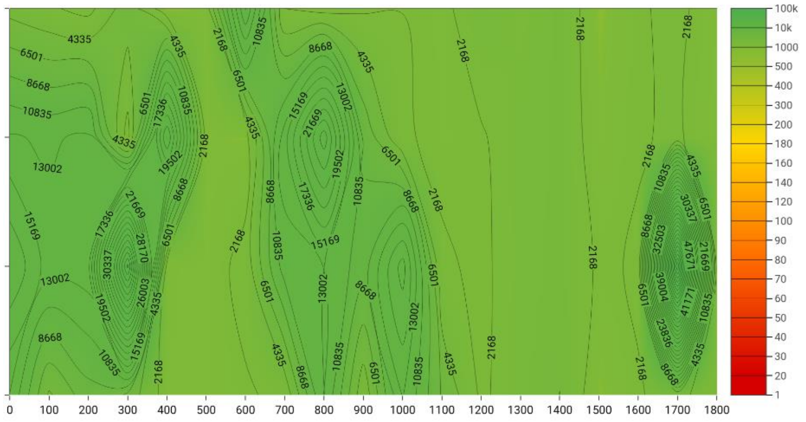

Corrosion Rate (μA/cm^2)

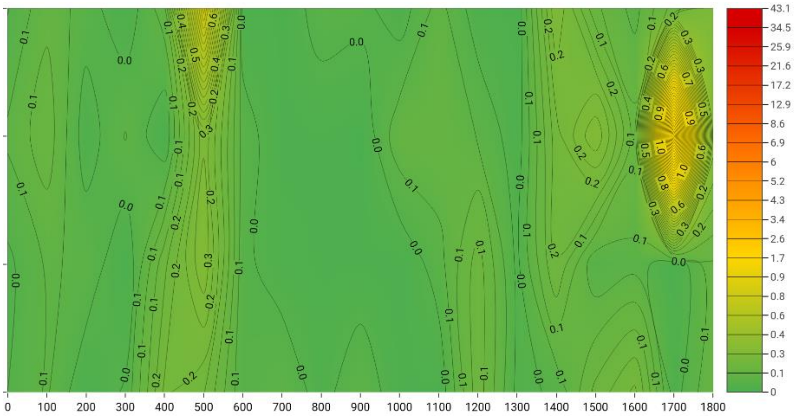

Figure B.2: Corrosion measurements B8-P47/46 girder.

Corrosion potential (mV/CSE)

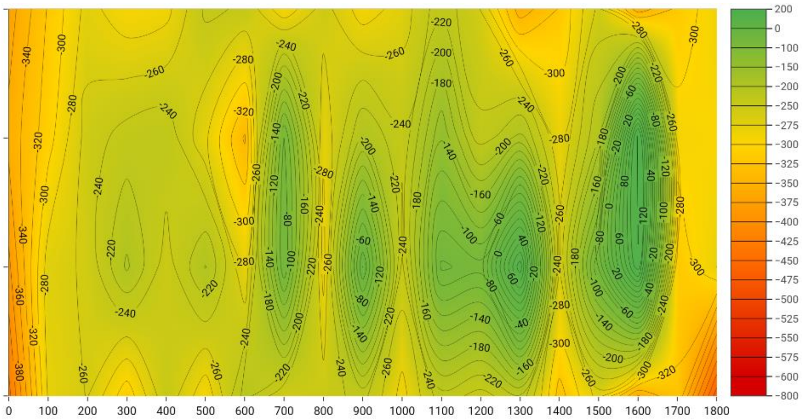

Concrete Resistivity (ohm.m)

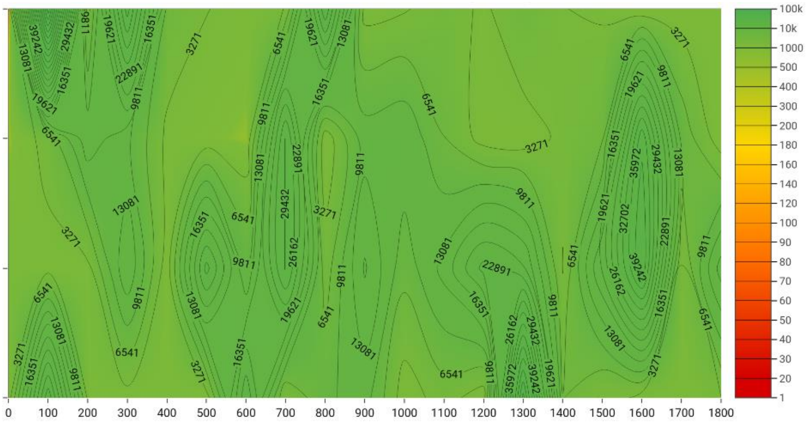

Corrosion Rate (μA/cm^2)

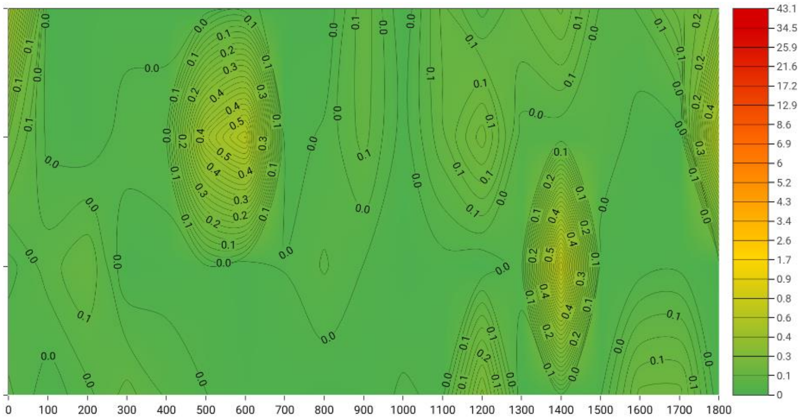

Figure B.3: Corrosion measurements B4-P47/46 girder.

Corrosion potential (mV/CSE)

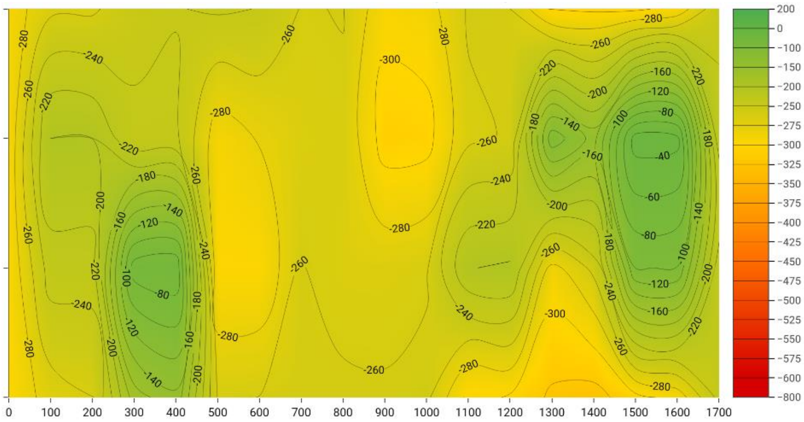

Concrete Resistivity (ohm.m)

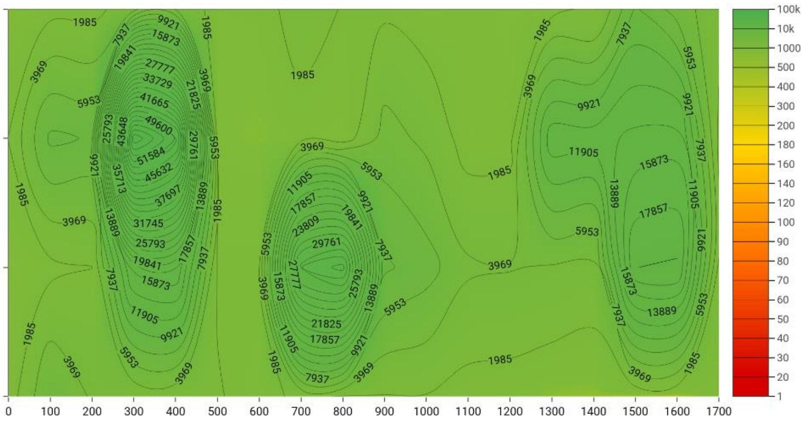

Corrosion Rate ($\mu A/cm^2$)

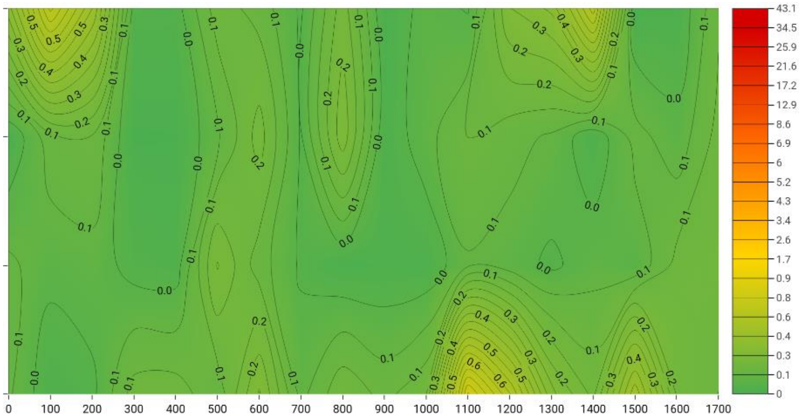

Figure B.4: Corrosion measurements B9-P47/46 girder.

Corrosion potential (mV/CSE)

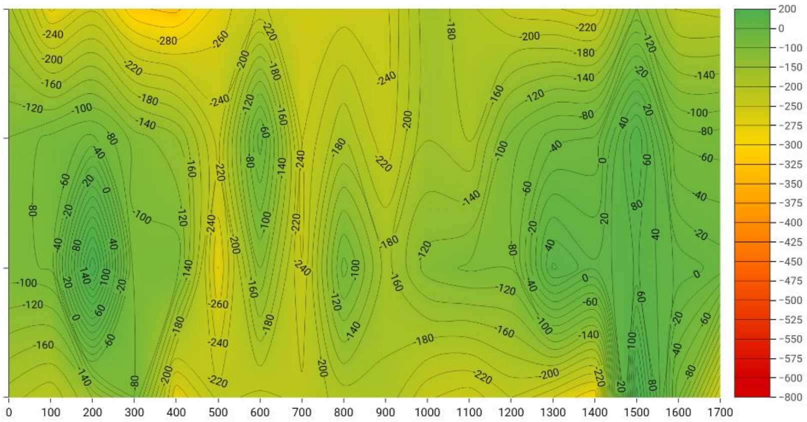

Concrete Resistivity (ohm.m)

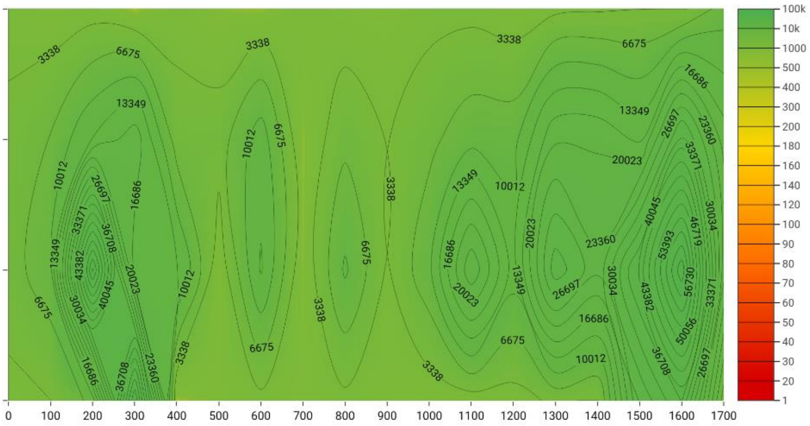

Corrosion Rate ($\mu A/cm^2$)

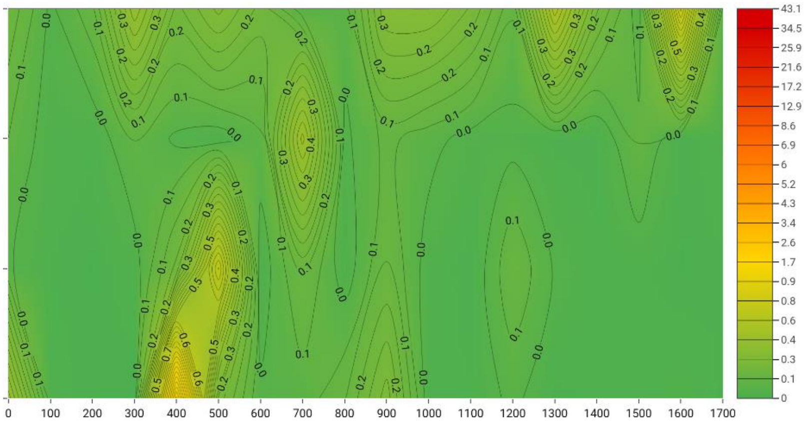

Figure B.5: Corrosion measurements B6-Ab/P47 girder.

Corrosion potential (mV/CSE)

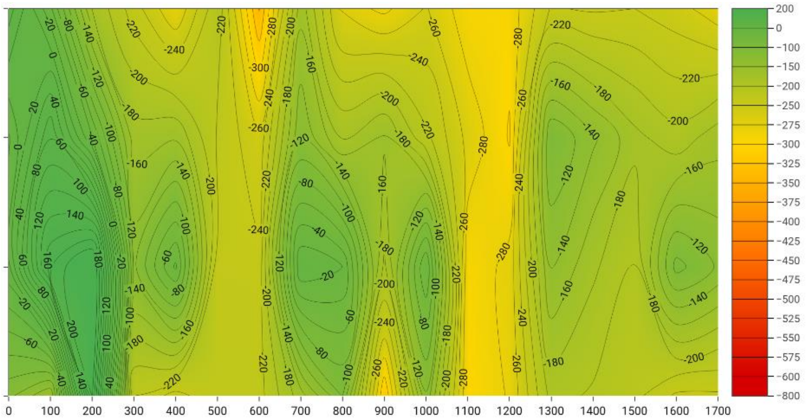

Concrete Resistivity (ohm.m)

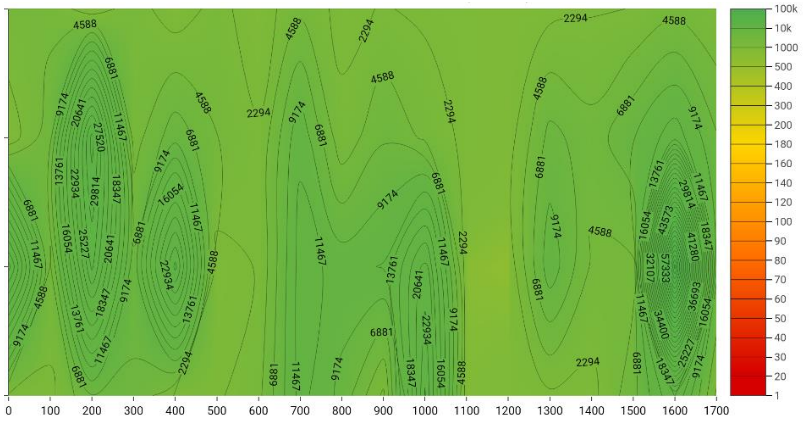

Corrosion Rate ($\mu A/cm^2$)

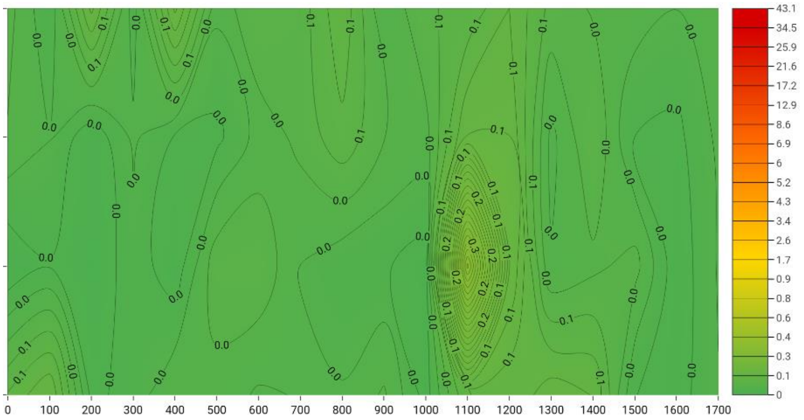

Figure B.6: Corrosion measurements B6-P48/49 girder.

Corrosion potential (mV/CSE)

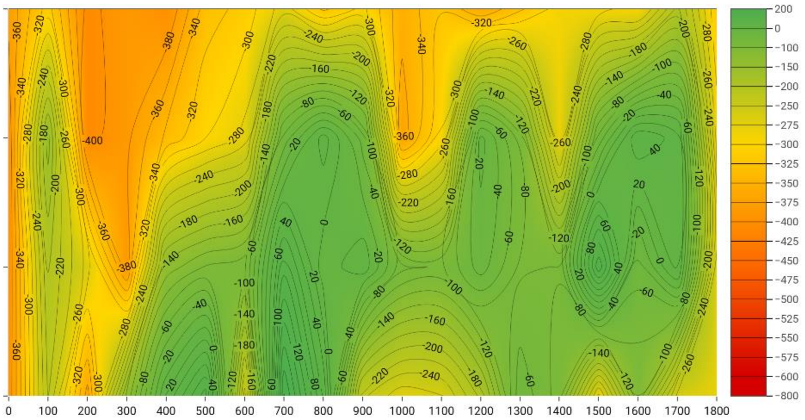

Concrete Resistivity (ohm.m)

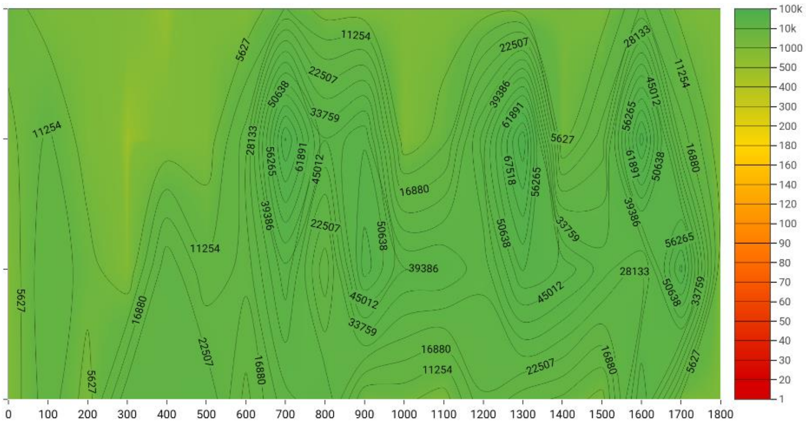

Corrosion Rate ($\mu A/cm^2$)

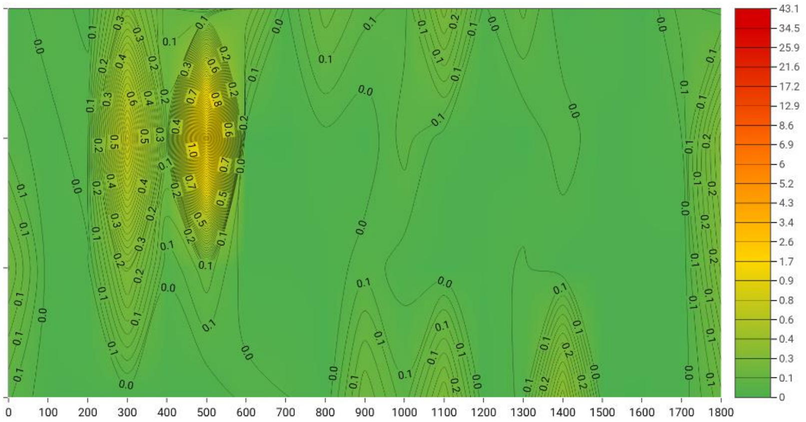

Figure B.7: Corrosion measurements B10-Ab/P47 girder.

Corrosion potential (mV/CSE)

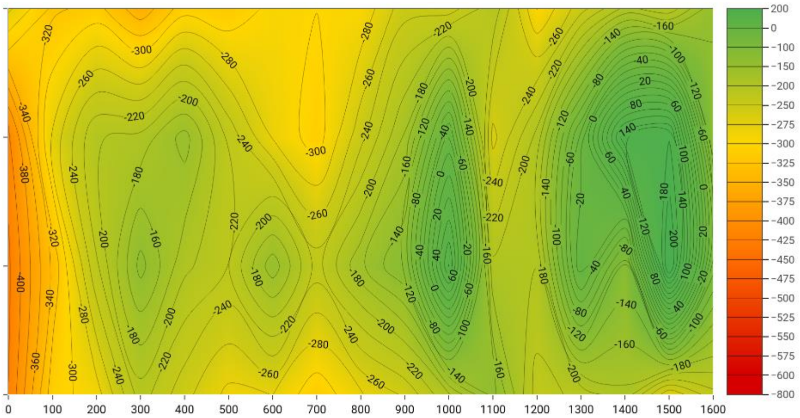

Concrete Resistivity (ohm.m)

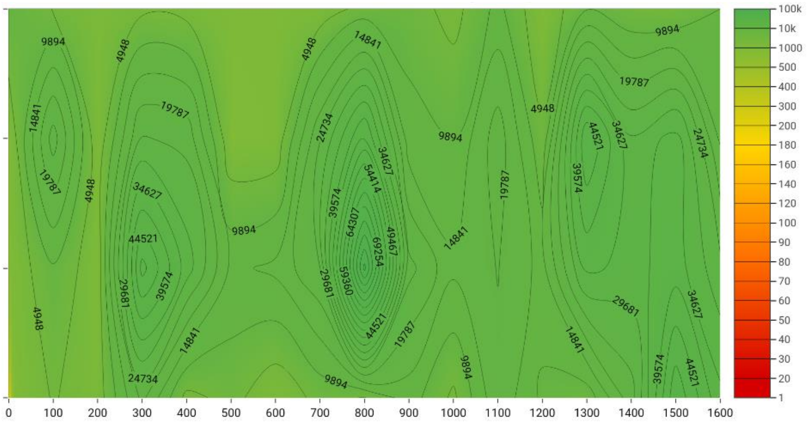

Corrosion Rate (μA/cm^2)

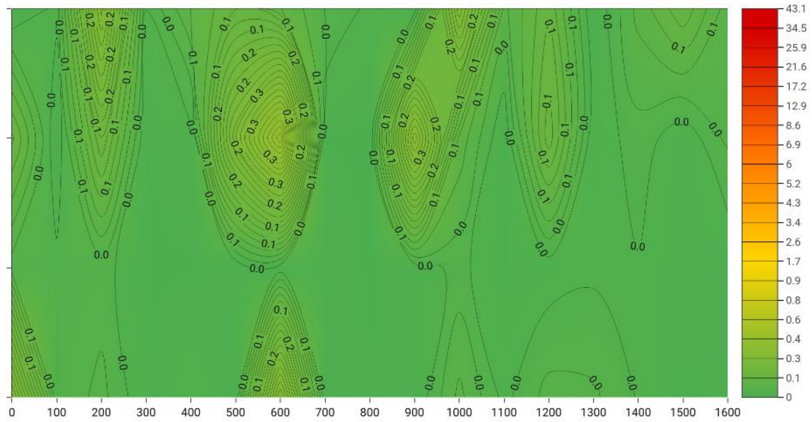

Figure B.8: Corrosion measurements B5-P47/46 girder.

Appendix C

Layout of the monitoring systems

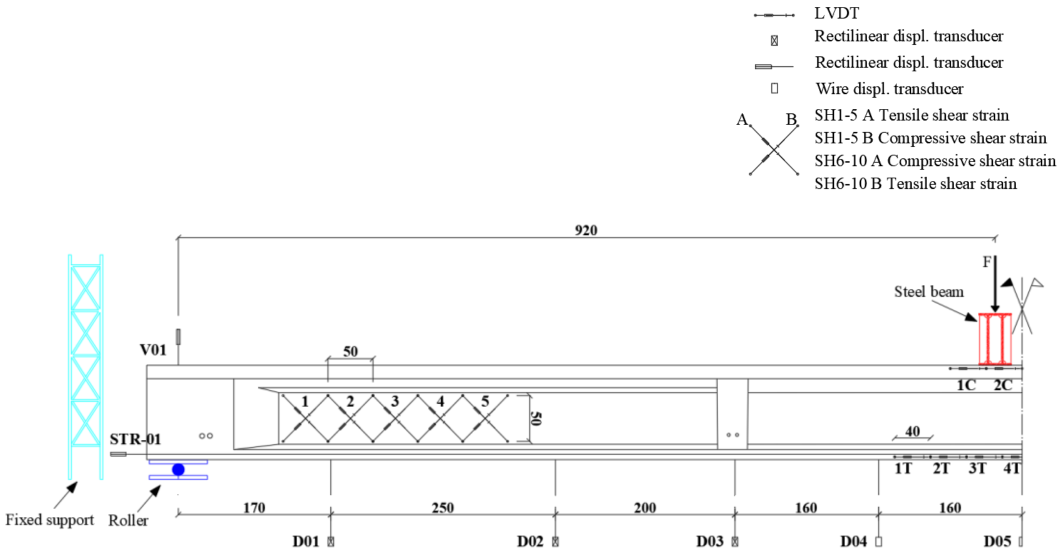

Figure C.1: Test setup and layout of the monitoring system installed on B3-P47/46 girder (unit: cm).

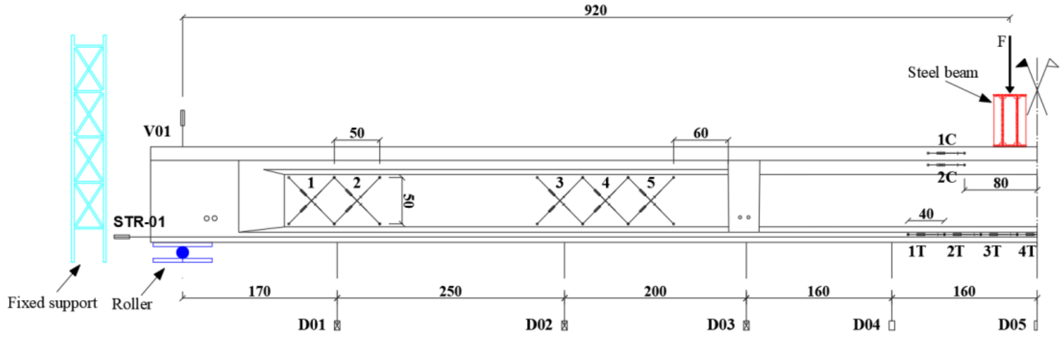

Figure C.2: Test setup and layout of the monitoring system installed on B8-P47/46 girder (unit: cm).

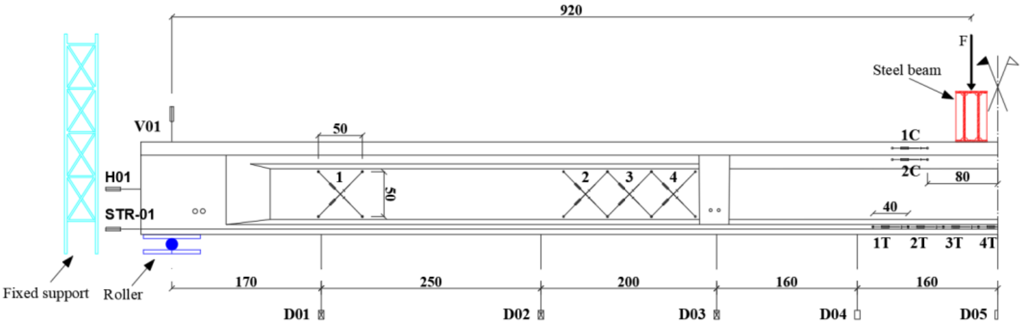

Figure C.3: Test setup and layout of the monitoring system installed on B4-P47/46 girder (unit: cm).

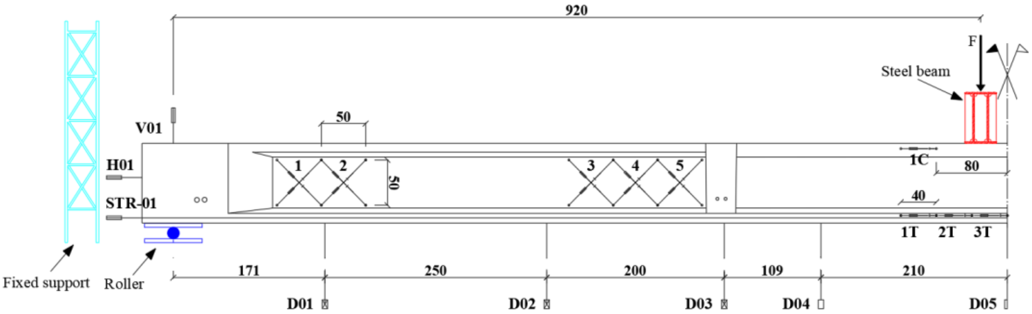

Figure C.4: Test setup and layout of the monitoring system installed on B9-P47/46 girder (unit: cm).

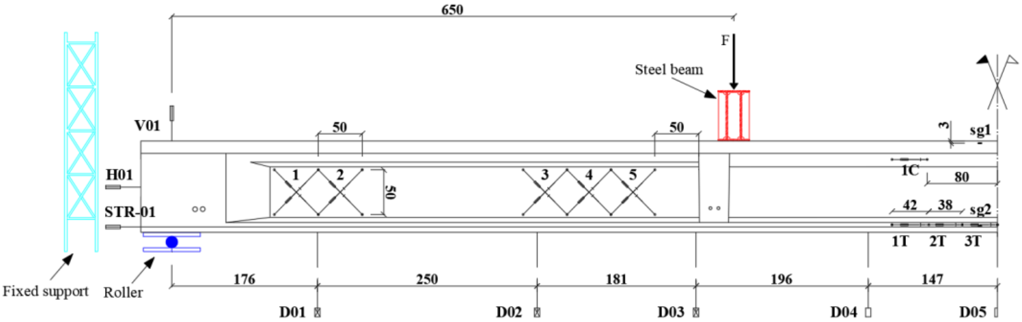

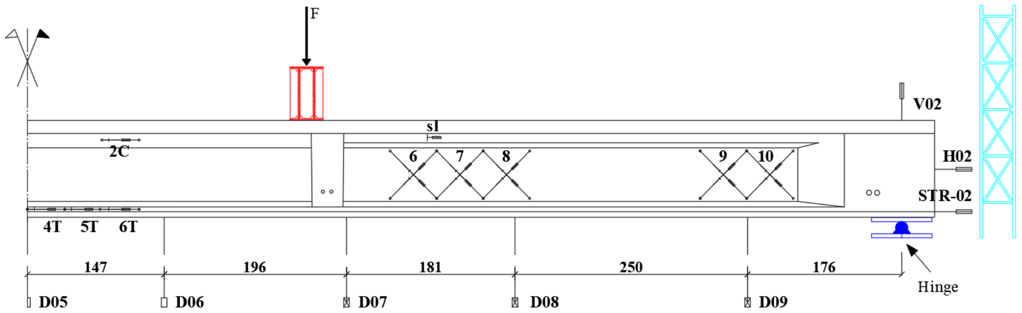

Figure C.5: Test setup and layout of the monitoring system installed on B7-P47/46 girder (unit: cm).

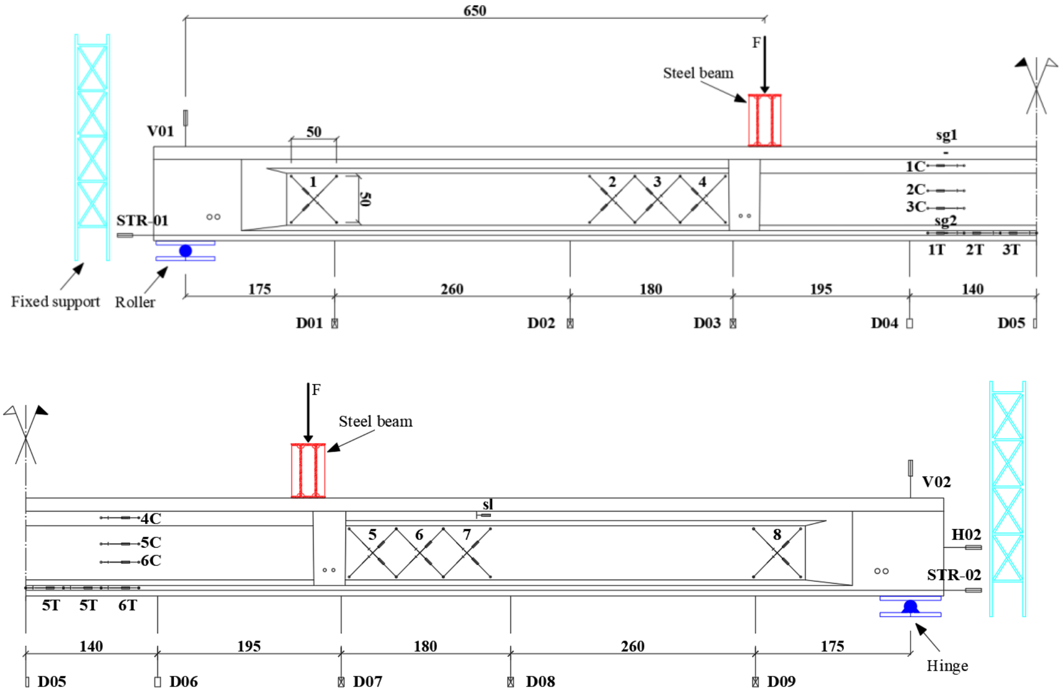

Figure C.6: Test setup and layout of the monitoring system installed on B6-Ab/P47 girder (unit: cm).

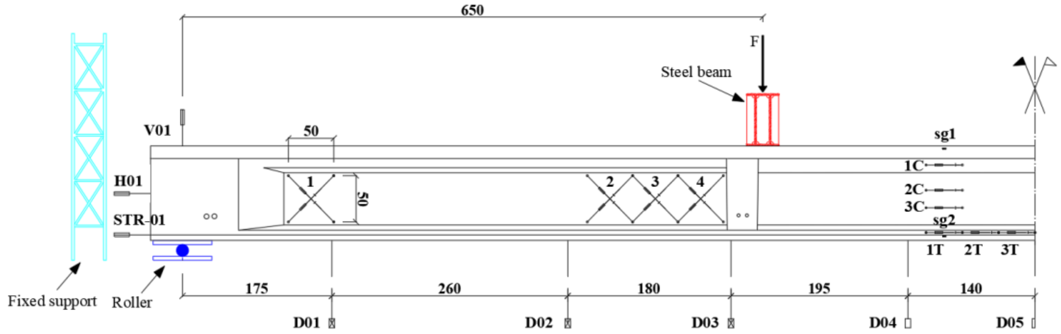

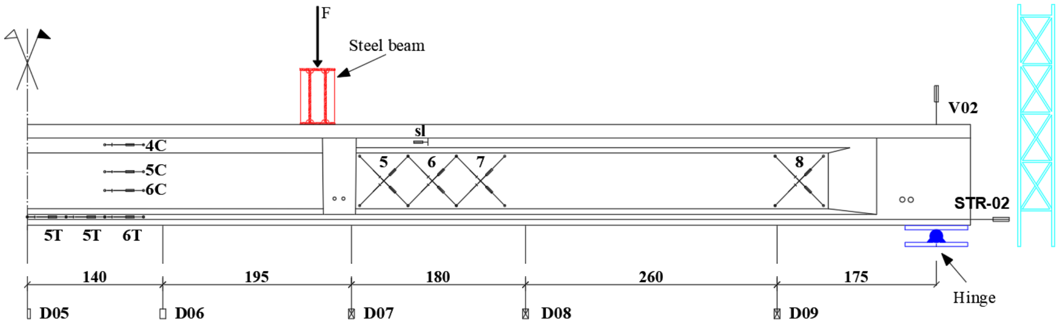

Figure C.7: Test setup and layout of the monitoring system installed on B6-P48/P49 girder (unit: cm).

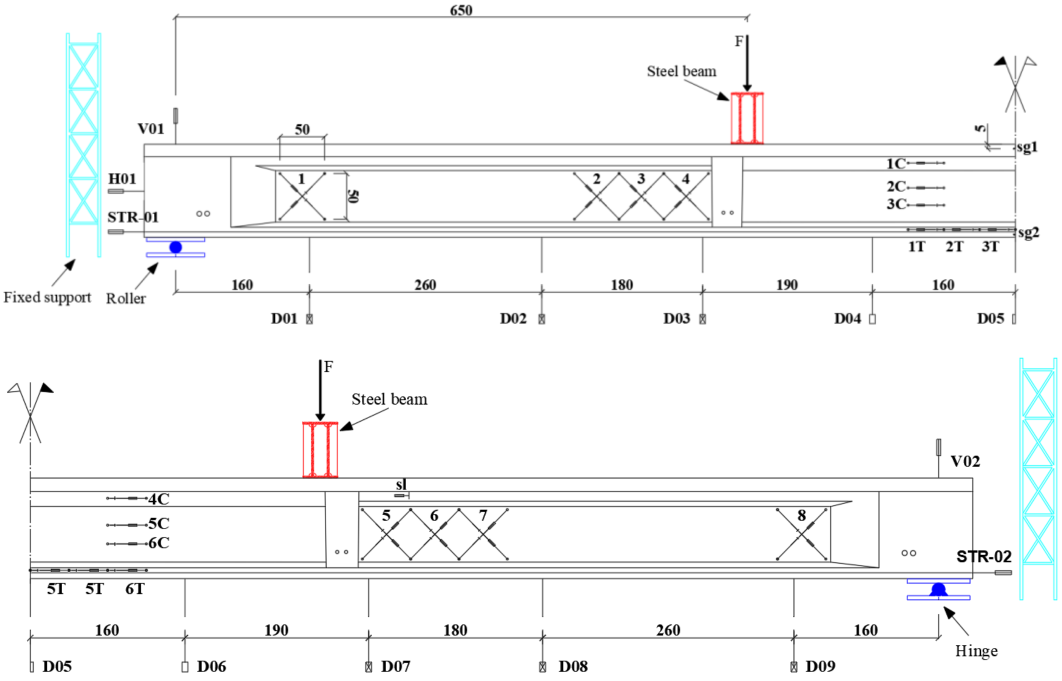

Figure C.8: Test setup and layout of the monitoring system installed on B10-Ab/P47 girder (unit: cm).

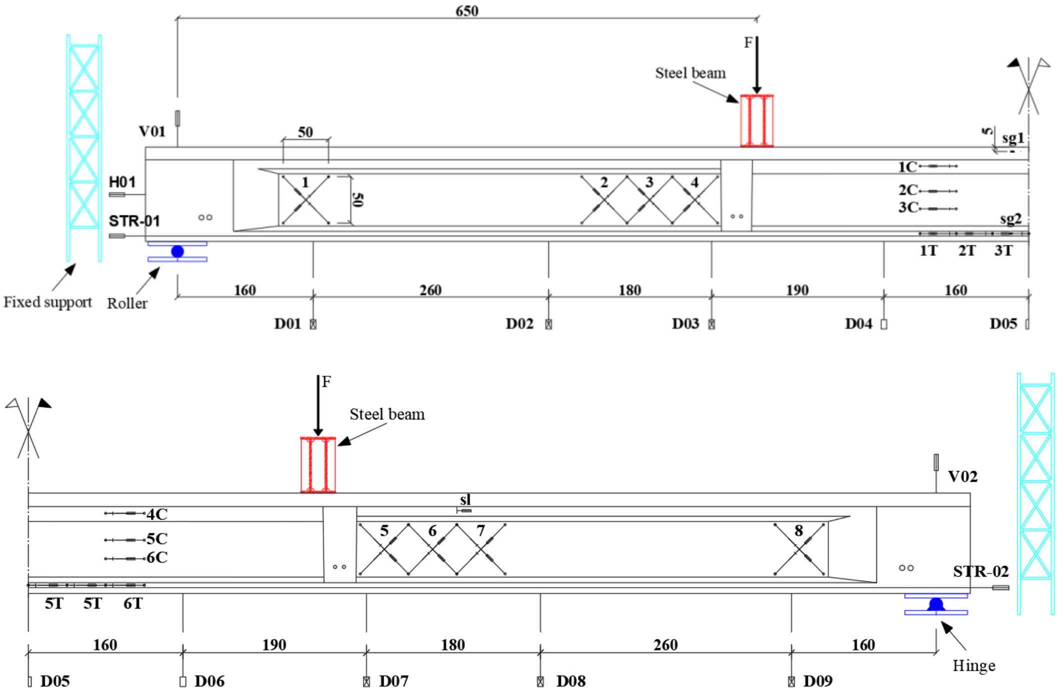

Figure C.9: Test setup and layout of the monitoring system installed on B5-P47/P46 girder (unit: cm).

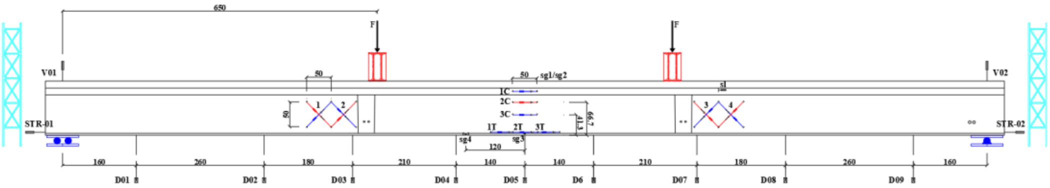

Figure C.10: Test setup and layout of the monitoring system installed on Bx2-Ab/P47 girder (unit: cm).

Appendix D

Three-point bending test: full measurements

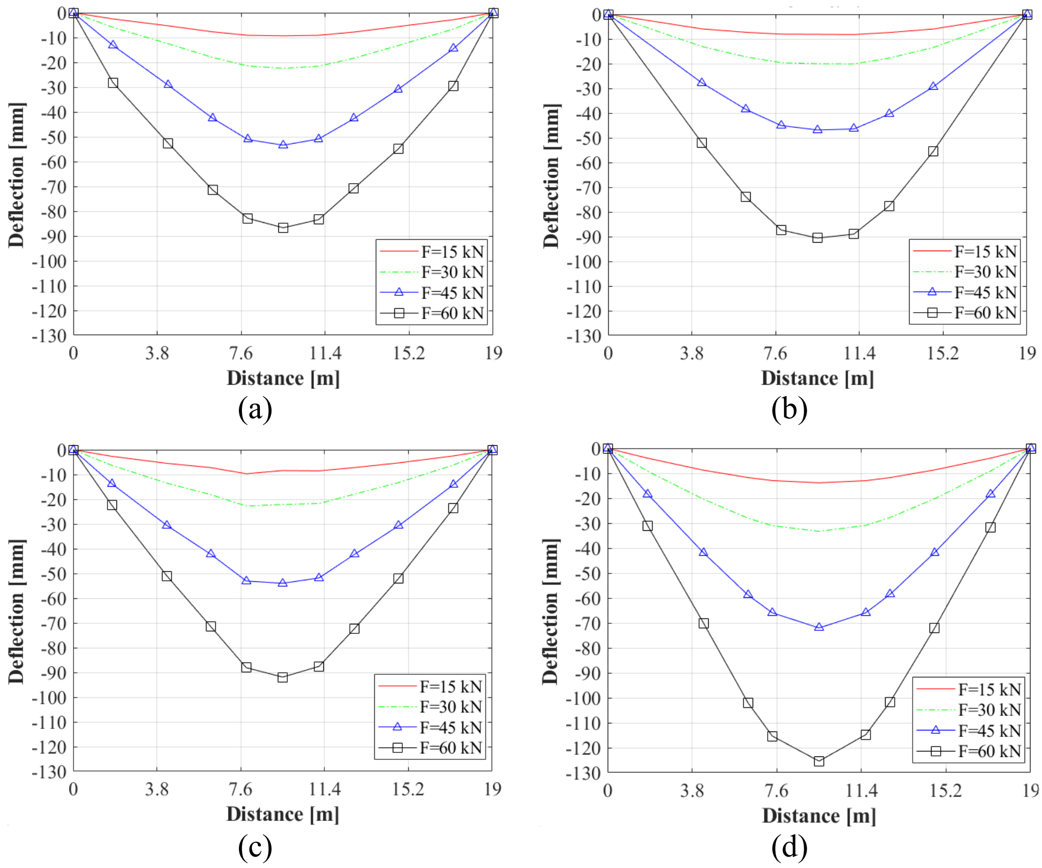

(a) (b) (c) (d)

Figure D.1: Deflection: (a) B3-P47/46, (b) B8-P47/46, (c) B4-P47/46, (d) B9-P47/46 girder.

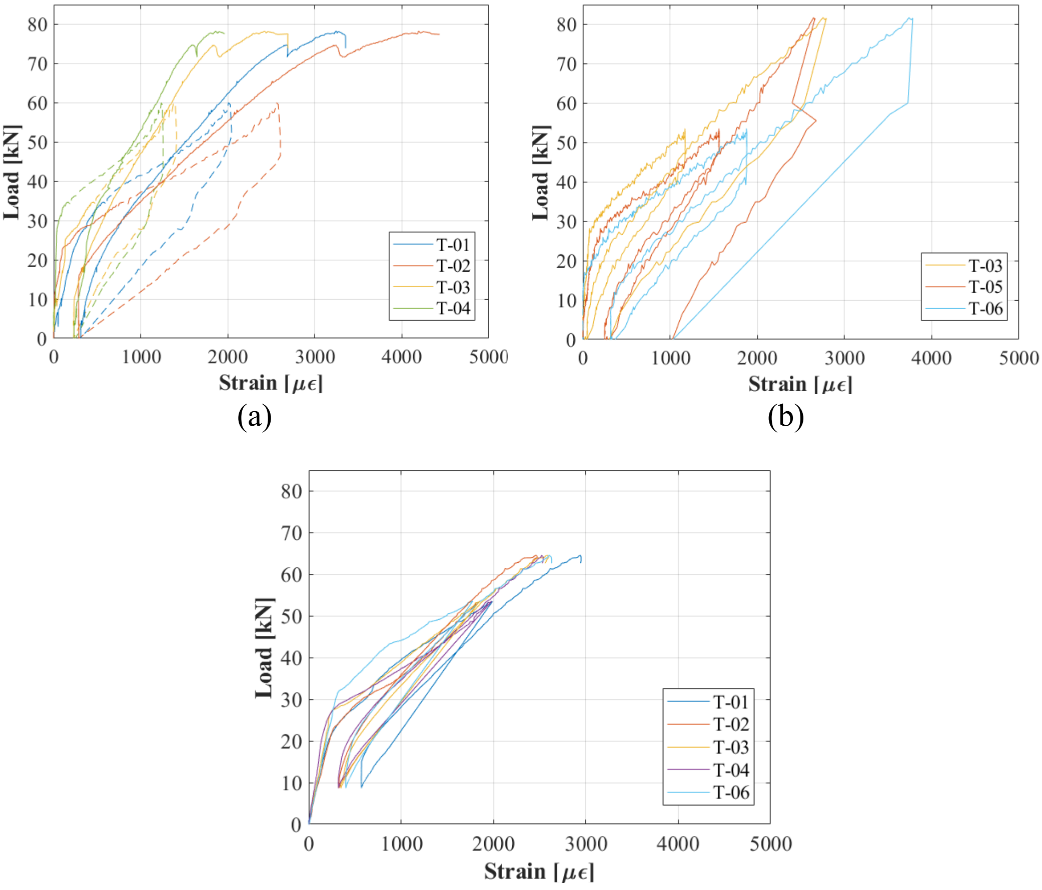

(a) (b)

(c)

Figure D.2: Load-tensile strain curves: (a) B3-P47/46, (b) B8-P47/46, (c) B9-P47/46 girder.

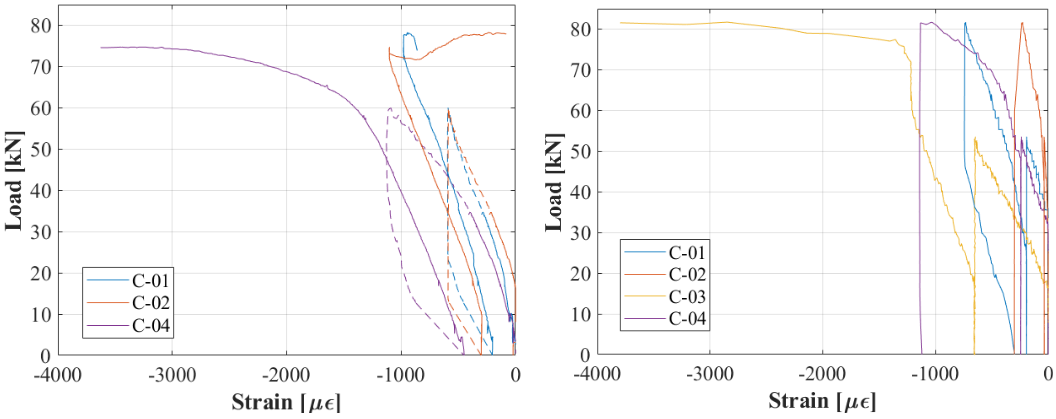

(a) (b)

Figure D.3: Load-compressive strain curves: (a) B3-P47/46, (b) B8-P47/46 girder.

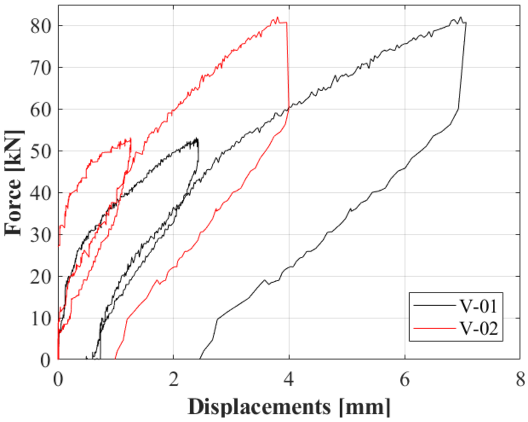

Figure D.4: Vertical displacement of the supports for the B8-P47/46 girder.

Four-point bending test: full measurements

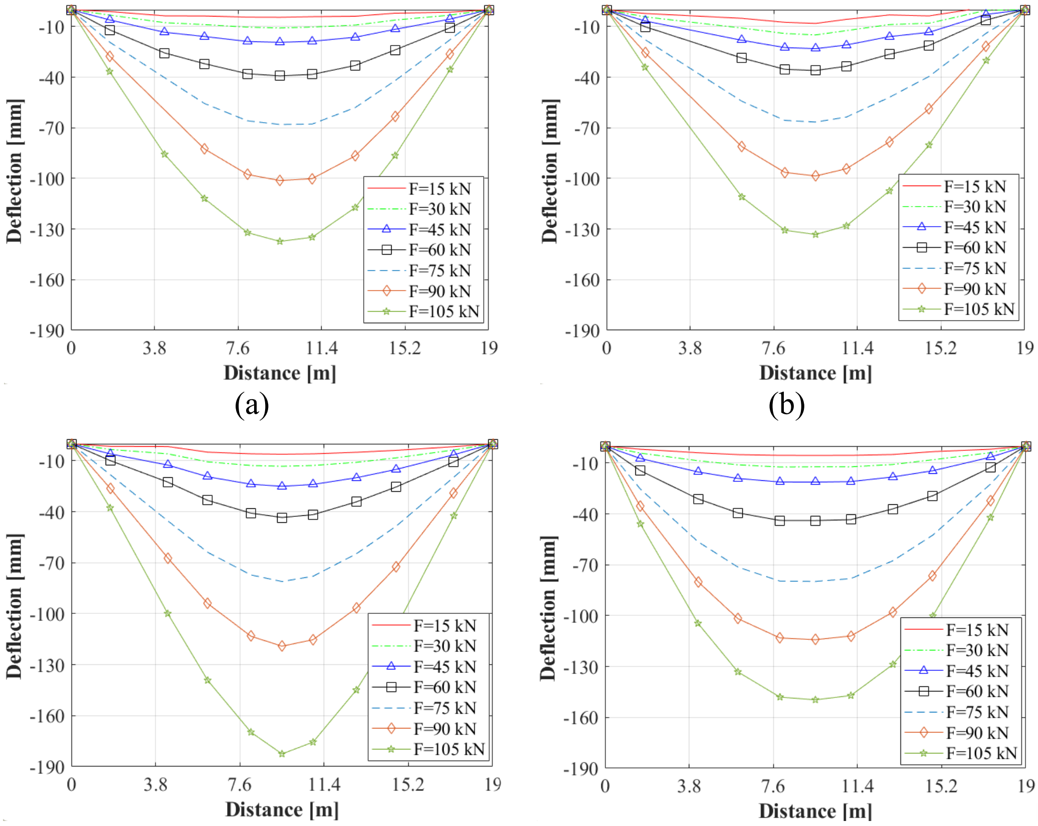

(a)

(b)

(c)

(d)

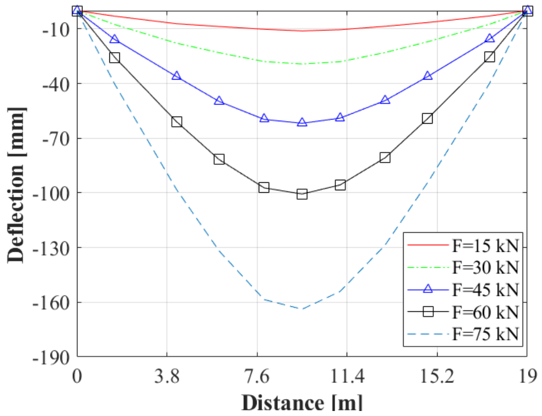

(e)

Figure D.5: Deflection: (a) B7-P47/46, (b) B6-Ab/P47, (c) B6-P48/49, (d) B10-Ab/P47, (e) B5-P47/46 girder.

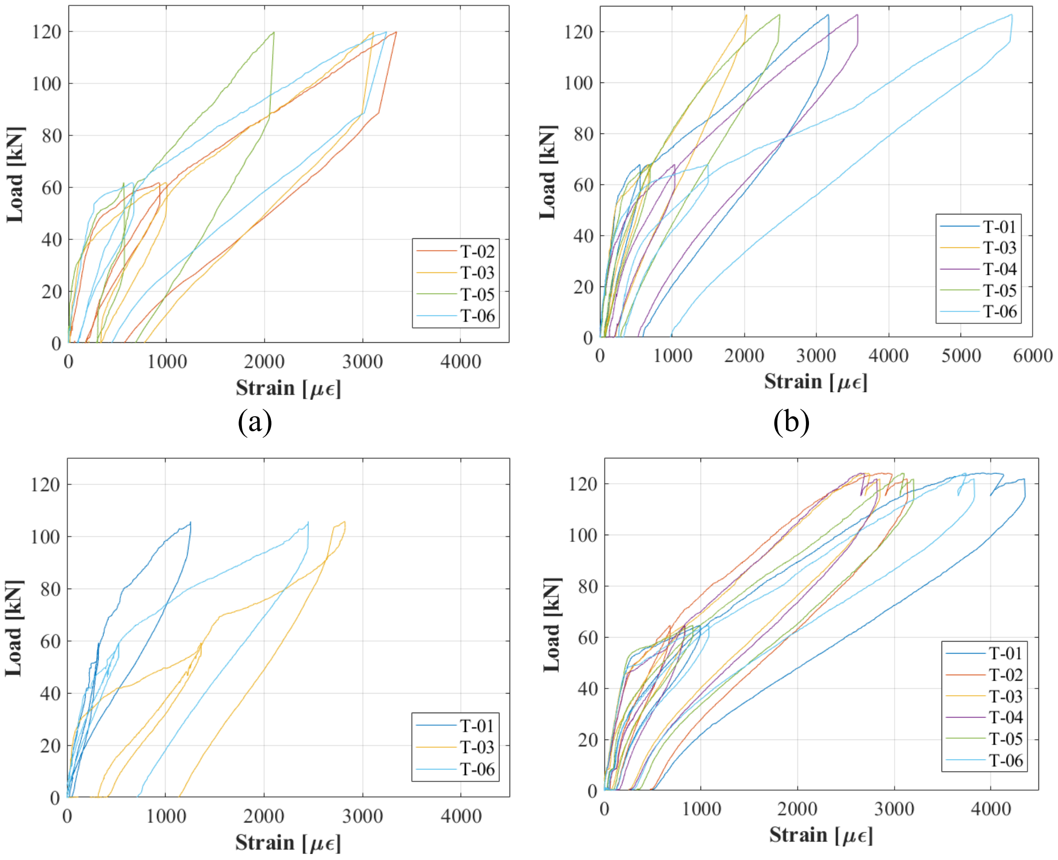

(a)

(b)

(c)

(d)

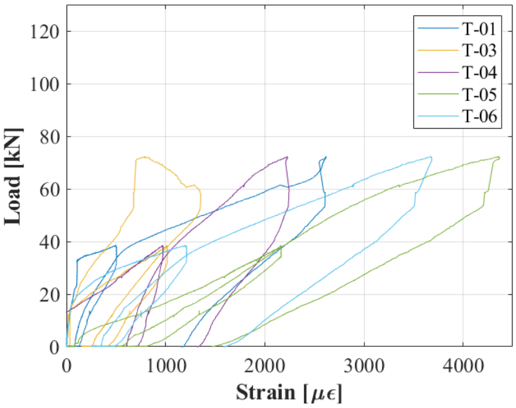

(e)

Figure D.6: Load-tensile strain curves: (a) B7-P47/46, (b) B6-Ab/P47, (c) B6-P48/49, (d) B10-Ab/P47, (e) B5-P47/46 girder.

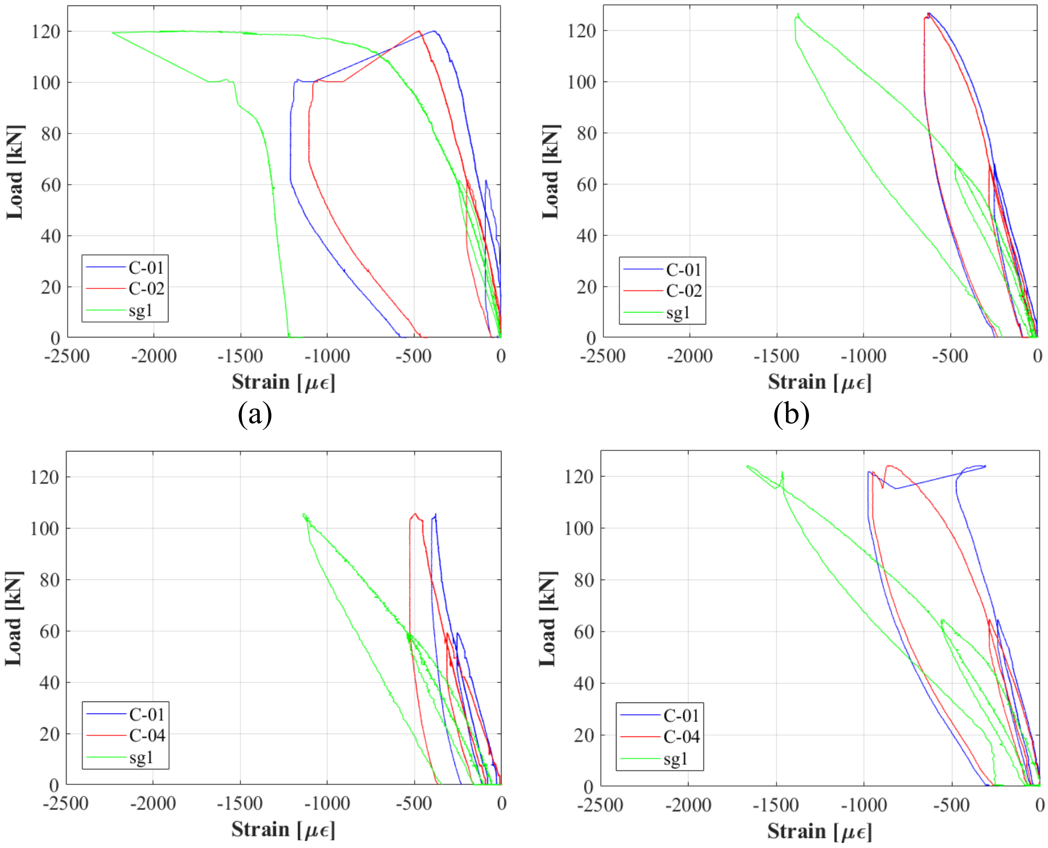

(a) (b)

(c) (d)

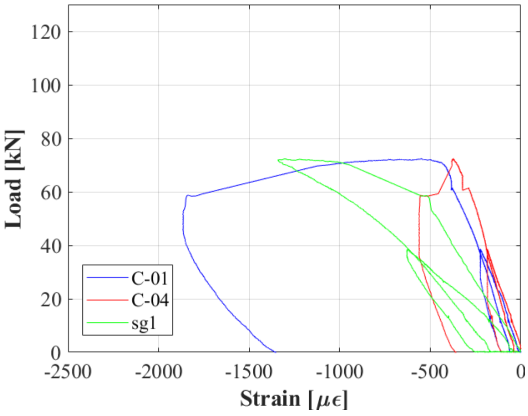

(e)

Figure D.7: Load-compressive strain curves: (a) B7-P47/46, (b) B6-Ab/P47, (c) B6-P48/49, (d) B10-Ab/P47, (e) B5-P47/46 girder.

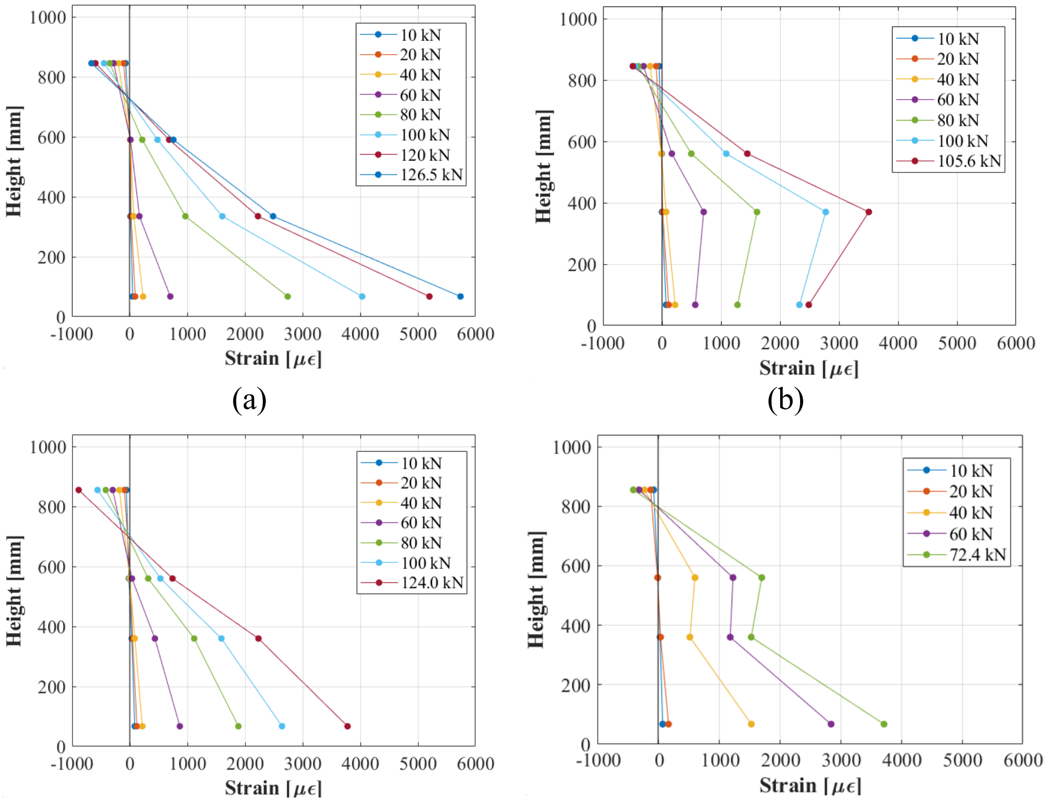

(a) (b)

(c) (d)

Figure D.8: Load-compressive strain curves (C-04, C-05, C-06, and T-06): (a) B6-Ab/P47, (b) B6-P48/49, (c) B10-Ab/P47, (d) B5-P47/46 girder.

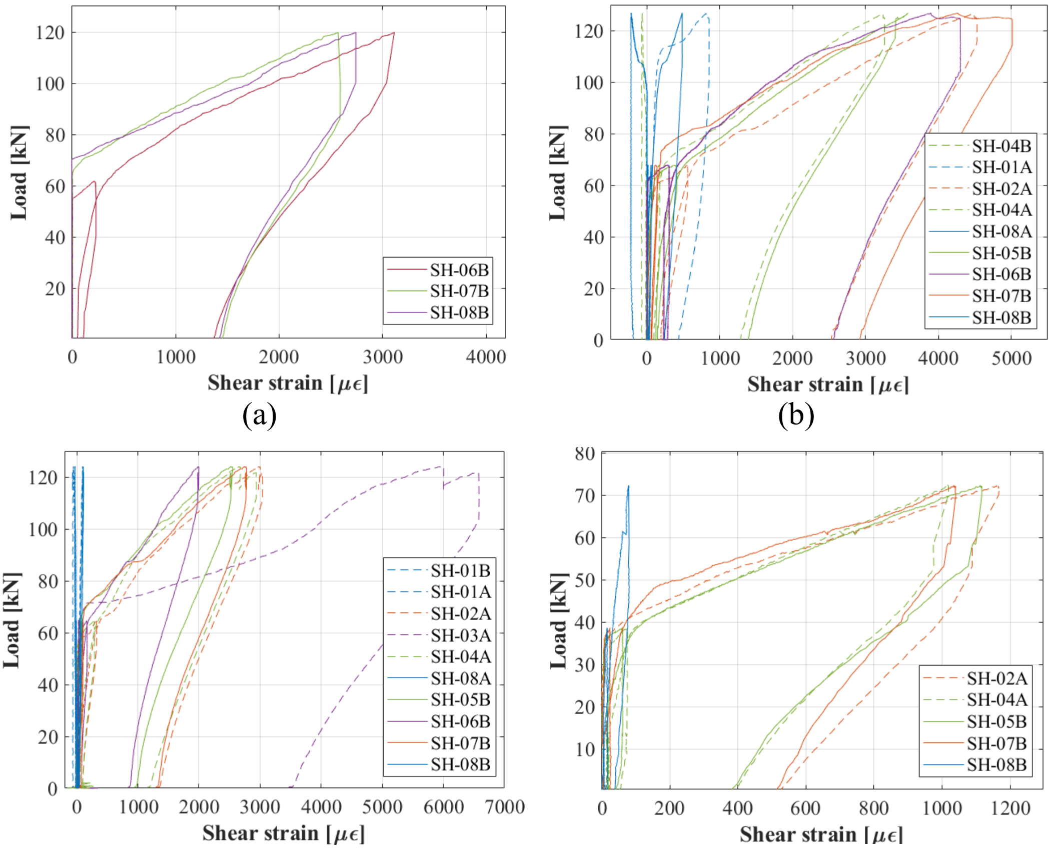

(a) (b)

© (d)

Figure D.9: Load-shear strain curves: (a) B7-P47/46, (b) B6-Ab/P47, (c) B10-Ab/P47, (d) B5-P47/46 girder.

Box girder load test: full measurements

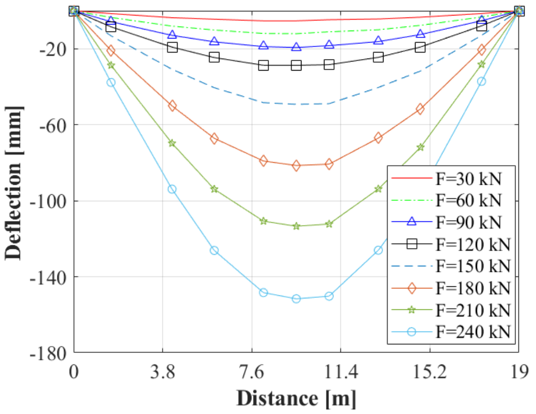

Figure D.10: Deflection of the Bx2-Ab/P47 girder.

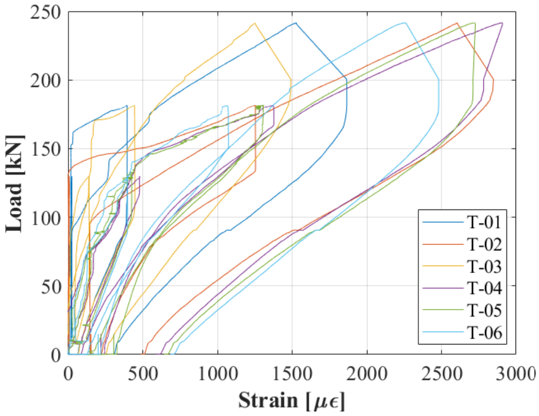

Figure D.11: Load-tensile strain curves of the Bx2-Ab/P47 girder.

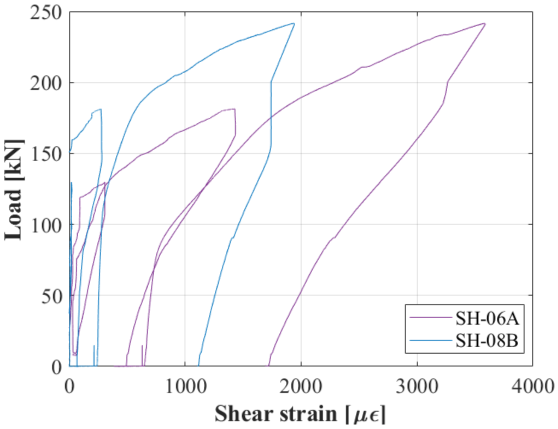

Figure D.12: Load-shear strain curves of the Bx2-Ab/P47 girder.

Appendix E

Normal distribution fitting of mechanical properties

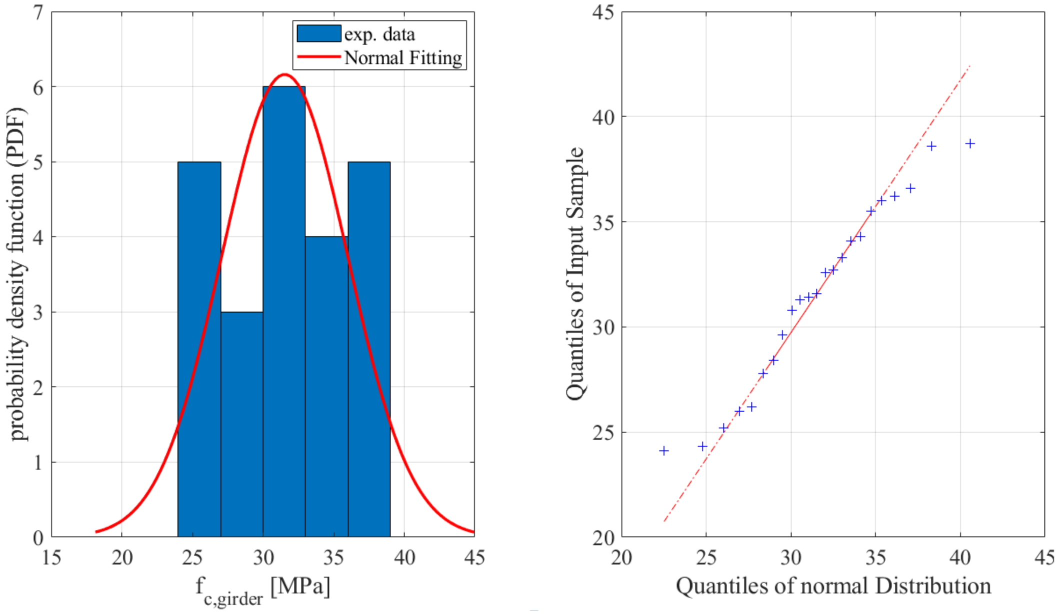

Figure E.1: Normal distribution fitting of girder concrete strength.

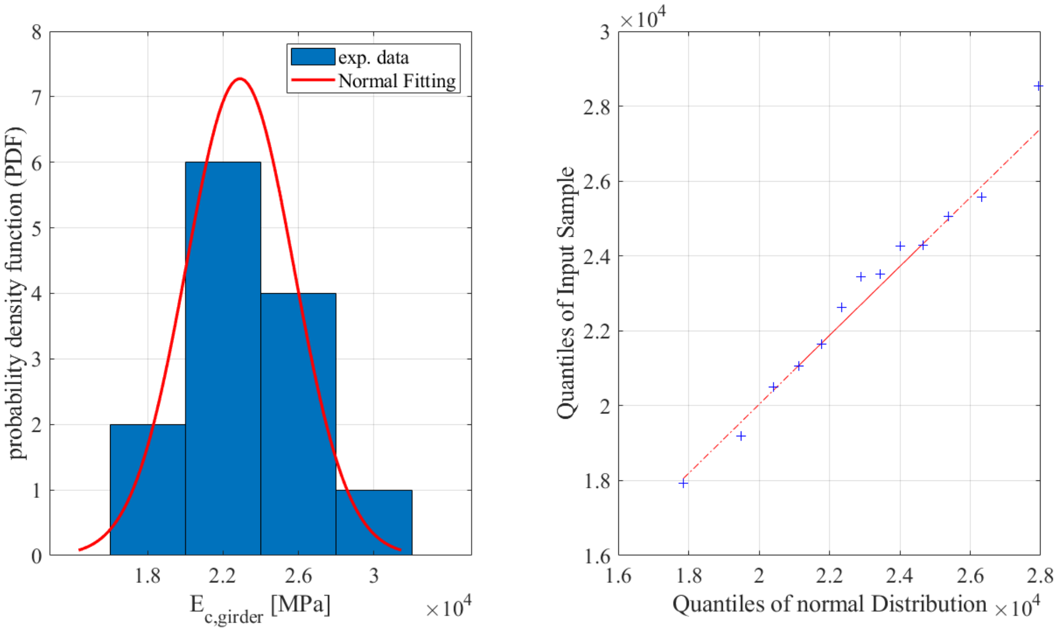

Figure E.2: Normal distribution fitting of girder concrete modulus of elasticity.

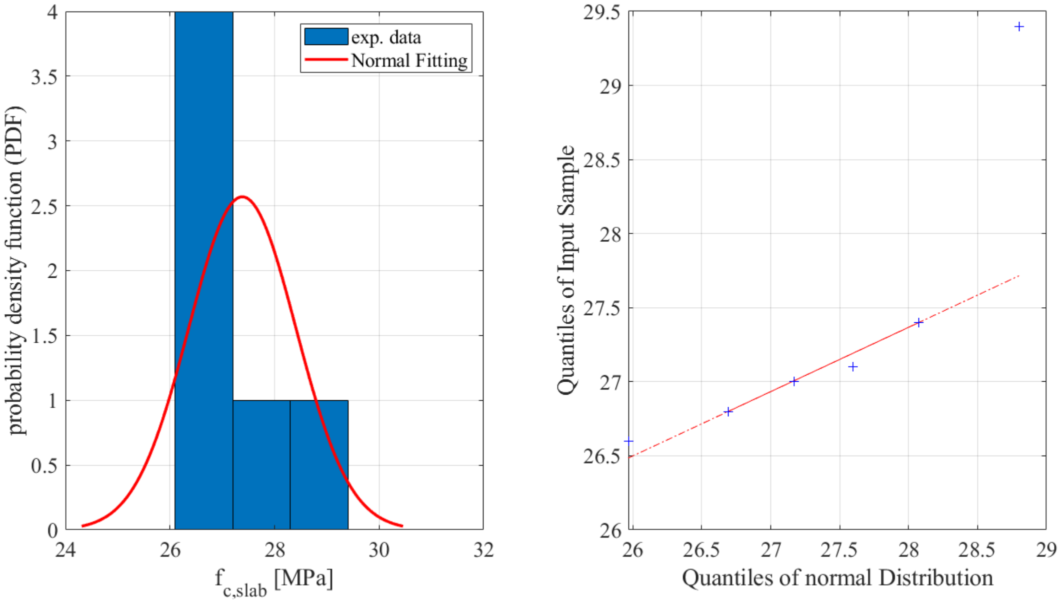

Figure E.3: Normal distribution fitting of slab concrete strength.

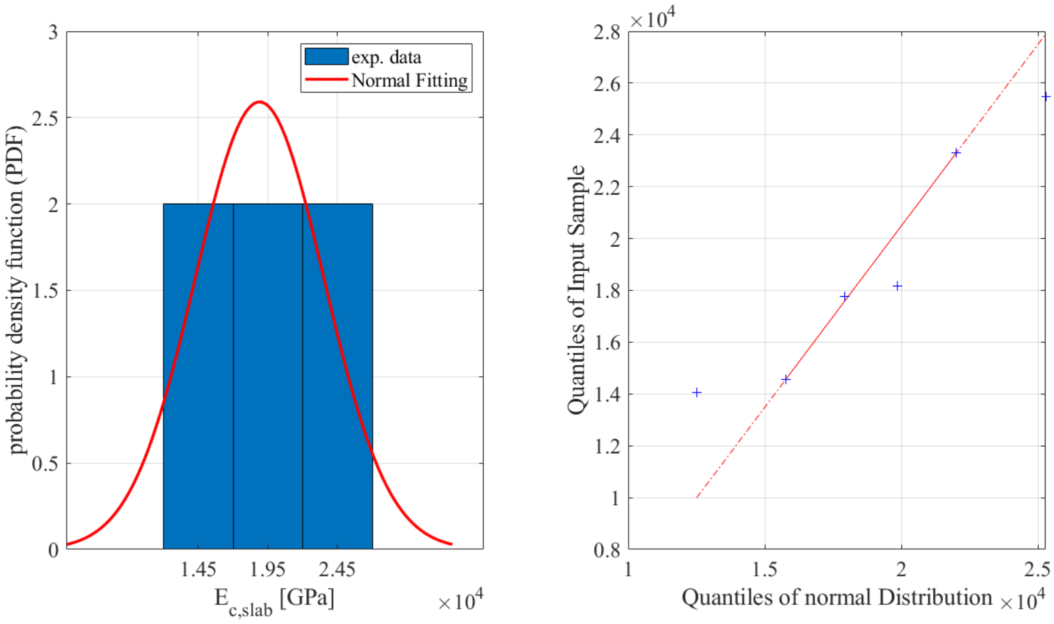

Figure E.4: Normal distribution fitting of slab concrete modulus of elasticity.

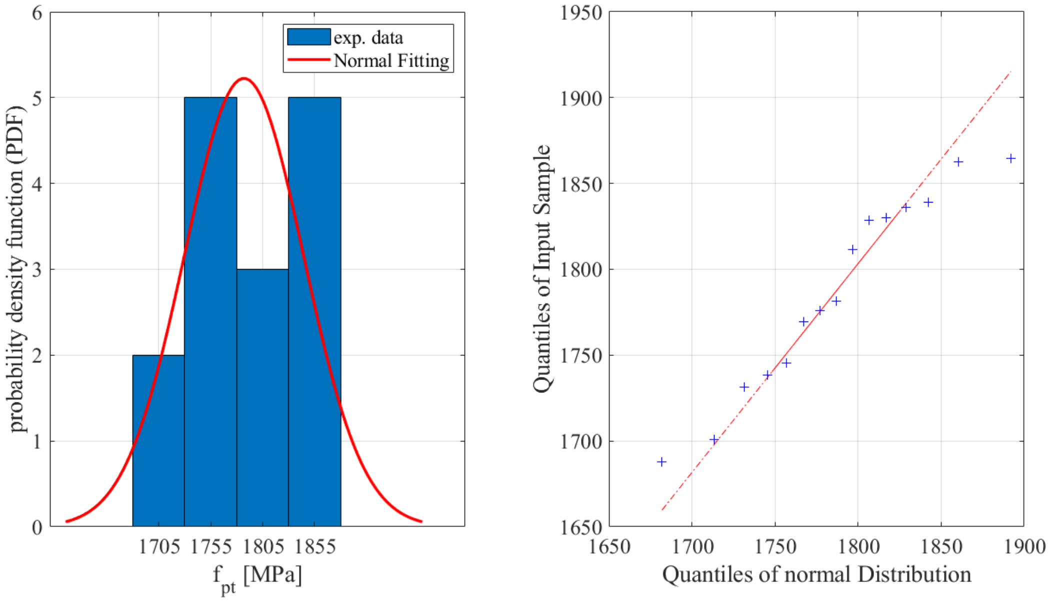

Figure E.5: Normal distribution fitting of strand tensile strength.

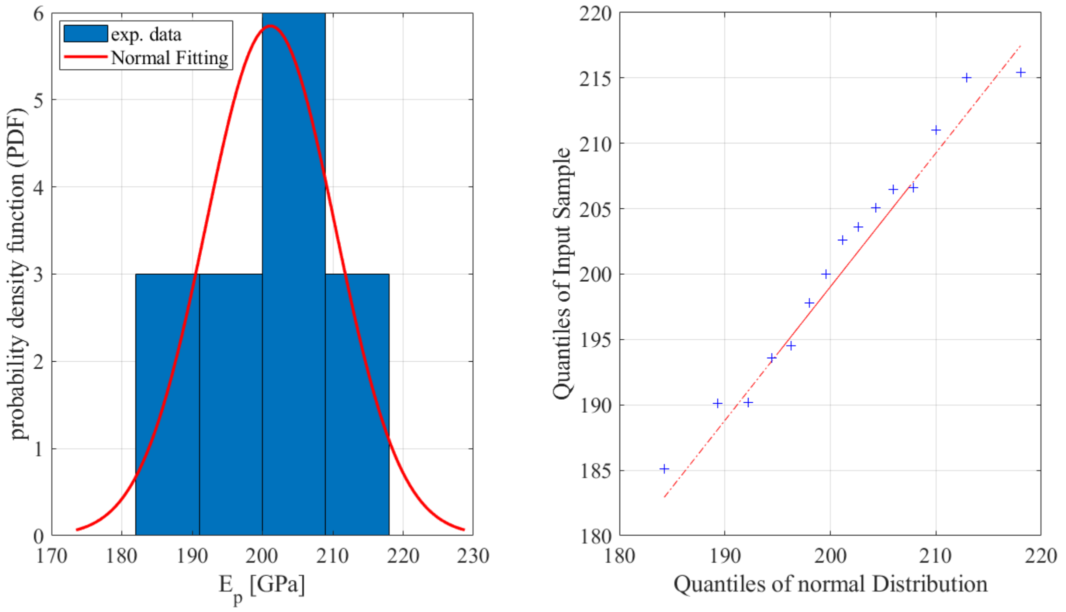

Figure E.6: Normal distribution fitting of strand modulus of elasticity.

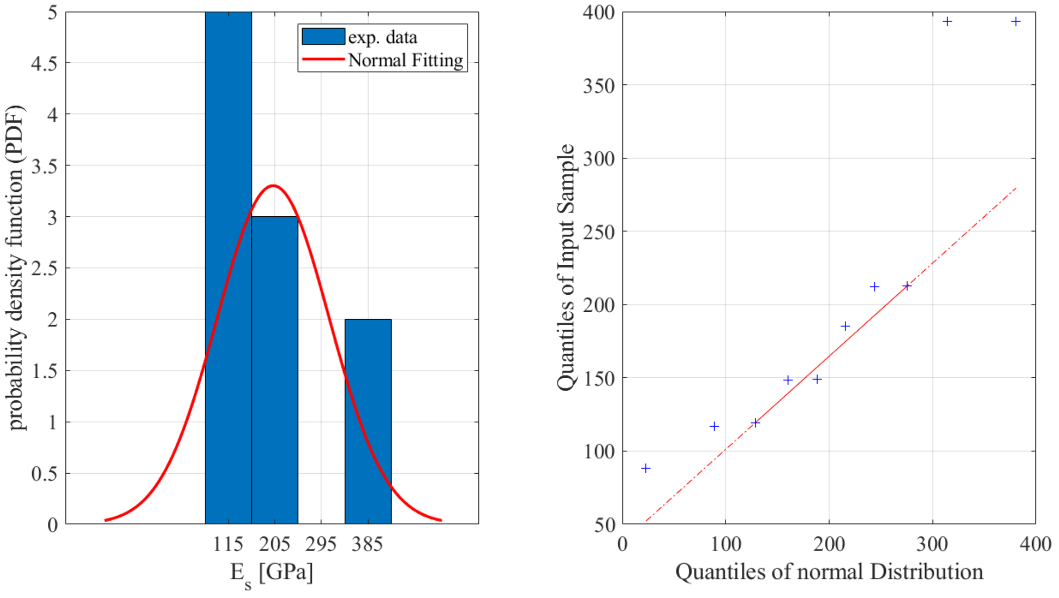

Figure E.7: Normal distribution fitting of rebar modulus of elasticity.

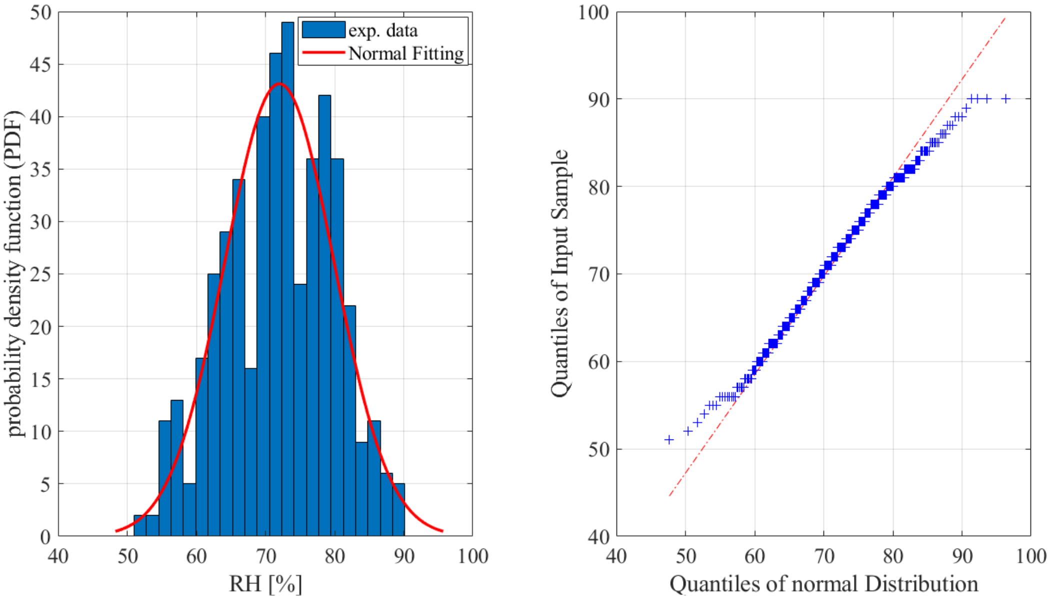

Figure E.8: Normal distribution fitting of relative humidity.